Lab-on-chip technological optimization for integration of high frequency acoustic functions : first application to actuation in a microfluidic channel

Sizhe Li

Année 2016

N° ORDRE : 16/15

THESE

présentée pour obtenir le diplôme de docteur de

L'UNIVERSITE DE VALENCIENNES ET DU HAINAUT CAMBRESIS
Sciences Pour l'Ingénieur (SPI)

Spécialité Micro et Nanotechnologies, Acoustique et Télécommunications

par

Sizhe LI

Optimisation technologique d'un laboratoire sur puce intégrant des fonctions acoustiques hautes fréquences : premières applications à l'actionnement en canal microfluidique

Soutenue publiquement le 25 Mai 2016
Soutenue à L'UNIVERSITE DE VALENCIENNES ET DU HAINAUT CAMBRESIS
Soutenue devant le jury composé de :

Pr Rosaria FERRIGNO	Rapporteur - l'Université Claude Bernard Lyon 1
Pr Michel AILLERIE	Rapporteur-l'Université de Lorraine– Central-Supélec
Pr Stéphane SERFATI	Le président du comité de soutenance/Examinateur-Université de Cergy Pontoise
Dr Florence RAZAN	Examinateur- École Normale Supérieur de Rennes
Pr Bertrand NONGAILLARD	Directeur de Thèse – Université de Valenciennes
Dr Georges NASSAR	Co-Directeur de thèse – Université de Valenciennes
Dr Julien CARLIER	Co-encadrant – Université de Valenciennes
Dr Fabrice LEFEBVRE	Examinateur - Université de Valenciennes
Pr XingZhong ZHAO	Membre invité- Professeur à l'Université de Wuhan

Ph.D. Thesis

Lab-on-chip technological optimization for integration of high frequency acoustic functions: first application to actuation in a microfluidic channel

Department : Institut d'Electronique, de Micro-Electronique et de Nanotechnologie/Département d'Opto-Acousto-Electronique (IEMN/DOAE)

Specialty : Micro et Nanotechnologies, Acoustique et Télécommunications

Name : Sizhe Li

Supervisors : Prof. Bertrand Nongaillard

Co-supervisors: Dr. Julien Carlier

Dr. George Nassar

Contents

Abstract

The interest of ultrasounds for media characterization or for actuation when using more power is well known. Nevertheless, the integration of these acoustic functions in silicon based Lab-on-chips requires specific technological developments. The possibility to use high frequency bulk acoustic waves in this kind of systems for characterization or detection has been presented previously in another PhD work.

The main objective of this work was to optimize acoustic energy transfer to a microfluidic channel in a frequency range between 500 MHz and 1000 MHz. To do that, the main technological developments achieved among others concern the coating of the guiding mirrors to avoid acoustic mode conversion and ZnO thick films sputtering for the fabrication of piezoelectric transducers.

The developed system has been used for particles detection or concentration evaluation. Moreover, a first evaluation of fluids/particles actuation was demonstrated, along with temperature evaluation using ultrasound were achieved in microfluidic channels.

Key words: High frequency acoustic, Lab-On-Chip, microfluidic, actuation

Résumé

L'intérêt des ultrasons pour la caractérisation de milieux ou pour l'actionnement à plus forte puissance n'est plus à démontrer. L'intégration de fonctions acoustiques substrats de silicium soulève en revanche de nombreux problèmes technologiques. Le travail de thèse présenté fait suite aux premiers développements technologiques qui ont permis la validation du concept de caractérisation acoustique haute fréquence en canal microfluidique.
Les principales avancées de ce travail concernent l'optimisation du transfert de l'énergie acoustique dans le canal microfluidique dans une bande de fréquence allant de 500 à 1000 MHz. Des dépôts de couches minces sur les miroirs et le développement de transducteurs en couches épaisses constituent les principales avancées.
Une première évaluation de l'actionnement de fluides ou de particules en canal microfluidique est également présentée ainsi qu'une application du système à la mesure de température en canal microfluidique par ultrasons.

Mots clés: Acoustique haute fréquence, laboratoire sur puce, microfluidique, actionnement

Acknowledegment

First of all, I would like to express my thanks to the reviewers, Prof. Rosaria FERRIGNO from Université Claude Bernard Lyon 1, Prof. Michel AILLERIE from Université de Lorraine – Central-Supélec, Prof. Stéphane SERFATI from Université de Cergy Pontoise and Dr. Florence RAZAN from École Normale Supérieur de Rennes. I have to thank also Prof. XiongZhong Zhao from Université de Wuhan who accepts to evaluate my Ph.D. work and to participate to the jury.

I would like to express my deep gratitude to all those who gave me the possibility to complete this thesis.

I would like to thank my supervisors Professor Bertrand Nongaillard and Professor Shishang Guo for their advices without reservation. They guided my experiments personally so that I learned valuable technique skills. Along with the academic ideas offered to build my thinking system step by step.

I would like to express my gratitude to my co-supervisor Dr. Julien Carlier. He guided my in detail from the experimental scheme implementation to the thesis modification. He also helped me a lot in my social life with university inscription.

I would like to express my gratitude to my co-supervisors Dr. George Nassar, Dr. Pierre Campistron who had given me abundant useful suggestions on the theoretical parts of my work.

I would like to thank my colleague Mr. Christophe Virgilio. He helped me with the simulation achieved to match my experiments. I would like to thank Dr. Weijiang Xu, he given me helpful suggestions in the lab.

I would like to express my gratitude to my friends Zhenkun Chen, Wei Wei and Tianchen Zhang. They sacrificed private time to help me with the SEM experiments.

I would also like to express my gratitude to all of you helped me in many ways. I have got a lot of helps from Mohamed Bentefrit, Sijia Gu, Tianjun Lin, Dr Tao Xu, Dr Jiaming, Dr Zhen Yuan and Dr. Xianglei Han. I would like to thanks all the engineers in the clean room of IEMN for their unselfish technical support and all the members in MAMINA group of IEMN –DOAE. I would also like to express my gratitude to all the staff in the Prof. ZHAO‟s group in city of Wuhan. In the lab of France I learned to have a moderate mind to face scientific research and life. In the lab of Wuhan I learned to work efficiently and summarize the results to publications in time. I appreciate the environment earn profit from the resource in both of these groups.

I would like to express my thanks to my parents for their lasting love and my wife Liying Weng. She always stood by the side of me in the long time passed by.

At last, I dedicate this dissertation to my mother Madam Deyu Xiao. Her continuous encouragement and meticulous care accompanied my growing up.

Thanks again and best wishes for all of you.

Abbreviations

LOC	lab on a chip
μTAS	micro total analysis system
CTCs	circulating tumor cells
POCT	point of care test
MEMS	microelectromechanical systems
IC	integrated circuit
MPA	Micropitette aspiration
PFF	pinched flow fractionation
DC	direct current
FACS	fluorescence activated cell sorting
μFACS	microfluidic flow cytometer
BSAW	standing bulk acoustic wave
SSAW	standing surface acoustic wave
IDTs	interdigital transducers
FIDTs	focused interdigital transducers
RF	radio frequency
WBCs	white blood cells
SBAT	single beam acoustic tweezers
PZT	lead zirconate titanate
SAW	scanning acoustic microscope
DRIE	deep reactive ion etching
TMAH	Tetramethylammonium hydroxide
IPA	iso-Propyl alcohol
LPCVD	Low Temperature Oxide
PECVD	Plasma-enhanced chemical vapor deposition
SEM	scanning electron microscope
ICP	Inductively coupled plasma
ZnO	Zinc oxide
PCB	printed circuit board
PDMS	Polydimethylsiloxane
EDM	electro discharge machining
UV	Ultraviolet Rays
DC	direct current
FBAR	thin film bulk acoustic resonator
FFT	Fast Fourier Transformation
L	longitudinal wave
S	shear wave
TFD	temperature-dependent fluorescent dye
TLCs	thermochromic liquid crystals
NMR	nuclear magnetic resonance
PS	polystyrene
KI	potassium iodide

General introduction of the thesis

Lab-on-chip is a highflying field developed in the several decades. It is a technology for manipulating small volumes of fluids in a highly integrated microchip, which provides the possibilities to miniaturize complex laboratory procedures in an automatic means. There are abundant advantages that microfluidics supplies, including high surface volume ratio, low consume of samples, multiple functions integration and fast sampling times. This flexible platform takes benefit of a versatile format for the incorporation of various detection schemes, thereby leading to increased sensitivity. At present, the optical, magnetic, electrical and acoustic modules had been already combined in a single microfluidic device.

In the acoustic-microfluidic field, the interest of bulk acoustic wave (BAW) and of the surface acoustic wave (SAW) has been demonstrated. Concerning the cells manipulation, the standing-wave based method is widely explored. In the standing wave field, particles/cells can be trapped into nodes or anti-nodes, depending on the density and compressibility which are different from the surrounded medium. Meanwhile, particles/cells can be separated depending on the size difference in continuous flow. However, these acoustic methods in microfluidics are mainly working in low frequency (less than 50 MHz) and are applied for cell clusters.

The single cell measurements at high resolution can help to analyze and interpret cellular heterogeneity. The “acoustic tweezers” technology offers a flexible tool for studying behaviors of an individual cell in a non-contact mode. An essential condition of this method is the high frequency applied so as to match the acoustic wavelength and cell dimension. At present, the most used high frequency acoustic device in medical field is the acoustic microscopy, which requires a bulky, expensive set-up and the characterization method is only imaging. The on-chip acoustic characterization at high frequency is under development.

In another aspect, there are a handful of studies for acoustic deflection of several cells in lab-on-chip. Cells can be deflected to different outlets then collected, or the positions of cells are controlled in the acoustic field to study intercellular communication in cell culture. These methods integrate surface acoustic wave technology in microchips. However, the surface acoustic wave methods are limited in these disadvantages: hard to fabricate at high frequency, difficult to be integrated on silicon/glass material, lack of on-chip characterization and low-throughput in manipulation. If we target single stem cell research and low concentration rare cells screen, the interest of high frequency bulk wave (above 200 MHz) integrated in microfluidics is emerging. For a better integration, the acoustic device associates with both functions of characterization and manipulation is more attractive.

Previous work in our group had demonstrated a novel silicon -based high frequency (GHz range) bulk acoustic wave sensing microsystem. Waveguiding was achieved in the microsystem and on-chip acoustic detection of red blood cells was acheived in low concentration (1%). However, the channel width is limited to less than 50 μm due

to the high acoustic attenuation, and bushing phenomenon which limits the potential cancer cell characterization.

In this thesis, we demonstrated an improved device making it possible to achieve high frequency characterization and actuation in microfluidic platform. The working frequency of the transducer was restricted in around 500 MHz to 850 MHz. The maximum channel width was 300 μm and cylindrical lens were designed to focus the energy.

In the first chapter, various sensing and actuation technologies based on the microfluidic systems are reviewed. Different methods are compared for cell mechanical properties evaluation in lab-on-chip, especially single cell viscoelasticity characterization. Acoustic microscope is particularly suitable for quantitative measurements of mechanical properties of single cell, because the measured sound speed and attenuation are closely linked to the acoustic impedance of the cell. Compared with optical, magnetic and electrical methods, acoustic measurements is dispensable of marker labeling. Likewise, the acoustic manipulation in microfluidics show these benefits, and the applications including fast mixing, enrichment of cells and separation cancer cells in continuous flow.

Meanwhile, the high frequency bulk acoustic device can offer a flexible means for cell manipulation in single cell resolution, in the case that the wavelength is close to the cell dimension. The existing methods of “acoustic tweezers” in microfluidics are introduced, which are mainly based on bulk standing waves and surface standing waves to generate nodes and anti-nodes in the channel for particles/cells deflection. However, few references of high frequency methods are developed in lab-on-chip. The high frequency acoustic platform showed great potential in cell manipulation for the research of the cellular interaction in cell culture.

In the second chapter, we present the technological development for the improvements of the acoustic characterization chip. Several parameters had to be improved to optimize acoustic wave guiding in that frequency range, including the thickness and geometry of ZnO film, the depth of 45° mirrors and microchannel, as well as the optimization of cylindrical lens for focusing the acoustic beam in local area. Simulations made it possible to determine the optimal thickness of layers on 45° mirrors, so as to avoid mode conversion and reduce acoustic noise in the propagation. Concerning the ZnO film fabrication, the ground electrodes were replaced from Pt to Ti, and then the internal stress during sputtering process was reduced thanks to multi-layers process.

In the third chapter, we used S parameters to characterize the acoustic propagation. Gold, copper and silicon oxide layers were deposited on 45° mirrors and S_{21} parameters were tested to compare the longitudinal wave conversion. We designed various systems including one vertical mirror, two vertical mirrors and lens structures. KI solutions of different concentrations were used to characterize the acoustic sensitivity in different systems. The attenuation coefficient of KI was measured thanks to the comparison with the measurements using water. Acoustic reflection evaluations in systems integrating lens structures showed high resolution and the possibility to detect particles presence in the microchannel. It was also possible to evaluate the

temperature of water inside the microchannel thanks to the variation of attenuation of the liquid depending on the temperature Moreover, particle manipulation *via* high frequency acoustic forces was observed. Travelling waves were used to push particles and also to rotate particles in the acoustic field. Furthermore, the lens focused acoustic forces induced strong acoustic streaming and actuated particles in a high speed with low input power. Meanwhile, this structure showed the possibility to separate particles with different diameters in the microchannel within the acoustic field.

Chapter1

Introduction to lab-on-chip

With the development of biological science and biomedical medicine, current detection and analysis methods meet the bottle-neck for the internal need of requirement. Considering the multiplicative biochemical samples and excessively high price, there is a definite demand for developing a high throughput, fast reaction, low-cost and high sensitivity platform. Meanwhile, the analysis equipment is progressing toward microminiaturization, integration, intelligence and portability. Lab-on-chip, or Microfluidics, is a technology that integrates basic functions of biology/chemical laboratories into a chip, and the function modules are in micrometer/nanometer scale. It consists in a microchannel network, micro pumps and micro valves so that controllable fluid can run through the whole device, while different kind of sensors based on physical measurements make it possible to supervise chemical reactions or physical phenomenon. A significant advantage for microfluidic chip is that various unit techniques can be made up flexibly and large scale integration is possible in a micro-platform [1].

In recent years, lab-on-chip technology has a booming development which extends to food safety, clinical diagnosis, chemical synthesis, new drug screening, and ecological environment monitoring. The integrated functions into a micro-chip include pre-treatment, manipulation and reaction of samples and detection of reaction product. The advantages of these microchips are fast-response, real time, high throughput and low cost detection and analysis. Lab on a chip technology has also shown great abilities for precise manipulation of tiny samples in biology (DNA, protein and viruses in nanometer scale while cell and microorganism in micrometer scale) and *in situ* detection analysis.

Research at cellular level can be explored in microfluidic chips such as intercellular communication, stem cell research, single cell manipulation and cell co-culture [2]. Optical, electrical, magnetic and acoustic means are mainly combined in the lab-on-chip field to achieve at the micrometer scale the operations of cellular characterization and manipulation. There is a high interest in developing acoustic wave devices due to the non-contact and non-invasive properties. The existing approaches focus on surface acoustic waves (SAW) detection and induced acoustic streaming for bio-samples manipulation, and also on bulk acoustic waves (BAW) for cell clusters capture but in low frequency. Our microsystem integrates ultrasound transducers dedicated to bulk acoustic wave generation into the microfluidic platform with a working frequency range from 500 MHz to 800 MHz. The transmission mode is used for chemical detection and systems integrating lens were also designed for particle manipulation. The high frequency acoustic sensors and actuators in microfluidic device can present many potentialities in the cell research, especially in circulating tumor cells (CTCs) capture and release on-chip.

1.1 Microfludics and lab-on-chip technology

1.1.1 Basic concept and historical aspects:

Microfluidic Chip, called Micro Total Analysis Systems (μ -TAS) in Europe or Lab on a Chip in USA, come into being in the twentieth century and served as chip capillary electrophoresis at the beginning. With the co-operation of A. Manz and Harrison in 1992, the capillary electrophoresis separation technique based on micro-fabrication chip was firstly reported [3], thus presented the potential of μ -TAS as a new tool of analytical chemistry. In 2000, G. Whitesides et. al proposed the concept of "soft lithography" for rapid prototyping *via* fast molding in Polydimethylsiloxane (PDMS) [4]. The advantage of PDMS based chip is flexible fabrication and low-cost. Quake et al. put forward highly integrated chip with thousands of micro valves and hundreds of micro-reaction chamber in 2002 [5]. This landmark work introduced microfluidic chips from academic world to industry. The relative journal "lab on chip" started in 2001 and lead development of microfluidic chip in the whole world.

A special issue of "lab on a chip" was published in *Nature* in 2006 to elucidate the history, current situation and prospects of lab on a chip from different points of view [6]. G. M. Whitesides also indicated in the editorial that lab on chip will be the technology of the century. At this point, the strategic significance of lab on chip was identified by academic and industry in higher level and larger scale.

1.1.2 Applications and outlook

Since the 20th century, microfluidic chip has been developed from the laboratory to commercial product application stage in order to meet the needs with measuring and testing, along with various functions of microfluidic products coming into the market. Its application scope has been extended to micro reaction (biological and chemical synthesis), drug transport (micro injection, sustained release, targeted delivery mechanism), industrial and environmental monitoring, analysis processing, pharmaceutical and life science research, disease diagnosis in vitro and the food hygiene inspection, etc. So far, the representative key technologies based on microfluidic chip included three aspects:

(1) Microfluidics-based point of care test (POCT). POCT is defined as medical diagnostic testing that can be performed both in the time and place of direct patient care. This method can provide quick and effective biochemical indicators for each patient, and makes on-site guidance, disease detection, diagnosis and treatment to be a continuous process. The developing trend of POCT is miniaturization, simplicity of operation and fast response with body fluid importing directly. Microfluidic chip incorporation is a top priority for POCT considering the possessed properties of multi units grouped in a controllable platform and scale integration [7].

(2) Ultrahigh throughput screen platform- droplet-based microfluidics. When two insoluble liquids are introduced into the microfluidic chip, micro-droplets can be

formed by adjusting the flow speed in the special construction of the channel. These droplets (dispersion phase) can be used as a microreactors or carriers of biochemical samples [8]. The generated droplets can be operated flexibly with homogeneous sizes, altered shapes and excellent heat transfer properties. Single cells could be encapsulated in these microcompartments to measure expression of a reporter gene. Besides, the droplets generation frequency can reach hundreds of KHz, which shows enormous potentiality on high throughput drug screening.

(3) *In vitro* manipulation platform for mammalian cells- biomimetic laboratory. Microfluidic chip provides micro-channels in the similar dimensions of cells, and the on-chip physical and chemical content can be controlled to match the extracellular microenvironment, thus it can be the most interesting platform for simulating the way that cells work. Cell culture arrays can be achieved in microfluidics for long-term cellular monitoring, and cell analysis can be applied in drug screening, bioinformatics and quantitative cell biology. As shown in figure 1.1.1, there are several steps from on-chip cell culture to cell analysis of interest.

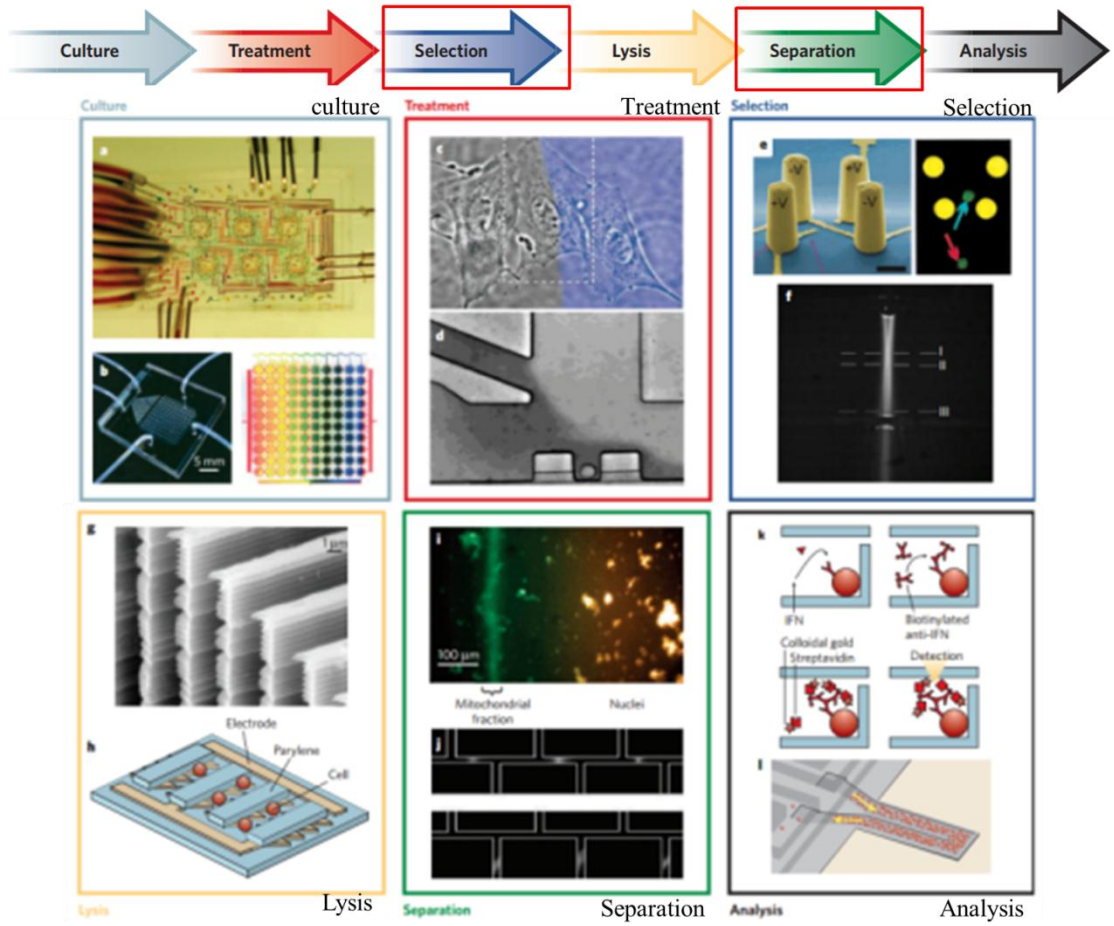

Fig 1.1.1 Micro system cells related experiments, including all the steps in cell analysis [9]. The acoustic functions can be used for the "selection" and "separation" domain.

1.1.3 Chip fabrication with MEMs techniques

Microelectromechanical systems (MEMs) are miniature devices integrating mechanical and electrical components. They are fabricated thanks to integrated circuit (IC) batch processing in size dimension from 1 to 100 μm. MEMs are manufactured by sophisticated manipulations of silicon and other substrates. The micromachining processes could selectively remove parts of the silicon or integrate special structural layers, so as to form mechanical and electromechanical components. Thanks to the electrical properties of silicon, electronics can be integrated close to the sensor, actuator and controller at micro-scale.
MEMs mainly consist of mechanical microstructures, microsensors, microactuators and microelectronics as shown in figure 1.1.2. Microstructures are usually levers, gears, lens and pillars; Microsensors can detect the minimum changes in the environment of mechanical, magnetic, thermal and chemical information. Microactuators can accelerate the physical and chemical reactions in tiny space and also manipulate particles.

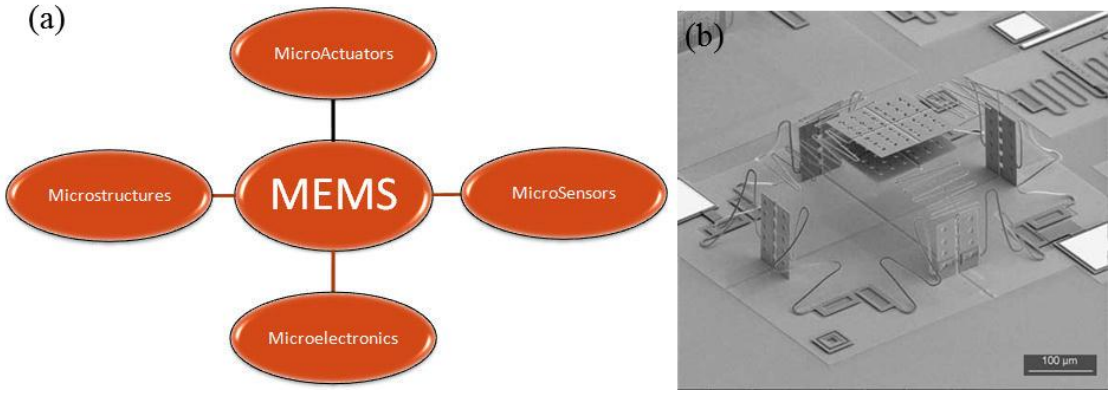

Figure 1.1.2 (a) Schematic illustration of MEMS components, (b) SEM image of a dual assembled platform MEMS cap.

Relied on MEMs technology, microelectronics and micromechanical structures are also integrated in microfluidic system enabling interdisciplinary application, and the chip-format scaling of single or multiple lab processes can be implemented. The basis process for most lab-on-chip (LOC) fabrication is photolithography directly derived from microelectronic fabrication. For specific optical characteristics, bio or chemical compatibility, lower production costs and faster prototyping, new processes have been developed such as glass, ceramics and metal etching, deposition and bonding, PDMS process or soft lithography, as well as fast replication methods *via* electroplating, injection molding and embossing.

In the present microfluidic chips, commonly used materials are silicon, quartz, glass, organic polymer compound, etc. The selecting rules of materials include these aspects: 1. favorable biocompatibility and no reaction with sample; 2. good electrical isolation and heat dissipation; 3. Good optical performance and few disturbances to signal detection; 4. Surface modification can be implemented for electroosmotic flow generation or immobilization of macromolecule; 4. Low-cost and simple process. However, each material has its advantages and disadvantages, and the choice for chip fabrication depends on the chip functions.

Silicon material has favorable thermal stability and chemical inertness. Moreover, there is already mature micromachining technology of silicon. There have been some imperfections in silicon material, that it is not transparent, fragile, high cost, and relative complex processing requirement. For acoustic wave device integrated in lab on chip, silicon substrate is the top choice due to the high speed and low attenuation of sound propagation.

Quartz and glass material can provide good electroosmotic flow and show excellent optical feature, also they can be structured using MEMs techniques such as photolithography and wet etching. For on-chip optical experiments, quartz is still the first choice for chip fabrication. Besides, quartz and glass present hydrophilic properties so that they are widely used in drop-based microfluidic chips.

In recent years, polymer materials are often used in microfluidic chip fabrication. The benefits of relative easy machine shaping and low price are convenient for mass production of disposable microfluidic chips. The representative organic polymers for chip processing are Polydimethylsiloxane (PDMS), Polymethylmethacrylate (PMMA) and Polyurethane (PU). In the cell experiments, PDMS plays an irreplaceable role due to its good air permeability and non-toxicity.

1.2 Cell detection in microfluidics and acoustic sensor integration

1.2.1 Cell mechanical properties detection

Cell *in vitro* studies play an important role in revealing the life phenomenon, disease prevention and disease progression. Cell responses closely related to surround microenvironment, so the similarity between cell growth in local microenvironment and real environment will largely affect their *in vitro* and *in vivo* researches. According to the performance, it can be divided into biochemical and biophysical factors. Biochemical factors mainly include the concentration of cytokine (CK) and action of extracellular matrix (ECM); biophysical factors mainly include the extracellular matrix materials hardness, density and porosity, as well as some mechanical force.

Dynamic balance in cell microenvironment is a significant condition for normal cell proliferation, differentiation and metabolism [10]. The mechanical property of cell is one factor which influences the environment change. Among them, the cell-substrate adhesion is an essential process for survival, differentiation, and migration of many types of cells. In this process, a cell experiences the contact with the substrate, loose

attachment and the spread of its membrane over the substrate surface can be studied. By means of restructuring, the cell-substrate adhesion plays a fundamental role in regulating migration, proliferation, and differentiation of cells [11].
Microfluidic chips are particularly suitable for cell study, because the dimensions of microchannels are matched with cell size and liquid control can be precisely realized. Microfluidic chip can also mimic the vasculature *in vivo* to transmit cell medium, interstitial fluid and cellular metabolism. Moreover the biochemical and physical parameters can be adjusted for on-chip cell culture. In addition, with the integration of micro sensors and actuators, various functions can be achieved such as buffer mixing, transfer, separation and capture.

1.2.2 Acoustic detection in lab-on-chip

Acoustic method has been widely developed in biology and medicine. The famous applications in commercialization are scanning acoustic microscope and ultrasonography. The core components are ultrasonic transducers using piezoelectric effect for acoustic beam generation. The acoustic technique can implement a gentle way to biological samples in a non-contact mode and reveal their internal structures. In another aspect, the transducers can be fabricated in the microdevice and the acoustic energy can be guided within the microchannel fabricated by MEMs technology. This property has paved the way for the acoustic modulus integrated in the lab-on-chip field. The miniaturization and high integration of acoustic modulus into a small chip show the promising solutions that meet the requirement of the Point-of-care testing (POCT) [12]. The analyte types include proteins, cells, nucleic acids, and metabolites.
The commercialized acoustic sensors in medicine are ultrasound probes based devices, including ultrasonography [13], d-mode ultrasonic diagnostic apparatus [14] and scanning acoustic microscopy [15]. The acoustic modulus is also integrated in microfluidics for biosensing applications. Current study mainly demonstrates two types of acoustic devices: Bulk acoustic wave (BAW) based quartz crystal microbalances (QCM) sensors and surface acoustic waves (SAW) based sensors. Here we focus on introducing the acoustic devices for on-chip applications, meanwhile, the scanning acoustic microscopy technology is discussed which is waiting to be integrated into lab-on-chip.

- Scanning acoustic microscopy (SAM)

A major innovation of acoustic sensor is scanning acoustic microscopy, which is a form of microscopy based on the generation and detection of elastic waves in objects. Scanning acoustic microscopy (SAM) allows the study of elastic properties of biological cells, especially the density, elasticity, sound speed and attenuation. An ideal modification of the SAM that enables measuring all necessary parameters of a cell is the time resolved acoustic microscope [16]. The time-resolved, high frequency acoustic microscope was commonly used on quantitative measurements of the local

mechanical properties of single cultured cells *in vivo*, as shown in figure 1.2.1.

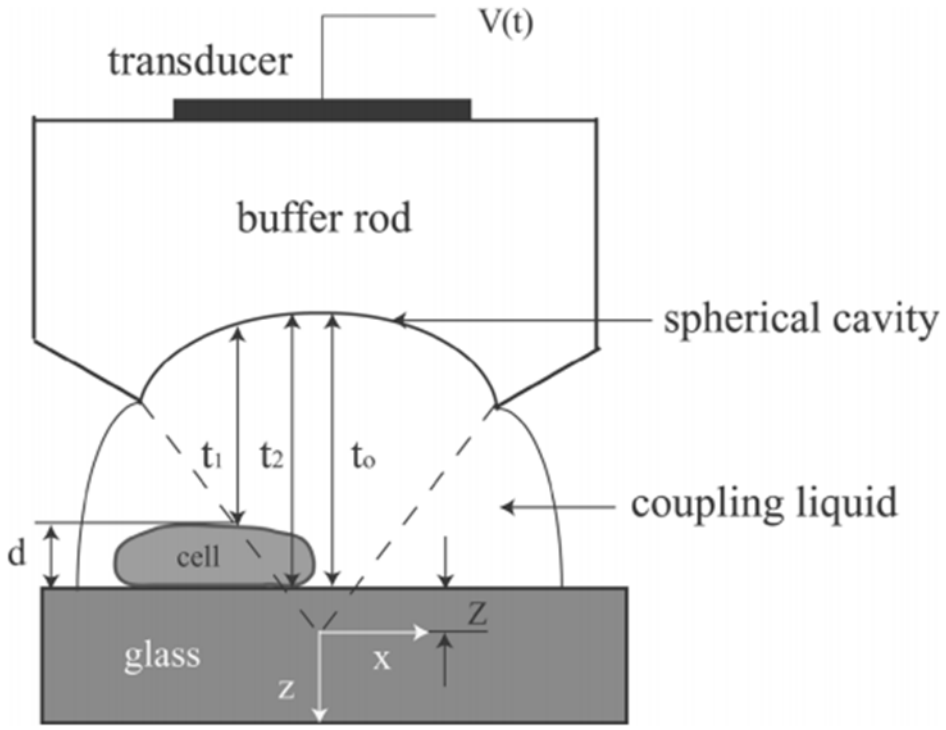

Figure 1.2.1 Setup for a quantitative, time-resolved, acoustic microscopy.

The main parameters obtained with an acoustic microscope are sound velocity and sound attenuation, as well as the dimensions of the cell. Sound velocity is a measure of the compression modulus, which is related to Young‟s modulus and Poisson‟s ratio. Attenuation of cytoplasm is a measure of the molecular interactions. T. Kundu computed the cell profile by counting the interference rings and estimating the value of the longitudinal wave speed in the cell. Then the cell thickness was roughly estimated at different pixels or cell positions [17].
Among the methods for the determination of mechanical properties of living cells, acoustic microscopy provides some extraordinary advantages: it is non-invasive, the intensity is low enough and it does not interfere with the cell [18]. In the ultra-high frequency range of GHz, the invasiveness is minimal which does not cause any damage or disturbance of the cells [19]. However, the acoustic microscopy system is bulky and expensive. The ultrasonic probes have to be moved manually close to the detected objects, which lower the flexibility and manipulation resolution. Meanwhile, its complex methods of characterization are mainly in imaging, thus the spatial resolution for cell analysis is limited. Therefore, the integration of acoustic microscopy into microfluidic chips can bypass these disadvantages and bring their superiority into full play.

- Quartz crystal microbalance (QCM)

Quartz crystal microbalance (QCM) has been well developed to be a powerful

bioanalytical sensor that is capable of evaluating the properties of complex biological medium. QCM shows great interests such as label-free, non-invasive, and highly sensitive in cell biology, pharmaceutical development and medical diagnosis. This technic can real-time detect the changes in mass and energy dissipation coupled to the surface of the sensor crystal. In the past two decades, this unique feature has spread QCM devices into cell biology studies with a special focus on the interaction between cells and their attached surface.

QCM is made of AT-cut quartz disk connected with metal electrodes on both sides. When a voltage is applied, the resonant frequency in a shear mode of the crystal is very sensitive to the changes in mass coupled to the surface (nanogram-scale). Sauerbrey demonstrated the linearly relationship between the resonant frequency and the change in mass [20]

$\Delta m = -C/n\Delta f_n$

Where Δm is the mass per unit area on crystal surface, C is the mass sensitivity constant of the device, Δf_n is the change in resonant frequency and n is the vibrational mode number.

In the cell-substrate adhesion, the interfacial interaction between the cell membrane and surface could influence the changes in mass [21- 22] and cell surface coverage [23-24]. Then QCM sensor also be sensitive to differences in the attachment and spreading of cells on the substrate, which indicate the variation of cell type [25-26] and surface coating [27]. Besides, the information of cell-cell adhesion junctions can also be deduced by examining the cell-substrate adhesion [28]. This indirect approach has enabled an assessment of cell-cell contact in cell-substrate spreading.

QCM technology provides a noninvasive, real-time assessment of cell mechanics and cell-substrate adhesion. However, the throughput is limited due to detection distance within the close vicinity of the sensor surface, and the detection range and sensitivity still remain to be improved.

- Surface acoustic wave biosensors

Surface acoustic waves (SAWs) are oscillations which propagate on the free surface of a piezoelectric crystal. When fabricating interdigitated transducers (IDT) on a piezo-electric substrate, the voltage applied to IDT generates the acoustic wave between input and output fingers. In this manner, the acoustic energy is strongly confined at the surface of the substrate, thus the SAW sensors are very sensitive to changes in mass loading, density, viscosity and acoustic coupling phenomena. For employing mass loading on SAW sensors, their substrate surfaces should be functionalized by selective coatings. The interaction between specimen and substrate will cause a mass loading, which produces a shift in resonant frequency or phase changes, which then can be measured to analyze the mechanical properties in the media contacting the sensitive surface. The fundamental principle is shown in Fig.1.2.2

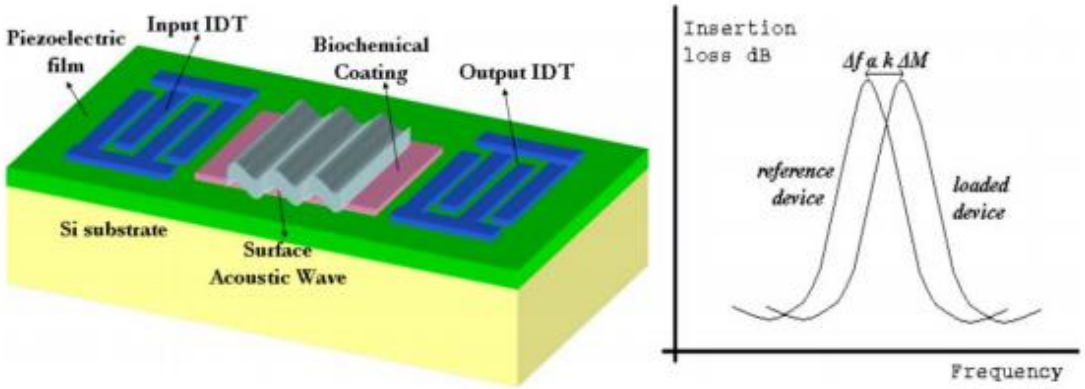

Figure 1.2.2 Sketch of a typical SAW-based bio/chemical sensor using the frequency-shift based response. The center frequency shift from the reference to the loaded devices when there is a change in the mass that modifying the SAW propagation [29].

Different directional cut of the piezoelectric material are determining the SAW types, including "shear-horizontal" SH-SAW (Love waves) or "shear-vertical" SV-SAW (Rayleigh waves). Rayleigh waves involve a deformation of the substrate in the direction normal to the surface. Wohltjen and Dessy firstly demonstrated such a SAW sensor using "Rayleigh-type" surface acoustic waves (RSAW) for organic gas detection, after coating with a sensitive polymer layer [30].
SAW sensors are well applied on whole cells experiments of bacteria and yeasts [31]. SAW sensors can be used to specifically detect eukaryotic cells *via* selective proteins or antibodies at low concentrations, and also measurements of adhesion of mammalian cells to sensor surfaces indicating the characterization in high sensitivity of advanced binding processes [32].
Compared to the traditional fluorescence detection, the acoustic detectors require no-labeling of buffer media and avoid photo-bleaching. In such types of device, the resonant frequency of the transducer is very sensitive to the acoustic properties variation coupled to the surface, such as mass loading and viscosity. By measuring the central frequency change, small molecules deposition onto surfaces, mass-loading and cell-substrate adhesion can be monitored in a noninvasive, real-time assessment. However, the test sample has to be placed on the surface of the oscillating crystal, and the detection distance is limited to the close vicinity of the sensor surface. Then the substrate has to be coated with a biospecific layer according with the analyte in certain immunodetection, so the flexibility of active area and sample concentration are restricted. In addition, a high frequency of QCM device is hard to achieve, because the device will become too thin and too fragile for practical use. In SAW sensors the energy propagation path is highly localized inside the guiding layer. However, higher working frequencies are desirable so as to increase the mass sensitivity.

1.3 Microfluidic approaches of cell manipulation

1.3.1 Cell manipulation significance

All the organisms apart from the virus are composed of cells, and even the virus can survive only in the environment of cells. Cell is the basic unit of the biological morphology and life activities. The cells‟ study are important in heredity and evolution in biology, including the organization and function, growth and development, metabolism and reproduction, movement and communication, aging and death. In the other side, cell culture and manipulation is the basis of cell research.
Microfluidics as a form of miniaturized platforms for bio-analysis can provide promising tools for the lab-on-a-chip based cell biology research field, since it has the ability to mimic heterogeneous cellular environment by multiplexing and precisely control the cellular environment, and also to analyze sub-cellular information by high-contents screening assays at the single-cell level. The inherent advantages of scale effect on microfluidics include:
(1) Compatible scale. The size of channels ranges from several to hundreds of micrometers, which is close to single cell and cell cluster, for the convenience of cells manipulation.
(2) Unique fluidic phenomena. Laminar flow happens under low *Re* number and micro-droplet could be generated as well as cells switch be implemented.
(3) Integration of multiple functions. Diversified multiple microstructures can be fabricated in the chip and various functionalities can be introduced. Various kinds of physics methods can be integrated in parallel or cascade, for the purpose of further applications are used.
(4) Large specific surface area. Microfluidic chips often possess much larger surface-area-to-volume ratio than conventional apparatus, facilitating fast chemical reaction on-chip and ultra-fast mixing as well as surface-dependent applications like capturing cells by affinity.
Cell manipulation in microscale is different from common particle manipulation. First of all, cell has activity and need to maintain its activity in culture medium. Factors of transmembrane potential, joule heat and shear force will affect cell activity. Besides, cell‟s physical, chemical and mechanical properties vary from common particles. For example, the outermost layer of the cell membrane and internal cytoplasm and nucleus constitute the cell structure. This multi-layers structure has a significant impact on the properties such as dielectric constant, compressibility, refractive index and so on. Cell manipulation mainly includes the positioning and capture, separation of cells and cell fusion.
Some representative methods in lab on chip were shown in table 1.3.1. It indicates that most existing methods for on-chip acoustic manipulation are in low system complexity, but show a low resolution for single cell trapping. To make up for the technical shortcomings, the most efficient method is to increase the acoustic frequency for manipulation, thus the wavelength can match the cell dimension.

Trapping technique	Buffer demands	System complexity (non-contact mode)	Single cell trapping	Cell cluster trapping	Trapping force (pN)	Trapping resolution
Hydrodynamic		Low	Low	Medium	NA	Low (10 μm)
Optical	Transparent	Medium/high	High	Low	100-2000	High (50 nm)
Dielectrophoretic	pH, ion,clean surfaces	Medium	Medium	Medium	200-400	Medium (1 μm)
Magnetic		High	Medium	High	2-1000	Medium (1 μm)
Acoustic	single cell trapping	Low	Low	High	100-400	Low (100 μm)

Table 1.3.1 Main manipulation methods in microfluidics and relative characterization [33].

1.3.2 Passive manipulation

Here we introduce some typical passive manipulation for cell with only fluid force introduction.

As shown in figure 1.3.1, K. J. Morton et al. proposed a feasible pillar structure to direct particles entrained in a fluid along trajectories. The asymmetric array of the posts can generate deterministic lateral displacement where particles choose different paths depending on their size: Particles larger than a critical size are deflected at an angle to the flow, while smaller particles would move along streamline paths.

Yamada's group developed "pinched flow fractionation (PFF)" method for cell separation. Laminar flows were used to introduce liquid with particles and without particles in different inlets. By controlling the flow rates, particles can be focused on one sidewall in the pinched segment. Then, by utilizing the spreading flow profile at the boundary between the pinched segment and the following broadened segment, the slight difference between the positions of large and small particles could be amplified, and these particles could then be separated perpendicularly to the flow direction according to size. By employing microchannels with multiple outlets, the separated particles could be individually recovered. This method is advantageous for particle sorting, since continuous processing can be achieved without complex structures or operations.

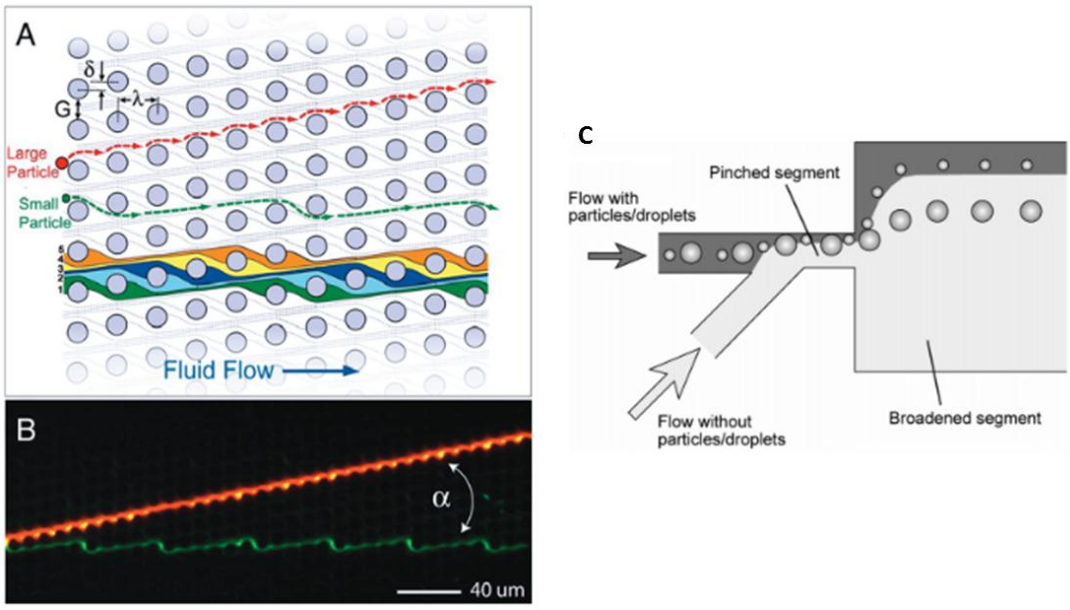

Figure 1.3.1 Size-based particle separation in an asymmetric array of posts. (A) Schematic of a deterministic lateral displacement (DLD) array showing definitions of the array parameters, (B) Separation of 2.7 μm red fluorescent beads and 1.0 μm green fluorescent beads by using the array [34], (C) Schematic diagram showing the basic principle of "pinched flow fractionation" for size-dependent separation of particles/droplets. The initial region of the flow containing particles/droplets is gray colored [35].

1.3.3 Active manipulation

- Optical manipulation

Optical tweezers can trap tiny small objects close to 5 nm and can exert forces more than 100 pN, which corresponds to an ideal range for exerting forces on biological systems and receiving their responses. Optical manipulations for chip-based systems have demonstrated fixing cells in the fluid flow for the detection of fluorescence and Raman spectroscopy. In addition, this is applied for enriching particles, stretching cells for an elasticity deformation, trapping nanoparticles. The optical trapping technique utilizes a momentum transfer from one or two highly focused laser beams. For objects much larger than the wavelength of light, force is given mainly by refraction and reflection (Mie scattering); for objects less than the optical wavelength, the net optical force is proportional to the gradient of light intensity, and its direction is accordant to the increasing intensity (Rayleigh scattering). The laser beam with the Gaussian profile can draw the objects into the center of the beam. A microscope objective lens is normally integrated in the optical router to create a tightly focused laser beam with high numerical apertures. Through moving the laser beam and changing the focus length, trapped particles can be manipulated in three dimensions. The forces exerted on a trapped object can be measured by calibrating the optical parameters, so the viscoelasticity of cells can be characterized in very high resolution.

The first demonstration of an optical trap was implemented by Ashkin in1970. Using two divergent, co-aligned and counter-propagating laser beams, 3 μm latex beads were drifted towards a stable equilibrium point in the optical field and directed towards a chamber [36]. A dual optical tweezers was also implemented for a very high precision manipulation DNA and actin [37]. In this work, a polystyrene bead was attached to each end of the filament beforehand, and the bead was driven by optical tweezers so as to tie a knot on the filament. The principle and the phenomenon were shown in figure 1.3.2.

The combination of optical manipulation with microfluidic systems creates a powerful tool for investigations of cell responses to environmental stimuli. One benefit of the systems is transparent materials used as components, which can easily be implemented under microscopes. Cells can be immobilized in a laminar flow of different chemical properties by optical force or be moved reversibly between two different media [38].

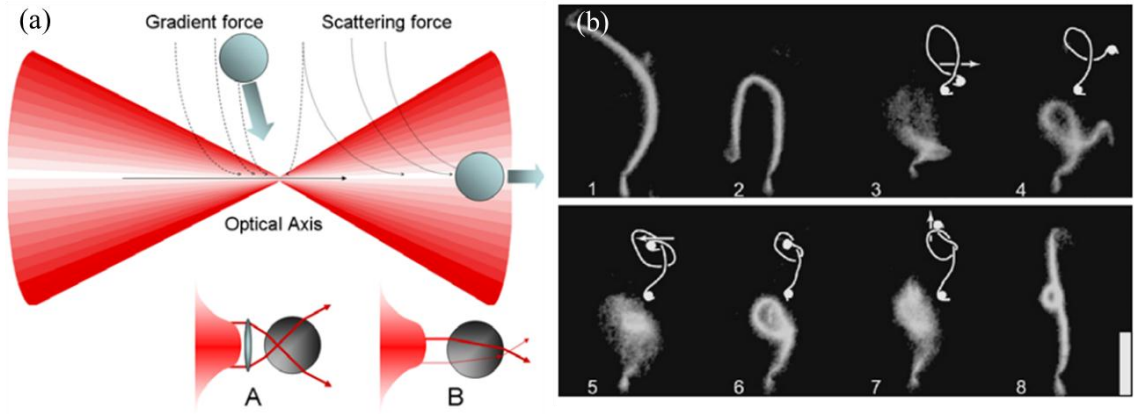

Figure 1.3.2 (a) Schematic graphs of optical forces acting on a dielectric sphere. The gradient force and scattering force push the particle into the region of highest intensity. Under the right conditions, the particle will be trapped in the laser focus (case A). If the optical conditions are not optimal, the scattering force directs the particle in the direction of the light (case B). (b) Knots were tied on a single actin filament in different geometries through moving the optical tweezers [37].

- Electrical manipulation

Electrical manipulations are mainly divided into electrophoresis and dielectrophoresis. Electrophoresis uses direct current (DC) method to guide suspended particles toward an oppositely charged electrode. Because negative charge can be adsorbed on cell surface, the electrophoretic force which is proportional to the charge can push cells toward to the positive electrode. With a fluorescence modulus detection in the upstream, Takahashi et al. distinguished labeled cells and switched them in a microchip *via* electrostatic force [39]. A similar device was implemented by Yao et al. Gravity was taken advantaged to process cells in an upright orientation and avoided

convective flow influence [40]. Guo et al. presented a higher throughput of electrophoretic sorting chip with the encapsulated cells in water-in-oil droplets [41]. As shown in figure 1.3.3, diluted cell solutions were focused in laminar flow and encapsulated into droplets so that single cell in each droplet can be deflected when they move through the electrical field area.

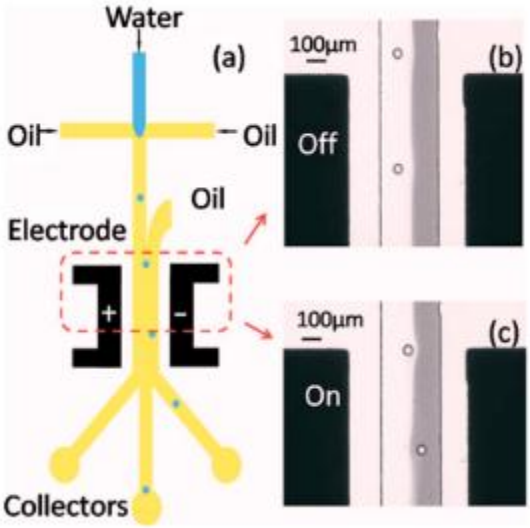

Figure 1.3.3 (a) Schematic of the droplet-based electrophoresis system. (b) droplets in one laminar flow without the electrical field and (c) droplets moved into the other laminar flow due to the electrical force [41].

- Fluorescence-activated cell sorting (FACS)

By the combination of the optical trapping, DEP deflection and the fluorescence microscopy techniques, the flow cytometry has offered new tools and capabilities for cell research. Fluorescence-activated cell sorting (FACS) is a specialized type of flow cytometry with fast developing. The typical FACS system utilizes charged droplets that went through an electrostatic deflection system and optical detection area. Cell is encapsulated in the droplet *via* flow focusing and moved along the flow in a high speed. Target cells can be directly identified based on their intrinsic optical characteristics, such as a light absorption and a refractive index, thus a large optical intensity pattern is induced. Meanwhile, some of the laser light is scattered by the cells which can be used to count the cells. After the optical signal feedback was transmitted to the system, the electric field force is excited and exerted on the charged droplet to direct them toward the specified outlet.
Conventional flow cytometry devices are limited because of bulky, mechanically complex and consuming a high volume of sample. Combined with the advantages of microfluidic chips to integrate functionalities at micro scale, such as fluid pumping and mixing, the development for microfluidic flow cytometer (μFACS) achieved innovative architectures and highly integration level. As the light scattering and fluorescent characteristics of each cell vary, a heterogeneous mixture of biological

cells can be sorted simultaneously in microfluidics. L. Mazutis et al. demonstrated a droplet-based microfluidic chip to detect antibodies secreted from single mouse hybridoma cells [42-43].

1.3.4 Magnetic manipulation for in CTCs detection

Cancer is a group of diseases characterized by the abnormal growth of cells which can invade surrounding tissues and metastasize to distant sites within the body. Cancer remains one of the major causes of death, and the number of terminal cancer patients, who can survive more than five years after the treatment, is relatively less. Early cancer detection is crucial for improving survival rate and quality of life of patients, as well as the saving of manpower and financial resources. Early detection of cancer greatly increases the chances for successful treatment. Early diagnosis is particularly relevant for cancers of the breast, cervix, mouth, larynx, colon and rectum, and skin.
In 1869, T. R. Ashworth discovered tumor cells in the blood of an individual with metastatic cancer which were supposed to indicate the origin of several tumors present in the patient. These cells, that have travelled into the vasculature from a primary tumor and circulated in the bloodstream, are named as Circulating Tumor Cells (CTCs) [44]. CTCs have been identified in patients with malignant lung, breast, prostate, colon, melanoma and pancreatic cancers. Besides, the concentration of CTCs in blood is used to predict patients‟ survival and provide unique information of prognosis in patients. Clinical data showed that through a period of cancer therapy, numbers of CTCs declined with decreases of tumor sizes in patients. Study the relationship between the number of CTCs and the subsequent development of metastases hold great promise for monitoring the effectiveness of cancer treatments, identifying drug-sensitivity and cancer biomarkers. However, the isolation of CTCs from blood is particularly challenging due to their extreme rarity, with only a single CTC per billion normal blood cells in advanced cancer patients.
Conventional cancer cell sorting techniques, including centrifugation, chromatography, and fluorescence and magnetic-activated cell sorting, are limited in yield, purity and risks of damage to cells. The use of lab-on-a-chip (LOC) could isolate viable CTCs with high efficiency, purity and throughput for post-processing. This platform would be an ideal tool to mimic an *in vivo* environment to retain the isolated CTCs in their native states for accurate characterization [45]. In consideration of these advantages, various microfluidic platforms have been developed for capturing rare cells including CTCs, circulating fetal cells, and stem cells.
Superparamagnetic beads were widely utilized for magnetic cell capture. A superparamagnetic bead is made of an internal magnetic core and non-magnetic coating outside which can be chemically modified with active groups. As an example, Liu et al. demonstrated the first microfluidic device combined with magnetic manipulation for cancer cell separation [46]. As shown in figure 1.3.4, nickel micro-pillars was firstly fabricated at the bottom of a microfluidic channel by electroplate, then superparamagnetic beads were biologically modified with specific antibodies prior to injecting into the microchannel. Thanks to the interaction between

the specific antibodies and N-acetylglucosamine on the cell membrane, A549 cancer cells spiked in RBCs were effectively captured and separated from the diluted blood.

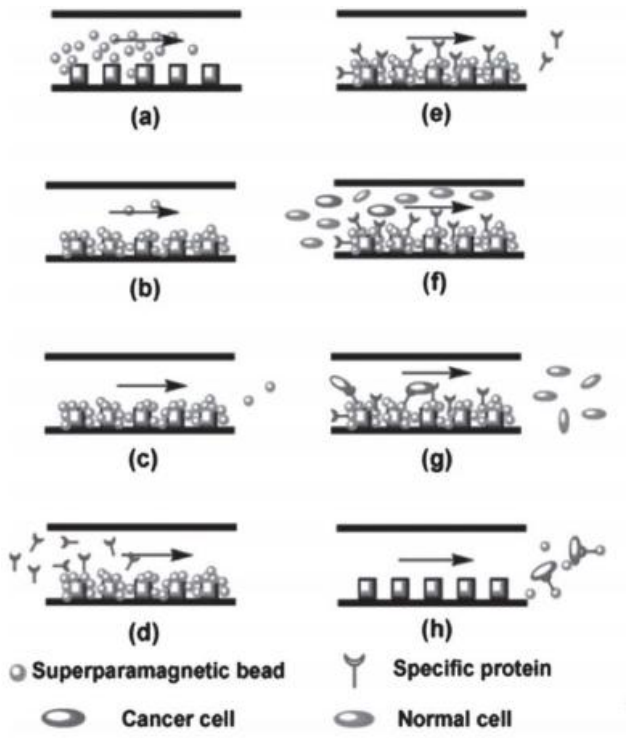

Figure 1.3.4 Schematic graphs of a magnetic activated micro-cell sorting device [46].

1.4 Acoustic manipulation in microfluidic systems

1.4.1 Bulk standing wave manipulation in lab on chip

Acoustic pressure wave can be applied directly on an object to control its movement. The acoustofluidic technology, which integrates acoustic modules in the microfluidic chip, developed a new area for tiny samples manipulation. Acoustic forces can provide precise spatial control of small objects in fast response. In addition, acoustic methods are widely implemented in biology and medicine [47-48].

Acoustic standing waves supply a non-invasive mode for objects manipulation in micrometer scale, which makes it a promising approach in particles and cell handling in microsystems. An acoustic standing wave is formed through superposition of two waves of same frequency, but the opposite direction of propagation. Then nodes and antinodes in a single stationary wave can be generated. In the locations of nodes the amplitude is at a minimum and there is no pressure fluctuation, and at antinodes the amplitude is at a maximum that exhibits alternating pressure maxima and minima.

A standing acoustic wave will generate stationary pressure gradients to drive particles in a liquid medium moving to the nodes or antinodes. The direction of particles movement induced by acoustic forces depends on the density and compressibility of particles. On the basis of acoustic field, nearly all the elastic particles can be affected by standing wave forces as long as their acoustic properties differ from the

surrounding medium.

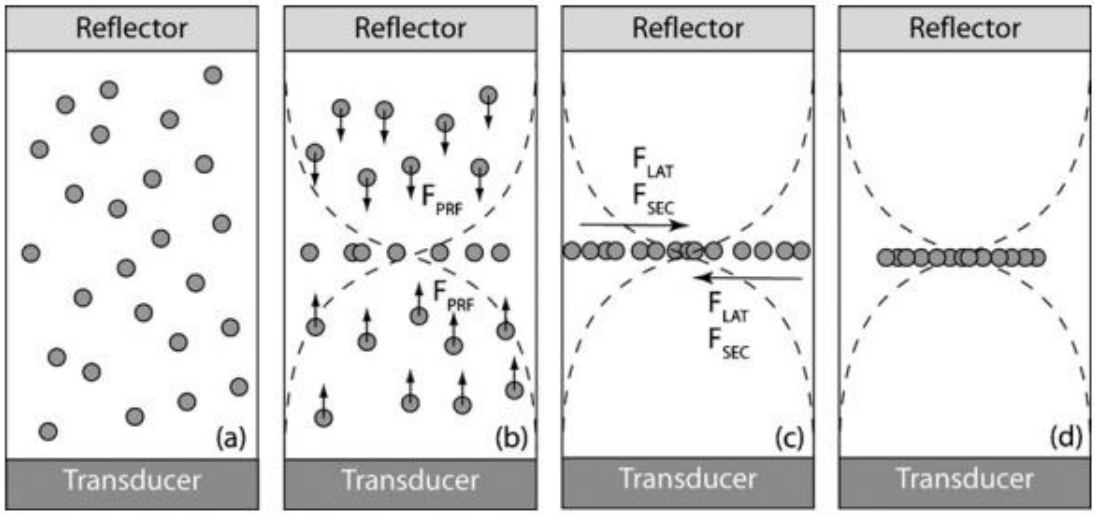

Figure 1.4.1 Schematic diagram of particles handling in standing wave field. (a) Particles in a medium randomly, (b) when a single node standing wave generated, particles moved towards the node by the primary radiation force, (c) Lateral forces lead particles towards the central axis, (d) the secondary acoustic forces contributes to particles agglomeration [49]. F_{PRF} is the primary force, F_{LAT} is the transverse component of and F_{PRF}, F_{SEC} is the secondary radiation force.

As shown in figure 1.4.1, the standing wave force exerted on particles is a combination of the primary force and secondary radiation force. Nilsson et al simplified the equations of the primary force which corresponding to the strongest acoustic force [50]. The primary force is produced directly from the standing wave field

$$F_r = -\left(\frac{\pi P_0^2 V_c \beta_w}{2\lambda}\right)\cdot\phi(\beta,\rho)\cdot\sin(2kx)$$

and $\phi = \frac{5\rho_c - 2\rho_w}{2\rho_c + \rho_w} - \frac{\beta_c}{\beta_w}$

where F_r is the primary force, x is a certain position in the wave propagation, k is the wave number, λ is the wavelength, P_0 is the acoustic pressure amplitude, V_c is the volume of the particle, and Φ is the acoustic contrast factor. The density of the medium and particles are denoted by ρ_w and ρ_c respectively and the corresponding compressibilities are β_w and β_c.
The secondary forces are induced by ultrasonic waves scattered by particles.

$$F_B(x) = 4\pi a^6\left[\frac{(\rho_c - \rho_w)^2(3cos^2\theta - 1)}{6\rho_w d^4}v^2(x) - \frac{\omega^2\rho_w(\beta_c - \beta_w)^2}{9d^2}p^2(x)\right]$$

where a is the radius of the particle, d is the distance between the particles and θ is the angle between the center line of the particles and the direction of propagation of

the incident wave. When particles are driven in acoustic nodes by the primary force, the secondary force starts to play a role in the aggregation and sedimentation of the gathered particles.

T. Laurell's group integrated the standing acoustic wave force into microfluidic device and developed this technology in a variety of applications. They developed a "Lund method" for a silicon-based acoustic device within the microchannel. In this method, the ultrasonic sources are bulk piezo-ceramic elements that coupled into the device *via* a matching layer in a thickness of a quarter of wavelength. The microchannel was wet etched in silicon wafer with a glass bonding for chip package. The width of the channel is matched to an integral multiple of half-wavelength, meanwhile, the sidewalls of the channel are vertical surfaces, so as to generate a resonator between the side-walls in the flow channel. When adjusting the excitation frequency of the single ultrasonic source, a standing wave is formed within the channel with one or several nodes.

The resonator used to generate standing wave field can be silicon-silicon, silicon-glass or glass-glass layers. As the conditions required are that distance between two layers is multiple of half-wavelengths, and the roughness of the surface should be lower than a quarter of wavelength. For a silicon-based resonant, the direction of wave propagation can either be perpendicular to wafer surface in case the channel depth is close to one wavelength, or the direction of wave propagation can be parallel to the wafer surface if the channel width is a multiple of half-wavelength.

Spengler and Coakley used ultrasonic trap to move latex microparticles into the pressure node for monitoring the aggregation mechanism of particles in different media [51]. As shown in figure 1.4.2, Evander et al. achieved acoustic noncontact trapping platform in a silicon-glass channels for performing cell and particle based assays in continuous flow [52]. Neural stem cells were trapped and showed viability *via* fluorescence observation after 15 min, as well as yeast cells were captured and cultured for 6 h while being perfused by the cell medium. This method opened a further prospect for extended studies, including gene expression profile analysis and protein expression mapping of small cell populations. Guo et al improved the fabrication of this method to obtain a more flexible and cost-effective device [53].

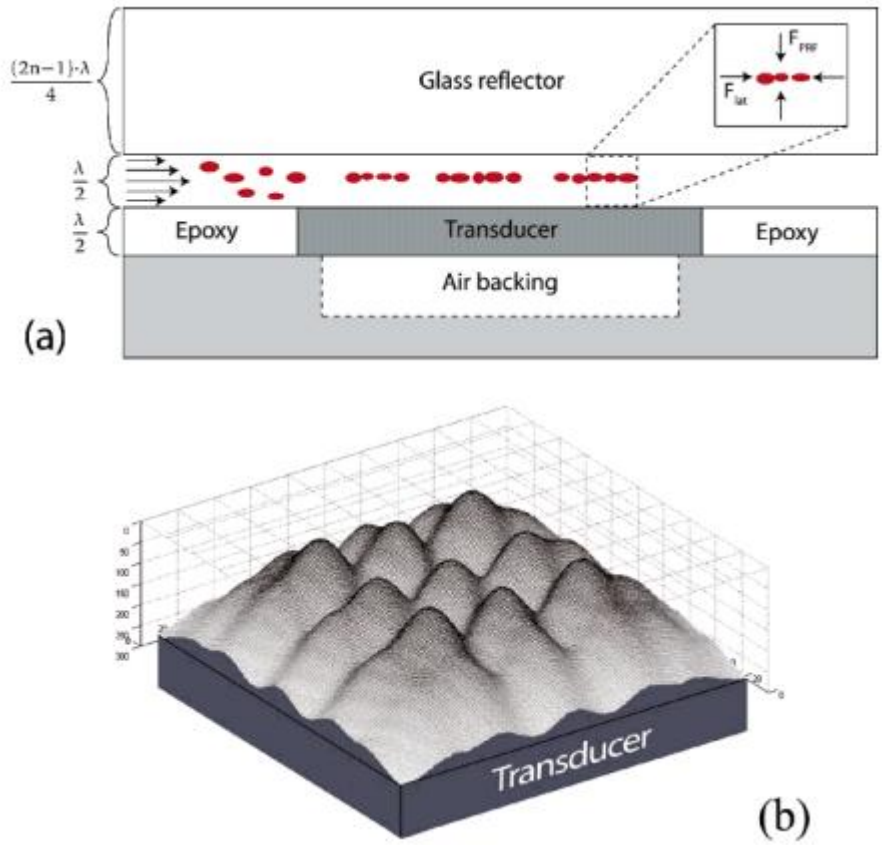

Figure 1.4.2 (a) Side-view schematic of the acoustic resonant in the microfluidic device. (b) 3D image of simulation presented the actual trapping sites distribution [52].

In the acoustic separation micro-chip, when the channel width is a half wave length, a pressure node is generated in the middle of the channel while antinodes at the sidewalls. Thanks to the laminar flow phenomenon in the microfluidic channel, particles could move along streamlines respectively prior to the pass through acoustic field. While the acoustic forces act in the lateral direction, different particles which suffer various acoustic forces will be driven to disparate outlets. F. Petersson et al. presented a representative work of the acoustophoresis for particles separation in dynamical flow [54]. A 370 μm wide channel matched a half wavelength (2 MHz central frequency of transducer). The net power on the piezoelectric element ranged from 0.5W to 2.0 W. Depending on the sizes of the particles, the lateral displacement induced by the acoustic force are in direct proportion to the particle sizes, types and the suspending medium. As particles at different sizes were driven to diverse streamlines, they were collected into different outlets producing different streamlines as shown figure 1.4.3.

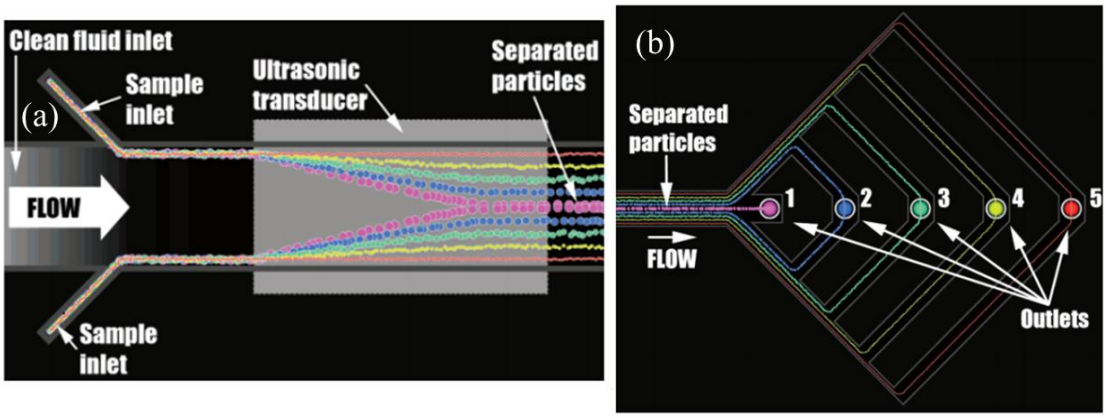

Figure 1.4.3 (a) Illustration of a particle suspension passing through the standing wave field which located above the transducer. Particles are driven toward the center of the channel at a rate determined by their acoustic properties. (b) Illustration of particles with various sizes moved into different outlets [54].

1.4.2 Surface standing acoustic wave method

For bulk standing acoustic wave (BSAW) separation on particles/cells, the single-cell-level deflection is hard to achieve due to the large acoustic actuation area related to the bulk piezoelectric elements. Thereby very low cell concentrations for samples are required which makes it difficult to obtain very high sorting throughput. On the other hand, standing surface acoustic waves (SSAW) means based cell separation had also reported. The advantage of SSAW-based cell sorters is that it has better control for the position of sorted cells due to the restricted function area.

Based on the acoustic standing wave trapping principle, Tony Jun Huang‟s group carried forward a standing surface acoustic wave (SSAW) technique to manipulate cells and microparticles. In the SAW propagation, most of the acoustic energy is confined within several wavelengths on the surface of the substrate. This energy restriction characteristic makes SAW an energy-efficient tool for manipulating biomaterials and droplets. Interdigital electrodes are deposited on a piezoelectric substrate in a parallel direction or orthogonal arrangement, thus the generated acoustic nodes are organized in lines or in arrays.

As shown in figure 1.4.4, the standing surface acoustic waves (SSAW) were used to manipulate and pattern cells and microparticles. A radio frequency (RF) signal is applied to the pair of IDTs to induce two equal SAW propagating either in the opposite direction or orthogonal direction. Different patterns can be achieved dependent on the angle between the IDTs. In the acoustic field, particles or cells can be subjected to the pressure gradients and stably patterned in the „„wells“ corresponding to the pressure nodes in the SSAW. The microchannel width should always larger than half of the wavelengths to formed nodes.

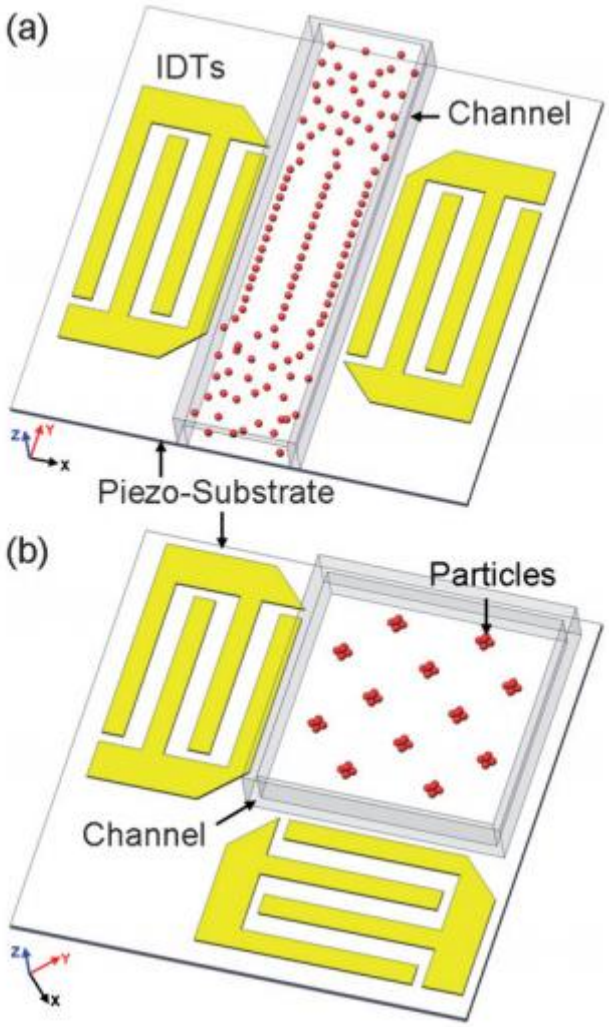

Figure 1.4.4 Schematic of the SSAW-based patterning devices. (a) 1D patterning using two parallel IDTs, (b) 2D patterning using two orthogonal IDTs [55]. The power of the applied SAW was 200 mW.

Based on the SSAW platform, Ding et al. successfully manipulate single particles, cells, and organisms in a single-layer microfluidic chip for the first time [56]. The working frequency range of the IDTs was from 18.5 MHz to 37 MHz, corresponding to SAW wavelengths of approximately 100 μm to 200 μm. As the excitation frequencies are higher than previous bulk standing acoustic waves (BSAW), particle are manipulated in a higher resolution of distances. Besides, the acoustic power density is reduced to 0.5 nW/μm^2 for the manipulation of 10 μm polystyrene beads.
Guo et al. promoted the method by controlling the spatial arrangement of cultured cells through the "standing acoustic wells". As shown in figure 1.4.5, Individual cells were pushed together with micrometer precision and shape of "acoustic wells". With tunable geometric configurations, thousands of cell assemblies can be formed in a high throughput. This SSAW platform for cell-cell and cell-matrix adhesion could be further developed for the immunology, developmental biology, neuroscience, and cancer metastasis.

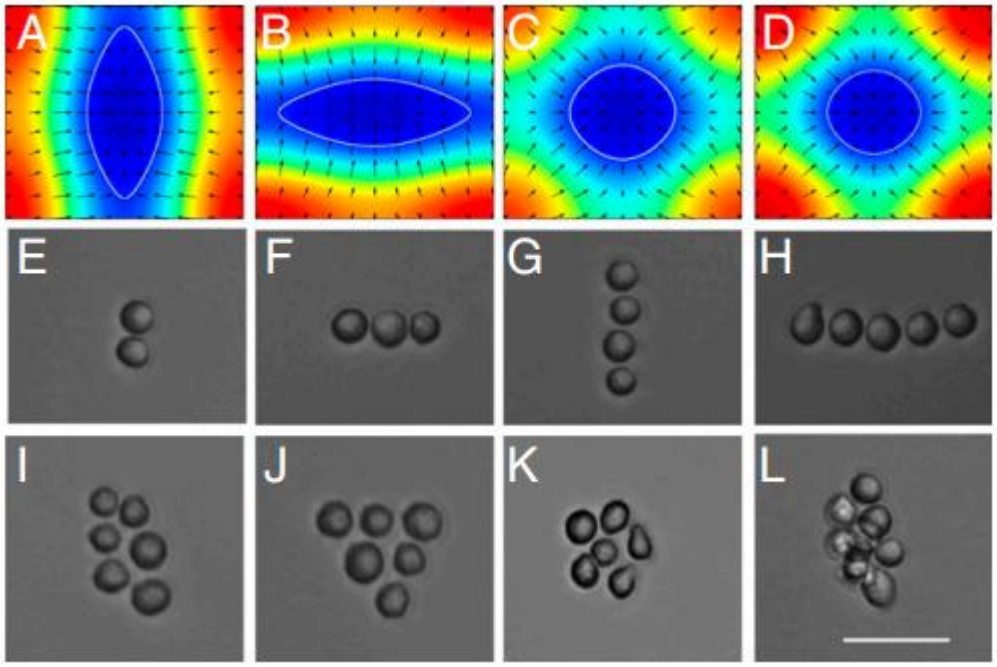

Figure 1.4.5 Cells assembly in different geometries after acoustic capture. (A–D) Simulation results of acoustic potential distribution in an acoustic well with various amplitudes. The white line indicates an acoustic potential with the same magnitude. (E–H) HeLa cells assembly in a linear shaped acoustic well. (I–K) Single-layer and (L) cell assembled in a spherical shape [57]. Scale bar: 50μm.

P. Li et al. demonstrated at tilted-angle standing surface acoustic waves to deflect cancer cells in the cell culture lines from white blood cells (WBCs). Larger CTCs experience a larger acoustic radiation force than white blood cells, and they can be collected in bifurcate outlets [58]. L. Ren et al. combined SSAW and fluorescence activated cell sorters (FACS) for the particles sorting in high speed. Focused interdigital transducers (FIDTs) were implied for high energy intensity and a throughput of commercial level was reached [59].

1.4.3 Traveling waves inducing acoustic streaming

While most acoustically actuated microfluidic devices make use of bulk standing waves or surface standing waves, traveling acoustic waves inducing acoustic streaming have also been used to manipulate cells in the microfluidic regime.
Acoustic streaming is a well-known phenomenon within the acoustics community. When a travelling wave transfers a momentum to the fluid, the wave irradiates energy into the liquid which gives rise to internal streaming inside the fluid. This phenomenon is called “acoustic streaming” and has been utilized to actuate drops on open surfaces. Acoustic streaming was analyzed with theoretical model firstly in 1884 by Rayleigh [60]. When travelling wave passes through the liquid, part of the acoustic

energy is absorbed in the fluid and significant attenuation of acoustic energy appears. Meanwhile, the consumption of the acoustic energy leads to the fluid motion in a short range. In the interaction between an acoustic wave and a solid boundary, as well as the oscillatory acoustic field in the medium, the generated acoustic streaming is a time-averaged process. The magnitude and mode of acoustic streaming is affected by the geometry of microchannel in the microfluidic chip.

The dissipation of an ultrasonic wave in a fluid produces acoustic streaming in the same direction as the wave propagation. The induced acoustic force $F = \beta c^{-1} I_{ac} e^{-\beta x}$, where F is the acoustic force acting on the fluid, I_{ac} is the initial intensity, c is the acoustic speed in the fluid, and β is the attenuation coefficient [61].

The acoustic streaming phenomenon provides interesting benefits in microfluidic applications, such as fast mixing for laminar flow in the microchannel, micropumping, cells lysing and small biosamples handling. Employing acoustic streaming effect for actuating particles is independent of their acoustic properties, therefore it is particularly useful for small particles.

T. Franke et al. used a tapered shape of IDT to provide a particularly narrow wave path width for the acoustic wave propagating on the substrate, then generated the acoustic streaming forces and induced the acoustic streaming on the fluid. The streaming deflected the flow in a small region and redirect fluid from one outlet to an adjacent outlet [62]. Later they introduced the fluorescence-activated cell sorter with the cooperation of travelling surface acoustic waves. Cells of interest were successfully deflected into parallel outlets in a very short response time [63].

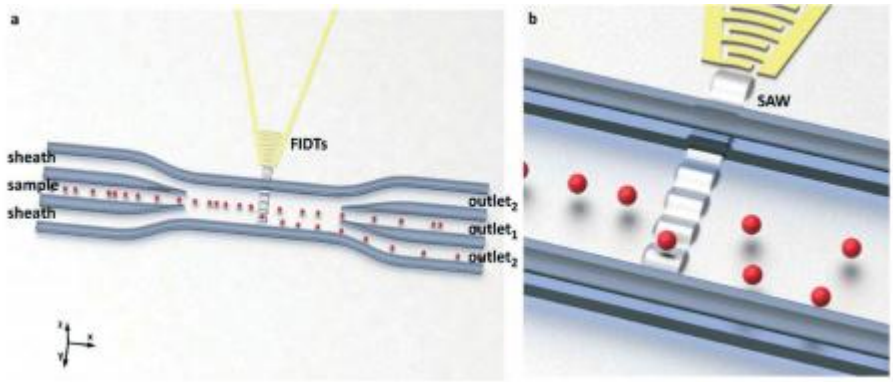

Figure 1.4.6 Schematic of the acoustic device. (a) Two sheath flows are used to focus the particles prior to the acoustic field. (b) A highly focused SAW is used to sort at the single-particle level [65].

Based on the tapered shape of IDT, David et al. firstly deflect particles by a highly focused SAW at a high-frequency of 386 MHz, as shown in figure 1.4.6. In high frequency range, the dimensions of the acoustic actuation region become smaller so that inaccurate sorting through a range of sample concentrations can be effectively avoided. In another aspect, there are very few work presented for high frequency bulk acoustic wave integrated in microfluidics for particle manipulation.

Due to the low *Re* number of the flows in the microchannel, the laminar flow

phenomenon happens in the microfluidic chip. Though the effect of steady laminar flows is beneficial for samples observation and collection, it is hard to implement on-chip applications such as fast chemical reactions and cell lysis, and so forth. Acoustic streaming effect attracted remarkable interest in lab-on-chip field for active mixing of droplets and flows.

Frommelt et al. studied the use of surface acoustic waves (SAWs) to generate time-dependent flow patterns which promote mixing in microfluidic devices [64]. These SAWs are a type of elastic energy along the surface of the fluid, which can induce acoustic streaming through the fluid when excited. The produced streamlines have been shown to cause efficient mixing within systems of fluids and movement of liquid droplets even at low Reynolds numbers. Acoustic based mixing methods are a versatile technique that can easily be implemented into microfluidic devices to mix fluids within a channel or in open geometries.

D. Ahmed et al. presented ultra-fast homogeneous mixing inside a microfluidic channel *via* single-bubble-based acoustic streaming. A horseshoe shaped feature was used to trap air inside the microfluidics device so as to mix two laminar flows as they combine inside a larger channel, as shown in figure 1.4.7.

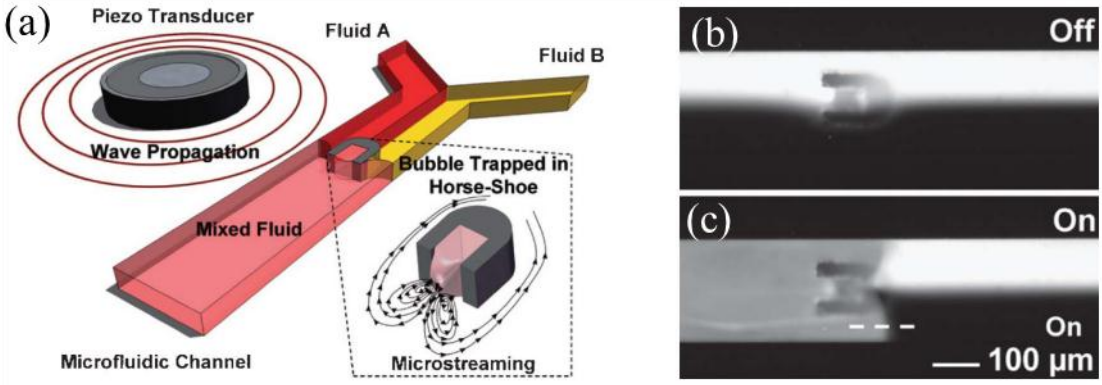

Figure 1.4.7 Schematic of the experimental setup of for acoustic streaming generated from a microbubble trapped in a horseshoeshaped structure (a) and a demonstrated device with a mixing a water flow and a fluorescent dye solution. (b) without acoustic streaming the laminar flow in channel, (c) fast mixing around the bubble with acoustic streaming [66].

The transducer required for BAW generation is bulky, hindering device integration and miniaturization. SAW technique overcomes those shortcomings and can be used in the soft polymer materials (PDMS etc.). However, it is difficult with SAW device to reach very high frequency in the GHz range.

1.5 Acoustic tweezers development in micro-system

1.5.1 Concept of acoustic tweezers

Acoustic tweezers is a technology that is able to manipulate micro/submicron objects by sound waves. The initial concept on acoustic tweezers was firstly demonstrated by

Wu in 1991 [67]. In his work, latex spheres and frog eggs were captured using two opposit sound beams. The main forms of acoustic tweezers are single beam acoustic tweezers (SBAT) and standing wave acoustic tweezers, the latter is widely developed in lab-on-chip in our previous introduction. Single beam acoustic tweezers (SBAT) uses a high-frequency array transducer with lens to generate highly focused acoustic beam and trap particles toward the focus plane. Its feasibility was first demonstrated by Lee and Shung in both theory and experiments [68]. At high frequency, the acoustic wavelength is comparable to the diameter of single cells, thus the single beam acoustic tweezers shows great potential to manipulate single particle or cell rather than clusters, because the acoustic energy is concentrated upon with one wavelength. For standing wave acoustic tweezers, objects controlled by an acoustic radiation force will move to special regions (nodes and antinodes), depending on their acoustic properties such as density and compressibility

In the comparison of similar manipulation for objects, dielectrophoretic forces affect the surface charges on particles and generated in non-uniform fields, meanwhile, magnetic force can drive bead-labeled particles to magnetically material. These two approaches presented broadly applications in miniaturized device but limited in single particle trap, cell viability and pre-labeling necessary.

Comparing to the optical tweezers, the acoustic counterpart is simpler with lower cost. The non-invasive and no-contact properties are beneficial to the biological and medical applications. Particularly as the portable, hand-carried ultrasonic devices are being more frequently implemented in medicine today, research and development of point-of-care acoustic chip will be vigorously promoted for further extension around the world.

1.5.2 Single beam acoustic tweezers (SBAT)

Experimental results already demonstrated that single beam acoustic tweezers could trap particles of a size either larger than a wavelength (Mie particles) or smaller than a wavelength (Rayleigh particles). The ultrasonic trapping force in a Gaussian beams could be affected by various parameters, such as frequency, physical dimension of particle, beam width, axial position and so on.

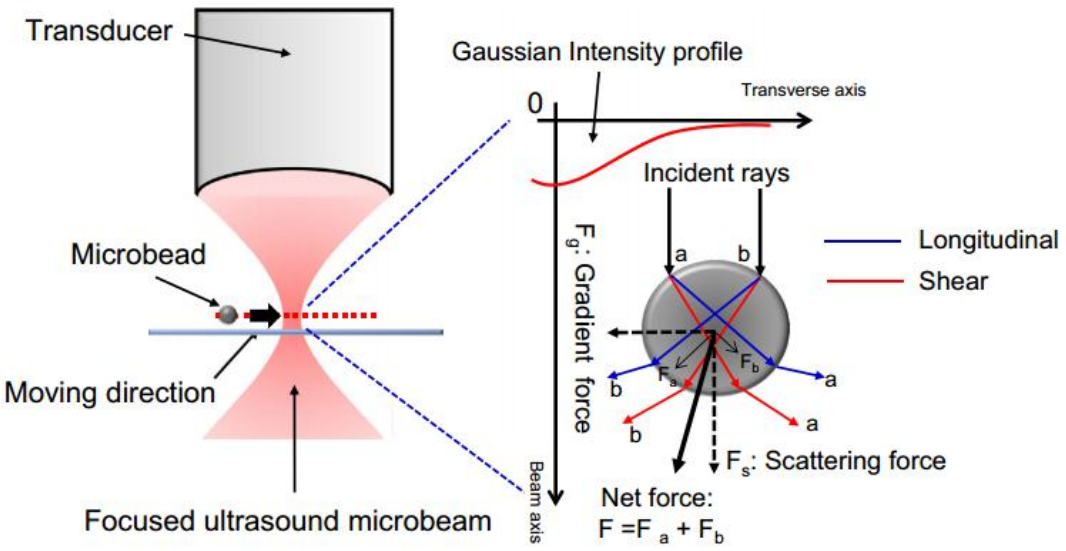

Figure 1.5.1 Illustration of the acoustic mechanism for two incident rays in a Gaussian intensity field trapping a microbead in water [69].

As shown in figure 1.5.1, focused ultrasound beams introduced both longitudinal and shear wave propagated inside the microbead, but only the longitudinal mode was present as the microbead was in water. The incoming ray changed their directions when they passed through the microbead due to momentum transfer. Then the acoustic radiation force (F_a or F_b) was applied on the microbead with dimension greatly larger than acoustic wavelength. Considering the asymmetric intensity distribution, a net force $F = F_a + F_b$ will direct the microbead toward the central beam axis. The trapping forces contained two components, scattering and gradient forces. The scattering force F_s was induced from acoustic reflection by the particle, which rejected the microbead away from the beam axis. In contrast, the gradient force F_g was originated from refraction and attracted the microbead toward the center axis.

For single microparticle manipulation, high frequency with short wavelength is extraordinary suitable since the acoustic energy is can be concentrated in a smaller area. However, it has been quite a challenge for high frequency acoustic device fabrication with acceptable working performance. At frequencies higher than 100MHz, the thickness of piezoelectric layers of the transducers is in a range of few tens of microns, which is not easy to achieve with conventional approaches such as lapping and grinding. In the meantime, it is also a challenge to produce a highly focused configuration in cases of thin piezoelectric layers.

The group of K. Kirk Shung had tried to apply acoustic tweezers in the microchannel. The 24 MHz single element lead zirconate titanate (PZT) transducer was used to form the array for a tight focusing in a ultrasonic probe [70]. Li et al. trapped particles in a rat aorta by single beam acoustic tweezers to evaluate the feasibility of SBAT *in vivo* inside of a blood vessel [71]. A. Marzo et al. show that acoustic levitation can be employed to translate, rotate and manipulate particles using even a single-sided emitter [72]. These results suggest that this non-contact ultrasonic tweezers have the great promise for cell manipulation and study of intracellular signaling on single cell

basis.

1.5.3 On-chip high frequency acoustic characterization

In the ultra high frequency application, Scanning Acoustic Microscope (SAM) is an instrument generally used to analyze medical samples. When a focused acoustic beam propagates into the sample, this acoustic wave is then scattered, absorbed, reflected or transmitted. The pulse responses are reflected back to the transducer with certain amplitudes and energy can be point-by-point interpreted so that the cell topography can be deduced. In industry field, the acoustic microscope could detect internal features, including defects such as cracks and voids. In biology and medicine aspect, SAM can provide analysis on the elasticity of cells and tissue in a non-destructive way.

Thanks to its excellent performances and various features, SAM have been commercially used in many fields. However, there are still a lot of limitations in biological and medical applications, especially in 3D cell topography, elastic properties of biological cells and high integration for point-of-care testing. Recently, the development of the integration of acoustic microscopy in microfluidics opened a new frontier for miniaturization of SAM applications. Conventional acoustic microscopy requires a bulky, complex and high-cost machine which is difficult to integrate in a small chip for on-line evaluation.

Flexible structures have to be fabricated for bulk acoustic wave guide and transmission. Wang et al. demonstrated a feasible fabrication of a microsystem for controlling 1GHz high frequency bulk acoustic wave in a silicon wafer [73]. Passive 45˚ mirror planes in (100) silicon were obtained by wet chemical etching and were used to employ the reflection of the bulk acoustic wave. Zinc oxide (ZnO) thin film transducers were deposited on the other side of the wafer and aligned with the mirrors. One transducer acted as emitter and the other one acted as receiver while transducers were overlapped by mirrors to make full use of the acoustic energy. This platform makes it possible to achieve bulk acoustic wave guiding in three dimensions (3D) and the transmission direction was parallel to the silicon wafer surface. Based on this structure, Gao et al. inserted a microfluidic channel between 45˚ mirrors to utilize the transmission acoustic energy for detection [74]. In this structure, there are parasitic noises emerging in the acoustic propagation. The generated acoustic beams are reflected by the top surface of the wafer, bottom of the microchannel and sidewalls of the wafer. One part of the beams from the emitter transmits under the microchannel to the receiver, which introduces more noise and lowers the resolution of measurements.

As shown in figure 1.5.3, two vertical mirrors were added in the acoustic transmission beam path to limit the reception of the parasitic signals. The depth of vertical mirrors is designed to be the same as the microchannel, so as to filter the acoustic waves propagating only under the microchannel. The vertical mirrors filter effectively removes part of the parasitic noises, but increases the propagation path.

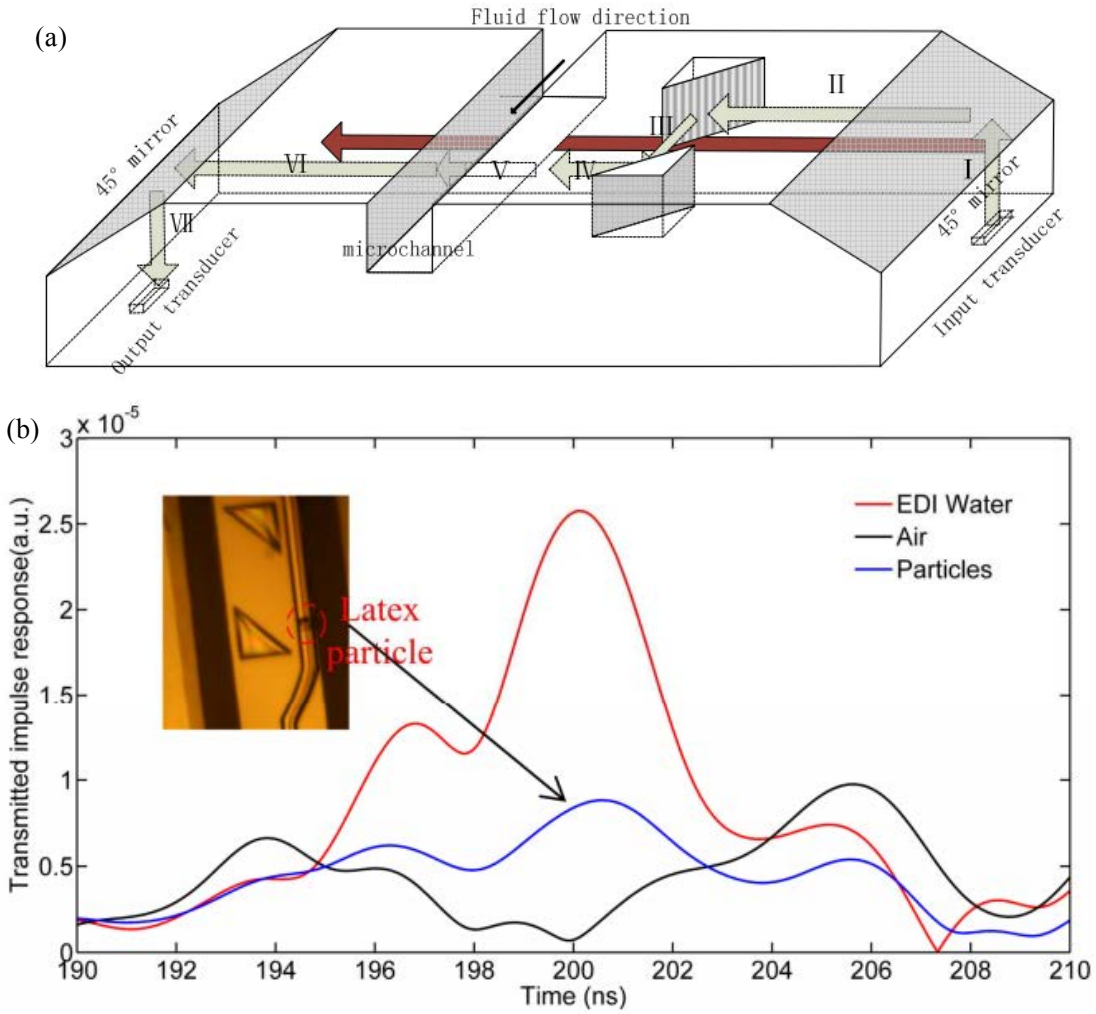

Figure 1.5.3 (a) Schematic illustration of the transmission path in the acoustic guide platform. (b) Modulus of the impulse response (S_{21}) for water and particle characterization. (red: channel filled with EDI water, blue: 0.1% concentration of latex particles in EDI water, black: empty channel) [74].

After control of inject flow rate, different concentrations of KI solution were characterized and single polystyrene particle were detection. In medical application, low concentration of red blood cells (less than 1%) was characterized in a focused cylindrical structure. As the acoustic attenuation is high in GHz range, the channel width was less than 50 μm to avoid too much acoustic attenuation in the microchannel. However, the experiments with a high concentration of cells were not available due to narrow channel width. Moreover, characterization of cancer cells in larger dimension (>25 μm) would be difficult. To improve the channel dimension, a direct way is to decrease the working frequency of the transducer. Correspondingly, the total system has to be optimized to match the working frequency.

1.6 Conclusion and perspective

The integration of acoustic microscope into lab on chip exhibits many benefits, such as low cost and low sample volume, fast response, simplified sample cleaning and preparation, as well as non-destructive to biological samples. At present, the bottlenecks concerning our systems are mainly the sample blocking and parasitic noise which makes it more difficult of the discrimination of the useful signals. A lower central frequency transducer is necessary to be included in this system, and the whole device has to be optimized.

Nevertheless, the on-chip acoustic manipulation in high frequency range is an interesting tool. The acoustic characterization and manipulation could be carried out in the same device, which would improve the level of integration of the chip. The higher the acoustic frequency, the lower the acoustic wavelength, then the wavelength would be closer to the object dimension. Therefore, the acoustic manipulation in high frequency shows interesting potentialities in spatial control of single cell.

The high frequency acoustic integration in lab-on-chip field opens a new frontier in medical applications. For further development, these bottlenecks can be improved: (1) the size of the mainchannel need to be enlarged to avoid sample clogging, especially for sample with high concentration and viscosity such as human blood; (2) higher-throughput is requested for commercial applications; (3) reducing the working frequency for lower attenuation; (4) optimization of the connections and electrical matching of the transducers, so as to limit power consumption for cost-effective commercial applications and portable device.

References

[1] J. Melin and S. R. Quake, “Microfluidic large-scale integration: the evolution of design rules for biological automation”, Annu Rev Biophys Biomol Struct. 2007; 36:213-31.

[2] E. Tumarkin, L. Tzadu, E. Csaszar, M. Seo, H. Zhang, A. Lee, R. Peerani, K. Purpura, P. W. Zandstra and E. Kumacheva, “High-throughput combinatorial cell co-culture using microfluidics”, Integr Biol (Camb). 2011 Jun;3(6):653-62.

[3] A. Manz, N. Graber and H. M. Widmer, “Miniaturized total Chemical Analysis systems:A Novel Concept for Chemical Sensing”, Sensors and Actuators, B 1 (1990)244–248.

[4] J. C. McDonald, D. C. Duffy, J. R. Anderson, D. T. Chiu, H. Wu, O. J. Schueller and G. M. Whitesides, “Fabrication of microfluidic systems in poly(dimethylsiloxane)”, Electrophoresis. 2000 Jan;21(1):27-40.

[5] T. Thorsen, S. J. Maerkl and S. R. Quake, “Microfluidic Large-Scale Integration”, Science 18 Oct 2002: Vol. 298, Issue 5593, pp. 580-584

[6] G. M. Whitesides, “The origins and the future of microfluidics”, NATURE|Vol 442|27 July 2006

[7] C. D. Chin, V. Linder and S. K. Sia, “Commercialization of microfluidic point-of-care diagnostic devices”, Lab Chip, 2012, 12, 2118-2134.

[8] J. C. Tormos et al. “Droplet-Based Microfluidic Platforms for the Encapsulation and Screening of Mammalian Cells and Multicellular Organisms”, Chemistry & Biology 15, 427–437; May 2008
[9] J. E. Ali, P. K. Sorger and K. F. Jensen, “Cells on chips”, NATURE|Vol 442|27 July 2006
[10] Daniel A. Fletcher and R. D. Mullins, “Cell mechanics and the cytoskeleton”, Nature 463, 485-492,2010
[11] M. A. Wozniak, K. Modzelewska, L. Kwong and P. J. Keely, “Focal adhesion regulation of cell behavior”, Biochim Biophys Acta, 2004, 1692: 103-119.
[12] W. Jung，J. Han，J. W. Choi and H. A. Chong, “Point-of-care testing (POCT) diagnostic systems using microfluidic lab-on-a-chip technologies”, Microelectronic Engineering 132 (2015) 46–57.
[13] T. J. DuBose, “Fetal Biometry: Vertical Calvarial Diameter and Calvarial Volume”, Journal of Diagnostic Medical Sonography, 1985, 1 (5): 205.
[14] T. J. DuBose and A. L.Baker, “Confusion and Direction in Diagnostic Doppler Sonography”, Journal of Diagnostic Medical Sonography, 2009, 25 (3): 173–7.
[15] H. Lüers, K. Hillmann, J. Litniewski, J. Bereiter-Hahn, “Acoustic microscopy of cultured cells. Distribution of forces and cytoskeletal elements”, Cell Biophys, 1991, 18 (3): 279–93. [16] G. Y. H. Lee and C. T. Lim, “Biomechanics approaches to studying human diseases” Trends in Biotechnology, vol. 25, pp. 111-118, Mar 2007.
[16] A. Briggs, Acoustic Microscopy. Oxford: Clarendon Press, 1992.
[17] T. Kundu, J. B. Hahn and K. Hillmann, “Measuring elastic properties of cells by evaluation of scanning acoustic microscopy V (Z) values using simplex algorithm”, Biophys, 1991 J.59:1194 –1207.
[18] T. Kujawska, J. Wójcik and L. Filipczyński, “Possible temperature effects computed for acoustic microscopy used for living cells”, Ultrasound in Medicine and Biology, vol. 30., no. 1, pp. 93-101, 2004.
[19] J. B. Hahn, “Probing biological cells and tissues with acoustic microscopy”, Adv. Acoustic Microsc, 1995, 1:79 –115.
[20] G. Sauerbrey (1959) Verwendung von Schwingquarzen zur Wägung dünner Schichten und zur Mikrowägung Zeitschrift für Physik 155: 206-222.
[21] D. M. Gryte, M. D. Ward and W. S. Hu, “Real-time measurement of anchoragedependent cell adhesion using a quartz crystal microbalance”, Biotechnol Prog, 1993, 9: 105-108.
[22] J. Wegener, S. Zink, P. Rösen and H. Galla, “Use of electrochemical impedance measurements to monitor beta-adrenergic stimulation of bovine aorticendothelial cells” Pflugers Arch, 1999, 437: 925-934.
[23] M. S. Lord et al. “Monitoring cell adhesion on tantalum and oxidised polystyrene using a quartz crystal microbalance with dissipation”, Biomaterials, 2006, 27: 4529-4537.
[24] C. Modin et al. “QCM-D studies of attachment and differential spreading of pre-osteoblastic cells on Ta and Cr surfaces”, Biomaterials, 2006, 27: 1346-1354.
[25] J. Redepenning, T. K. Schlesinger, E. J. Mechalke, D. A. Puleo and R. Bizios

"Osteoblast attachment monitored with a quartz crystal microbalance", Anal Chem, 1993, 65: 3378-3381.
[26] J. Wegener, A. Janshoff and H. J. Galla, "Cell adhesion monitoring using a quartz crystal microbalance: comparative analysis of different mammalian cell lines", Eur Biophys J, 1999, 28: 26-37.
[27] J. Li, C. Thielemann, U. Reuning and D. Johannsmann, "Monitoring of integrinmediated adhesion of human ovarian cancer cells to model protein surfaces by quartz crystal resonators: evaluation in the impedance analysis mode", Biosens Bioelectron, 2005, 20: 1333-1340.
[28] T. Zhou, K. A. Marx, A. H. Dewilde, D. McIntosh, S. J. Braunhut, "Dynamic cell adhesion and viscoelastic signatures distinguish normal from malignant human mammary cells using quartz crystal microbalance", Anal Biochem, 2012, 421: 164-171.
[29] O. Tigli, L. Bivona, P. Berg and M. E. Zaghloul, IEEE TRANSACTIONS ON BIOMEDICAL CIRCUITS AND SYSTEMS, VOL. 4, NO. 1, FEBRUARY 2010
[30] H. Wohltjen and R. Dessy, "Surface acoustic-wave probe for chemical-analysis. I. Intro-duction and instrument description", Anal Chem, 1979, 51:1458–1464
[31] A.K. Deisingh and M. Thompson, "Biosensors for the detection of bacteria", Can. J. Microbiol. 50 (2) (2004) 69–77.
[32] S. Hong, E. Ergezen, K. Barbee and R. Lec, "BAEC adhesion analysis using Thickness Shear Mode sensor", Conf. Proc. IEEE Eng. Med. Biol. Soc. 1 (2005) 1047–1050.
[33] J. Nilsson, M. Evander, B. Hammarström and T. Laurell, "Review of cell and particle trapping in microfluidic systems", Analytica Chimica Acta, 2009, 649(2): 141–157.
[34] K. J. Morton, K. Loutherback, D. W. Inglis, O. K. Tsui, J. C. Sturm, S. Y. Chou and R. H. Austin, "Hydrodynamic metamaterials: Microfabricated arrays to steer, refract, and focus streams of biomaterials", Proc. Natl. Acad. Sci U. S. A. 2008 May 27;105(21):7434-8.
[35] H. Maenaka, M. Yamada, M. Yasuda and M. Seki, "Continuous and size-dependent sorting of emulsion droplets using hydrodynamics in pinched microchannels", Langmuir. 2008 Apr 15;24(8):4405-10.
[36] A. Ashkin, "Acceleration and Trapping of Particles by Radiation Pressure", Phys. Rev. Lett. 1970 24 (4): 156–159.
[37] Y. Arai et al, "Tying a molecular knot with optical tweezers", NATURE VOL 399, 3 JUNE 1999
[38] S. Umehara, Y. Wakamoto, I. Inoue and K. Yasuda, "On-chip single-cell microcultivation assay for monitoring environmental effects on isolated cells", Biochemical and Biophysical Research Communications, 2003, Vol. 305
[39] K. Takahashi, A. Hattori, I. Suzuki, T. Ichiki and K. Yasuda, "Non-destructive on-chip cell sorting system with real-time microscopic image processing", J. Nanobiotechnol., 2004, 2
[40] B. Yao, G. Luo, X. Feng, W. Wang, L. Chen and Y. Wang, "A microfluidic device

based on gravity and electric force driving for flow cytometry and fluorescence activated cell sorting", Lab Chip, 2004, 4, 603–607.
[41] F. Guo, X. H. Ji, K. Liu, R. X. He, L. B. Zhao, Z. X. Guo, W. Liu, S. S. Guo and X. Z. Zhao, "Droplet electric separator microfluidic device for cell sorting", Appl. Phys. Lett., 2010, 96, 193701
[42] L. Mazutis, J. Gilbert, W. L. Ung, D. A. Weitz, A. D. Griffiths and J. A. Heyman, "Single-cell analysis and sorting using droplet-based microfluidics", Nat. Protoc., 2013, 8, 870–891.
[43] M. E. Piyasena and S. W. Graves, "The intersection of flow cytometry with microfluidics and microfabrication", Lab Chip, 2014, 14, 1044
[44] T. R. Ashworth, "A case of cancer in which cells similar to those in the tumours were seen in the blood after death", Australian Medical Journal, 1869, 14: 146–7.
[45] J. Chen, J. Libc and Y. Sun, "Microfluidic approaches for cancer cell detection, characterization, and separation", Lab Chip, 2012, 12, 1753-1767
[46] Y. J. Liu, S. S. Guo, Z. L. Zhang, W. H. Huang, D. Baigl, M. Xie, Y. Chen and D. W. Pang, "A micropillar-integrated smart microfluidic device for specific capture and sorting of cells", Electrophoresis, 2007, 28, 4713–4722.
[47] J. Friend and L. Y. Yeo, "Microscale acoustofluidics: Microfluidics driven via acoustics and ultrasonics", Review of Modern Physics, 2011, 83(2):647-704.
[48] A. Lenshof and T. Laurell, "Continuous separation of cells and particles in microfluidic systems", Chem. Soc. Rev., 2010, 39, 1203–1217
[49] M. Evander, "Cell and Particle Trapping in Microfluidic Systems using Ultrasonic Standing Waves", Department of Electrical Measurements and Industrial Engineering and Automation, Lund University, Lund, 2008
[50] A. Nilsson, F. Petersson, H. Jönssonb and T. Laurell, "Acoustic control of suspended particles in micro fluidic chips", Lab Chip, 2004, 4, 131–135.
[51] J. F. Spengler and W. T. Coakley, "PARTICLE AGGREGATE GROWTH IN AN ULTRASOUND STANDING WAVE TRAP", Langmuir, 2003, 19, 3635–3642.
[52] M. Evander, L. Johansson, T. Lilliehorn, J. Piskur, M. Lindvall, S. Johansson, M. Almqvist, T. Laurell and J. Nilsson, "Noninvasive Acoustic Cell Trapping in a Microfluidic Perfusion System for Online Bioassays", Anal. Chem, 2007, 79 (7), pp 2984–2991.
[53] S. S. Guo et al. "Ultrasonic particle trapping in microfluidic devices using soft lithography", APPLIED PHYSICS LETTERS 92, 213901 (2008)
[54] F. Petersson, L. A¡berg, A. M. S. Nilsson and T. Laurell, "Free Flow Acoustophoresis: Microfluidic-Based Mode of Particle and Cell Separation", Anal. Chem., 2007, 79 (14), pp 5117–5123
[55] J. Shi, D. Ahmed, X. Mao, S. S. Lin, A. Lawit and T. J. Huang, "Acoustic tweezers: patterning cells and microparticles using standing surface acoustic waves (SSAW)", Lab Chip, 2009, 9, 2890–2895
[56] X. Ding et al. "On-chip manipulation of single microparticles, cells, and organisms using surface acoustic waves", Proc Natl Acad Sci U S A. 2012 Jul 10; 109(28), 11105-11109.
[57] F. Guo et al. "Controlling cell–cell interactions using surface acoustic waves",

Proc Natl Acad Sci U S A. 2015, 112(1), 43-48.
[58] P. Li, et al. “Acoustic separation of circulating tumor cells”, doi/10.1073/pnas.1504484112
[59] L. Ren et al. “A high-throughput acoustic cell sorter”, Lab Chip,2015,15,3870
[60] L. Rayleigh, “On the Circulation of Air Observed in Kundt's Tubes, and on Some Allied Acoustical Problems”, Philos. Trans. R. Soc. London, 1884, 175, 1–21.
[61] S. Lighthill, “Acoustic streaming”, J. Sound Vib., 1978(61), 391–418.
[62] T. Franke, S. Braunmuller, L. Schmid, A. Wixforth and D. A. Weitz, “Surface acoustic wave actuated cell sorting (SAWACS)”, Lab Chip, 2010, 10, 789–794.
[63] L. Schmid, D. A. Weitz and T. Franke, “Sorting drops and cells with acoustics: acoustic microfluidic fluorescence-activated cell sorter”, Lab Chip,2014, 14, 3710–3718.
[64] T. Frommelt, M. Kostur, M. W. Schäfer, P. Talkner, P. Hänggi, and A. Wixforth, “Microfluidic Mixing via Acoustically Driven Chaotic Advection”, Phys. Rev. Lett. 100, 034502
[65] D. J. Collins, A. Neild and Y. Ai, “Highly focused high-frequency travelling surface acoustic waves (SAW) for rapid single-particle sorting”, Lab Chip, 2016, 16, 471–479
[66] D. Ahmed, X. Mao, J. Shi, B. K. Juluri and T. J. Huang, “A millisecond micromixerviasingle-bubble-based acoustic streaming”, Lab Chip, 2009, 9, 2738–2741.
[67] J. R. Wu, “Acoustical tweezers”, J Acoust Soc Am. 1991 May;89(5):2140-3.
[68] J. Lee and K. K. Shung, “Radiation forces exerted on arbitrarily located sphere by acoustic tweezer”, J Acoust. Soc. Am.120 (2), 1084 (2006)
[69] J. Y. Hwang, C. W. Yoon, H. G. Lim, J. M. Park, S. Yoon, J. Lee and K. K. Shung, “Acoustic tweezers for studying intracellular calcium signaling in SKBR-3 human breast cancer cells”, Ultrasonics 63 (2015) 94–101
[70] C. Lee, J. Lee, H. H. Kim, S. Y. Teh, A. Lee, I.Y. Chung, J. Y. Park and K. K. Shung, “Microfluidic droplet sorting with a high frequency ultrasound beam”, Lab Chip, 2012, 12, 2736–2742
[71] Y. Li, C. Lee, R. Chen, Q. Zhou and K. K. Shung, “A feasibility study of in vivo applications of single beam acoustic tweezers”, Appl Phys Lett. 2014 Oct 27;105 (17):173701.
[72] A. Marzo, S. A. Seah, B. W. Drinkwater, D. R. Sahoo, B. Long and S. Subramanian, “Holographic acoustic elements for manipulation of levitated objects”, NATURE COMMUNICATIONS| 6:8661 | DOI: 10.1038/ncomms9661
[73] S. Wang, J. Gao, J. Carlier, P. Campistron, A. NDieguene, S. Guo, O. B. Matar, D. -C. Dorothee, and B. Nongaillard, “Controlling the transmission of ultrahigh frequency bulk acoustic waves in silicon by 45° mirrors,” Ultrasonics, 2011, 51(5),532–538.
[74] J. Gao，J. Carlier，S. Wang，P. Campistron，D. Callens, S. Guo, X. Zhao and B. Nongaillard, “Lab-on-a-chip for high frequency acoustic characterization”, Sensors and Actuators B: Chemical, 2013, 177(2), 753－760.

Chapter 2

Technological development and acoustic reflection enhancement

2.1 Introduction of the problems and improvements

Dedicated to Doctor Gao's work, there were numerous technical skills developed for 1 GHz acoustic characterization in Lab-on-chip, such as:

(1) 120 μm depth of 45° mirrors wet etching;
(2) 80 μm depth of microchannel with vertical walls by DRIE;
(3) 2.4 μm thickness of ZnO transducer coupling of silicon wafer;
(4) PDMS bonding on silicon for device package.
(5) Vertical mirrors integration so as to limit parasitic signals received.

As discussed in chapter 1, so as to avoid channel blocking and achieve on-chip particles/cells manipulation, we have to improve the following points:

1. We need to enlarge the channel width and decrease the working frequency (less acoustic attenuation).
2. We need to improve the signal to noise ratio (SNR) for characterization: it requires optimizing the fabrication of the chip.
3. We need to improve the transfer of acoustic energy for acoustic manipulation, but also to reduce the losses of the acoustic –

(1) lower the acoustic diffraction;
(2) avoid conversion mode;
(3) lower the transmission losses through the channel;
(4) achieve electrical matching of transducers.

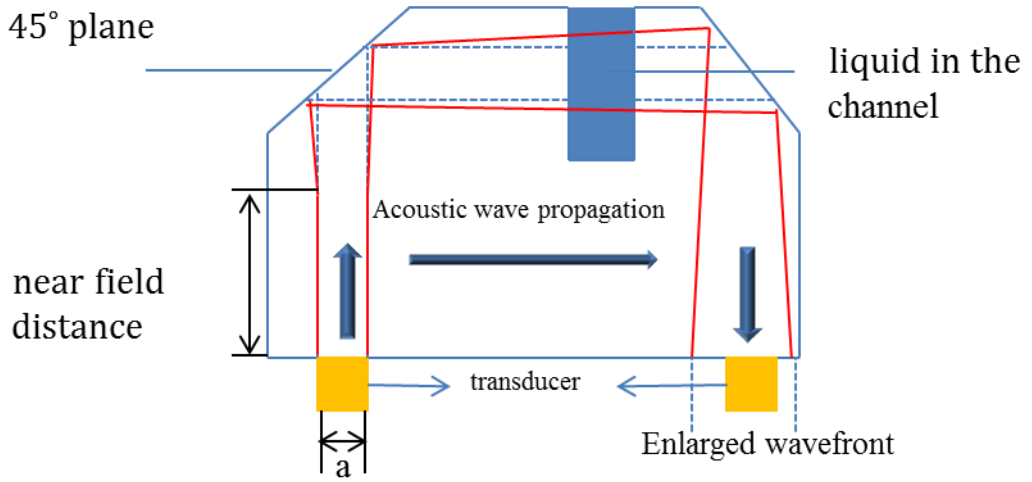

Figure 2.1.1 plane wave diffraction in our system. Near field distance d=214 μm, for a given transducer width a=120 μm and central frequency f=500 MHz. The acoustic beams propagate mainly in the path of far field.

When we decrease the working frequency of the transducers, the acoustic diffraction phenomenon has to be taken into account. As shown in figure 2.1.1, the near field distance $d=a^2/4\lambda$ is determined by the wavelength and width of transducer. For $d < \frac{a^2}{4\lambda}$, the acoustic beam propagates in near field which is heterogeneous and the geometry of the acoustic wavefront lies on a plane perpendicular to the axis of the source. Over this distance, the acoustic beam is in the far field and the wavefront becomes more spherical.

The -3dB width h of the diffracted beam in the far field, for a given distance d of the observation plane, can be approximated by:

$$h_{-3dB} = 1{,}4\lambda \frac{d}{a}$$

From the equation, it can be deduced that in order to increase the distance of near field and reduce acoustic energy diffraction, the effective ways are to increase the width of the transducer when we decrease the working frequency of the transducer. Meanwhile, the acoustic propagation paths should also be reduced.

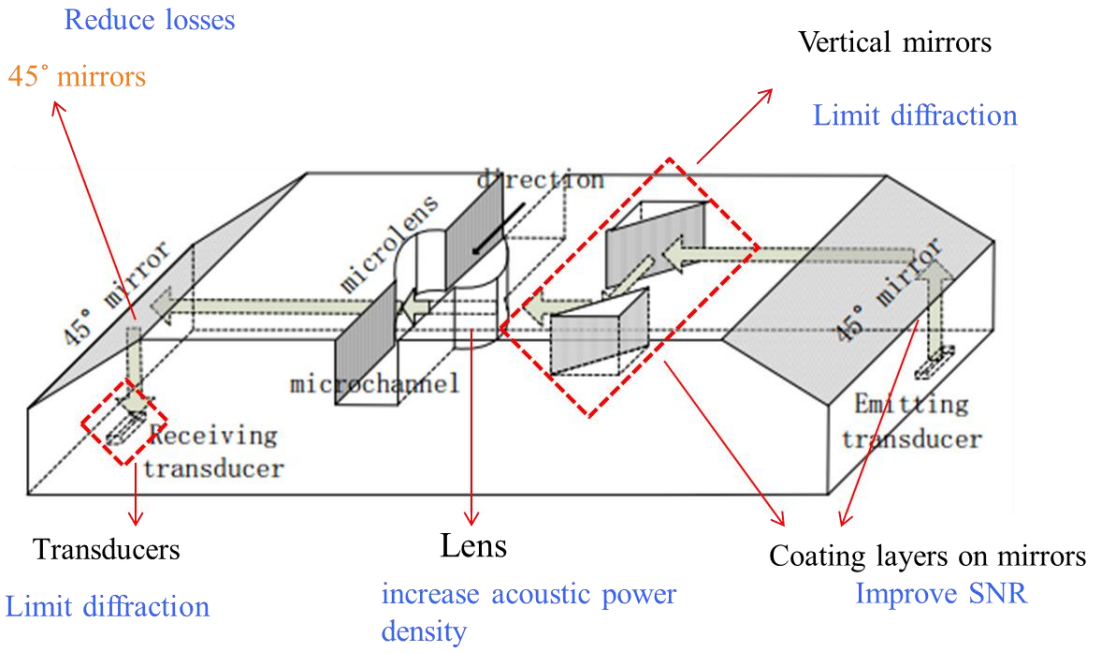

Figure 2.1.2 Global sketch map of the technological points to be studied.

We target an optimized device at 500 MHz central frequency and the improvements include: 1. limit diffraction; 2. reduce losses; 3. improve signal to noise ratio (SNR); 4. increase acoustic power density. To achieve this, as shown in figure 2.1.2, the modified elements are global design to limit the acoustic path, transducers, 45° mirrors, coating layers on 45° mirrors and vertical mirrors, as well as lens structure:

1. 45 ° mirrors element: If the width of the transducer is enlarged, we have to increase the depth of 45 ° mirrors so as to reflect the generated acoustic beams as much as possible. For the deeper 45 ° mirrors fabrication, the roughness, flatness

and underetching have to be optimized to reduce the reflection losses.

2. Vertical mirrors element: we have to optimize the vertical mirrors structures to shorten the acoustic path so as to limit diffraction.
3. Coating layers element: we have to deposit coating layers on mirrors to avoid mode conversion, in order to improve signal to noise ratio in the measurements (associated with Doctor Fabrice LEFEBVRE).
4. Lens element: we also have to integrate lens structure into microchannel to focus acoustic beam , so as to improve detection sensitivity for small size particle detection or for specific actuation functions development (increase local acoustic power density).
5. Transducer element: The central frequency of the transducer film is inversely proportional to its thickness. We have to fabricate thicker films to target the 500 MHz for the central frequency of the transducer. In the other side, the width of the transducer is enlarged to limit diffraction.

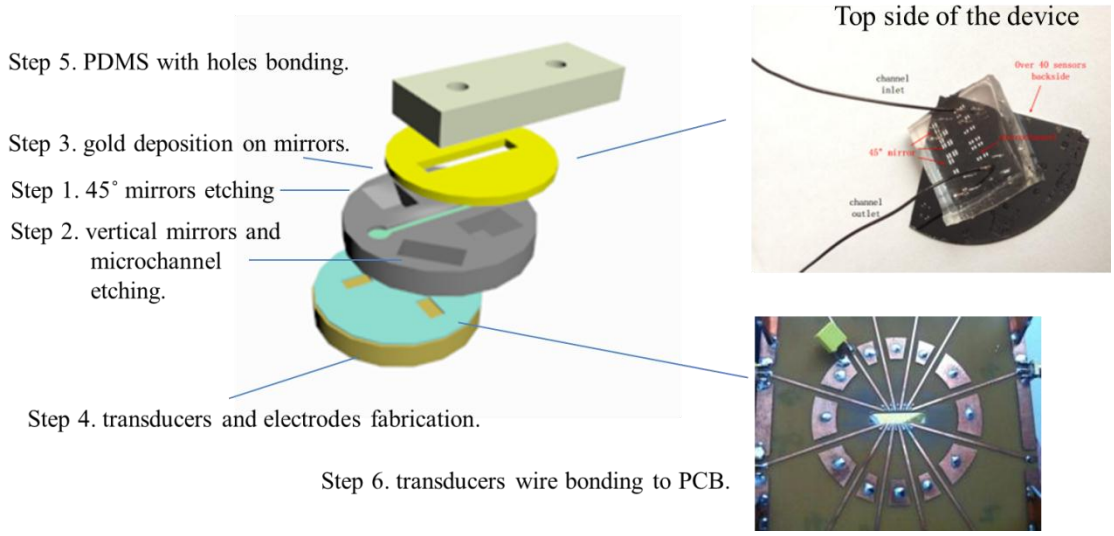

Figure 2.1.3 Identified process of lower frequency device.

To give an overview of the chip fabrication process, and as shown in figure 2.1.3, there are six steps for the final device fabrication. After the chip fabrication, a PDMS layer with drilled holes is bonded to silicon wafer by O_2 plasma. Holes are pre-aligned to the inlets and outlets in the microchannel prior to the bonding, then Teflon tubes are plugged into PDMS layer to import and export sample. Finally, transducers are connected to a PCB using gold wire bonding.

2.2 45° mirrors fabrication and improvement

2.2.1 45° plane wet etching in silicon

The manufacture of micro mirrors inclined at 45° towards the substrate has attracted

attentions in MEMS development because it can provide 90˚ out-of-plane reflection for the application of optical switching or interconnecting. Similar to the optical mirror, 45˚ acoustic mirrors were used as our reflectors for acoustic wave transmission in the direction parallel to the wafer surface. For this anisotropic silicon etching, the strong alkaline substances (pH > 12) such as aqueous KOH- or $TMAH^-$ solutions are chosen to etch Si [1] *via*

$Si + 4\ OH^- \rightarrow Si(OH)_4 + 4e^-$

Si etching in alkaline etchants is highly anisotropic because the bonding energy of Si atoms is different for each crystal plane, which means that the etch rate is dependent on the crystal orientation. Due to the anisotropy limitation in their smallest dimensions, the angle in (100) oriented silicon between the <100> and <111> direction is 54.74˚ (figure 2.2.1), but the angle between the <100> and <110> direction is 45˚.

For silicon etching in alkaline solution, the fastest etching plane is usually the (100) plane, while the (111) plane has the lowest etch rate and acts as an etch stop. Different wet anisotropic etchants will have different selectivity rates between <100> and <111> and appear different aspect ratios.

KOH aqueous solution is widely used in silicon etching in (110) plane. Because the (111) surface activation energy and the atom density is greater than the (100) plane, its corrosion rate is fastest in (100) plane. Nevertheless the transverse reaction rate is slow due to the (111) surface is perpendicular to (100) silicon slice, finally it is formed a (111) side wall and (100) bottom structure with 54.74˚ included angle. In another case of KOH-IPA-Water system, the final structure is different. The addition of IPA competes with OH^- to reduce the reaction in (110) surface, and results in the (110) surface to be a geometric constraint in the etch process. Using this character, when a (100) oriented Silicon wafer is patterned with an etch mask and the etch front is bounded by the (100) planes, the etched channel will move forward along the aperture of the mask in the KOH-IPA-Water system, as a result the {110} mirror planes as side walls are obtained with an inclination of 45˚ to the (100) bottom plane, as shown in figure 2.2.2. For rectangle mask used, the limiting (111) planes will appear on the corner which may also be affected by the components of etching solution [2].

To achieve such mirrors on {100} silicon, two conditions must be satisfied simultaneously: the etch mask must be aligned in the <100> direction and surfactants such as IPA additive must be used with the alkaline solutions [3]. In this kind situation, the anisotropy is strongly dependent on the etching solution. The rate selectivity of different crystal planes and the etching homogeneity depend on the temperature, atomic defects and intrinsic impurities of the silicon crystal, the concentration of Si atoms already etched. Thanks to the control of etching time, the dominant <110> planes are limited to be the 45˚ V groove plane. The fabrication of {110} mirror planes with an angle of 45˚ is a key step for high frequency acoustic wave guiding in our system.

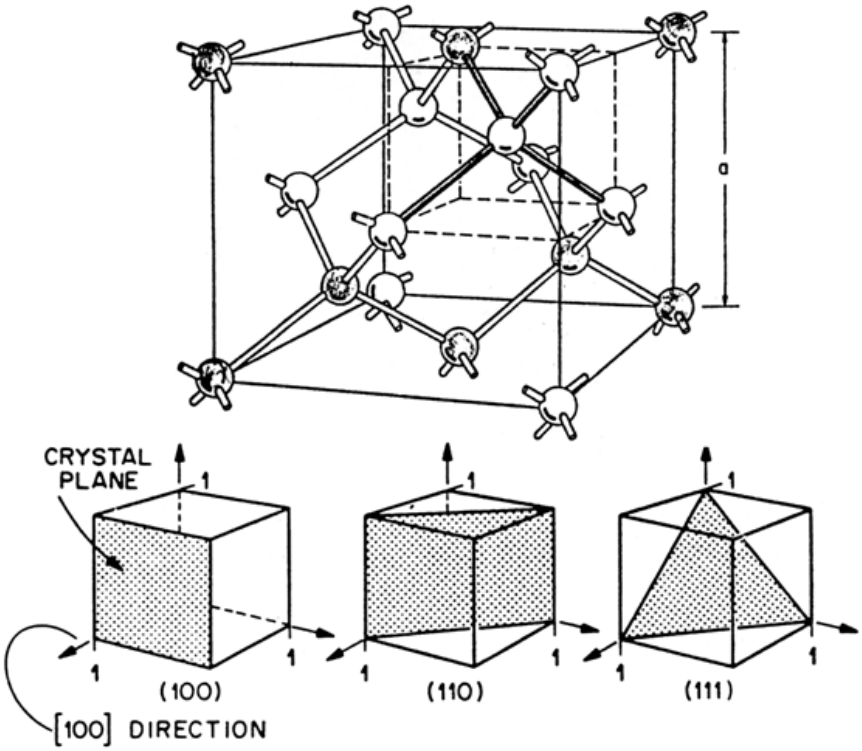

Figure 2.2.1 High anisotropic in different crystal plane of silicon [2].

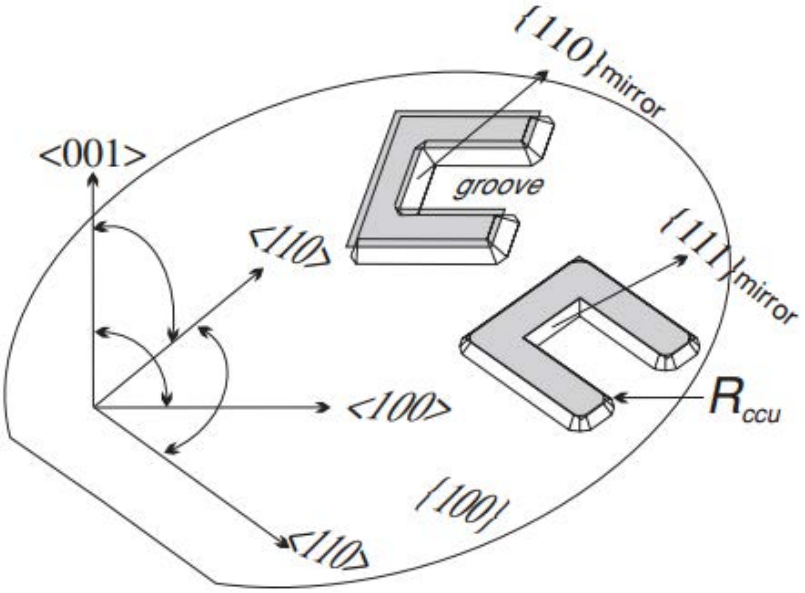

Figure 2.2.2 Orientation of mask and resulting microstructure appearance on (1 0 0) silicon wafer [3].

2.2.2 45° mirrors fabrication improvement

The Tetramethylammonium hydroxide (TMAH) is a kind of organic base with excellent etch selectivity of <100> silicon: silicon oxide 1:5000. The addition of TMAH in the solution can introduce the excess concentration of hydroxyl ions that are essential for the formation of the water soluble silicate complex [4-5]. The reaction is as follow:

$(CH_3)_4NOH \rightarrow (CH_3)_4N^+ + OH^-$

Isopropyl alcohol (IPA) was used as a surfactant as a fact that surface tension decline on low-dimensional features during the etching process. With only TMAH to be the etchant, there are hillocks and patches appearing. But the etching reaction is moderate with the introduction of IPA, due to the adsorption of the larger ionic species from IPA onto specific surface sites [6-8]. Based on the present technique, we use the TMAH-IPA mixture reagent for 45° mirrors etching, and the optimum reaction conditions are characterized.

Heating is necessary in the wet etching process to accelerate chemical reaction. However, considering the boiling point of IPA at 82.6 ˚C in usual case, the reflux condensation equipment is used to avoid IPA concentration sharply decreasing in the process of etching.

There are two kinds of containers used in our setup as shown in figure 2.2.3:

(a) TMAH (20-25% aqueous solution), IPA and DI-water are mixed in a conical flask of 3L total volume. A 3 inches silicon wafer is suspended in the etching solution by a holder to avoid the contact with the magnetic stirrer. Thermocouple is immersed in the solution and used to monitor the real-time temperature. A long condenser tube is fixed on top of the device to cool down the IPA gas;

(b) TMAH – IPA - DI-water system in a beaker with maximum 1L total volume. Moreover, the thermocouple is removed and the hotplate of the magnetic stirring apparatus is used to define the heating temperature. In this situation, IPA particles evaporated and fell down again in the etchant, and a precise control of a stable temperature can be achieved.

Compared to the conical flask, we use a smaller volume of reagent for etching in the beaker, which makes it easier the homogenization of the solution. After removing the thermocouple, we use a hotplate to acheive both functions of heating and temperature monitoring. As the temperature gradient exists in the vertical direction of the reagent, the real temperature around the wafer may largely different from the measurement of the probe. In another aspect, the measurement of the hotplate may reflect a more accurate value of the temperature of the liquid surrounding the wafer. It should be noted that the measured temperature is not the real temperature inside the liquid, but the two values are linked (e.g. 180 ˚C hotplate temperature means 80 ˚C liquid temperature). In fact, the temperature control is a key point in the silicon etching process.

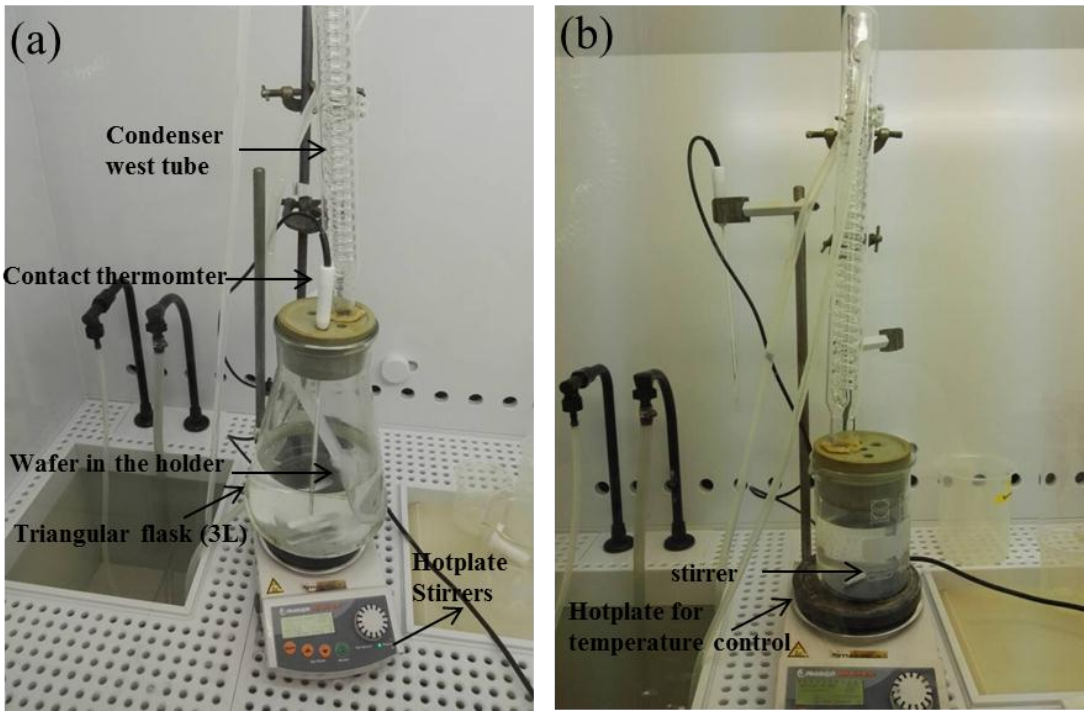

Figure 2.2.3 Schematic of the wet etching equipment (a) in 3L conical flask and thermomter control temperature and (b) in 1L beaker and hotplate control temperature.

SiO_2 layer is chosen to be the protection layer in the wet etching considering its negligible etch rate in TMAH solution. At the beginning, two layers of silicon oxide (800 nm) are deposited on both sides of silicon wafer (n-type <100>, 390 µm thick, double sides polished, Siltronix, France) by Low Temperature Oxide LPCVD using Tempress systems TS 6. To achieve designed patterns, lithography steps were implemented on top side of the wafer. The rectangle patterns of the mask were aligned in the <100> direction of the wafer by SUSS MicroTec MA/BA6 exposure system. After lithography process, the outer surfaces of SiO_2 patterns were etched by plasma using Bâti OXFORD Plasmalab 80 Plus. The parameters were presented in table 2.1.

resist	S1828
spin coating	3000/1000/20s
pre-bake	110 ˚C for 2 minutes
UV intensity	610 mW/cm^2
development	MF322 for 3 minutes
plasma gas	CF4 40sccm and CHF3 40 sccm
input power	180W
pressure	50 mTorr
time	40 minutes

Table 2.1 Parameters for SiO_2 patterns etching.

After the plasma etching, the protection resist S1828 was removed by Acetone as shown in figure 2.2.4.

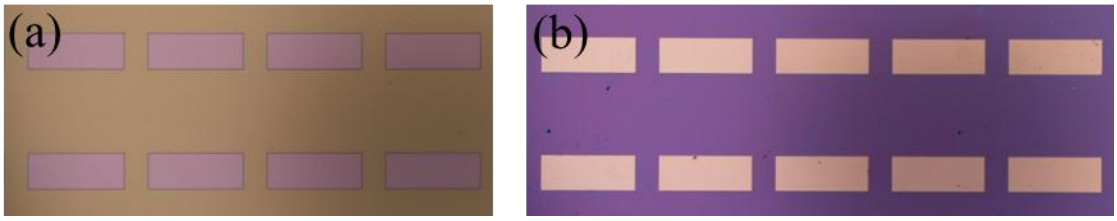

Figure 2.2.4 (a) 3 μm S1828 resist patterns on SiO_2 layer, (b) 800 nm SiO_2 patterns after plasma etching.

It is well known that in silicon etching, TMAH systems have shortcomings such as slow etching rate and a tendency to form a rough surface such as hillocks [9]. Thus we investigate the relationship between the etching speed (in <100> direction), IPA content and heating temperature. The 10% concentration of TMAH is fixed but different IPA concentrations are tested. Liquid is kept at 80 ˚C in the conical flask, as shown in figure 2.2.3 (a), and with agitation by a magnetic stirrer at 250 rpm. In this situation, the IPA reached the boiling point and evaporated rapidly in the reaction. Thus a condensation collecting tube is necessary to cool down gaseous IPA then re-drop into reagent. It is found that different concentrations of IPA played an important role on 45˚ crystal planes formation.

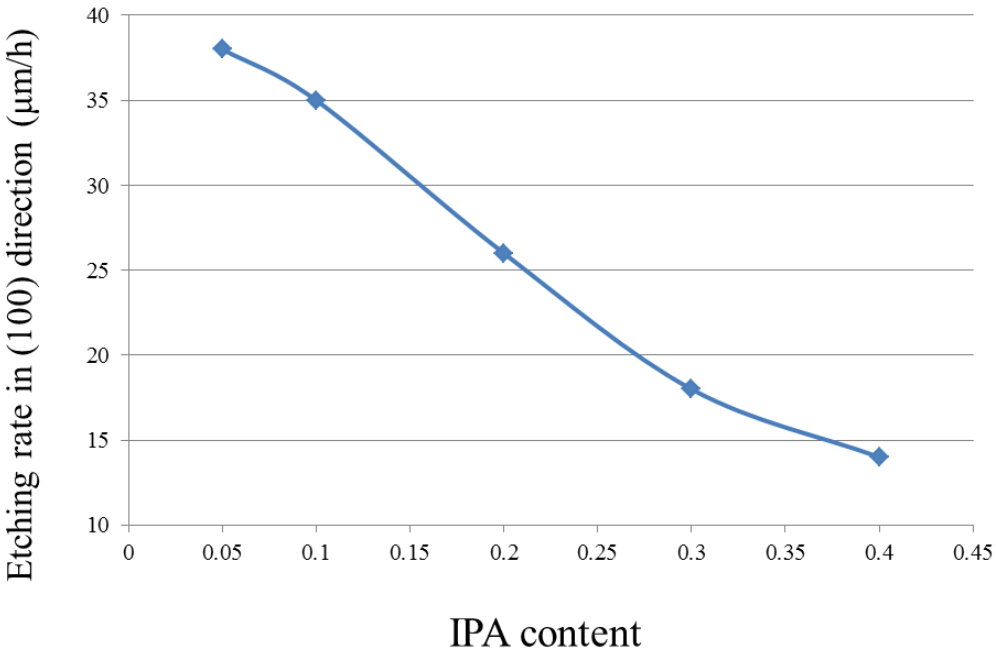

Figure 2.2.5 {1 0 0} etch rate of silicon versus content of added IPA to 10% (V/V) TMAH at 80°C.

In figure 2.2.5, five different concentrations of IPA addition (5-40% V/V) are introduced into the 2600 mL etching solution with 10% TMAH. The etched depth in <100> direction is measured by surface profiler DektakXT Stylus Profiler. When IPA particles were absorbed on the etched surfaces, they hindered the access of reactive OH^- ions which results in the decrease of etching rates in <100> direction. However, at 80 ˚C, gaseous IPA particles evaporate rapidly which take away the generated hydrogen on the silicon surfaces. This phenomenon promotes the etching reaction.
The etching speed in in <100> plane thereupon is influenced. In the overview, the etching speed decrease as the IPA increase. When IPA concentration increase from 5% to 10%, the etch rate has a slow decrease from 38 μm/h to 35 μm/h. At a 20% concentration of IPA, the blocking effect of the surfactant hold dominant situation, thus the etch rate decrease intensively to 26 μm/h. At a 40% concentration, the evaporated IPA particles are in high number, thus the etching reaction slows down.

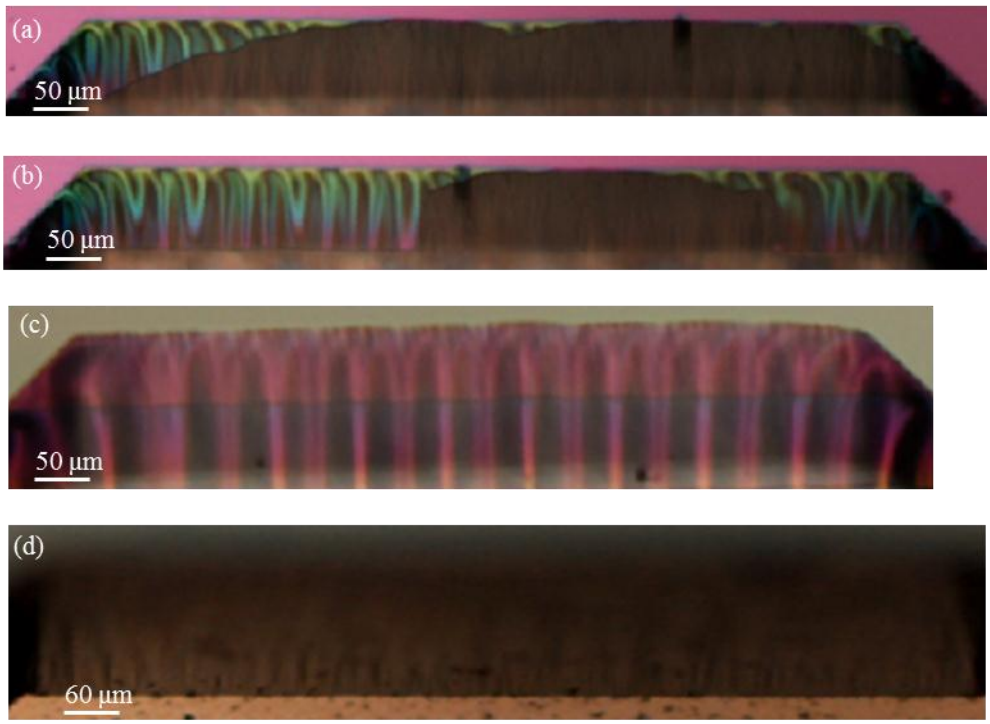

Figure 2.2.6 Optical mirror observation after wet etch: (a) 10% TMAH+ 10% IPA for 4h etch, (b) 10% TMAH+ 20% IPA for 5h etch, dashed box is the breakaway SiO_2 mask, (c) 10% TMAH+ 30% IPA for 7h etch, d) 10% TMAH+ 40% IPA for 9h etch and SiO_2 removed.

For a global monitoring of the 45˚ mirror fabrication after long etching time, we checked SiO_2 mask integrity, shape edge flatness and bottom flatness. As shown in the figure 2.2.6, after etching in 10% IPA, most SiO_2 masks are split away off the mirror surfaces, and vast hillocks can be seen on the bottom of the groove. After etching in 20% IPA the situation of SiO_2 masks cracks were lessened. In 30% IPA for 7 hours etching, nearly all the SiO_2 masks stay on mirror surfaces with flat edge. In 40% IPA for 9 hours etching, the mirrors appearance looks nice with smooth bottom after the SiO_2 masks were removed manually. It can be also deduced that the generated SiO_2

cracks during wet etching process may induce the irregular shape on the mirror surfaces.

To satisfy the high sensitivity for acoustic beam transmission, the roughness of the mirrors should be less than one-tenth of the wavelength - 1μm for 800 MHz acoustic wave in silicon. Figure 2.2.7 shows the 3d mapping curve and scanning electron microscope (SEM) images of the etched mirror surfaces with 10% TMAH and 30% IPA mixer solution. It can be seen that the 45˚ angle slope for the etched mirror and the smooth surface with roughness *Ra* less than 20 nm can be obtained. It has to be noted that the accurate measurements of *Ra* is hard to achieved, due to the unstable contact between probe and the 45˚ plane. Taken into account parameters such as etch rate, mirror roughness and shape distortion, we use 10% TMAH and 30% IPA mixture solution for etching targeted 190 μm depth of 45˚ mirror.

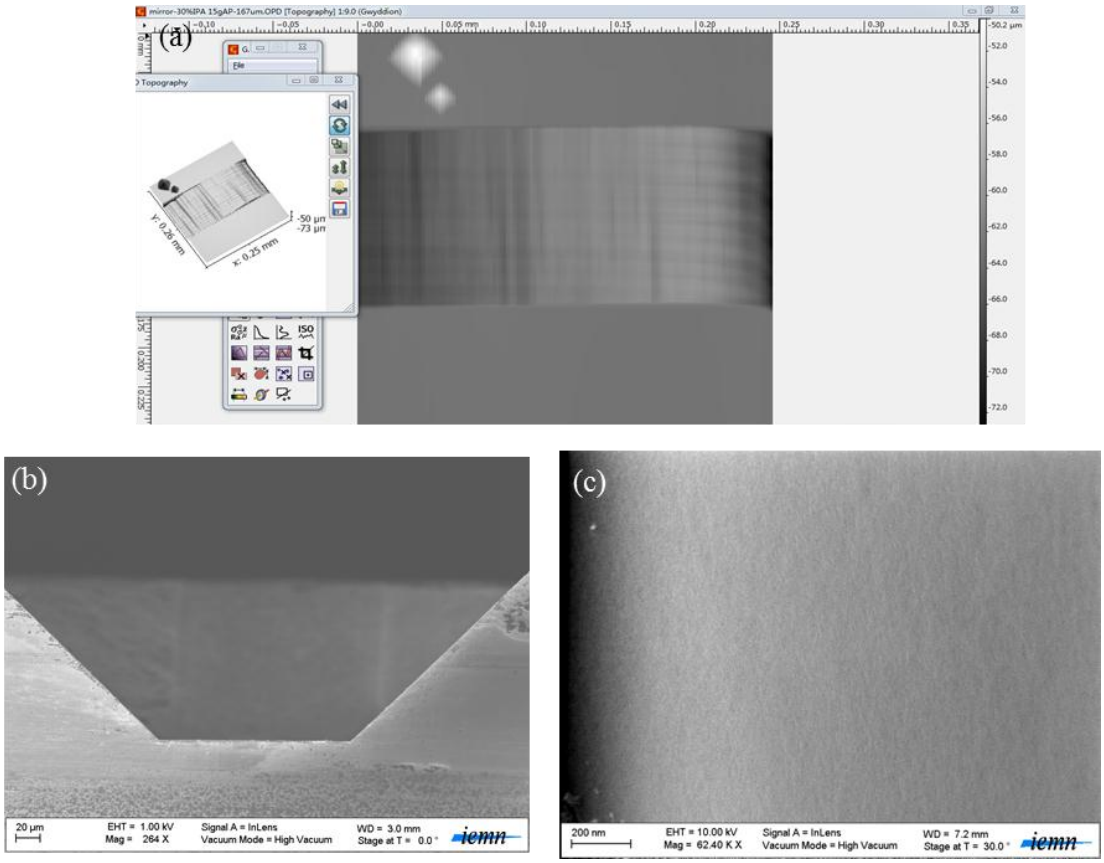

Figure 2.2.7 (a) 3d mapping measurement of mirror surface, (b) cross-section view for 45˚ mirror and c) top view for 45˚ mirror surface.

However, in the multiple tests for 45˚ mirror etching, it is found that this approach is confronted with challenges from the mirror shape stability. Fig 2.2.8 shows the deformation we observed after wet etching in the recipe using 10% TMAH and 30% IPA at 80 ˚C at 250 rpm. The thermocouple control and magnetic stirring apparatus is Heidolph MR Hei-End. In fig 2.2.8 (a), one side of the mirror is distorted apparently lager than the other side. The bent parts are corresponding to the changes of the color

in the SiO_2 mask layer. In fig (b), part of the SiO_2 layer dropped out from the mirror and a clear distortion of the mirror surface can be seen at the breaking off point. As seen in figure (c) after long time etching two surfaces of the mirror coincided, and visible roughness of the mirror surface appeared. In figure (d) serious distortion and deformation are visible for some mirror patterns.

Reasons are not clear why sometimes the etched mirrors show the unwanted deflection results. The unstable phenomena may come from that:
(1) For the 2600 ml volume etch solution, the heating come from the hotplate in the bottom leading to a temperature gradient from bottom to top, so different parts of the wafer sample may undergo various heating conductions.
(2) Considering the heat exchange for big volume solution in the conical flask to the outside, there is a large inertia for the feedback from the thermocouple to the hotplate for heating. The actual temperature around the sample may have much deflection than the apparatus indication.
(3) Fast evaporation of IPA and reflux condensation aggravate the uneven distribution in the thermal conduction, as well as the heterogeneity of the IPA concentration, which affects mirror etching for different parts on the 3 inches wafer.
(4) The chemical etching process would introduce strong internal force, along with the difference of the heating area and fluid force, so part of the SiO_2 mask may break and split away off the surface, resulting in distortion patterns.
In general, the local temperature control is the key point with the limitation of the experimental condition, especially in large reagent volumes. Though we could not obtain the precise temperature value for real-time monitor of each mirror pattern, nevertheless the shortcoming can be limited by small changes during the experiment.

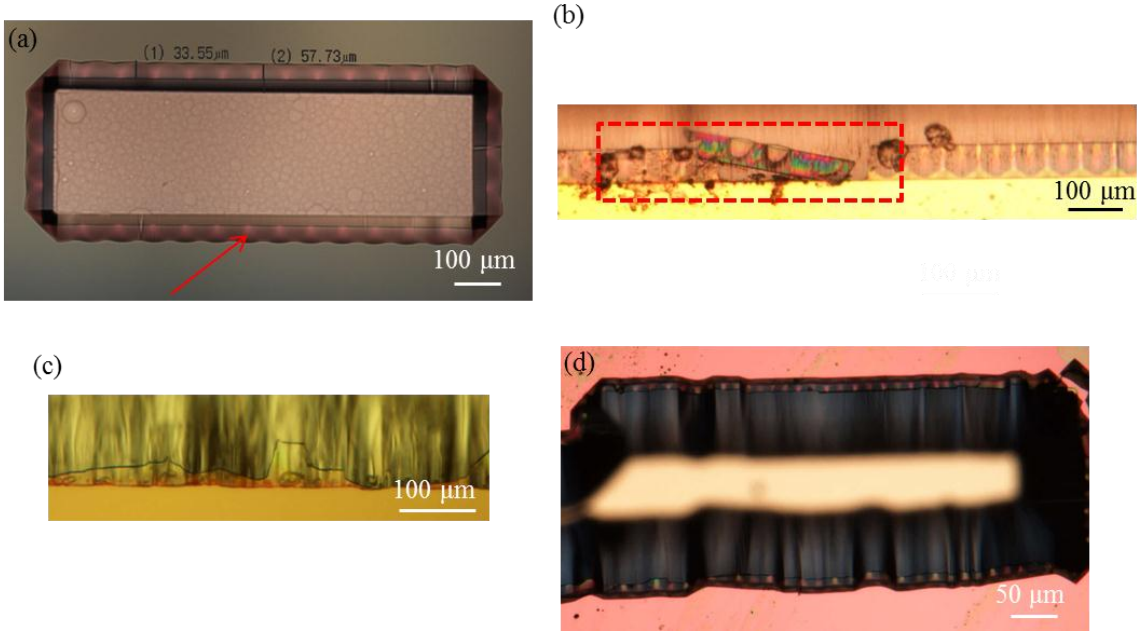

Figure 2.2.8 (a) two hours etching and mirror edge distortion can be observed, (b) 6 hours etching and SiO_2 layer start to split away (dash box), (c) 11 hours etching with visible roughness, d) 4 hours etching and serious deformation.

As shown in figure 2.2.3 (b), the smaller beaker was used to replace the big conical flask. The thermocouple sensor was removed and the hotplate was used to heat and monitor the temperature in the same time. The hotplate was set to 180˚C to heat the solution for at least 2 hours prior to the deposition of the sample. It is found that the temperature in the beaker solution can be stable at 80 ˚C (using probe to check) when using hotplate heating at 180 ˚C for several hours. The reduced total volume of liquid also lowered the IPA evaporation and the temperature distribution inhomogeneity. When using the hotplate to achieve the temperature control, the detected temperature is closer to the temperature on wafer surface, considering the wafer is deposited on the bottom of the beaker. However, we observed that the temperature fluctuation is around ±3 ˚C, thus it is difficult to indicate the real-time temperature in the liquid, but the detected temperature of hotplate has approximately a linear variation with the temperature inside the liquid.

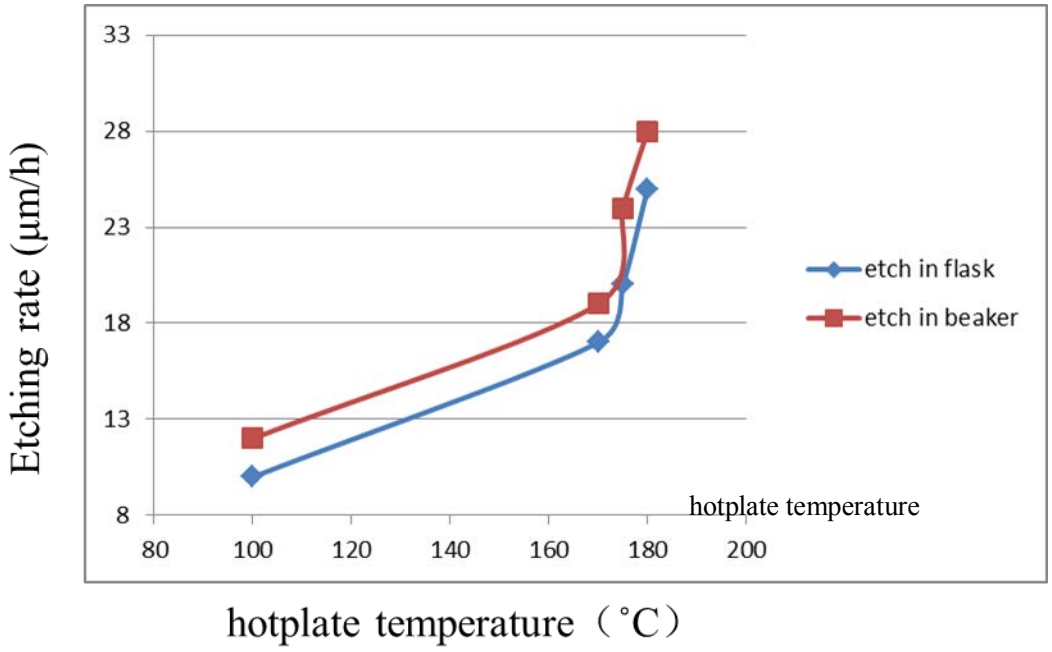

Figure 2.2.9 {1 0 0} etch rate of silicon versus different setting temperature of hotplate.

Through keeping the temperature of the hotplate constant to control the temperature of the etchant in the container, the instability of the mirror etching phenomena were effectively reduced. Here we compare the etch rate in two devices at different temperature, and all the temperatures are measured by hotplate. As shown in figure 2.2.9, the higher value of the hotplate temperature is corresponding to higher internal temperature in the actual etchant, which results in high etching speed. In the long time etching process, the temperature of liquid in the container becomes stable.

The experimental results reveal interesting examples of etch rate variation due to volumes variation of the etchant. The thermal convection inside the system and heat exchange towards the environment goes faster with fewer reaction solution, along

with less non-uniformity of IPA concentration distribution in the liquid, thus the temperature feedback for the heating machine can be more accurate. At 180 ˚C of hotplate measurement, the reagent inside the container is around 80 ˚C thus IPA particles reach boiling point. As IPA evaporate rapidly, they can take away the hydrogen bubbles generated in the etching process and increase largely the etching speed. In the meantime, we observed a mass of bubbles escaped from the surface of silicon which stirred the wafer and finally a high etch rate was achieved.
We survey the mirror surface morphology at different depth using an etching solution of 275ml TMAH, 265ml IPA and EDI 210 ml mixture at 180 ˚C of hotplate. As shown in Figure 2.2.10, (a) the side lines are straight and the SiO_2 layers are unbroken for the 70 μm deep mirror, (b) at a depth of 160 μm, after removing SiO_2 layers by HF for observation, the surface looks smooth as well as the side planes, and the roughness was 400nm measured by surface profiler, (c) with very deep mirror etched at 210 μm, there are irregular areas in the side planes with a maximum amplitude of 4 μm, and the roughness on the surface is measured about 1 μm.

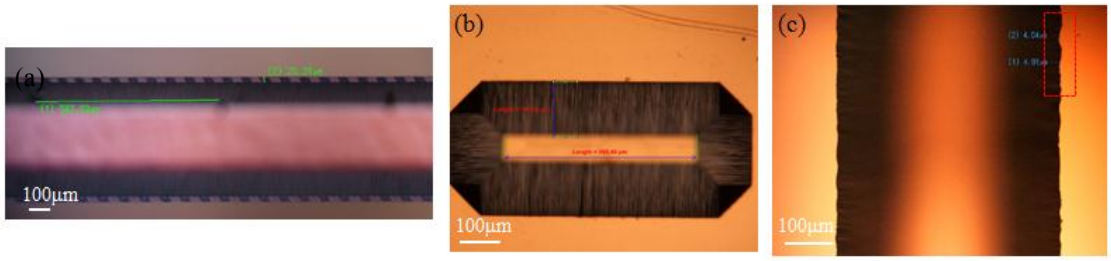

Figure 2.2.10 (a) 3h etching for 70 μm depth mirror. SiO_2 layers with diffraction patterns are on the mirrors , (b) 7h etching for 160 μm depth mirror, (c) 9h etching for 210 μm depth mirror.

Paired with above factors, the final recipe we used is 275ml TMAH, 265ml IPA and EDI 210 ml mixture in the beaker at 175 ˚C of hotplate for 7.5 hours etching. Small magnetic stirrer was used at 50 rpm to reduce the potential heterogeneous etchant distribution in the whole process. The mirror depth is around 180 μm and the lateral displacement for each side of mirror pattern is 50 μm. The large underetching phenomenon always appears in the IPA wet etching procedure. In our experiment, this point should be taken into account when we design the allocated position of transducer, so as to minimize the reflected acoustic energy losses.

2.3 acoustic reflection and optimization

2.3.1 Acoustic wave reflection on solid-air interface

When the acoustic wave propagates in a solid material, mode conversion can appear after reflections. A common case is that, when a longitudinal wave hits an interface at an angle, the energy transfer may cause particle movements in the transverse direction, thus a transverse wave is induced. Mode conversion occurs when a wave encounters

an interface between two materials of different acoustic impedances.

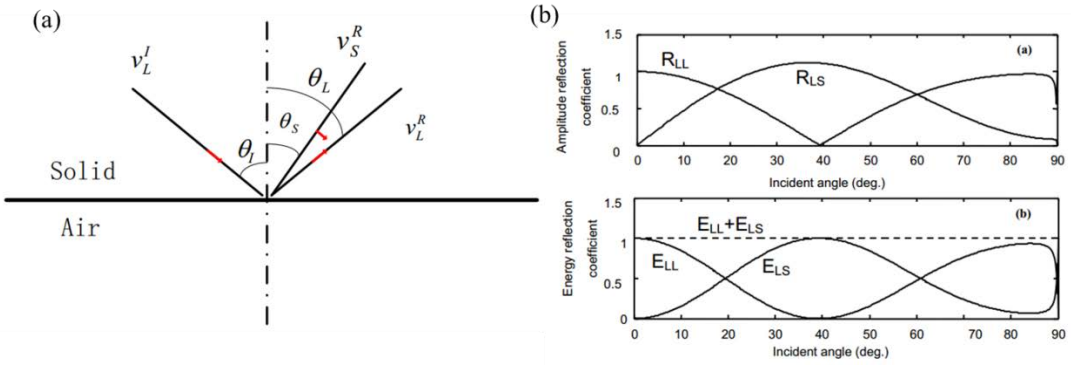

Figure 2.3.1 (a) Reflection of a plane longitudinal wave at the free surface of isotropic solid, (b) Reflection coefficient of longitudinal mode LL and shear mode TL for a longitudinal wave incidence at silicon-vacuum interface [10].

As shown in figure 2.3.1 a, in the acoustic reflection through a boundary between two different isotropic media, the relationship between the angles of incidence and refraction obeys Snell"s law as below:

$$\frac{sin\theta_i}{v_i} = \frac{sin\theta_L}{v_L} = \frac{sin\theta_s}{v_s}$$

where v_i is the velocity of the incident wave, θ_i is the incident angle, v_L and v_s are the velocities of the reflected longitudinal wave and the reflected shear wave respectively, and θ_L and θ_s are the reflected angles of the longitudinal wave and the shear wave respectively.

For acoustic transmission in silicon, the longitudinal wave speed v_i= 8432 m/s, and the shear wave speed v_s= 5398 m/s.

The reflection coefficient for the longitudinal wave R_{LL} is deduced

$$R_{LL} = \frac{U_L}{U_I} = \frac{\sigma^2 sin2\theta_I sin2\theta_s - cos^2 2\theta_s}{\sigma^2 sin2\theta_I sin2\theta_s + cos^2 2\theta_s} \text{ and } \sigma = \frac{v_s}{v_L}$$

and the coefficient for converted shear wave R_{LS} is

$$R_{LS} = \frac{U_S}{U_I} = \frac{2\sigma sin2\theta_I sin2\theta_s}{\sigma^2 sin2\theta_I sin2\theta_s + cos^2 2\theta_s}$$

As shown in figure 2.3.1 b, at the 45˚ incidence angle the R_{LS} is close to 1 but R_{LL} is close to 0, which indicates almost all the incident longitudinal wave is converted into shear wave after reflection. After reflection by 45˚ mirrors as to achieve wave guiding, the major energy of longitudinal wave is converted into shear waves. To avoid the mode conversion, a 4 μm SiO_2 layer were deposited on the mirrors by PECVD to modify the acoustic impedance at 1GHz acoustic characteristic [10].

As shown in figure 2.3.2, at 45˚ reflection plane, 90 % of the longitudinal wave was

reflected at the frequency of 1.7 GHz. However, as the required thickness of the coating layer is inversely proportional to the central frequency of the transducer, for the actuator integration at 500 MHz frequency at least 8 µm SiO_2 layer is required to avoid conversion mode. It is very difficult to achieve this homogeneous film due to the technology limitation.

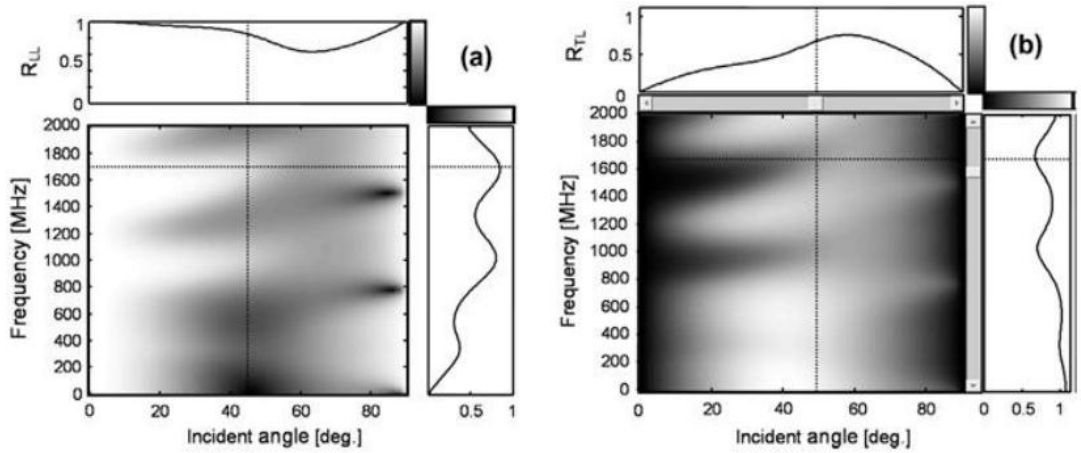

Figure 2.3.2 Reflection coefficient of a longitudinal wave in (a) longitudinal mode R_{LL} and (b) transverse mode R_{TL} at silicon –SiO_2 interface (4 µm thickness of SiO_2 layer) -vacuum interface. (longitudinal wave velocity in SiO_2 : v_L= 6050 m/s and shear wave velocity v_s = 4100 m/s) [10].

2.3.2 Coating layer calculation

As previously mentioned, optimizing the signal-noise-ratio (SNR) in longitudinal waves requires one or more matching layers on the mirror. Before engaging complex technological operations, numerical simulations of reflection coefficients in longitudinal and shear waves were performed. The developed code is also able to assess the overall performance of the system in pulse mode before its fabrication. In the following, we present the theoretical basis used in the simulation model.

We concentrate our efforts in a one dimensional propagation model without anisotropic effects which is sufficient to highlight the main characteristics of the system.

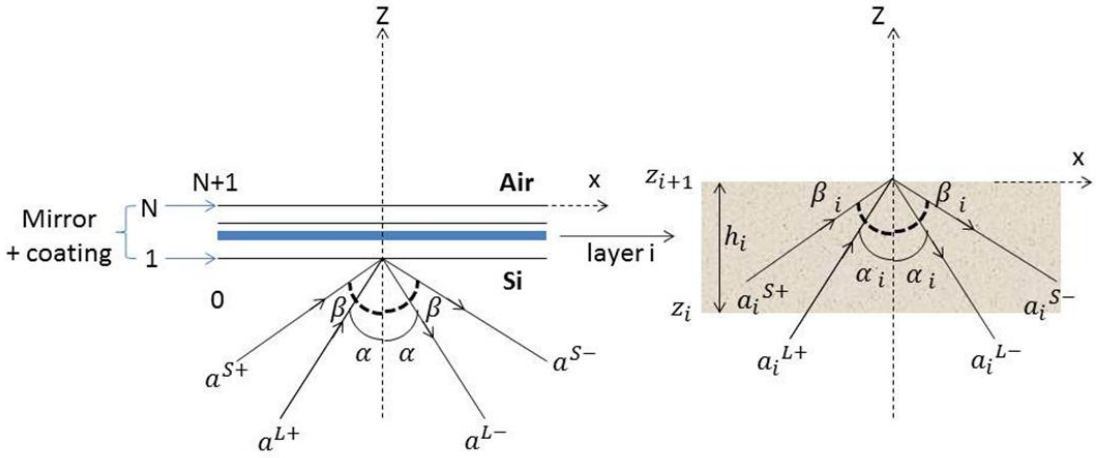

Figure 2.3.3 the geometry of the problem of depicted.

As shown in figure 2.3.3, considering harmonic waves propagation in the (O,x,z) plane, we can define a wave amplitude vector in the i[th] layer as:

$$\overrightarrow{A_i} = [a_i^{L+} \quad a_i^{S+} \quad a_i^{L-} \quad a_i^{S-}]^T$$

And the total displacement vector as:

$$\overrightarrow{u_i}(x,z) = \sum_p \overrightarrow{A_i}\, e^{j(k_{x_i}^p.x + k_{z_i}^p.z)} e^{j\omega t}$$

With $p \in \{L+, S+, L-, S-\}$ witch indicates the polarization (L hold for longitudinal and S for shear) and the direction of propagation (+ or -).

$k_{x_i}^p$ and $k_{z_i}^p$ are the x and z component of the wave vector of polarization p.

The stress/displacement vector in the i[th] layer at z_i is defined as:

$$\overrightarrow{M_i}(z_i) = [u_{xi} \quad u_{zi} \quad T_{xi} \quad T_{zi}]^T = L_i.P_i(z).\overrightarrow{A_i}$$

Where L_i is the layer matrix given:

$$L_i = \begin{bmatrix} \sin\alpha_i & -\cos\beta_i & \sin\alpha_i & \cos\beta_i \\ \cos\beta_i & \sin\beta_i & -\cos\alpha_i & \sin\beta_i \\ j\omega Z_i^L \cos 2\beta_i & j\omega Z_i^L \sin 2\beta_i \frac{\sin\beta_i}{\sin\alpha_i} & j\omega Z_i^L \cos 2\beta_i & -j\omega Z_i^L \sin 2\beta_i \frac{\sin\beta_i}{\sin\alpha_i} \\ 2j\omega Z_i^S \sin\beta_i \cos\alpha_i & -j\omega Z_i^L \cos 2\beta_i & -2j\omega Z_i^S \sin\beta_i \cos\alpha_i & -j\omega Z_i^L \cos 2\beta_i \end{bmatrix}$$

Where Z_i^L and Z_i^S are the longitudinal and shear characteristic impedances of the i[th] layer, α_i and β_i are the incidence angles of longitudinal and shear waves impinging the i[th] layer.

$P_i(z)$ is a diagonal propagator matrix in the z direction:

$$P_i(z) = \begin{bmatrix} e^{jk_{z_i}^{L+}.z} & 0 & 0 & 0 \\ 0 & e^{jk_{z_i}^{S+}.z} & 0 & 0 \\ 0 & 0 & e^{jk_{z_i}^{L-}.z} & 0 \\ 0 & 0 & 0 & e^{jk_{z_i}^{S-}.z} \end{bmatrix}$$

where $k_{z_i}^p$ with $p \in \{L+, S+, L-, S-\}$ denote the wave vector of longitudinal (L)

and shear (S) waves in the positive and negative z directions.
With these definitions, the transfer matrix T_i of the i[th] layer is easily build considering the stress/displacement vector at the interfaces z_i and z_{i+1}. For commodity, we introduce the i[th] layer thickness $h_i = z_{i+1} - z_i$:

$$\overrightarrow{M_l}(z_{i+1}) = T_i . \overrightarrow{M_l}(z_i)$$

With: $T_i = L_i . P_i(h_i) . L_i^{-1}$
The transition between the i[th] layer and (i+1)[th] layer at z_i is described by the boundary relation:

$$\vec{M}_{i+1}(z_i) = B_i . \overrightarrow{M_l}(z_i)$$

where B_i is the bond matrix.
For simplicity, we consider here that $B_i = I$ where I is the identity matrix. This assumption corresponds to perfect interface condition: $\vec{M}_{i+1}(z_i) = \overrightarrow{M_l}(z_i)$.

Combining these relations for a stack N of layers, a global transfer matrix G linking the stress/displacement vector in the silicon substrate $\vec{M}_{Si}$ and the stress/displacement vector in the backing medium $\vec{M}_0$ (air in our case) can be derived:

$$\vec{M}_0(h) = G . \vec{M}_{Si}(0)$$

with $G = \prod_{i=1}^{N} T_i$ and $h = \sum_{i=1}^{N} h_i$, the total thickness of the N layers.
For the silicon substrate and the backing medium, the following relations hold:

$$\vec{M}_{Si} = L_{Si} . P_{Si}(0) . \vec{A}_{Si}$$

$$\vec{M}_0 = L_0 . P_0(h) . \vec{A}_0$$

So, a relation between wave amplitude vectors in silicon and backing can be written:

$$\vec{A}_0 = W . \vec{A}_{Si}$$

with $W = P_0^{-1}(h) . L_0^{-1} . G . L_{Si} . P_{Si}(0)$
It should be noticed that, because the backing is air $a_0^{L-} = a_0^{T-} = 0$ and the previous relation can be written as follows:

$$\begin{cases} \vec{T} = W_{11}\vec{I} + W_{12}\vec{R} \\ 0 = W_{21}\vec{I} + W_{22}\vec{R} \end{cases}$$

where $\vec{T} = \begin{bmatrix} a_0^{L+} \\ a_0^{T+} \end{bmatrix}$, $\vec{I} = \begin{bmatrix} a_{Si}^{L+} \\ a_{Si}^{T+} \end{bmatrix}$, $\vec{R} = \begin{bmatrix} a_{Si}^{L-} \\ a_{Si}^{T-} \end{bmatrix}$ and $W = \begin{bmatrix} W_{11} & W_{12} \\ W_{21} & W_{22} \end{bmatrix}$.

Solving for $\vec{R}$, we get:

$$\vec{R} = Q\vec{I} \text{ with } Q = \begin{bmatrix} Q_{11} & Q_{12} \\ Q_{21} & Q_{22} \end{bmatrix} = -W_{22}^{-1} . W_{21}$$

Introducing the components of $\vec{R}$ and $\vec{I}$, it is easy to show that the reflection coefficients are given by:

$$R_{LL}(\theta_0, f_0, h) = \frac{a_{Si}^{L-}}{a_{Si}^{L+}} = Q_{11}$$

and

$$R_{LT}(\theta_0, f_0, h) = \frac{a_{Si}^{T-}}{a_{Si}^{L+}} = Q_{21}$$

As indicated in the previous expressions, we restricted the study to the case of a single matching layer. The reflection coefficients are functions of the frequency f_0, the angle of incidence θ_0 and the thickness h of the matching layer.
For a fixed angle of incidence $\theta_0 = 45°$ and a central frequency $f_0 = 1\,GHz$, we computed the reflection coefficients $R_{LL}(\theta_0 = 45°, f_0 = 1GHz, h)$ and $R_{LT}(\theta_0 = 45°, f_0 = 1GHz, h)$ as functions of the matching layer thickness h for gold and copper.

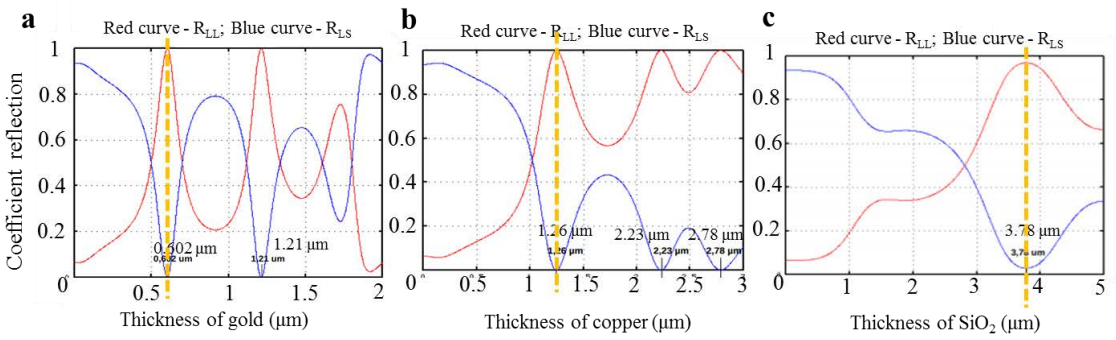

Figure 2.3.4 Simulation for the thickness of the matching at 1GHz harmonic frequency. (a) for gold, (b) for copper and (c) for SiO_2.

As presented in figure 2.3.4, simulations show that with the matching coating layer, the longitudinal to shear reflection R_{LS} varies from 1 to 0 and the longitudinal to longitudinal reflection R_{LL} varies from 0 to 1. For 1 GHz harmonic frequency of the transducer, the optimized matching layers can be a 600 nm gold layer, a 1.26 µm copper layer or a 3.78 µm SiO_2 layer, which makes it possible to obtain R_{LL} close to 1 and R_{LS} close to 0, and which means that the mode conversion can be avoided for longitudinal wave reflection. The relevant experiments and results were characterized in chapter 3.

2.4 Micro-system design and fabrication

2.4.1 Improved structure: 1 vertical mirror system and single lens system

Lens structures are widely used in the optical and acoustic system for focusing and

imaging. In high acoustic frequency field, there are already developed applications for removal of particles *via* focused acoustic beam using acoustic lenses [11]. For our on-chip acoustic measurements, single cylindrical lens systems were integrated for acoustic power focusing.

As indicated in fig 2.4.1, the focused acoustic beams introduce strong power intensity gradient on the focusing plane, and two acoustic streaming was generated which affect particles in the acoustic field. Thanks to combined actions of the added-mass force, acoustic radiation pressure and streaming inducing drag forces, particles at the focus could be trapped or dislodged at a short distance from the focusing plane. Through adjusting the duty cycles and power levels of the input signals, it was possible to manipulate individual particles in several micrometers diameter with setting the focusing plane on the channel wall.

Similarly to optical lenses, there is also the geometric distortion that exists in acoustic lens focusing [12]. The geometrical aberrations of an acoustic lens which come from the acoustic reflection dispersion by the lens structure can be much less than a wavelength. Considering this phenomenon in the acoustic lens for focusing particles, we may observe a small shift between the theoretical focusing plane and the effective one for particles dislodging. When we design the lens structure, different focal lengths have to be characterized to find the best focal plane.

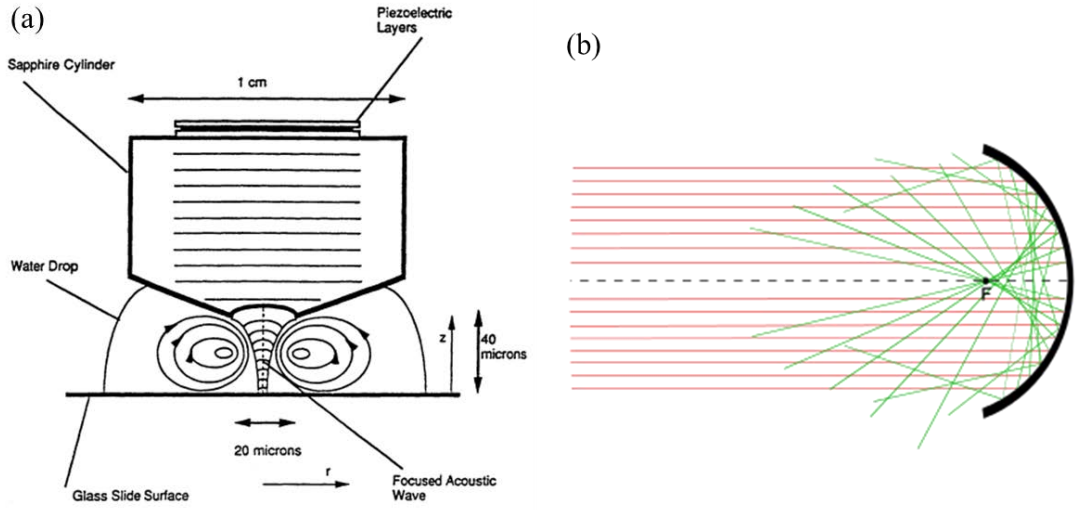

Figure 2.4.1 (a) Acoustic spherical focusing in a plane of gigahertz-frequency waves, (b) geometric distortion of lens aberration [11].

For the purpose of higher sensitivity of acoustic characterization and high frequency on-chip acoustic manipulation of particles, we optimized the channel structures and integration of lens structure.

As shown in Fig 2.4.2, compared to Dr Gao's work, our main improvements of structures cover two aspects:

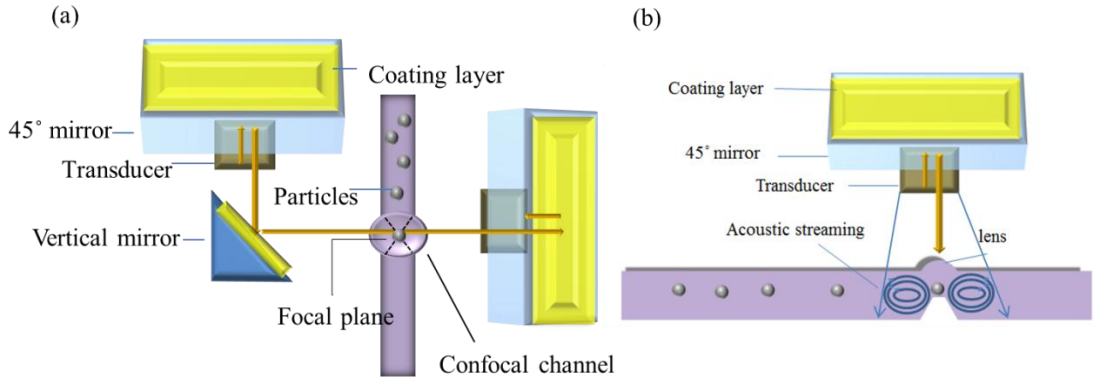

Figure 2.4.2 (a) one vertical mirror for wave guiding prior to the confocal lens of the channel, (b) lens-focusing for higher resolution acoustic characterization and manipulation. Arrows indicated the scope of the acoustic field.

(a) We use one vertical mirror system to replace two vertical mirrors system in acoustic characterization. Though parts of the parasitic noises are filtered through the two vertical mirrors [13], however, the acoustic propagation paths are evidently increased due to the double reflections by the two successive mirrors. As a result, the acoustic diffraction lowers signal-to-noise ratio, particularly in our 500 MHz system. Using the one vertical mirror system, the acoustic diffraction is restrained. Besides, a coating layer with certain thickness is deposited on both 45° mirrors and vertical mirrors. Thus the mode conversion is largely restrained. In the final results, we find that the signal-to-noise ratio from one vertical mirror system is remarkably optimized than in two vertical mirrors system.

(b) Single lens structures can be integrated for both acoustic characterization and manipulation. Compared to the one vertical mirror system, the acoustic propagation path is further shortened thus the diffraction is less. In the lens structure, a narrow flat surface was set on the focusing plane of the lens as a reflector. Meanwhile, the reflection mode is used in lens system for acoustic characterization, which introduces less noise than using the transmission mode in the vertical mirrors system. Apart from the function of characterization, the acoustic manipulation in the same structure could also be achieved. When ultrasound beam is focused, the acoustic energy could be directed to the focal region and generate highly localized velocity and acceleration fields. Around the reflector, two strong acoustic vortexes may be generated due to streaming.

2.4.2 Microchannel fabricated by dry etch

In deep reactive-ion etching (DRIE) the most popular method is the Bosch Process which is named from the German company Robert Bosch GmbH. This method is a high-aspect ratio etching technology which repeats the cycle of isotropic etching followed by protection film deposition. For silicon etching with fluorine, it is naturally isotropic. In order to transform isotropic to anisotropic etching, it requires the alternate etching and deposition steps. Usually the plasma based on SF6 etches

with O_2 to achieve fast etching, and the plasma of C4F8 creates a protection layer. A bias voltage was implemented to get energetic ions to remove the protective polymer layer selectively on the feature bottom to expose Si atoms to fluorine action, as shown in figure 2.4.3.

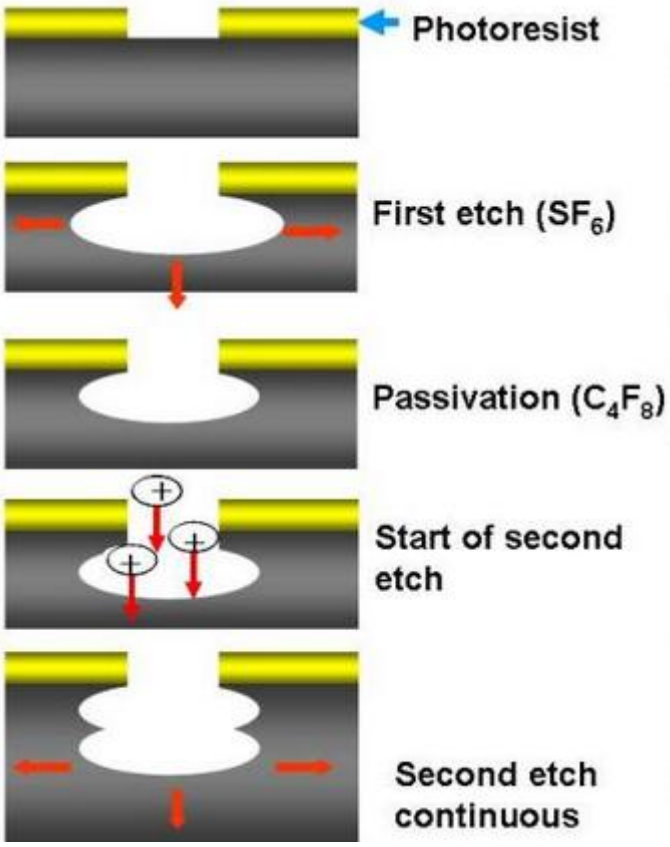

Figure 2.4.3 Step of Bosch methods for Si dry etching [14].

After wet etching of the 45˚ mirrors, we used Bosch process to etch the microchannel for sample injection and vertical mirrors for acoustic parasitic signals filtration. Detailed recipe was presented in table 2.2.

resist	AZ 9260 7 μm
plasma gas	SF6 450 sccm/O_2 45 sccm and C4F8 300 sccm
etch/pass time	8.5s/3.5s
coil/platen power	2000W/50W
temperature	0 ˚C
etch rate	7 μm/min

Table 2.2 Recipe of Bosch process for channel etching.

As shown in figure 2.4.4, the roughness of the sidewall is less than 100 nm, which had almost no impact on the resolution of high frequency acoustic transmission, and a

nearly vertical sidewall for the channel with a depth of 140 µm was obtained.

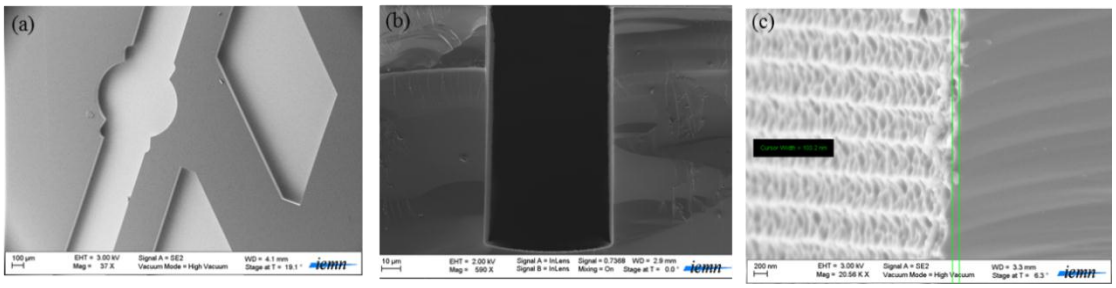

Figure 2.4.4 SEM photos for the survey after DRIE. (a) top view of the channel and vertical mirrors, (b) cross section view of the 140 µm depth, (c) enlarged area of the side wall.

After we etched deep channel above 140 µm in silicon, it was found that there are damages in different levels on the 45˚ mirrors after ICP process. As shown in figure 2.4.5, some defects were visualized on mirror surfaces and spread along the edge. After 21 minutes plasma etching for channel formation, the resist AZ9260 used as a mask were heated by continuous plasma bombardment in radio frequency power. For resist on plane surface, the global topography stays correct. However, the resist on 45˚ mirrors are not spin-coated uniformly sometimes. The roughness of the mirrors and the angle of inclination, as well as the irregular shape of mirrors can cause stress in the resist after lithography.

Thus in the ICP process, where there are thermal exchanges and physical impacts between plasma and on the resist, a strong internal stress appears and results in the peel and crack of the coated resist. Without the protection of the resist on mirrors, the plasma would etch the silicon atoms and induce many defects. These defects will confuse the acoustic signals reflection by the mirrors and introduce more acoustic noise. Meanwhile, the crack on the mirror edge would insert air between the 45˚ mirrors and the microchannel, as shown in figure 2.4.5 a, thus part of the reflected acoustic beam can be prevented to propagate into the channel.

To solve this problem, we used double layers resist coating on mirrors used as a mask in the ICP process. PMGI was spin-coated as a first layer on the wafer to fulfill the gap in the mirrors and smooth the substrate. Then the AZ9260 was used to form the channel patterns for the next dry etching step. Subsequently, the continuous ICP etching process was divided into several steps. For each 7 minutes of the etching process with 50 µm depth of the channel achieved, a 15 minute break time was added to cool down the resist. In this way, most defect phenomena can be avoided and the 45˚ mirrors show a better performance in the acoustic reflection.

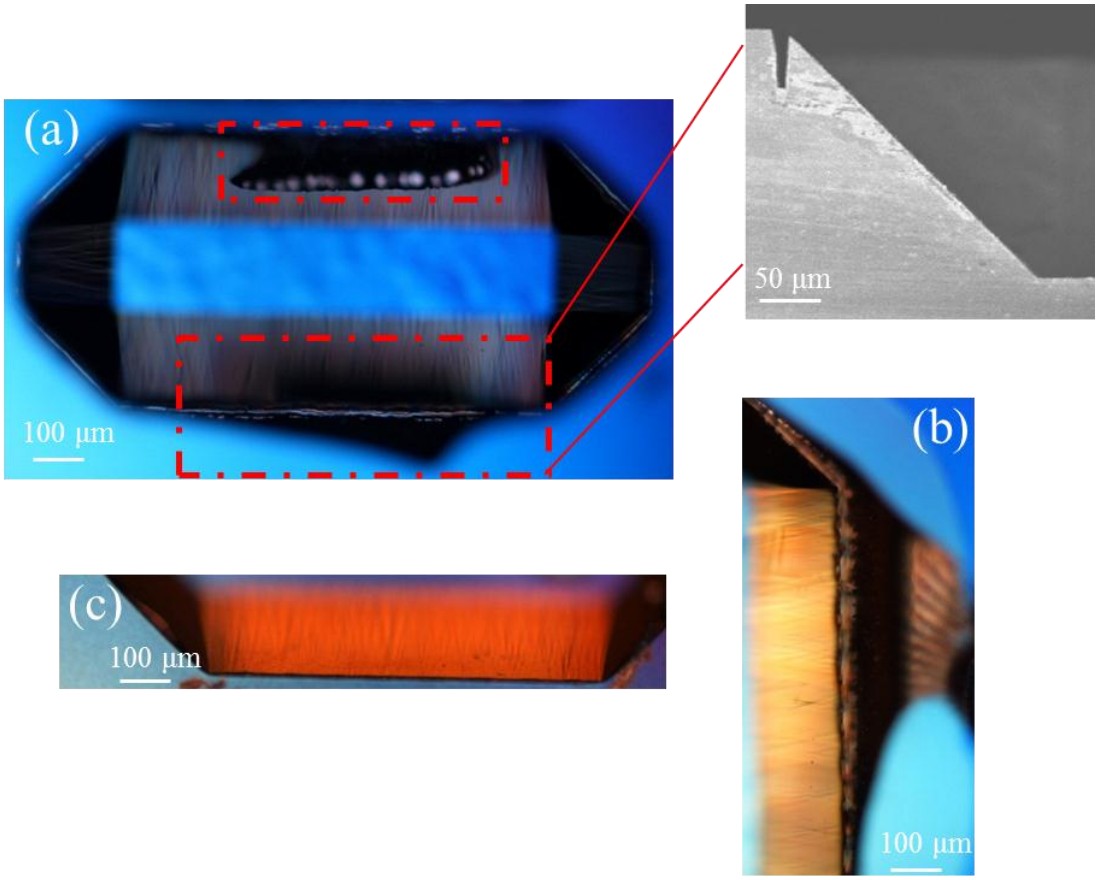

Figure 2.4.5 Damage and defect by ICP process after treatment (a) on 45˚ mirror surfaces, enlarged area and SEM of cross-section in dash box, (b) on the edge of the 45˚ mirror with gold coating, (c) better mirror surfaces with gold coating after improvement of ICP process.

2.4.3 Gold deposition on mirrors and vertical channels

Gold was chosen to be the material used for acoustic matching layer in our device because it requires the lowest thickness in comparison to the other materials investigated. From the simulation shown in figure 2.18, it is known that 600 nm thick gold layer can be used for matching at 1 GHz working frequency so as to avoid mode conversion. Depending on the linear relationship between the thickness and frequency, it can be deduced that 750 nm thickness of gold layer is required for 800 MHz acoustic characterization and 1.2 µm thickness of gold layer for 500 MHz frequency.

At the beginning, we tested gold deposition through lift-off process. In this progress, the resist patterns would determine the final gold patterns. However, we found that there are large deformation happened in the normal photography process, which lead to the heterogeneous adhesion of gold deposition.

As shown in figure 2.4.6 (a), the heterogeneous distribution phenomenon happened of resist on the surface in lithography process. This phenomenon always appears for resist deposit on deep channels or grooves. As we have such a deep 45˚ mirrors (180 µm) and deep channel/vertical mirrors (140 µm), it is difficult to achieve spin-coating of the resist on the channel bottom with acceptable flatness. Afte the spin-coating of resist, there will be some bubbles unresolved inside the channel. These bubbles

expand in the heating, and give rise to the resist split away off the substrate, and in addition destroy the expected patterns for next step.

To release internal tension induced by bubbles, we do the annealing process for the sample after lithography. The slowly heating and cooling process remit the internal pressure inside the resist and help bubbles escape to outside. In our recipe, we introduced PMGI SF19 for pre-coating on the channel prior to AZ 9260 resist with SAWADEC low speed controlled steps of heating and cooling.

This procedure works as shown in figure 2.4.6 (b): resist could stay after lithography but was not totally homogeneous, thus the gold layer distribution after lift-off is less uniform. This problem still remains to be solved for further exploration, but it can preliminarily satisfy the requirements of our process using manual operations.

After the fabrication of the microchannel and vertical mirrors, a 750 nm gold layer was sputtered on the full side of the wafer. Then the resist AZ 1512 was injected into the 45˚ mirrors and vertical mirrors using a needle. Thanks to the capillarity action the resist can stay in the mirror patterns rather than overspread to the microchannel. With 110˚C baking for 5 minutes, the resist is solidified and the sample was placed in the gold etch solution for 1 hour at room temperature. The etched solution used is composed of KI : I_2: H_2O = 4 g : 1 g : 40 ml. Figure 2.4.6 (c) shows the optical view of gold on mirrors after etching and (d) shows gold by SEM photos.

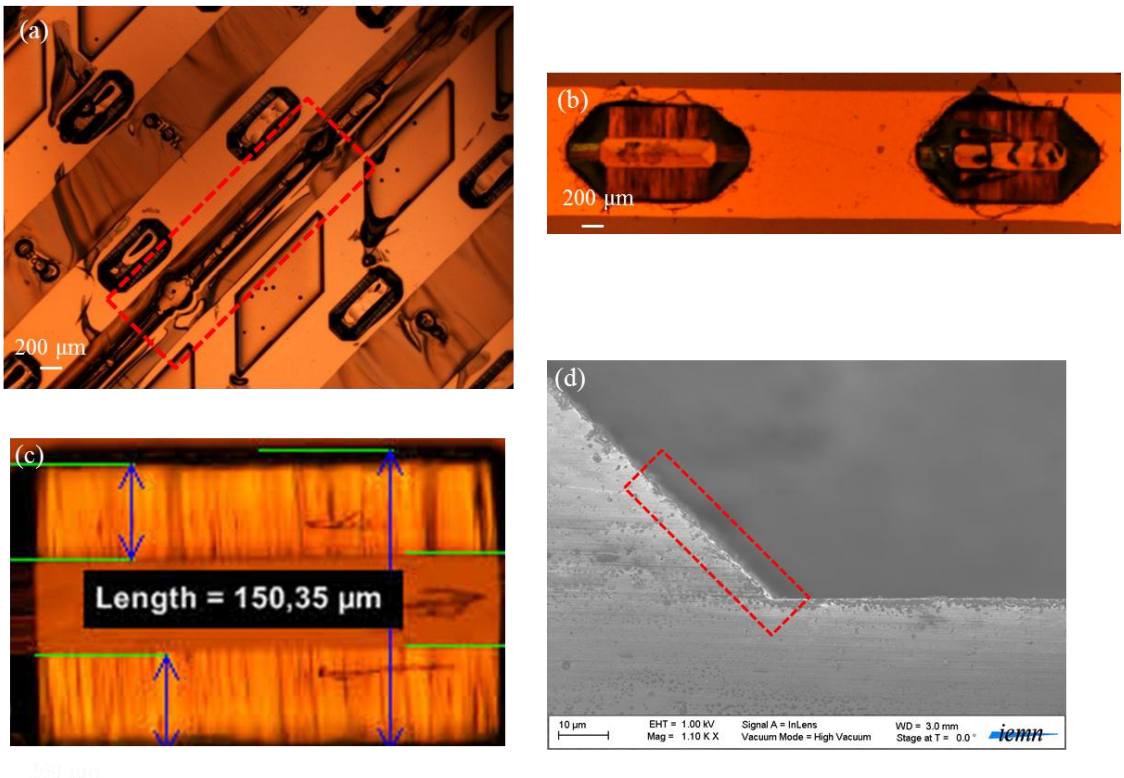

Figure 2.4.6 Improvement for the gold deposition on mirrors. (a) heterogeneous adhesion for resist on the channel surface, (b) gold film on mirrors with less uniformity, (c) gold deposition after manually coating resist, d) SEM photos of 1µm gold on 45˚ mirrors (dash box).

2.5 Piezoelectric transducer fabrication and characteristics

2.5.1 Piezo-electric transducers choice

For our high frequency acoustic device, the key step is the selection of an appropriate piezoelectric material for transducers. Commonly used piezoelectric materials include PZT ceramics [15-16], PVDF piezo-polymer [17], $LiNbO_3$ crystals [18], ZnO films [19] and so forth. Among them, Zinc oxide (ZnO) film can be an excellent candidate which shows low dielectric permittivity, electromechanical coupling performance, high longitudinal sound velocity and excellent biocompatibility [20]. Taking these advantages ZnO is widely used in a variety of applications including acoustic wave devices, photoconductors, thin-film transistors and nanowire devices.
As shown in figure 2.5.1, the zinc atoms are stacked tightly in hexagon along with inserted oxygen hexagonal structure. Four oxygen atoms are around one zinc atom with (3/8) c space, where c is the main symmetry axis of the crystal [21]. The asymmetry in c axis determined the piezoelectricity of ZnO crystal structure thus ZnO possess higher piezoelectric modulus in c axis than in other directions. The piezoelectric response along [0 0 1] direction, favorable stability and availability make it one of the most popular piezoelectric materials for thin-film device applications. Here we used the radio-frequency (RF) magnetron reactive sputtering method for c axis orientation ZnO film thanks to its compact film layer fabrication advantages, low temperature deposition and high sputtering speed [22].

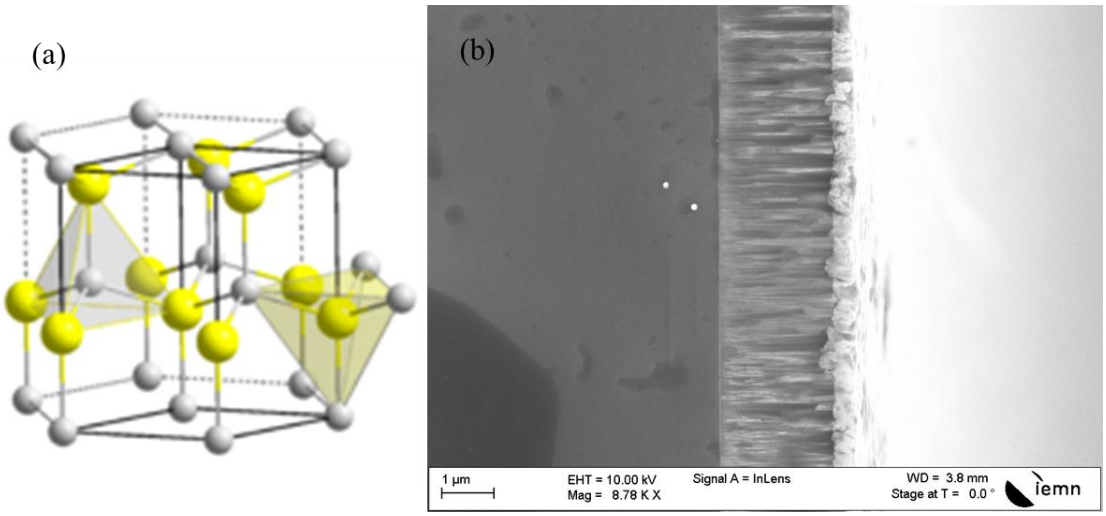

Figure 2.5.1. (a)The wurzite model for ZnO crystalline structure, (b) cross section of SEM for sputtered 2.6 µm ZnO film on Pt ground electrode and gold top electrode.

When driven by an electric field perpendicular to the substrate, the sputtered ZnO films show a strong tendency to grow with the c-axis and therefore suitable for longitudinal wave excitation. As a matter of fact, it is difficult to obtain a 90˚ c-axis with respect to the target on the whole substrate. Thus the c-axis is inclined at some

angle depending on the position on the wafer. Usually an angle between 10˚ and 20˚ exists in the ZnO film growth process. In addition the mechanical displacements of the quasi-longitudinal and quasi-shear waves are inclined with respect to the propagation direction. The polarization angle α appears as a function of the inclination angle χ as shown in figure 2.5.2. When the inclination angle χ increases from 0˚ to 43˚, the resonant modes transfer from pure longitudinal mode to quasi shear and for the longitudinal mode, the polarization angle α varies from 0˚ to -4˚. At χ=43˚, the quasi-longitudinal wave speed reaches a minimum value 5936 m/s and the quasi-shear wave speed with a maximum 3213 m/s. The electromechanical coupling coefficient squared K^2 reflects the acoustic energy converted. At χ=0°, only longitudinal mode will be excited, and at the inclination angle 43˚ and 90°, only shear wave mode is generated. As our transducers have an inclination angle much less than 43˚, most parts of generated longitudinal wave energy can be coupled, but the resulting noise due to shear waves (the inclination angle in our case is less than 10˚ depending on the position on the wafer) could not be ignored in the acoustic microfluidic device.

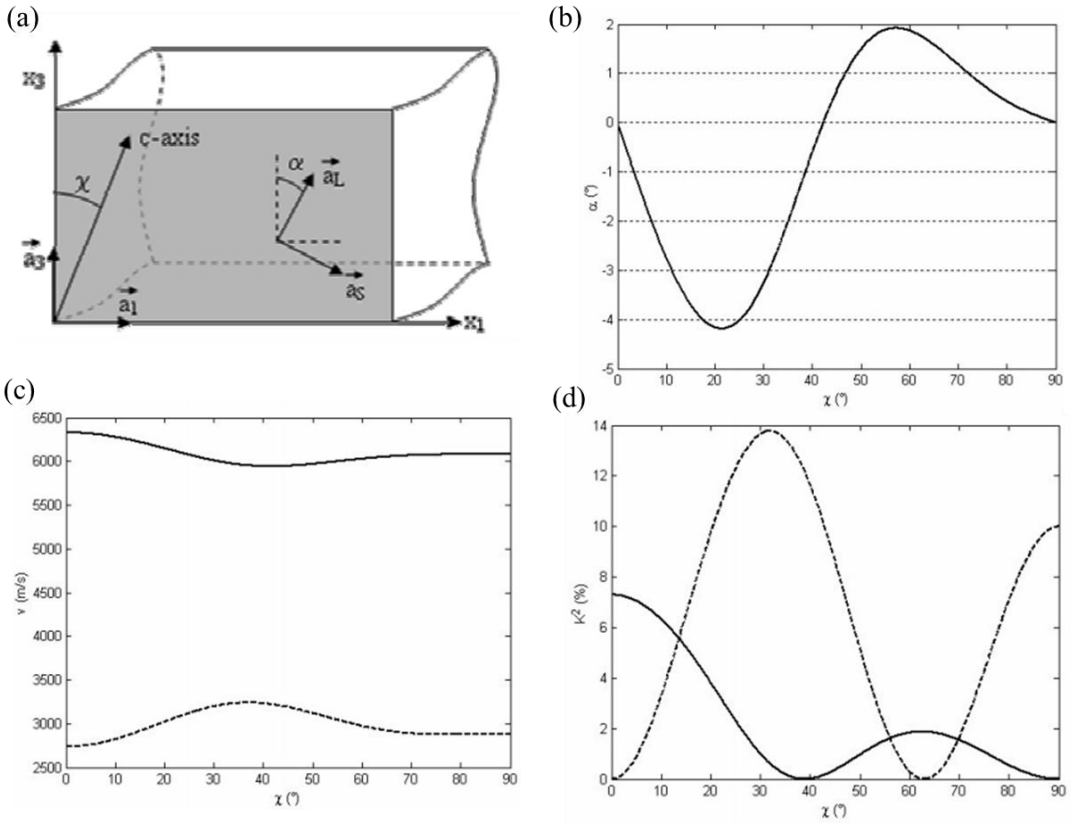

Figure 2.5.2 (a) coordinate system for simple c-axis inclined ZnO, the *stiffness, piezoelectric and permittivity tensors are expressed in the (x_1,x_3) referential, (b) with respect to the propagation direction, the polarization angle α as a function of the inclination angle χ, (c) acoustic velocities of quasi-longitudinal (solid line) and quasi-shear (dashed line) modes, (d) electromechanical coupling coefficient squared K^2 for longitudinal (solid) and shear wave mode (dashed) depending on c-axis inclination angle χ [23].*

The area of the piezoelectric transducer is determined in order to ensure that the real part of its electrical impedance is close from 50Ω at the resonance frequency f_r according the equation:

$$Z(f_r) = \frac{A}{Sf_r^2} - j\frac{1}{c_0}\frac{1}{2\pi f_r}$$

where A is a constant characterizing the piezoelectric material (A=1.0458 × 10^{12}Ω •m^2Hz^2 for ZnO), S is the area of the piezoelectric transducer and C_0 is the static capacitance which can be approximated by the classical formula applied for a planar capacitance

$C_0=\varepsilon S/e$

where ε and e are respectively the dielectric constant and the thickness of the ZnO.

From this equation, it can be deduced that the central frequency of ZnO transducer is linearly inversely proportion to the thickness of the film.

The ZnO film deposition technique for 1GHz frequency (2.5 μm thickness) has already been developed in our group. For lower working frequency, the required thickness is higher which may introduce more technical problems. Thus we evaluate different material for transducer fabrication and try to develop new technology for transducer integrate in the silicon device.

Material	$LiNbO_3$ Y/36˚	ZnO	PZT4
Relative dielectric permittivity ε_r	39	8.8	635
Surface transducer (μm^2)	55080	55080	2000
Frequency (GHz)	0.65	0.65	0.65
static reactance at resonance Xt (Ω)	-73.3	-277.9	-77.1
radiation resistant resonance Rt (Ω)	38.9	50.4	45
transducer thickness (μm)	5.7	4.9	3.5
Losses without matching (dB)	-2.3	-9.4	-2.2

Table 2.3 Comparison of fixed surface technologies at the same 650 MHz central frequency and 50Ω real-part impedance, the electrical properties of $LiNbO_3$, ZnO and PZT4.

As shown in table 2.3, we deduce the electrical properties for $LiNbO_3$ Y/36˚, ZnO and PZT4 at the same frequency of 650 MHz and 50Ω real-part impedance. The required surface of PZT4 is 2000 μm^2, which is too narrow for transducer fabrication in our device. Moreover, the acoustic diffraction will be large due to short transducer width, which may enhance more parasitic noise. The electrical losses for $LiNbO_3$ Y/36˚ is less than for ZnO, and in another aspect, the static reactance at resonance for $LiNbO_3$ Y/36˚ is much less than ZnO, which is easier to match. However, the high frequency $LiNbO_3$ bulk material device is hard to achieve due to the required very thin film which is usually fabricated by manually polishing. Besides, the coupling of $LiNbO_3$ layer in microfluidic device remains to be developed.

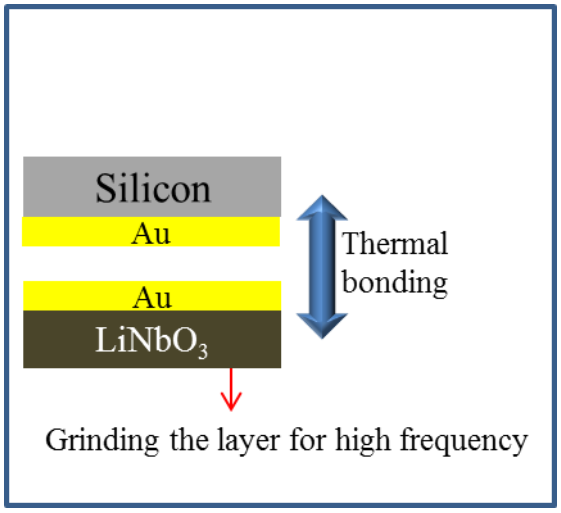

Figure 2.5.3 First development of bulk $LiNbO_3$ (30 MHz) and silicon bonding.

We have begun to work on a new fabrication for single crystal of $LiNbO_3$ bonding to the silicon using gold layer diffusion. As shown in figure 2.5.3, both sides of the crystal and silicon are evaporated by a gold layer, then thermal bonding is applied in 300 ˚C to connect the $LiNbO_3$ crystal and silicon in a certain pressure. After the bonding, the crystal layer is manually grinded to obtain a 30 MHz central frequency. This technique is still under study for higher frequency transducer. In our device, we choose the sputtering technology for ZnO transducer deposition.

2.5.2 Thick ZnO film deposit process

To form a ZnO film with a (001) orientation plane, the Pt was used as the ground electrode since the Pt-Pt distance in the (111) Pt plane was 2.77 Å, which was 16.8% smaller than the in-plane lattice constant (a-axis) of 3.24 Å in the (002) ZnO plane. This distance is low enough to allow an epitaxial influence for the formation of the high crystalline orientation of the ZnO film [24]. Sputtering parameters are presented in table 2.4, among these conditions, the O_2 concentration and sputtering input power will greatly influence the roughness of generated ZnO film and its internal stress.

For 1GHz acoustic characterization (2.4 µm thickness) ZnO transducer, we had already stable steps for the fabrication as shown in figure 2.5.4. In the first step, 10 nm Ti and 100 nm Pt were evaporated on the backside of the wafer as ground electrode using PLASSYS MEB 550S. Then lithography processes were done on the surface with PMGI SF19 (MicroChem Corp, Newton, MA; 7.2 µm) and S1828 (Shipley Corporation, 2 µm). Double-sided alignment lithography was performed to position the transducers patterns to be under the mirror {110} planes using a SUSS MicroTec MA/BA6 system. Next step is to sputter ZnO film directly on the resist prior to the evaporation of 10 nm Ti and 100 nm Pt as the top electrodes. After lift-off process, the ZnO transducers patterns are shaped on the backside of the wafer, which makes it useable for emission and reception of acoustic beam as the acoustic source.

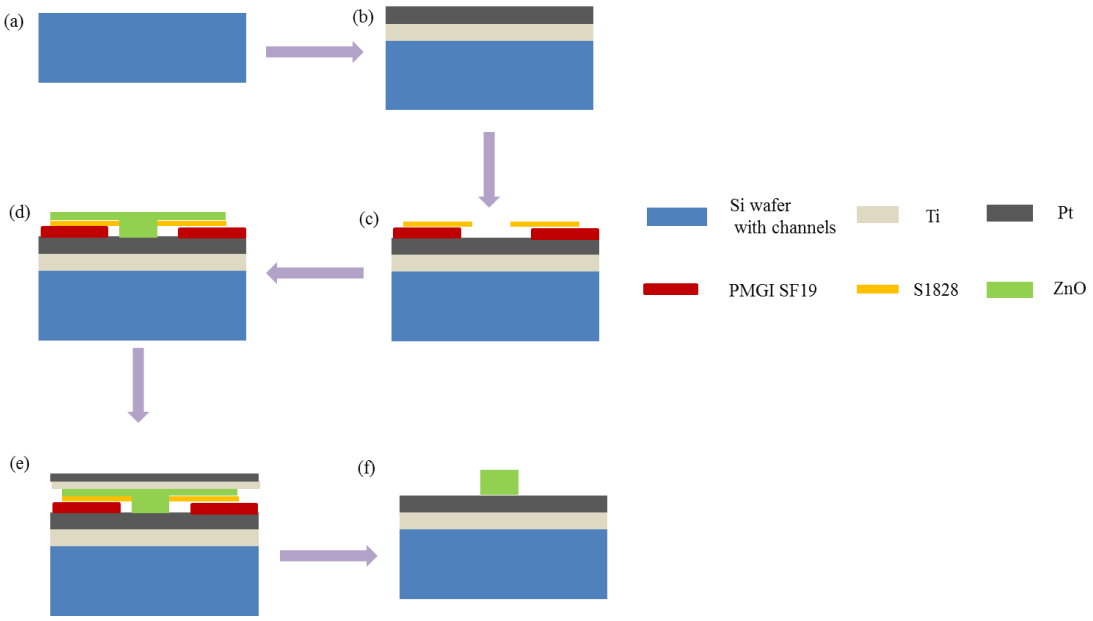

Figure 2.5.4 Procedures for the thin ZnO film fabrication.

Deposition parameters maintained during the deposition of ZnO films by RF magnetron sputtering	
Sputtering target	ZnO (99.9%) 3-inch diameter
Target to substrate distance	70mm
substrate	Silicon and Ti and Pt
O_2 gas flow rate	4.0 sccm
Ar gas flow rate	31.6 sccm
Ultimate pressure	5×10^{-5} mbar
Sputtering pressure	2.1×10^{-2} mbar
Substrate temperature	10˚C
Sputtering power	120W
Sputtering speed	0.9 μm/h

Table 2.4 parameters in our fabrication of ZnO film.

As discussed previously, for lower frequency acoustic sensors and actuators applications, we choose frequency ranges from 500 MHz to 800 MHz, which require ZnO thickness between 3~6 μm (half of the wavelength). When we started this ZnO film deposition using previous method, we would observe a bad adhesion of the ZnO film on Pt surface. As shown in figure 2.5.5, (a) a 1 μm homogeneous adhesion of ZnO film was spread on the substrate with good transparence, the double layers of the resist (PMGI and S1828) can be clearly seen. (b) 5 μm ZnO film patterns distribute and stack heterogeneously in each hole. We can see parts of the ZnO patterns splitting away off the ground electrode, thus various colors are observed under optical microscope corresponding to light diffraction on the cracking films with different thickness. In fact, the peeling phenomenon starts as soon as the chamber of sputtering

machine is open, which creates a temperature difference between two sides of the wafer. The side of the wafer which contacts the substrate of the sputtering machine is kept cooling, while the other side which contacts to air is warmed up to room temperature. This temperature contrast intensifies the peeling of ZnO film on ground electrode.

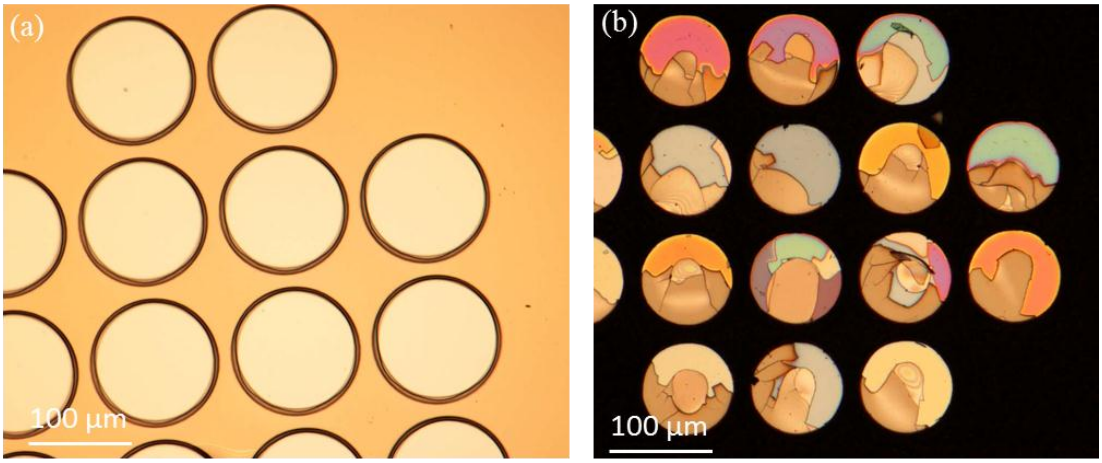

Figure 2.5.5 comparison of a) well deposited 1 µm ZnO film and b) heterogeneous adhesion for 5 µm ZnO film patterns deposition.

As shown in table 2.5, we compare different thermal expansion coefficient between the materials used for transducer fabrication. It is noted that there is an obvious difference between silicon substrate and the electrodes (Ti and Pt). The ZnO material is in between these two ones. For thicker ZnO material deposition, the sputtering time is also extended as well as the internal stress. On the other side, the double resist layers may distort in the heating due to long time sputtering. In our experiments, the ZnO film patterns are unstable when the thickness is above 3 µm.

10^{-6}/K	material
2.6-3.3	Pure silicon (Si)
8.4-8.6	Pure Titanium (Ti)
8.8-9.1	Pure Platinum (Pt)
5-6	ZnO direction perpendicular to c axis
3-4	ZnO direction parallel to c axis

Table 2.5 Linear coefficients of thermal expansion ranges at room temperature to 100 °C

In regard of these problems, we changed the method for thick ZnO film deposition:
1. We replaced Ti and Pt double layers by single Ti layer. In fact, TiO_2 layer is easy formed on the surface of a Ti layer is in the air, and the adhesion between TiO_2 and ZnO is better for these oxides. In addition, the single layer ground reduces the thermal expansion compared to double layers.
2. We sputtered full layer of ZnO film on the whole substrate, then fabricate top electrode patterns. In this way, the contact area between ZnO film and substrate is

enlarged, so that the internal stress is dissipated into the whole wafer, which induced a better adhesion. Moreover, the resist introduction is achieved after the ZnO sputtering process, thus the thermal deformation of the resist is avoided.

3. The sputtering process is divided in discontinuous steps. For each 2.5 hours sputtering, the sample is taken out and an annealing step is applied. Then the sputtering of ZnO starts again until the wanted thickness. Thus strong thermal deformation is avoided.

4. We change the top electrodes from Ti and Pt to Ti and gold layers. Then the top electrodes will be connected to a PCB by gold wire thermal bonding.

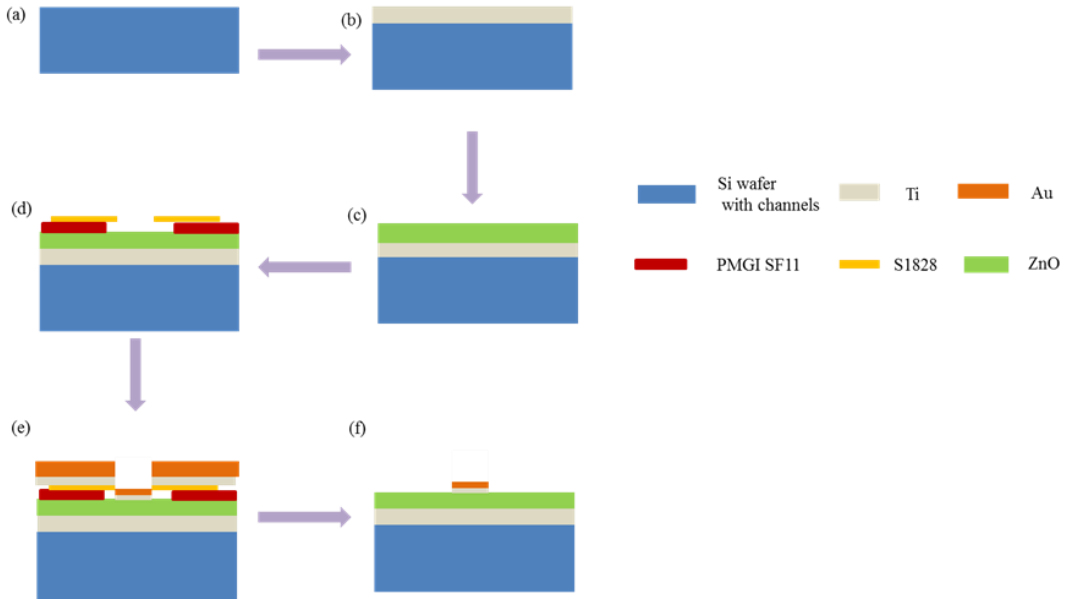

Figure 2.5.6 Improved procedures for the thick ZnO film fabrication.

As shown in figure 2.5.6, a single Ti layer of 100 nm is evaporated on the backside of silicon wafer, then ZnO film is directly sputtered on the full ground Ti layer. Each sputtering step of the film is limited to 2 μm and followed by an annealing step at 150 ˚C. Top electrodes were chosen to be achieved with 30 nm Ti and 300 nm gold, which replaced previous 10 nm Ti and 100 nm Pt. The top electrodes were fabricated on ZnO layer by lift-off and sputtering technology. The position for each pattern of top layer is underneath the 45˚ mirrors to guarantee most of the longitudinal acoustic beam can be reflected and received by the transducers.

On the figure 2.5.7 (a), we present the patterned ZnO with lower thickness using previous methods; (b) we present the patterned top electrodes on 5 μm ZnO full layer. The roughness of the edge planes on each transducer is better than the former one, due to less resist deformation during the sputtering step.

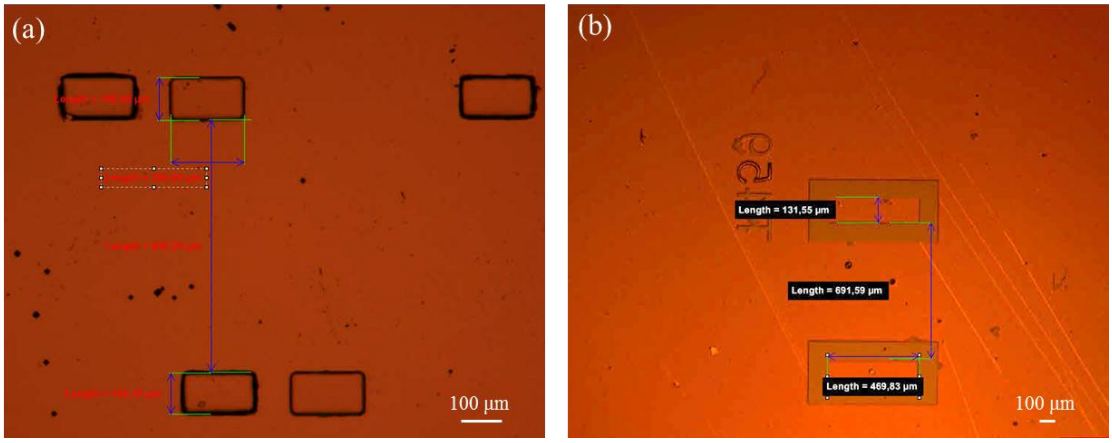

Figure 2.5.7 same size patterns for a) patterned 2.4 µm ZnO film and b) patterned top electrodes on 5 µm ZnO film.

When we tested the sputtering full layer ZnO on ground electrode, it could be clearly seen that the sample substrate bent approximately of 20˚ after 3 hours sputtering. This phenomenon indicated a big internal stress occurring after the ZnO deposition. As the ZnO was deposited on full layer ground compared to be patterned by lithography process, the thermal expansion stress was dispersed on the whole layer.
For fabrication of acoustic actuator working at lower frequency, above 5 µm ZnO layer in thickness was required which can be obtained by multiple steps sputtering. By repeating the sputtering and annealing, thicker ZnO films were obtained with good adhesion.

2.5.3 Ground and top electrodes optimization

For acoustic propagation in multilayered medium, the equivalent acoustic impedance can be calculated by the respective impedance and the thickness of the medium. As shown in figure 2.5.8, for the incident wave propagating from medium 1 into medium 2 and 3, the acoustic impedance Z_1 of medium 1 and Z_2 of medium 2 can be regarded as a whole equivalent impedance

$$Z_{12} = Z_1 \frac{Z_2 \cos(k_1 h_1) + jZ_1 \sin(k_1 h_1)}{Z_1 \cos(k_1 h_1) + jZ_2 \sin(k_1 h_1)}$$

where h_1 is the thickness of medium 1 which was inserted between two media and Z_2 for the transmission medium. k_1 is the wave number of medium 1.
Then the pressure reflection coefficients

$$\mathrm{R(f)} = \frac{Z_{12} - Z_0}{Z_{12} + Z_0}$$

where Z_0 is the mechanical impedance for the incident medium 0,

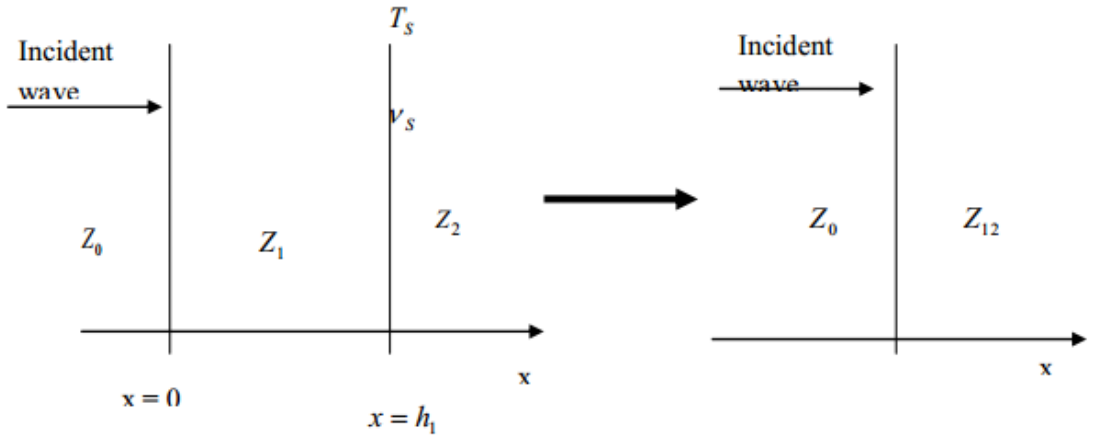

Figure 2.5.8 Acoustic propagation in medium 0, 1 and 2. Z_{12} is the equivalent acoustic impedance of medium 1 and medium 2.

For the thin-film bulk acoustic resonator fabrication to generate longitudinal waves, zinc oxide piezoelectric transducers were used with metal deposition on both the top and bottom for electrodes connection. To determine the electrical impedance of the transducer, all the layers that constitute the acoustic load have to be taken into account. As previously discussed, the Pt and Ti layers were evaporated on the bottom of the silicon wafer respectively to be the ground electrode. Otherwise, 300 nm Au layer was used to replace the 100 nm Pt layer for the top electrode connection, for the purpose of better connection using gold wire bonding with a Printed circuit boards (PCB), so that the electrical matching can be achieved with the transducers.

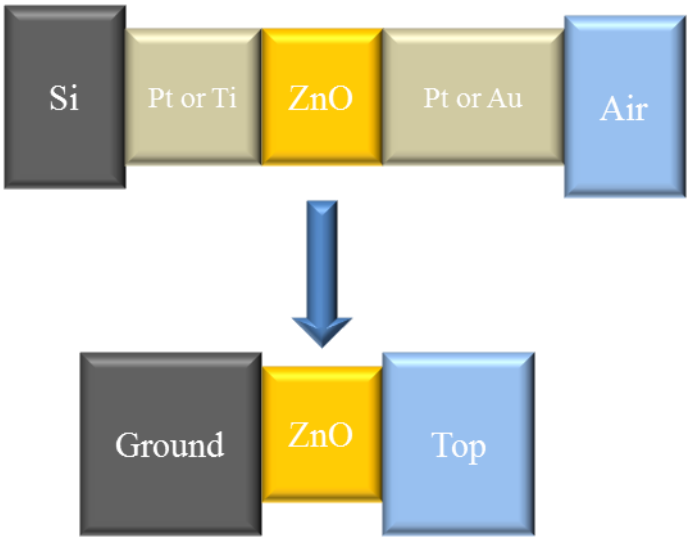

Figure 2.5.9 Sketch map for modeling of simplify the ground and top electrodes.

The simplified modeling of the transducer was shown in figure 2.5.9. The impedance of ground electrode was coupled by silicon and Pt or Ti as described

$$Z_{ground} = Z_{Si/Pt} = Z_{Pt}\frac{Z_{Si}\cos(\theta_{Pt})+jZ_{Pt}\sin(\theta_{Pt})}{Z_{Pt}\cos(\theta_{Pt})+jZ_{Si}\sin(\theta_{Pt})}$$ or

$$Z_{ground} = Z_{Si/Ti} = Z_{Ti}\frac{Z_{Si}\cos(\theta_{Ti})+jZ_{Ti}\sin(\theta_{Ti})}{Z_{Ti}\cos(\theta_{Ti})+jZ_{Si}\sin(\theta_{Ti})}$$

Similarly, the impedance of top electrode was coupled by air and Pt or Au as described

$$Z_{top} = Z_{Air/Pt} = Z_{Pt}\frac{Z_{Air}\cos(\theta_{Pt})+jZ_{Pt}\sin(\theta_{Pt})}{Z_{Pt}\cos(\theta_{Pt})+jZ_{Air}\sin(\theta_{Pt})} \quad \text{or}$$

$$Z_{top} = Z_{Air/Au} = Z_{Au}\frac{Z_{Air}\cos(\theta_{Au}) + jZ_{Au}\sin(\theta_{Au})}{Z_{Au}\cos(\theta_{Au}) + jZ_{Air}\sin(\theta_{Au})}$$

Where Z_{Air} is the acoustic impedance of air, Z_{Pt} is the impedance of platinum, Z_{Au} is the impedance of gold,

$\theta_{Pt} = 2\pi f\frac{d_{Pt}}{v_{Pt}}$ and $\theta_{Au} = 2\pi f\frac{d_{Au}}{v_{Au}}$, d_{Pt} is the thickness of platinum layer and d_{Au} is the thickness of gold layer. v_{Pt} is the velocity of longitudinal wave in the platinum layer and v_{Au} is the velocity of longitudinal wave in the gold layer, f is the central frequency of longitudinal wave.

Thus the electrical impedance of the transducer can be obtained from

$$Z_{elZnO} = \frac{1}{jC_{ZnO}2\pi f} + \frac{K_{ZnO}^2}{C_{ZnO}2\pi f}\frac{Z_{ZnO}}{\theta_{ZnO}}\frac{2Z_{ZnO}(\cos(\theta_{ZnO})-1) + j(Z_{top}+Z_{ground})\sin(\theta_{ZnO})}{Z_{ZnO}(Z_{top}+Z_{ground})\cos(\theta_{ZnO}) + j(Z_{ZnO}^2 + Z_{top}Z_{ground})\sin(\theta_{ZnO})}$$

$$\theta_{ZnO} = k_{ZnO}d_{ZnO} = 2\pi f\frac{d_{ZnO}}{v_{ZnO}}$$

Where Z_{elZnO} is the electrical impedance and Z_{Zno} is the acoustic impedance. K_{ZnO} is the electromechanical coupling coefficient of ZnO, $C_{ZnO} = \frac{\varepsilon_{ZnO}S_{ZnO}}{e_{ZnO}}$ is the static capacitance of ZnO transducer, e_{ZnO} is the thickness of the ZnO film, ε_{ZnO} is the dielectric permitivity and Z_{ZnO} is the characteristic impedance of ZnO, S_{ZnO} is the area of the transducer sureface. For the single crystal of ZnO oriented along the direction <100>, $v_{ZnO} = 6330m/s, \varepsilon_{ZnO} = 7.4\times10^{-11}F/m$, $Z_{Si} = 20MRayls$, $Z_{ZnO} = 36MRayls$, $Z_{Pt} = 70MRayls$, $Z_{Au} = 63MRayls$, $Z_{Ti} = 27MRayls$, $d_{Pt} = 100\,nm, d_{Au} = 300nm$, $k_{ZnO} = 0.27$.

From these equations, it can be deduced that the electrical impedance of the transducer varies with the acoustic impedance of top electrode, ground electrode, the thickness of ZnO film, the thickness of ground electrode and the dimensions of the transducer, as well as the adhesion of transducer and ground electrode (electromechanical coupling). Thus the central frequency value of transducer also varies which corresponds to the maximal value of the real part impedance.

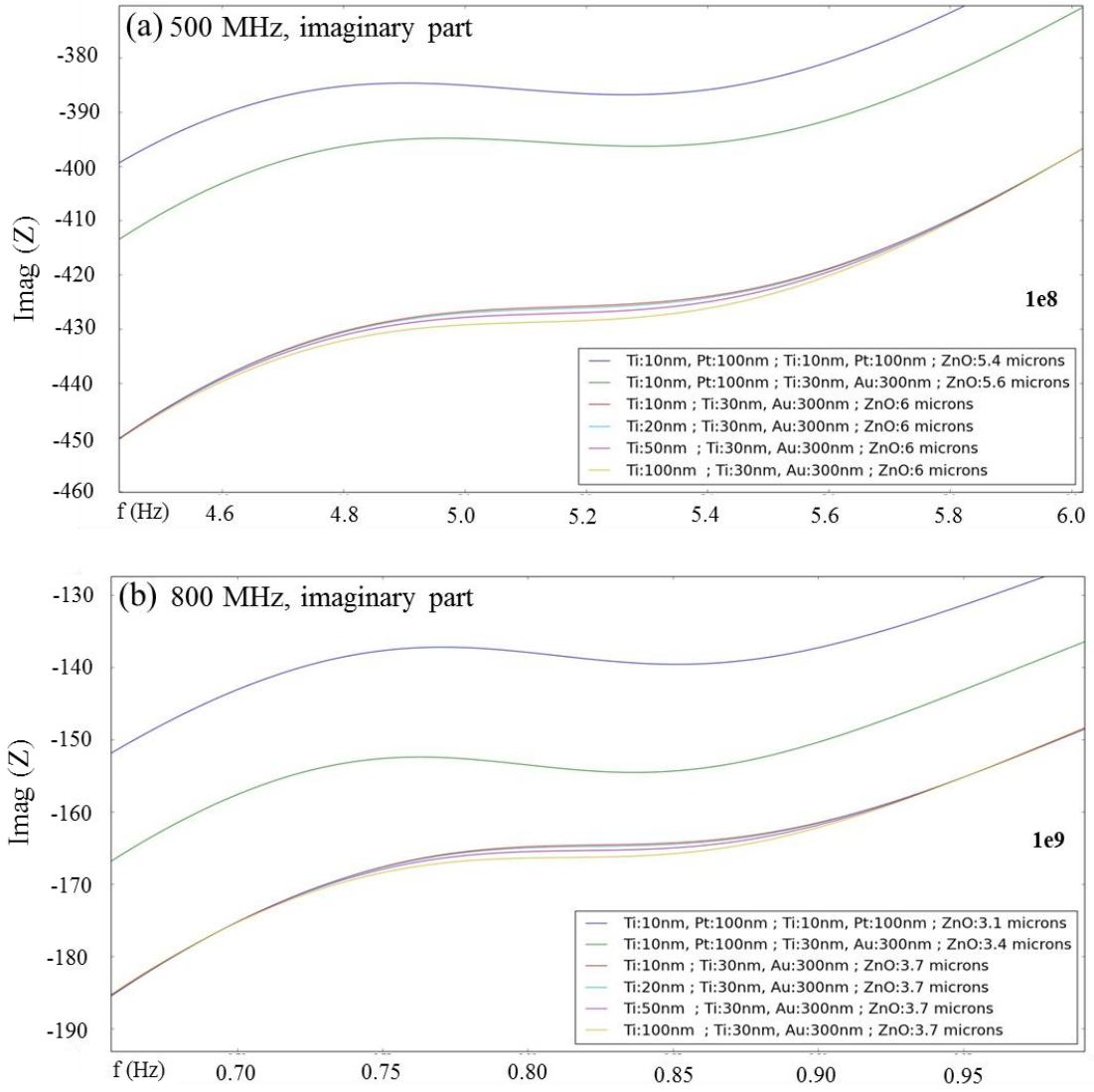

Figure 2.5.10 Impedance influence of ZnO transducer on different ground electrodes and top electrodes. (a) imaginary part impedance at 500 MHz and (b) imaginary part impedance at 800 MHz. In the description of electrodes, the first item is ground electrodes and the second item is top electrodes.

Considering the change of electrodes in our experiments, we simulate the impedance variation of different electrodes (different thickness of Ti ground electrode, Pt and Au layer), as shown in figure 2.5.10. For the imaginary part of impedance, the thickness of the transducer is the leading factor. It is observed that the imaginary part of the impedance decreases as the thickness of ZnO increase. For the same thickness and same top electrode of the ZnO transducer, the increasing of thickness of Ti ground electrode enhance a little modification of the imaginary part of the impedance.

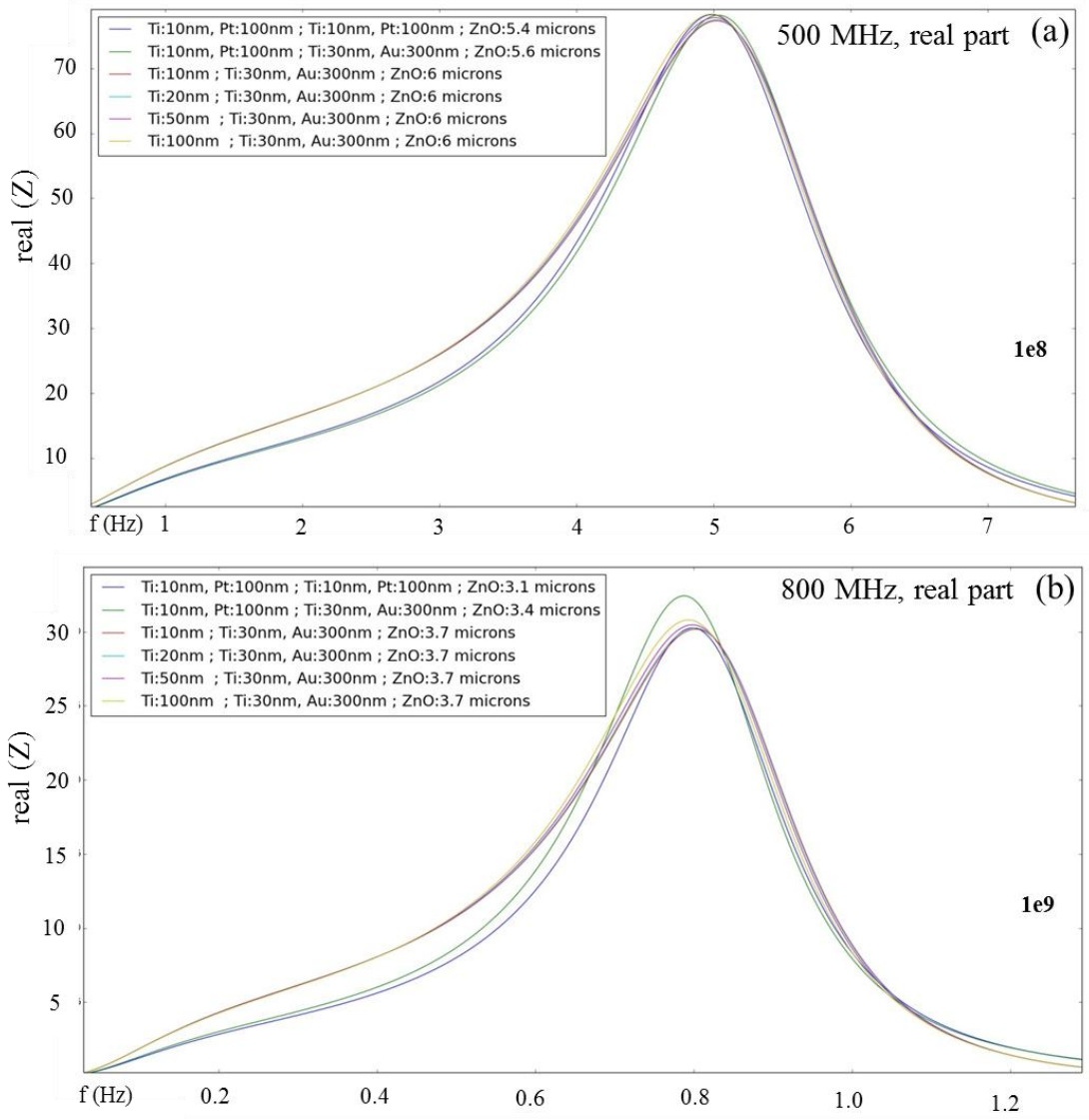

Figure 2.5.11 Impedance influence of ZnO transducer on different ground electrodes and top electrodes. (a) real part impedance at 500 MHz and (b) real part impedance at 800 MHz.. In the description of electrodes, the first item is ground electrodes and the second item is top electrodes.

For the real part impedance, the transducer shows different characterizations in the two frequencies, as shown in figure 2.5.11. At 500 MHz, the real part impedances have small variation even the thickness of film and electrodes are changed. However, at 800 MHz, the impedances have larger variation in different conditions. When ground electrodes are changed from Ti, Pt double layers to single Ti layer, the real impedance has significant difference. When only the thickness of single Ti layer varies from 10 nm to 100 nm, the real impedance is nearly constant. In the comparison, it is noted that the influence of electrodes to real impedance is more sensitive to higher central frequency. At lower frequency of 500 MHz, the matched thickness of transducer is higher, thus the variation of mechanical loading had less

influence. Hence the change of the ground electrodes had a small disturbance of the real part impedance of the transducer.

An interesting phenomenon is discovered in the characterization of thicker ZnO transducer. For example, about 5.7 μm thick ZnO film deposition on single Ti layer, we used 3 steps fabrication including two annealing procedures. As shown in figure 2.5.12, multiple central frequencies were found which were different with the harmonic frequencies. In the SEM we could observe boundary for each break of the deposition in the ZnO growth. It indicated that the break of the sputtering process with annealing made the ZnO nanowires discontinuous. The orientation in each layer varied in a small angle, besides, a bend bundle can be viewed in the contacted boundary. In a global view, the vibration mode of the thick ZnO film was complicated, but each standalone layer played a role in the energy transmission.

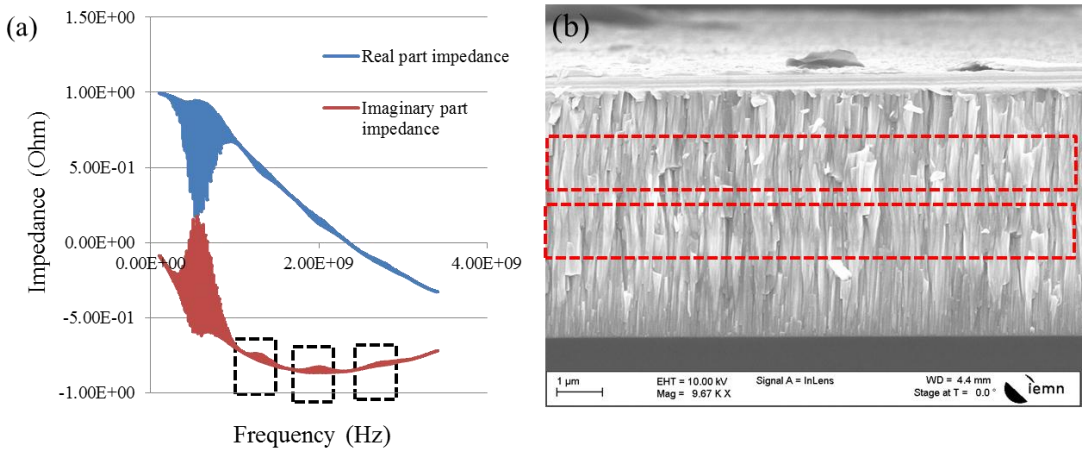

Figure 2.5.12 For the 5.7 μm ZnO film on 100 nm Ti ground electrode, the interpreted impedance by VNA (a) and the cross-section of SEM of ZnO nanowires (b). In the dash box it was observed the multi-frequency and their incentive – the layering of ZnO.

We characterize the electrical response of transducer in the frequency ranges from 100 MHz to 3400 MHz, with a subdivided four frequency range. Thanks to an inverse FFT in the signal processing, we obtain reflected signal S_{22} in a wide frequency band. Here we select signal S_{22} in time domain corresponding to each frequency range.

As shown in figure 2.5.13, the first peak in the figure 2.5.13 (a) presented a large echo with amplitude of 2.63×10^{-2}, which corresponded to a central frequency of 536 MHz. There were four multiple frequencies appearing in the four frequency range. In the 1960 MHz central frequency the echo response showed a peak with amplitude of 1.02×10^{-2}, indicated a strong reflected energy of the transducer and acceptable working performance. The amplitude of the peak was lower down one order of magnitude with 2.43×10^{-3} at 1280 MHz and 1.33×10^{-3} at 2790 MHz. The hierarchical ZnO films may introduce both shear mode and longitudinal mode in each layer, thus the emitted acoustic energy distributed widely in multiple frequency ranges. We could also observe other resonant modes. This new phenomenon indicates that we increase

the useful frequency range and the free switch between lower frequency and higher frequency, for both characterization and actuator applications.

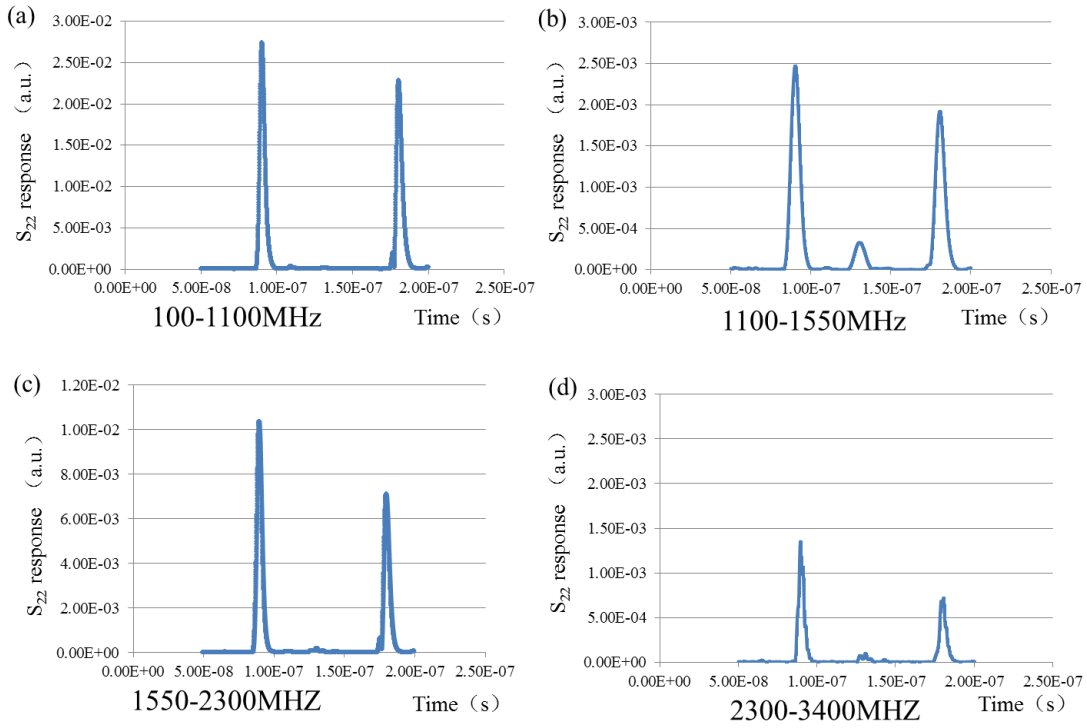

Figure 2.5.13 S_{22} response in the subdivided frequency areas for 5.7 μm ZnO film on single 100 nm Ti ground. (a) 536 MHz for the central frequency and the divided frequency range in 100 to 1100 MHz, (b) 1280 MHz for the central frequency and the divided frequency range in 1100 to 1550 MHz, (c) 1960 MHz central frequency and the divided frequency range in 1550 to 2300 MHz, (d) 2790 MHz for the central frequency and the divided frequency range in 2300 to 3400 MHz. The first peak is the first reflected echo and the second peak corresponds to the second reflected echo from the top of the substrate.

2.6 PDMS bonding for device package

The packaging has to protect the devices from the environment and allows the integration of different functions of the system. For the common used microfluidic device, the package of components is implemented thanks to the bonding between silicon - insulator, silicon - glass, glass – polymer and other materials [25]. The bonding process is composed of several steps. The first step is the treatment on the material surface. Particularly for crystal materials, the surface must be clean, smooth and flat enough. A general method is using the “piranha” solution or organic solvent to remove particles and organic pollutants with ultrasonic cleaning. Argon and oxygen plasma is used sometimes for totally cleaning.

The next step is the proper choice of the type of bonding. For material such as

common glass, method of glass - glass bonding in high temperature is chosen [26]: at fusion bonding temperature about 600 ˚C, the two glass sheets can obtain almost perfect bonding on the surface with high tensile strength. Besides, the anodic bonding between glass and silicon is often used in micro-device fabrication. Anodic bonding process uses Pyrex glasses that have a high concentration of alkali ions. In a sufficiently powerful electrostatic field, the Na^+ ions can drift to the cathode and generated a strong electrostatic force between the contacted substrates, thus the glass and the other substrate is bonded tightly [27].

Polydimethylsiloxane (PDMS) is a kind of macromolecule organic silicon compounds. Compared to other materials such as silicon and glass, it shows superior features such as: elastic, transparent, good contact with most substrates, favorable biological compatibility, gas permeability, insulation, thermal stability and so on. It is also suitable for massive template casting and stereo copy for micro-structure. At present, many droplet microfluidic chips are made in PDMS and glass [28]. The microchannels can be integrated in PDMS material which makes it possible important production and low cost operation.

PDMS before use is divided into an organic precursor A and a crosslinking agent B which can be separately stored and then mixed in a certain proportion when allocated, as shown in figure 2.6. After homogeneous mixing of the two components, it starts to solidify very slowly. The bubbles inside the PDMS can be removed with vacuum extraction prior to baking at 80 ˚C for 6 hours for full curing. After the complete solidification holes are drilled manually by hollow pipe for the formation of inlets and outlets of the microchannels.

PDMS is composed of repetitive siloxy groups. With a plasma treatment or ultraviolet light, the silicon alkoxide groups may be generated to replace the original methyl groups. Then the surface of PDMS shows a strong hydrophilic behavior which is in favor of the bonding and reversible sealing with silicon oxide [29].

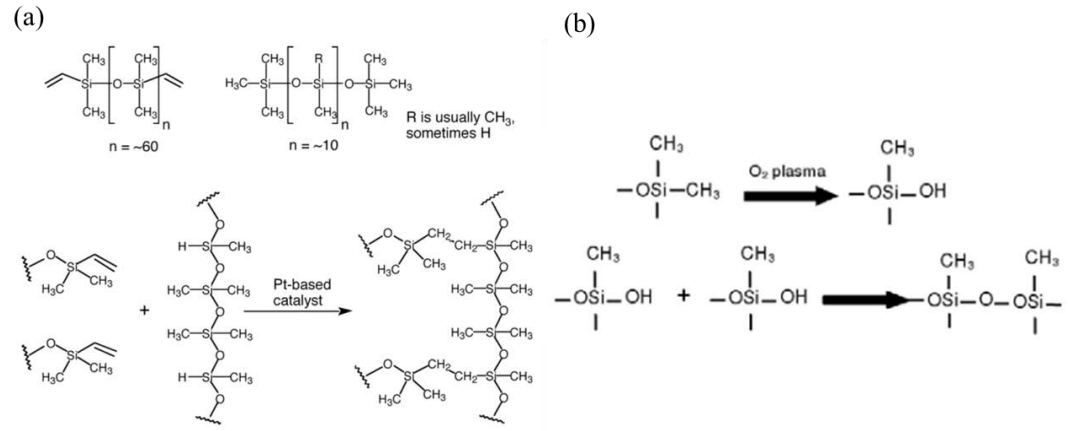

Figure 2.6 (a) Cross-linking of Polydimethylsiloxane, (b) plasma treatment with PDMS [29].

The silanization process of PDMS was done by PICO standard plasma system (electronic diener comp) at 150mT of O_2 pressure and 100 W for 30 seconds. The silicon sample is activated with PDMS together. After plasma treatment we contact

the two upper surfaces of the sample and PDMS for the tightly bonding. The time for bonding process should be less than 10 minutes after plasma so as to avoid depolarization.

2.7 Summary and Discussion

For the objective to extend frequency range for on-chip acoustic microscopy integration, we explored the optimization conditions for the acoustic wave guiding, and the chip fabrication were optimized as shown in figure 2.7. The optimization is concluded as follows:

(1) Deep 45˚ mirrors were achieved with smooth surface. The maximum depth of 45˚ planes we obtained is 210 μm so that most of the diffracted acoustic beam can be reflected. In the wet etching, the quality of SiO_2 mask, temperature and reagent concentration is optimized.

(2) Study of using coating layer on reflection interface to avoid mode conversion. For the designed gold, copper and silicon oxide layer as the acoustic matching layer, the relevant thickness matched for working frequency of transducer is simulated.

(3) Gold layers for acoustic matching were uniformly deposited on 45˚ mirrors and vertical mirrors. On the other hand, we avoided the gold deposition within the microchannel so as to reduce the acoustic losses from silicon to liquid.

(4) Thicker ZnO films (6 μm) were successfully deposited on the backside of the wafer. In the deposition process, we use ZnO full layer with top electrodes patterns (Ti and Au) to replace ZnO patterns, and we use single Ti layer to replace double layers as the ground electrode.

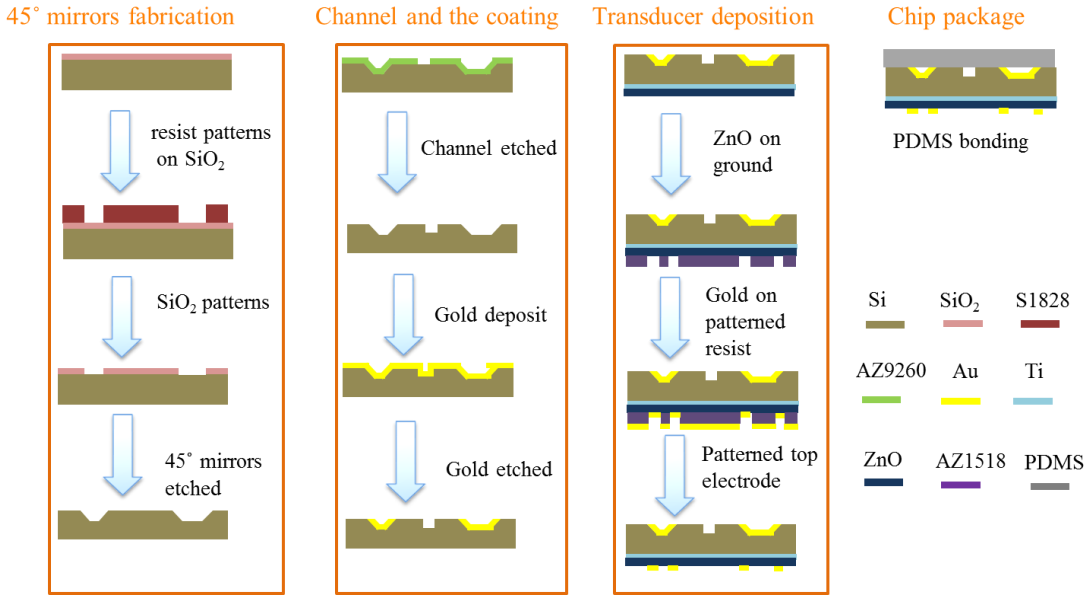

Figure 2.7 Procedures of the chip fabrication.

Appendix: main technology in our fabrication

MEMS are widely used in semiconductor device fabrication technologies in three classifications: bulk micromachining, surface micromachining and high-aspect-ratio micromachining (HARM), which includes technology such as LIGA (a German acronym from Lithographie, Galvanoformung, Abformung translated as lithography, electroforming and moulding). These techniques include molding and plating, wet etching (KOH, TMAH) and dry etching (RIE and DRIE), electro discharge machining (EDM), and other methods for manufacturing small components. The MEMs technologies are extensively used in our acoustic chip fabrication. Here we introduce primary aspects of it in micro scale:

- Photolithography

Photolithography is a typical technique in MEMS field which is used to transfer a designed pattern into a photosensitive material on a substrate, by selective patterns exposure to a radiation source such as light or electron beam [30]. The photosensitive material is an organic polymer that can have its chemical properties changed after absorbing enough light energy. Photoresists are classified in positive resists and negative resists. The positive resist is a type of resist which becomes soluble to the photoresist developer after exposing to UV light and the parts which is unexposed remains insoluble to the photoresist developer. The negative resist has inverse property that the parts exposed to UV light suffer light-cure reactions and become insoluble to the photoresist developer. The photo-mask for selective blocking light pass is usually consisted of a transparent glass plate coated with a chromium pattern.

For a whole step of lithography, the photoresist is coated uniformly on the substrate by the spin-coating machine, with a certain rotate speed which determined the thickness of the resist; then the sample is placed in a hotplate having a suitable controlled temperature for several minutes. This process is called “pre-bake” for the purpose of the solidification of the resist. Short pre-bake time may lead the resist to split away off substrate, but too long pre-bake time would increase the development time and the residue resist on the substrate.

After pre-baking, the optical mask is aligned on the top of the resist, prior to exposure to the high energy UV light. In the exposure procedure, the chemical reaction happened in the portion of resist which absorbed energy, which will make the resist be soluble (positive resist) or insoluble (negative resist). For micro scale pattern fabrication, photoresists are commonly used at wavelengths in the ultraviolet spectrum (<400 nm). In the other way, electron beams exposure will be introduce for nano scale patterns process due to its short wavelength and high resolution. Taking into account the optical diffraction and diffuse reflection on the boundary, usually the boundary contour has narrow top and wide bottom for positive resist, whereas for negative photoresist with wide top and narrow bottom, as shown in figure A1.

After exposure, the negative resist is currently required to bake again (post bake). the post bake could prompt the photo-chemical reaction to be completed thoroughly and further remove hydrosolvent in the resist. Then the photo-sensitive area in the positive resist will dissolve into the liquid in the development, and then the patterns on the mask are transferred to the material exposed. The development time for negative resist should be precisely controlled to avoid the inflation because the resist and the developing liquid are both organic polar.

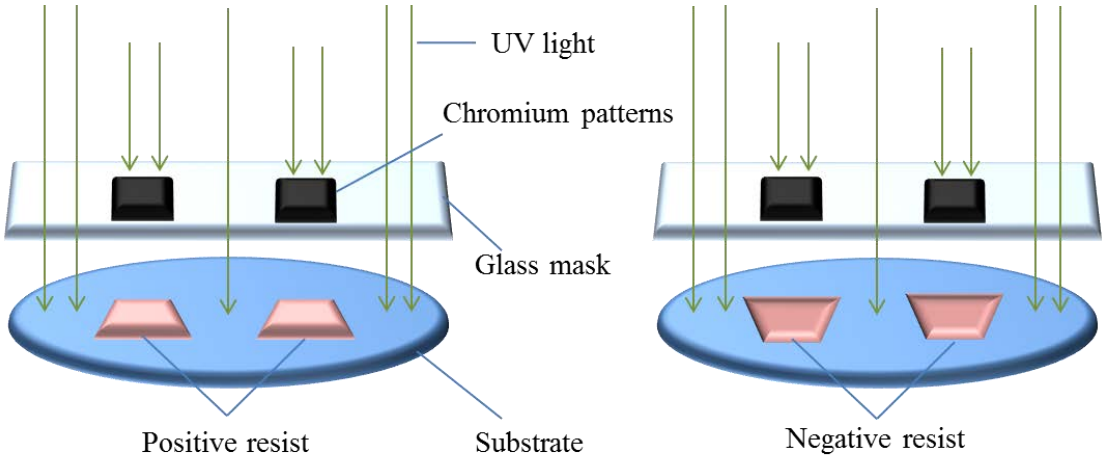

Figure A1 Different edge contour for positive and negative resist after development.

- .Wet etch

Wet etching is a process of material removal in chemical etchants, through the reaction in certain conditions in a liquid (figure A2). Commonly the patterns for etching are defined by masks on the wafer in the beginning. Then materials that are not protected by the masks are etched away by liquid chemicals, which can be isotropic or anisotropic.

Isotropic etchants etch the material in all directions. The etchants consequently remove material under the etch masks at the same rate as they etch through the material, but are limited by the geometry of the structure to be etched. On the other side, anisotropic etchants etch prominently fast in a preferred direction. For crystalline material etching, the crystal face can determine the rates for etching in liquid. Silicon etch is typically influenced by this effect which can allow very high anisotropy. For instance, the <111> crystal plane sidewalls can emerge when etching patterns by potassium hydroxide (KOH) in a <100> direction silicon wafer. Then resulting in a pattern shaped with pyramid sidewalls instead of rounded sidewalls.

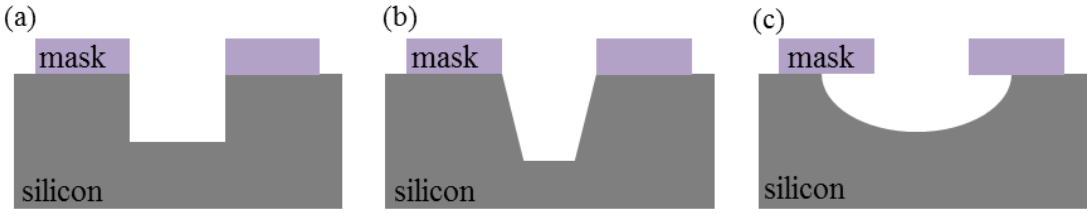

Figure A2 (a) Completely anisotropic (b) Partially anisotropic and (c) Isotropic etching of silicon

- Reactive Ion Etching

Reactive Ion Etching (RIE) is a plasma-based method of etching through suitably reactive gases to remove material deposited on substrates. In this process, sample is placed inside a reactor in which gases are introduced. Radio frequency (RF) power is used to break the gas mixture into ions, which are subsequently accelerated towards to the sample and react at the surface prior to another gaseous material is formed. Deep Reactive Ion Etching (DRIE) is a special subclass of RIE with higher-aspect-ratio etching that involves an alternating process of high-density plasma and protective polymer deposition to achieve high aspect ratios. The primary technology is based on the so-called "Bosch process" as shown in figure A3. Two different gas compositions are alternatively introduced in the reactor. The first gas composition creates a polymer on the surface of the substrate, and then the second gas composition come to etch the substrate. The polymer is immediately removed in the physically sputtering while only dissolves in a slow speed in the chemical etching. As a result, the sidewalls of the etched channels are protected and only the horizontal surfaces are etched, and then a high aspect ratio of etching is achieved. An inductively coupled plasma (ICP) is added as the plasma source to enhance the etching efficiency.

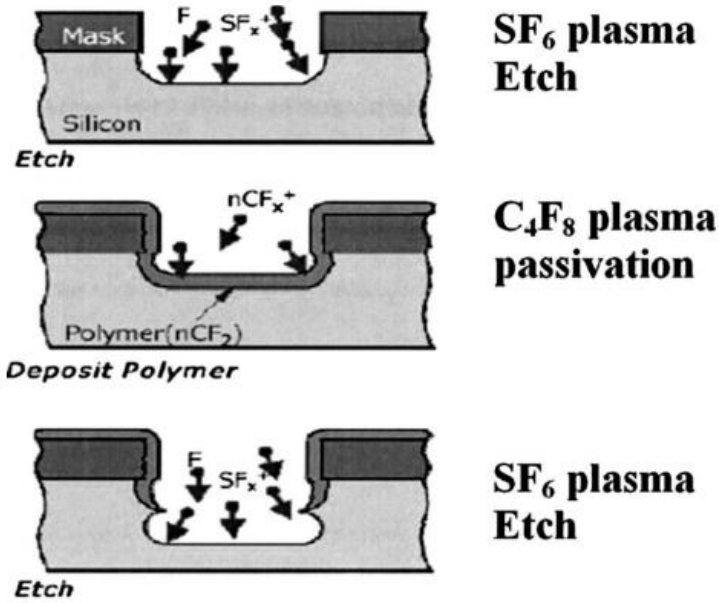

Figure A3 . alternative DRIE processes of etching and passivation [31].

- Lift-off

The lift-off method is a process sequence used to form microstructures in a thin film thanks to a sacrificial material (e.g. Photoresist). In the first step, an inverse pattern of thin films are created on the substrates (typically is the photoresist implemented on the wafer). The target layer of material is then deposited on the sacrificial layer and overlapped the whole surface of the etched regions. When the sacrificial layer is removed by enchants, along with the areas in which the target material is located on, then the remaining structures form the desired microstructure which directly contact with the substrate. The resolution of the generated structures ranges from tens of nanometers to centimeters. Lift-off process is applied in cases where a direct etching of structural material is hard to reach and widely used in the manufacture of integrated circuits (ICs) as well as microsystems.

- Sputtering

Sputtering is a technique used to deposit thin films of a material onto a substrate, or film etching and analysis. It begins when a substrate is placed in a vacuum chamber containing an inert gas, and then a negative charge is applied to a target source which will cause the plasma generated [32]. After gaseous plasma was created, the ions from this plasma are accelerated into the target. In this step, the source material is eroded by the arriving ions *via* energy transfer. Subsequently the source is transformed into individual atoms. These individual atoms are travelling in a straight line to the substrate, which will be coated by a thin film of the source material. If the applied current is direct current, it is D.C sputtering and suit for metal deposition; when the applied current is radio frequency current, it is RF sputtering and suit for insulating or poor conductivity target.

References

[1] KENNETH E. BEAN, “Anisotropic Etching of Silicon”, IEEE transactions on electron devices, vol. ED-25, no. 10, October 1978.

[2] H. Seidel, L. Csepregi, A. Heuberger and H. Baumgärtel, “Anisotropic Etching of Crystalline Silicon in Alkaline Solutions I. Orientation Dependence and Behavior of Passivation Layers”, J. Electrochem. Soc. 1990 volume 137, issue 11, 3612-3626.

[3] D. Resnik, D. Vrtacnik, U. Aljancic, M. Mozek and S. Amon, “The role of Triton surfactant in anisotropic etching of{110}reflective planes on (1 0 0) silicon”, J. Micromech. Microeng. 15(2005) 1174–1183.

[4] P. Sullivan, B. W. Offord and M. E. Aklufi, “Tetra-Methyl Ammonium Hydroxide (TMAH) Preferential Etching for Infrared Pixel Arrays”, TECHNICAL

DOCUMENT 3097 January 2000.
[5] J. T. L. Thong, W. K. Choi and C. W. Chong, “TMAH etching of silicon and the interaction of etching parameters”. Sensors and Actuators A: Physical 63: 243–249, 1997.
[6] K. P. Rola, K. Ptasinski, A. Zakrzewski and I. Zubel, “Silicon 45˚ micromirrors fabricated by etching in alkaline solutions with organic additives”, Microsyst Technol, DOI 10.1007/s00542-013-1859-z
[7] K. B. Sundaram, A. Vijayakumar and G. Subramanian, “Smooth etching of silicon using TMAH and isopropyl alcohol for MEMS applications”, Microelectronic Engineering 77 (2005) 230–241.
[8] I. Zubel and M. Kramkowska, “The effect of isopropyl alcohol on etching rate and roughness of (100) Si surface etched in KOH and TMAH solutions”, Sensors and Actuators A 93 (2001) 138-147.
[9] J. T. L. Thong, P. Luo, W. K. Choi and S. C. Tan, “Evolution of hillocks during silicon etching in TMAH”, J. Micromech. Microeng. 11(2001) 61–69.
[10] S. Wang, J. Carlier, P. Campistron, W. Xu, D. C. Debavelaere, B. Nongaillard and A. NDieguene, “A 45° silicon mirror for acoustic propagation parallel to the plane of the substrate”, Journal of Physics: Conference Series 269(2011) 012009
[11] Q. Qi and G. J. Brereton, “Mechanisms of Removal of Micron-Sized Particles by High-Frequency Ultrasonic Waves”, IEEE TRANSACTIONS ON ULTRASONICS, FERROELECTRICS, AND FREQUENCY CONTROL, VOL. 42, NO. 4, JULY 1995
[12] Brown and C. Duane, “Decentering distortion of lenses”, Photogrammetric Engineering. 32 (3): 444–462, May 1966.
[13] J. Gao, J. Carlier, S.X. Wang, P. Campistron, D. Callens, S. Guo, X.Z. Zhao and B. Nongaillard, “Lab-on-a-chip for high frequency acoustic characterization”, Sens. Actuator B-Chem., 177 (2013) 753-760
[14] Y. J. Hung, S. L. Lee and Larry A. Coldren, “Deep and tapered silicon photonic crystals for achieving anti-reflection and enhanced absorption”, Optics Express Vol. 18, Issue 7, pp. 6841-6852 (2010)
[15] S. Swartz, T. Shrout and T. Takenaka, “Electronic Ceramics R&D in the U.S. Japan,” Am. Ceram. Soc. Bull., vol. 76, pp. 59-65, 1997.
[16] T. Wu and W. Wang, “An experimental study on the ZnO/Sapphire layered surface acoustic wave device”, Journal of Applied Physics, vol. 96, pp. 5249-5253, 2004.
[17] J. A. Ketterling, O. Aristizábal, D. H. Turnbull and F. L. Lizzi, “Design and fabrication of a 40-MHz annular array transducer”, IEEE Trans Ultrason Ferroelect Freq Contr. 2005; 52:672
[18].Y. Osugi, T. Yoshino, K. Suzuki and T. Hirai, “Single crystal FBAR with LiNbO3 and LiTaO3 piezoelectric substance layers”, Microwave Symposium, 2007. IEEE/MTT-S International, page 873-876.
[19] W. Hu, Z. Liu, J. Sun, S. Zhu, Q. Xu, D. Feng and Z. Ji, “Optical properties of pulsed laser deposited ZnO thin films,” Journal of Applied Physics and Chemistry of Solids, vol. 58, pp. 853-857, 1997.

[20] N. D. Patel, S. X Fulford and P. S. Nicholson, “HIGH FREQUENCY-HIGH TEMPERATURE ULTRASONIC TRANSDUCERS”, Review of Progress in Quantitative Nondestructive Evaluation, Vol. 9, 1990.
[21] C. Klingshirm, A. Waag, A. Hoffmann and J. Geurts, “Zinc Oxide: from funamental properties towards novel applications,” Springer Series in Materials Science, vol. 120, 2010.
[22] J. Molarius, J. Kaitila, T. Pensala and M. Ylimlammi. J Mater Sci. 2003; 14:431-438.
[23] Mathias Link, “Study and realization of shear wave mode solidly mounted lm bulk acoustic resonators (FBAR) made of c-axis inclined zinc oxide (ZnO) thin films: application as gravimetric sensors in liquid environments”, PhD dissertation, Université Henri Poincaré- Nancy I, 2006.
[24] E. Benes, M. Gröschl, F. Seifert and A. Pohl, Proc. IEEE Int. Freq. Contr. Symp, 5 (1997).
[25] O. Geschke, H. Klank and P. Telleman “Microsystem Engineering of Lab-ona-chip Devices” 2004 Wiley-VCH ISBN: 3-527-30733-8
[26] H. Klank, J. P. Kutter and O. Geschke “CO2-laser micromachining and back-end processing for rapid production of PMMA-based microfluidic systems” Lab on a Chip, 2002, 1.
[27] G. Wallis and D. I. Pomerantz. "Field Assisted Glass-Metal Sealing". Journal of Applied Physics 40 (10). 1969, pp. 3946–3949.
[28] J. C. McDonald, D. C. Duffy, J. R. Anderson, D. T. Chiu, H. Wu, O. J. A. Schueller and G. M. Whitesides, “Fabrication of microfluidic systems in poly(dimethylsiloxane)”, Electrophoresis, 2000, 21 (1): 27–40.
[29] S. R. Quake and A. Scherer, “From micro- to nanofabrication with soft materials”, Science 2000 Nov 24;290(5496):1536-1540.
[30] Jaeger and C. Richard (2002). “Lithography”, Introduction to Microelectronic Fabrication (2nd ed.). Upper Saddle River: Prentice Hall. ISBN 0-201-44494-1
[31] Y. Q. Fu, A. Colli, A. Fasoli, J. K. Luo, A. J. Flewitt, A. C. Ferrari and W. L. Milne, “Deep reactive ion etching as a tool for nanostructure fabrication”, J. Vac. Sci. Technol. B 27(3), May/Jun 2009
[32] T. Schenkel, M. Briere, H. Schmidt-Böcking, K. Bethge, D. Schneider, et al. “Electronic Sputtering of Thin Conductors by Neutralization of Slow Highly Charged Ions”. Physical Review Letters, 1997, 78 (12): 2481.

Chapter 3

Lab-on-chip high frequency acoustic detection and manipulation

3.1 Acoustic wave characterization

3.1.1 Signal processing and method

Thanks to the electromechanical conversion using ZnO piezoelectric transducer, we can analyze the received acoustic signals by vector network analysis (VNA). Electronic RF components can be generally characterized by a two ports network through S parameters (scattering parameters) and Z or Y parameters (impedance or admittance parameters) can be deduced. The Z parameter measurements are mainly applied in low frequency circuit, for which the size of the device is usually less than one-tenth of the RF signal wavelength. However, in high frequency circuits above 1GHz, the size of electrical components becomes comparable to the RF signal wavelength, and then the distributed parameter model has to be applied using S parameters characterization.

After a calibration first step, Vector network analyzer can provide complex S(f) parameters over a predetermined frequency range. A frequency tunable signal source is applied in order to measure the S(f) response. An Inversed Fast Fourier Transformation (FFT) or chirp Z transform applied on the S(f) signal makes it possible to provide the time domain reflected or transmitted response.

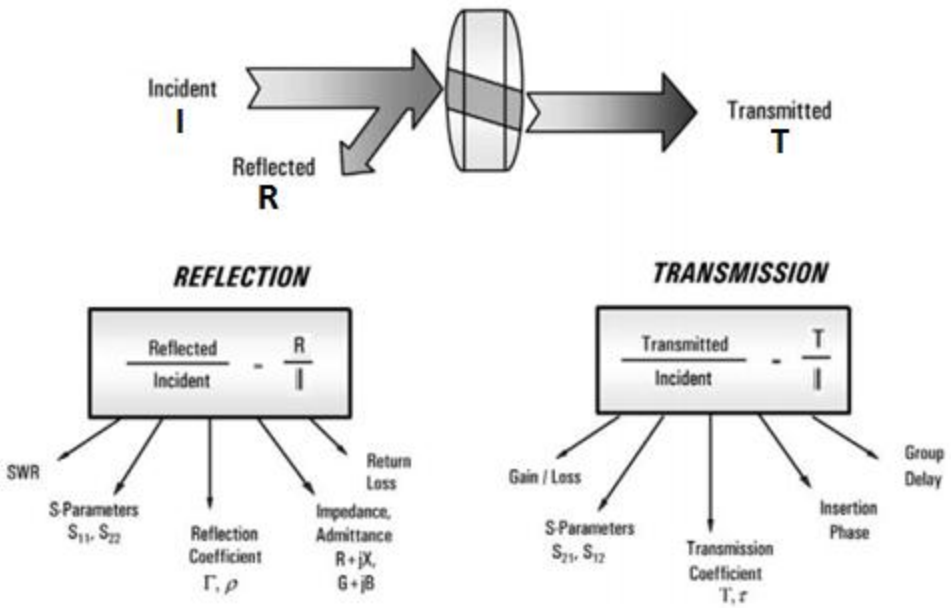

Figure 3.1.1 Principle of measurement of a network analyser [2].

The basic function of a network analyser includes measurements of traveling wave, reflected wave and losses along a transmission line, as shown in figure 3.1.1. “I” is used for the incident wave related voltage or power; the amplitude or power of the

reflected wave is measured through channel "R" and transmission wave is measured through channel "T". Using amplitude and phase information, the characteristics of reflection and transmission for a Device Under Test (DUT) can be presented in quantitative description [1]. The reflection coefficient Γ is calculated from the ratio of the reflected signal voltage to the incident one: $\Gamma = \frac{V_{reflected}}{V_{incident}} = \frac{Z_L - Z_0}{Z_0 + Z_0}$, where Z_0 is the characteristic impedance of a transmission line (50 ohms), Z_L is the impedance of the load. When Z_L is equal to Z_0, the maximum energy is transferred to the load and $V_{reflected}$ is zero; when Z_L is a short or open circuit, all the energy is reflected and $V_{reflected}$ is equal to $V_{incident}$.

The main interest of the VNA is the extreme sensitivity with a low noise level of around 110 dB and S parameters are used in the impedance matching conditions with a vector network analyzer. Relate to familiar measurements such as gain, loss, reflection coefficient, the measured S parameters can be cascaded to predict system performances of multiple devices [2].

The four S_{ij} parameters are defined by the incident wave and reflected wave at the input port and output port. As shown in figure 3.1.2, S_{11} is the input port voltage reflection coefficient, S_{12} is a reverse voltage gain, S_{21} is the forward voltage gain and S_{22} is the output port voltage reflection coefficient. The transfer parameters S_{12} and S_{21} are a measure of the complex insertion gain, and are determined by the magnitude and phase of the incident, reflected and transmitted voltage signals when the output is terminated in a matched Z_0. In our experimental setup, we used this parameter in order to determine the losses of the system and the losses through the fluidic channel. Otherwise, S_{11} and S_{22} are a measure of the input and output mismatch losses and of the absorbed signal. S_{11} is equivalent to the input complex reflection coefficient of the DUT, and S_{21} is the forward complex transmission coefficient.

For acoustic excitation integrated in the microsystem, especially in our microfluidic devices with liquid introduction, the incident acoustic wave undergoes various losses such as diffraction before being attenuated by the liquid in the channel. The losses include diffraction, absorption of acoustic energy by propagating media (mainly liquid in the channel) and reflection losses. The propagation loss is a key parameter for acoustic integrated systems which can determine the useful received signal to the acoustic noise ratio.

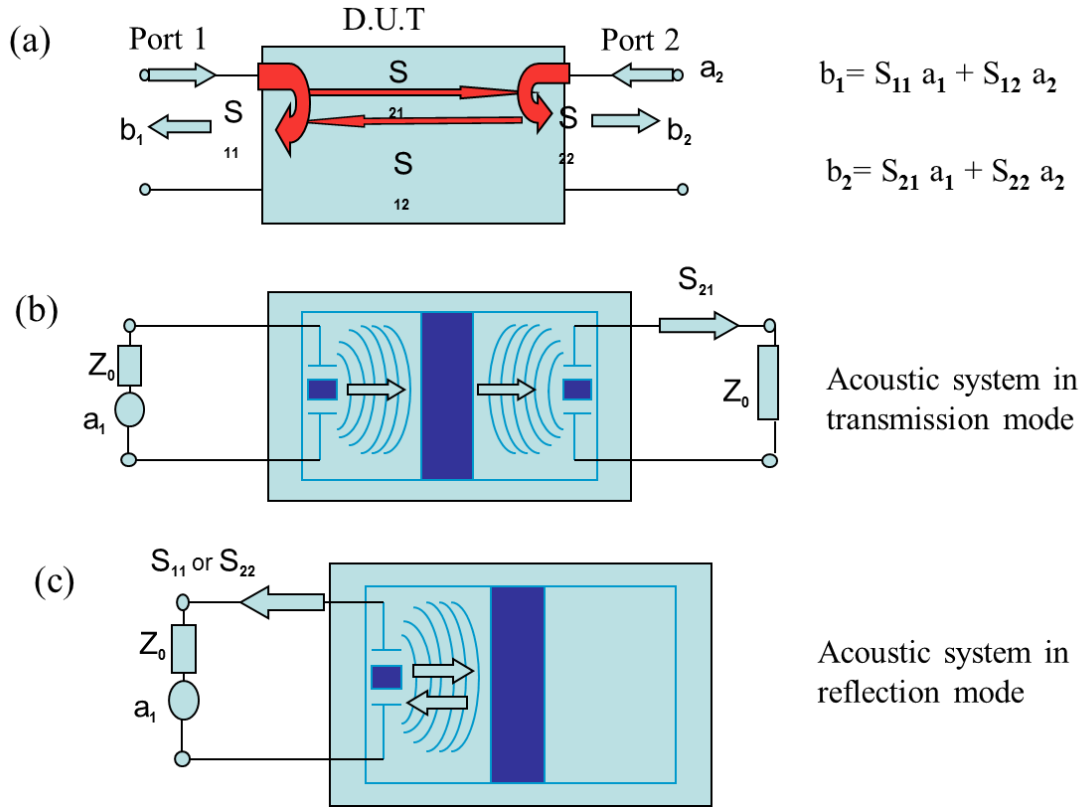

Figure 3.1.2 Relationship between the reflected, incident amplitude waves and the corresponding S-parameter matrix. (a) S-parameter matrix for the 2-port network, (b) acoustic system in transmission, (c) acoustic system in reflection mode.

A Vector Network Analyzer was used to measure complex response of the device in the frequency domain and provides the S(f) parameters. Thanks to a real time software these measurements can be converted into the time domain information through an inverse Fourier transformation or chirp Z transform. Wider is the frequency range, better will be the time resolution. In the case of acoustic measurements, the S parameters are composed by an electrical term S_{ij}^{elect} and an acoustical contribution S_{ij}^{acoust} [3]:

$$S_{ij}(f) = S_{ij}^{elect} + KS_{ij}^{acoust}$$

where K includes electromechanical conversion effects at the interfaces.

The electrical term comes from the reflection of the electrical signal on the transducer due to electrical mismatching in case of reflection measurements whereas it represents radiated electrical energy in transmission mode. In practical application, it is not easy to keep impedance matching for the transducer and the coaxial line, thus the electrical term of S parameters always exists. The second term represents the acoustic wave generated by the emitter, then propagating in the device and converted by the receiver into an electrical signal. The electrical term of S parameter enhances difficulties for the useful signals analysis in the frequency domain. As to eliminate this unwanted effect, we have to isolate this term in the results. As the S parameters can be interpreted as the impulse responses of the system by the inverse Fourier transform, it is possible to separate the two terms in time domain, taking advantage of the

propagation velocity difference between the reflected RF signal and acoustic wave.
After applying an erasing window We (t) which set the acoustical term to zero, the inverse Fourier transform of S parameter and We (t) in time domain will only keep the electric reflected signal so as to determine the electrical impedance of the transducer from the S_{11}^{elec} parameter:

$$S_{11}^{elec}(f) = \mathfrak{F}\{\mathfrak{F}^{-1}[S_{11}(f)] \cdot We(t)\} = S_{11}(f) \otimes \mathfrak{F}[We(t)]$$

Hence the acoustical term can be obtained by subtracting the electrical term from the measurement:

$$S_{11}^{acoust}(f) = S_{11}(f) - S_{11}^{elec}(f)$$

The first acoustic echo can be obtained using the same method. An erasing window Wa(t) can be used which sets to zero the whole signal except for the first acoustic echo:

$$S_{11}^{acoust-1}(f) = \mathfrak{F}\{\mathfrak{F}^{-1}[S_{11}^{acoust}(f)] \cdot W_a(t)\} = S_{11}^{acoust}(f) \otimes \mathfrak{F}[W_a(t)]$$

3.1.2 Experimental set up

In our acoustic detection system shown in figure 3.1.4, the liquid is pumped and injected into the microfluidic device by a pressure-driven flow controller. Then the signal is measured with a Signal/Ground (S/G) Suss Microtech prober which achieves the electrical contact with the transducer located on the backside of the wafer. Subsequently Rhode&Scharwtz vector network analyzer is used to measure the S parameters in time domain after signal processing.

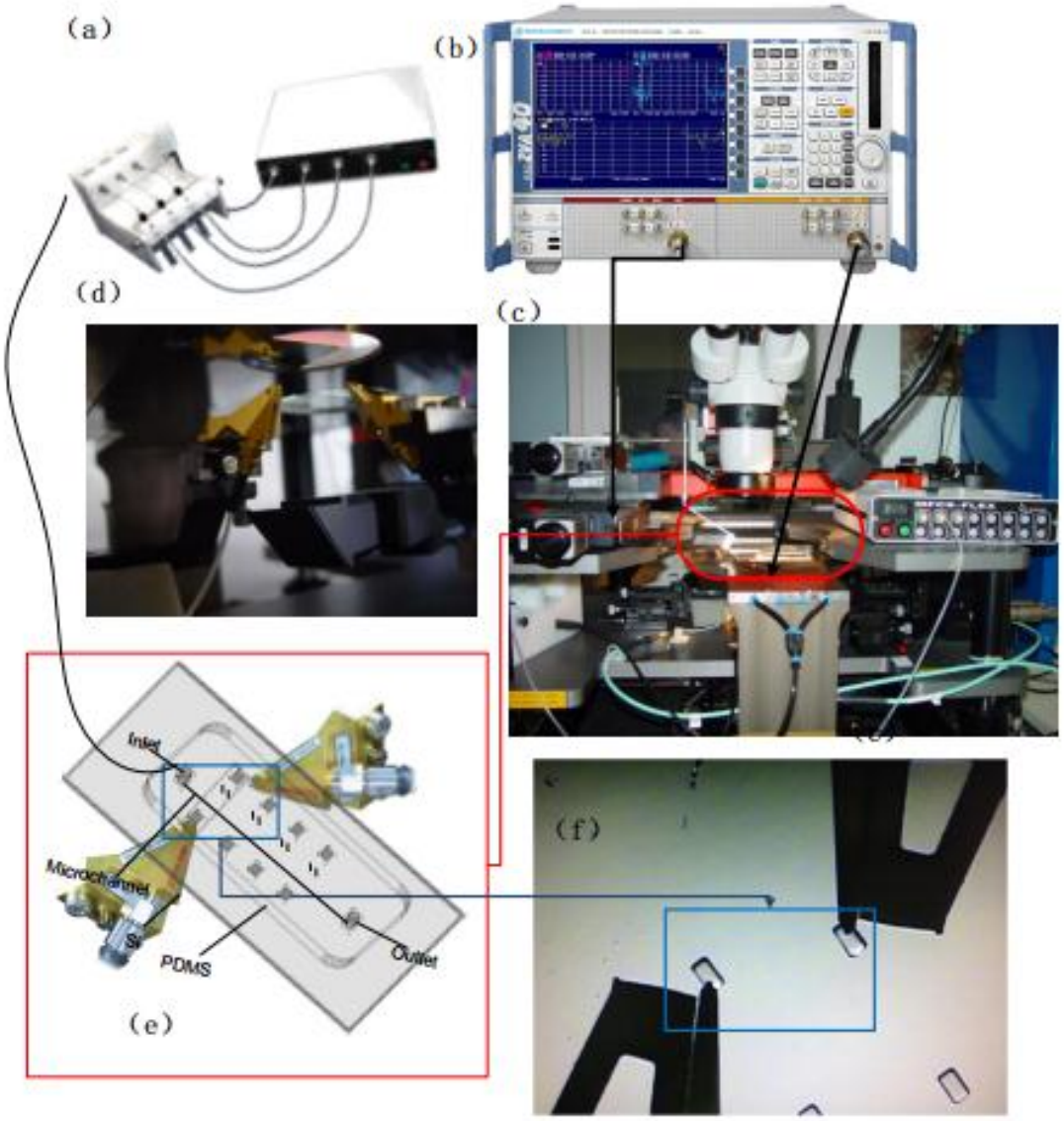

Figure 3.1.4 Schematic diagrams of the whole setup for acoustic signals detection: (a) Pressure-driven flow controller for the microfluidic system, (b) The multi-channel signal generator, (c) Rhode&Scharwtz vector network for data analysis, (d)physical map of the positioned probes on the backside of the sample, (e) Sketch map of a package of the device , (f) observation of two probes contacted on ZnO transducers.

As discussed in chapter 2, we use two methods for ZnO transducer fabrication. Method 1: sputtering ZnO film on patterned resist, then the localized ZnO patterns can be obtained by lift-off process, the ground electrode is Ti and Pt double layers;
Method 2: using single Ti as the ground layer, and a whole layer of ZnO film is deposited on Ti ground layer, then localized patterns of top electrode is fabricated by lift-off process.
As shown in figure 3.1.5, the way to measure the electrical signals of transducers are different. Finite Element Analysis is used to simulate the longitudinal wave propagation in both methods. It is presented that in the second method there are more

acoustic noise [9]. This phenomenon can be explained by the electrical interaction between the excited ZnO films under localized top electrodes and surrounded ZnO area. Then we have to take into account the excitation of the electric field between the top signal electrode and the ground top electrode which can generate a parasitic acoustic wave (surface, interface or Lamb wave).

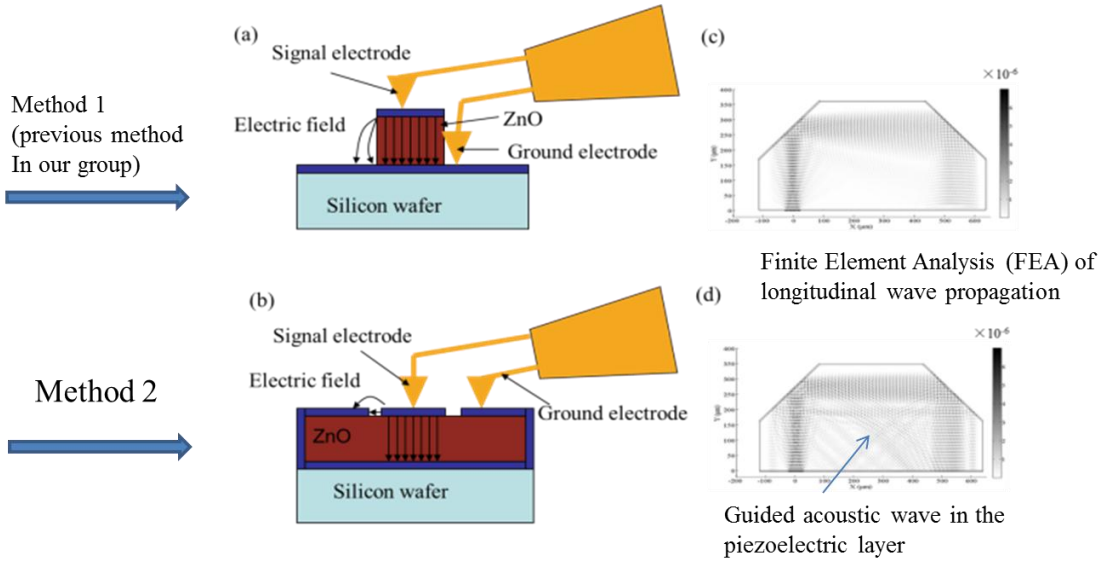

Figure 3.1.5 Scheme of the different configuration of ZnO transducer excitation and simulation for the amplitude of the longitudinal wave after reflected on 45˚ mirrors. (a) excitation on patterned ZnO, (b) excitation on ZnO full layer using patterned top electrodes, (c) simulation of longitudinal wave propagation from localized ZnO patterns, (d) simulation of longitudinal wave propagation from ZnO film on full layer but with localized top electrode patterns [9].

For higher frequency detection which requires thinner ZnO films, the first method can be chosen in order to reduce the acoustic noise. However, for lower frequency acoustic integrated systems which require thicker ZnO layers, the second method has to be used to improve the adhesion between ZnO films and the substrate. In the second case, the internal stress generated in the fabrication between the ZnO film and the substrate can be reduced due to larger contact area.

3.2 Acoustic waveguiding characterization and reduction of mode conversion

3.2.1 Acoustic reflection on 45˚ mirrors

The main benefits of our integrated acoustic system in lab chip are:

1. to separate the detection area from the top side of transducers.
2. to guide the acoustic beam crossing the channel which can be inject biological and chemical samples.

Meanwhile, more flexibility of structures can be integrated in this microfluidic device. To reach this target, the 45° mirrors structure is a key element deflect the acoustic wave so that the acoustic beam generated in the vertical direction can be switched into a transmitted wave in a direction parallel to the silicon wafer surface. This step makes

it possible to guide the acoustic waves in 3 dimensions and can be detected by the receiving transducer after crossing the microfluidic channel.

At a classical silicon-air interface, due to the mode conversion, a large amount of the longitudinal waves is converted into shear wave by the 45° mirror and these latter are totally absorbed by the fluid flowing in the channel. Moreover, the Z axis of the ZnO transducer used as a receiver is not sensitive to this acoustic mode. For these reasons, we have to avoid the mode conversion on the acoustic mirrors. Thanks to the simulation presented in chapter 2, we have used a coating layer to reduce the conversion mode and compared the performances of different layers, taking into account the ability of our process to deposit the right ZnO thickness corresponding to our working frequency.

As shown in figure 3.2.1 (a), the longitudinal wave generated by the emitting transducer is reflected and converted into a longitudinal wave (L) component and a shear wave (S) component on the first 45˚ mirror, later it is reflected and converted again by the second 45˚ mirror before being converted into electrical signal by the receiver.

According to the Snell‟s law, the calculated total reflection angle is approximated to 40° for shear wave, so that the incident shear wave component on the second mirror will be reflected by the 45˚ mirror at approximately 61° reflection angle. After reflection on the first 45˚ mirror, the transmitted longitudinal wave component will be also reflected in L wave and converted into S wave by the second 45˚ mirror. The thickness of the silicon wafer e is about 410 µm and the depth of the 45˚ mirror is about 165 µm. x, y, w, W1, W2, W3 parameters define the different distances between the 45˚ mirrors and the transducers as shown in figure 3.2.1 (b).

Due to the limitation for ZnO fabrication by RF sputtering technology, the ZnO thin film is not able to exhibit a perfect c -axis orientation perpendicular to the substrate surface. Thus the polycrystalline ZnO part will generate not only longitudinal wave but also shear wave.

In our case this shear wave signal can be seen but is too weak to be distinguished from the acoustic noise, so we escape its analysis in the comparison of coating layer performance.

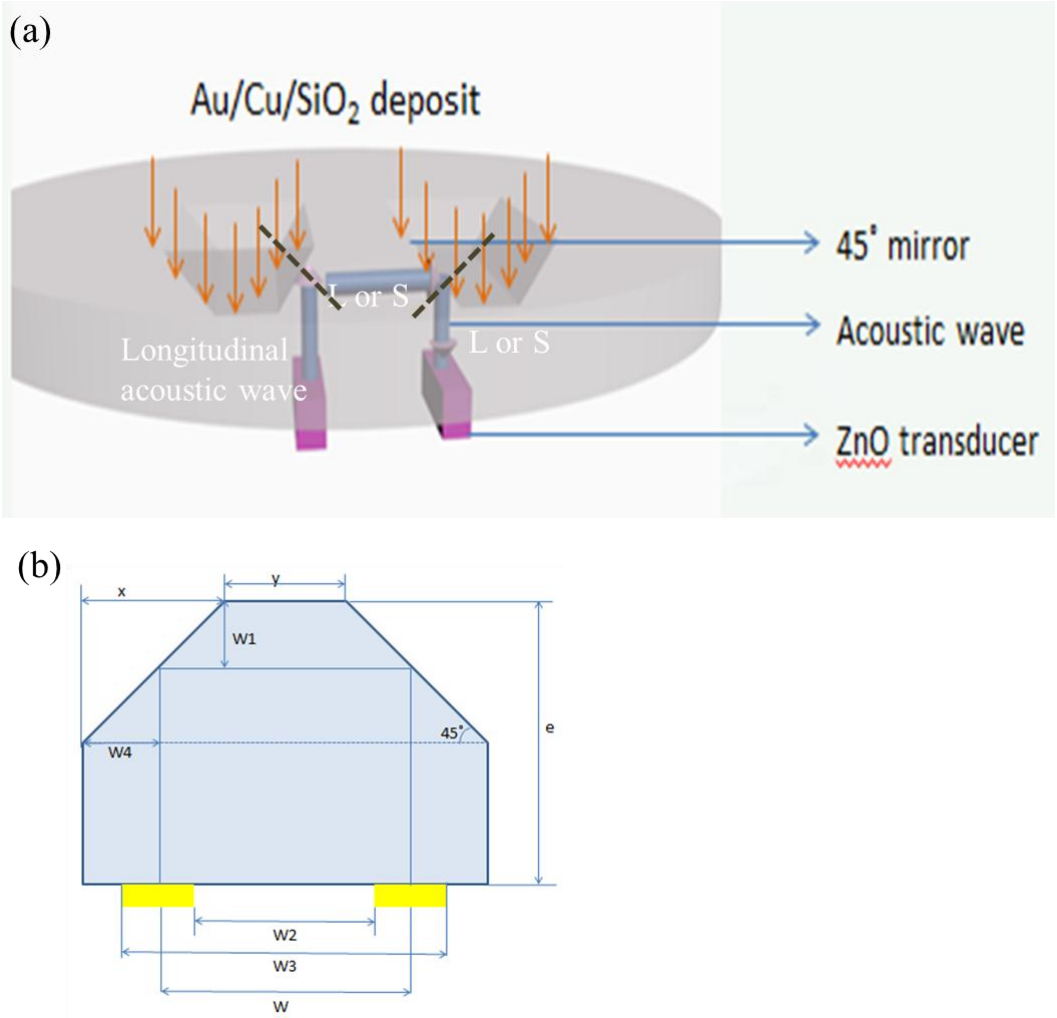

Figure 3.2.1 Schematic diagram of the wave guided by 45° mirrors (a) and structure chart for the analysis of time delay of reflected and of transmitted acoustic wave.

Analyzing the echoes generated by our system in the transmission mode, one can list three types of waves:

- the LLL echo refers to the longitudinal acoustic wave emitted by the transducer and reflected twice on the 45° mirrors before reaching the receiver.
- the LLS echo represents the longitudinal acoustic wave converted into a shear acoustic wave after being reflected on the second mirror during the propagation.
- the LSS echo represents the longitudinal acoustic wave converted into shear acoustic wave when reflected on the first mirror and remaining as shear acoustic wave after being reflected on the second mirror during the propagation.
- SSS echo represents the shear acoustic wave propagating from the emitter and being reflected twice on the 45° mirrors before reaching the receiver.

Taking advantage of the geometrical relationship of the 45° slope of the mirrors, the expected times of flight of the waves were calculated from the following

equations: $t_{LLL} = \frac{2e+y}{v_L}$

$$t_{LLS} = \frac{e + y + W_1}{v_L} + \frac{e - W_1}{v_s}$$

$$t_{LSS} = \frac{e + y + W_1}{v_s} + \frac{e - W_1}{v_L}$$

Where t_{LLL} is defined for the time delay for LLL type transmission; t_{LLS} refers to LLS wave type and t_{LSS} for LSS type. The velocity of the longitudinal acoustic wave in <100> silicon substrate v_L is 8432 m/s and the shear wave velocity v_s is 5398 m/s. From the acoustic velocity and the configuration of the microsystem, the expected time flight of the different echoes can be deduced. Here we compared 6 groups of transducers under 45° mirrors to accurately measure the time delay of acoustic echoes in the case of different received acoustic waves. The positional distance of transducers and mirrors are shown in table 3.2.1. The center to center distance of emitter and receiver is $w = \frac{W2+W3}{2}$ while $W1 = \frac{w-y}{2}$.

sample	x(μm)	y(μm)	w(μm)	w1(μm)	w2(μm)	w3(μm)
1	167	589	735	72	636	834
2	166	590	731	70	631	832
3	168	593	735	71	636	834
4	166	598	734	68	636	832
5	167	594	738	71	638	838
6	165	592	734	71	634	840
average	166.5	592.6	734.5	70.5	635.1	835
stdevp	0.95	2.92	2.06	1.25	2.19	3

Table 3.2.1 Measured distances in the structure graphing, their average value and Stdevp which is the Standard Deviation.

The calculation of the expected time of flight of the acoustic wave LLL, LLS, LSS are presented in table 3.2.2. For each acoustic propagation mode, the measured echo time delay can be distinguished depending on the expected time delay and the maximal peak. Figure 3.2.2 is the impulse response S_{21} corresponding to the time of flight in the system for sample 1. While the expected time echo of LLL is 167.3 ns and the measured time delay is 164 ns combined with the peak amplitude of S_{21} at 1.79×10^{-3}V (the amplitude of the transmitted signal on the linear scale of the network analyzer is normalized to 1V of the emitted signal). The second peak corresponds to a time delay of 199 ns. Considering the expected time delay for LLS of 189.9 ns, it can be deduced

that this strong peak echo is linked to the LLS echo. The amplitude of LSS is too low to be separated from the acoustic noise, so that we can only confirm an approximate location but not a precise analysis. The amplitude of LLS is always higher than LLL in the data plot of the six samples, which indicates that a large proportion of longitudinal wave energy has been converted to shear wave energy in the second reflection by the 45° mirror.

	LLL			LLS			LSS		
sample	Expected(ns)	Measured (ns)	Difference (%)	Expected(ns)	Measured (ns)	Difference (%)	Expected(ns)	Measured (ns)	Difference (%)
1	167.3	164	1.9	189.9	199	4.7	238.7	247	3.4
2	167.4	164	2	190.1	198	4.1	248	247	0.4
3	167.8	164	2.2	190.4	198	3.9	239.4	245	2.3
4	168.4	166	1.4	191.2	200	4.6	240.1	247	2.8
5	167.9	165	1.7	190.5	199	4.4	239.6	236	1.5
6	167.6	165	1.5	190.3	199	4.5	239.2	237	0.9
average	167.73	164.66	1.78	190.4	198.83	4.36	240.83	243.16	1.88
stdevp	0.36	0.74	0.27	0.40	0.68	0.28	3.23	4.77	1.05

Table 3.2.2 Expected and measured time delay of LLL, LLS and LSS modes of acoustic wave. The average value and the standard deviation Stdevp are also compared.

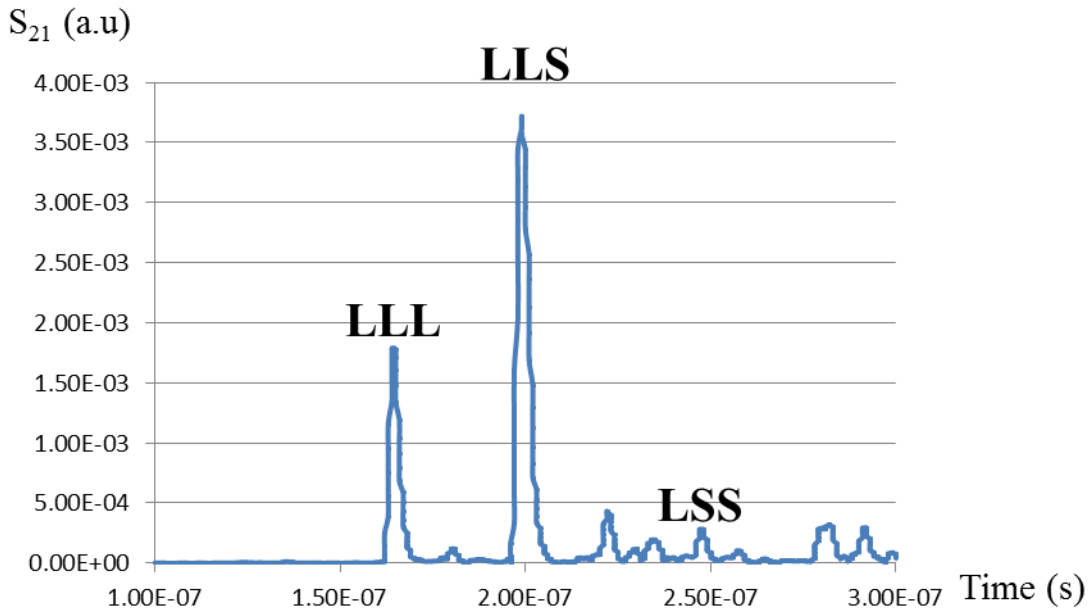

Figure 3.2.2 S_{21} impulse response for sample 1 in time domain.

3.2.2 Comparison of 45° mirrors coating layers performances

The propagation of 1 GHz longitudinal and shear acoustic waves in silicon reflected by the two 45° mirrors is simulated using the 2D COMSOL simulation sofware [4]. 4 µm SiO_2 layer was deposited on the mirrors as mechanical matching layer to avoid any mode conversion. As shown in figure 3.2.3, on the silicon-air interface at 45° slope, the longitudinal wave beam is strongly attenuated after the reflection by the first 45° mirror. The small increase in the amplitude of the longitudinal component after the second reflection can be explained by the mode conversion from longitudinal to shear wave. A small part of the converted shear wave is then transferred again into a longitudinal displacement on the interface of the second 45° mirror. In other words, the amplitude of the displacement for the shear wave beam increases strongly after two reflections.
After the SiO_2 layer is deposited on the mirrors, the amplitude of the displacement shows a high peak which indicates that a matching layer on the mirror could improve the reflection of the longitudinal wave on the mirrors.

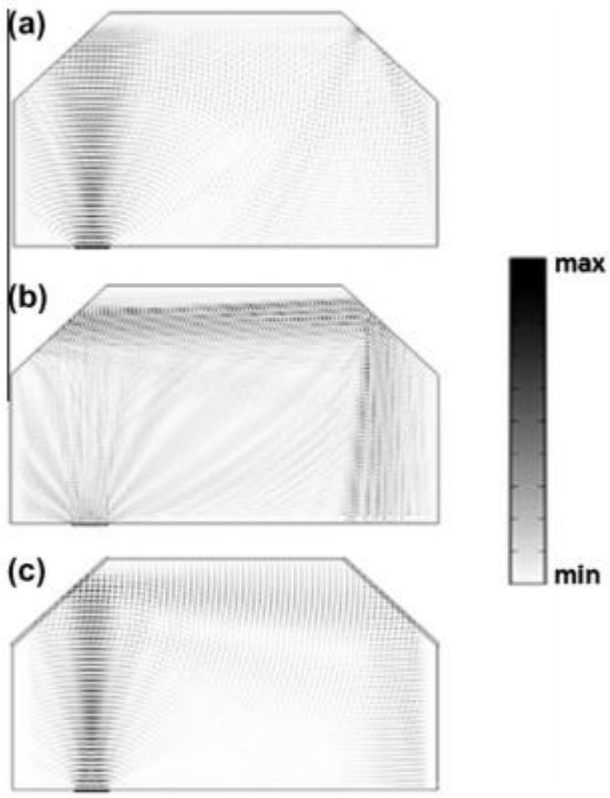

Figure 3.2.3 Simulation of the propagation of 1 GHz (a) longitudinall without any matching layer, (b) shear acoustical waves in the silicon wafer without silicon oxide layer on the mirror, (c) simulation of the propagation of 1 GHz longitudinal acoustical wave in the silicon wafer with a 4µm silicon oxide layer on the mirror [9].

In order to optimize and compare the performances of the acoustic matching layer for

the longitudinal wave reflection, we deposited Au, Cu and SiO_2 layers on the 45° mirrors. The thickness of the coating layer is chosen according to the simulation shown in chapter 2. Firstly, the 3.8 µm SiO_2 film, which was matched to 1GHz central frequency acoustic wave, was deposited on mirrors by PECVD and the acoustic characterization of one sample is shown in figure 3.2.4. It can be noticed that the magnitude of the LLS echo is more than two times higher than that of the LLL one.
With the SiO_2 film on the silicon mirrors, the amplitude of LLL is increased to 2.32×10^{-2}V and LLS decrease to 5.16×10^{-4}V. As a consequence of the SiO_2 matching layer, the amplitude of the LLL echo increases by a factor of 8.2. In parallel the amplitude of the echo LLS declined rapidly. This indicates that less shear wave appears after two reflections on the 45° mirrors, so that we can use the LLL amplitude as a reference measurement of the efficiency of longitudinal wave reflection and of the coating layer performances.

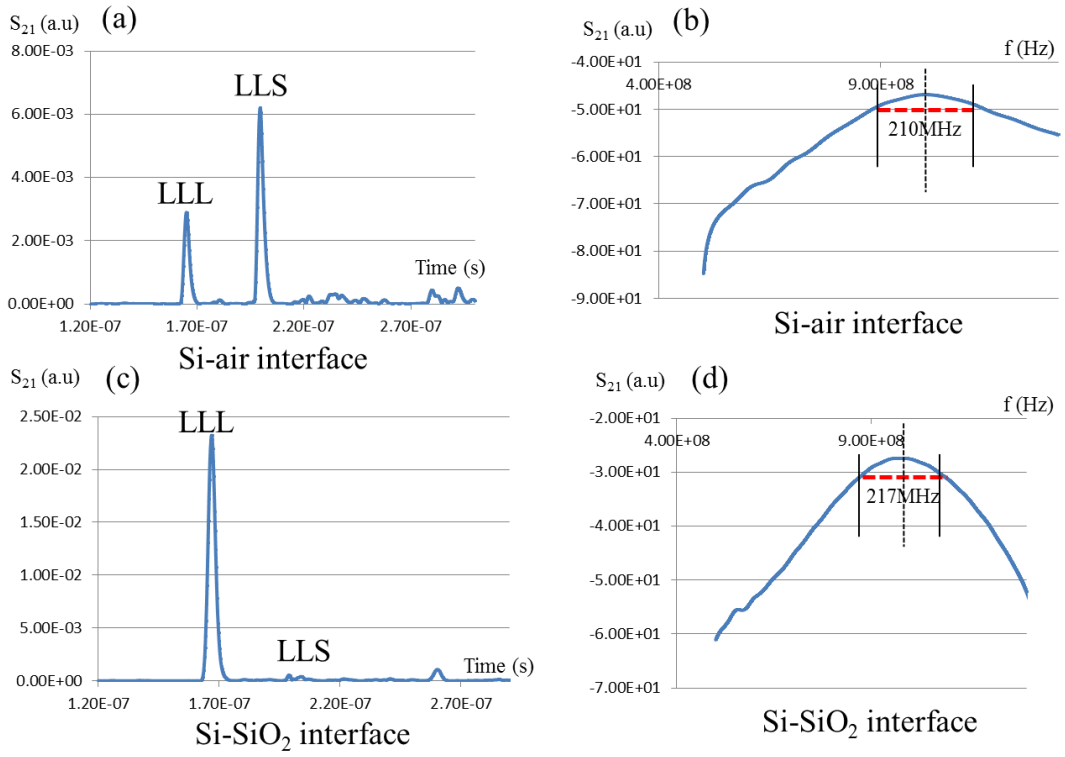

Figure 3.2.4 (a) *S_{21} impulse response in the case of reflection at Si-air interface, (b) S_{21} frequency response for reflection at Si-air interface, (c) S_{21} impulse response for reflection at Si- SiO_2 interface, (d) S_{21} frequency response for reflection at Si- SiO_2 interface. The width of dash line shows the -3dB bandwidth value.*

Another interesting point about the acoustic performances is the bandwidth for wave reflection at the interface with and without the coating layer. One can see on figure 3.2.4 (b) and (d), that these -3dB bandwidth ranges are about 250 MHz without the matching layer and decreases to 204 MHz with the SiO_2 matching layer. Thus the reduction bandwidth ratio is deduced to be 0.816.

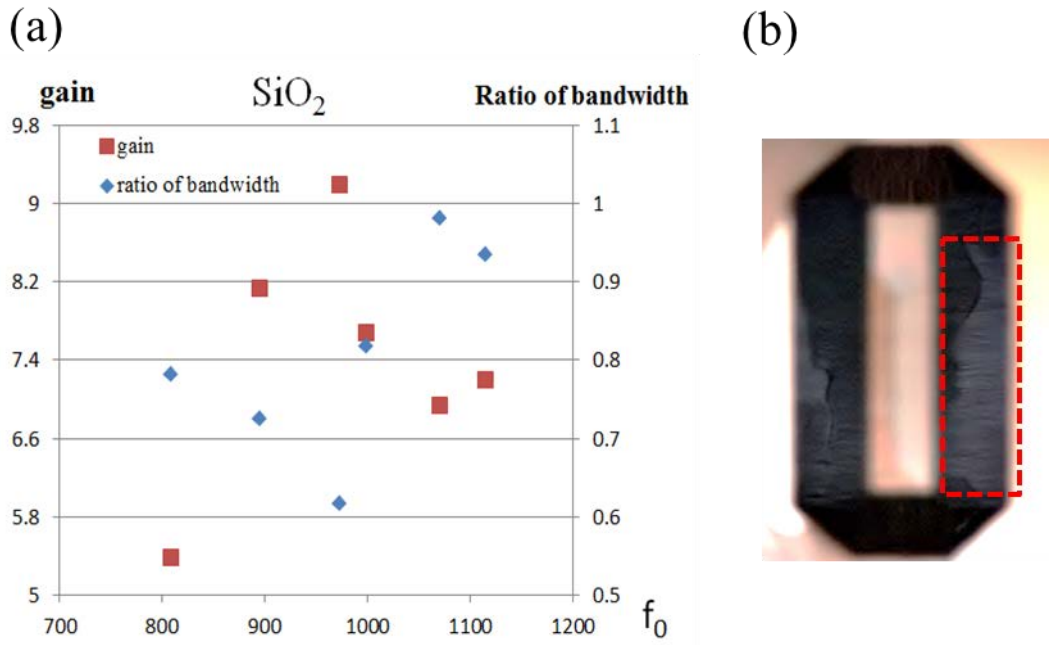

Figure 3.2.5 (a) Gain and bandwidth ratio comparison with a constant 3.8μm SiO_2 layer on the mirrors, (b) SiO_2 film partially damaged in dash box. f_0 is the experimental central frequency of the transducer. The frequency extends from 800MHz to 1200MHz.

We tested 6 samples and compared the gain and ratio of bandwidth changes after a same thickness layer SiO_2 film deposition versus the central frequency of the transducer. In our case, the diameter of the sputtering target used for the ZnO deposition which is close to the wafer diameter led to a natural dispersion of the thickness of the ZnO film. We have taken advantage of this thickness dispersion to evaluate the modification of the efficiency of the SiO_2 matching layer for a given thickness, with respect to the central frequency of the transducer. The thickness of a non-damaged SiO_2 layer can be assumed to be quite homogeneous over the whole sample.

It was found that the S_{21} gain and bandwidth show an irregular change with the experimental frequency rising. The maximum gain which is 9.2 at 1GHz is in good agreement with the simulation presented in chapter 2. But the minimum gain is 5.4 at 800MHz which shows a strong dispersion. The results differences are not only due to the central frequency of the transducers dispersion, but also to the homogeneity of the SiO_2 layer inducing partial peeling on the 45° mirrors. As shown in figure 3.2.5, after 3 hours deposit in the case of 3.8 μm SiO_2 film, we can observe a layer which is partly peeled on 45° mirrors.

It can be deduced that at 300 ˚C PECVD process the differential thermal expansion coefficient between Si, SiO_2 and the process itself generated a strong internal stress for thick SiO_2 film formation. Besides, the roughness of the 45° mirrors and the stress concentration increase a total adhesion stress of the SiO_2 film. Finally, for 3.8 μm SiO_2 film adhesion on mirrors, an unstable peeling and cracking appears at random

which modifies largely the acoustic reflection at the interface. The heterogeneity of films will lead to acoustic wave scattering and will introduce phase noise on the acoustic wavefront after reflection. Alternative materials have to be tested for a stable device application. The idea is to replace the silicon oxide film by a more ductile metallic film.

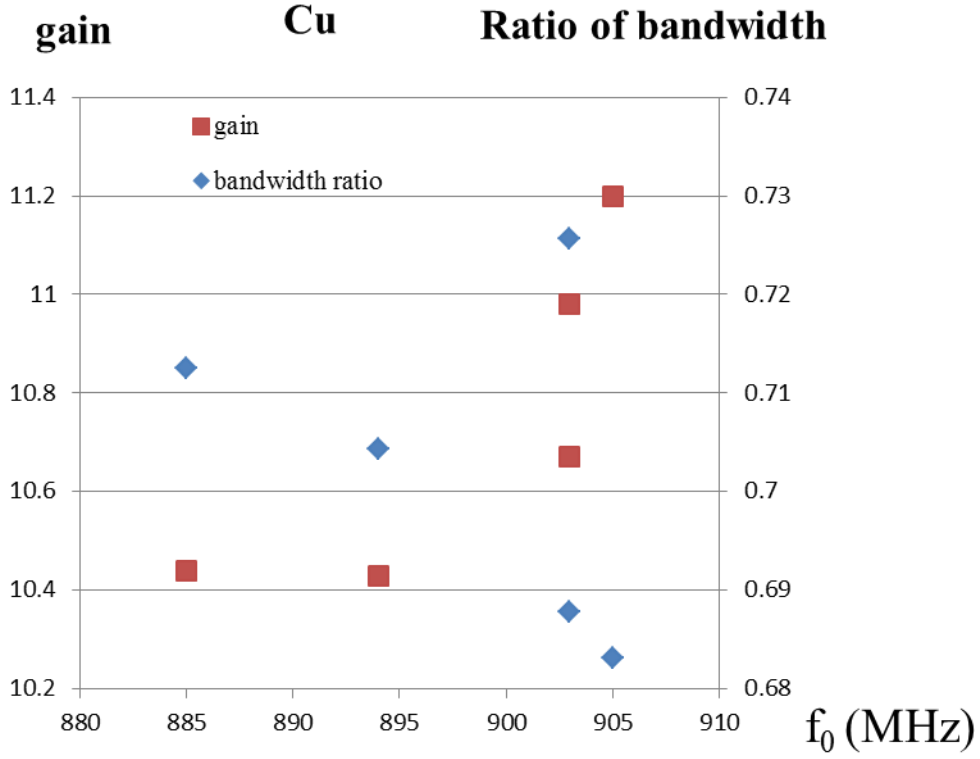

Figure 3.2.6 Gain and bandwidth ratio comparison with 1.26 µm copper layer on mirrors. f_0 is the experimental central frequency of transducer. The frequency ranges from 880MHz to 910MHz.

Copper films of 1.26 µm in thickness were deposited on the 45° mirrors and 5 samples were evaluated to characterize the acoustic performances. The thickness of copper film is matched for 1GHz central frequency of transducers. However, due to the limitation of ZnO film sputtering technology, the thickness of the transducers varies at different positions of the substrate. As the thickness of ZnO film is linearly linked to its central frequency, thus we obtain transducers in a central frequency range on the backside of the wafer.

As shown in figure 3.2.6, the fabricated transducers had a central frequency varying from 880 MHz to 910 MHz. It is observed that the gain increases as the experimental central frequency increases. The gain value is around 10.44 for frequency less than 900 MHz, but it rises quickly for frequency above 900 MHz and reaches a maximal value of 11.2 at 905 MHz frequency. This means that even the experimental central

frequency shifts 120 MHz away the pre-set central frequency at 1 GHz, the longitudinal wave attenuation at the reflection interface can be decreased more than 10 times with a copper coating, even if the thickness of coating layer fitted to a 1 GHz central frequency.
On the other hand, the bandwidth ratio varied from 0.68 to 0.72 in this frequency range, which is a classical result when the gain ratio is increased.

	S_{21} (10^{-6})		Gain	Central frequency (MHz)	Central frequency (MHz)	**Δf (MHz)**	Bandwidth (10^8MHz)	Bandwidth (10^8MHz)	ratio of bandwidth
sample	Si	Si-gold		Si	Si-gold		Si	gold	
1	1810	15100	8.34	894	898	**4**	2.3	1.38	0.6
2	2200	15900	7.22	974	935	**-39**	2.68	1.5	0.55
3	1330	11600	8.72	809	892	**83**	2.18	1.79	0.82
4	3020	23900	7.91	1000	928	**-72**	2.5	1.63	0.65
5	3640	28000	7.69	1071	943	**-128**	2.79	2.19	0.78
6	4350	30100	6.91	1116	1050	**-66**	3	4.28	1.42
7	3350	25700	7.67	1070	946	**124**	2.63	2.19	0.83
8	3420	25900	7.57	1070	945	**125**	2.63	2.23	0.84
9	4050	26000	6.41	1110	1050	**50**	4.3	4.19	0.97
10	3700	24300	6.56	1100	1003	**3**	2.65	3.34	1.26

Table 3.2.3: Acoustic characterization for improvement of mode conversion with 800 nm gold deposition on mirrors, including gain of S_{21} impulse response, bandwidth modification and central frequency shift.

S_{21} modulus of the impulse response of the system is compared with acoustic matching layer of 800 nm gold deposited on the mirror surfaces. The 800 nm gold layer is matched with 800MHz central frequency acoustic transducers which will be the working frequency of our integrated acoustic system, particularly in the next step of our work for acoustic detection in microfluidic channels [5]. Measurements in detail are presented in table 3.2.3 for an experimental central frequency from 800 MHz to 1200 MHz. We can notice that there is a shift of the central frequency of the transducers when introducing a coating layer. The final frequency bandwidth is the product of the different transfer functions bandwidth of the transducer and the layer. Measured frequency shift spans from 125 MHz to -128 MHz after 800 nm gold sputtered on 45° mirrors.
After gold coating, the amplitude gain for LLL echo measured using S_{21} in time domain(in comparison with the reflections on silicon mirrors without any coating layer) varied from 7.22 to 8.72 and shows that the conversion mode from longitudinal

to shear wave was limited and most of the longitudinal wave energy was kept. The increase of amplitude of the LLL signal reached 18 dB. Theoretically the bandwidth will be smaller after the gold matching layer coating on mirrors and the ratio should be lower than 1. However, the factual bandwidth ratio we obtained varies from 0.55 to 1.42 which can be explained by the shift of the central frequency of the transducer and of the resonance frequency of the coating layer. The resultant frequency responses exhibit multiple maximal and large variations versus the shift of the maximum of the initial curves. It is then difficult to apply a criterion to quantify the bandwidth.

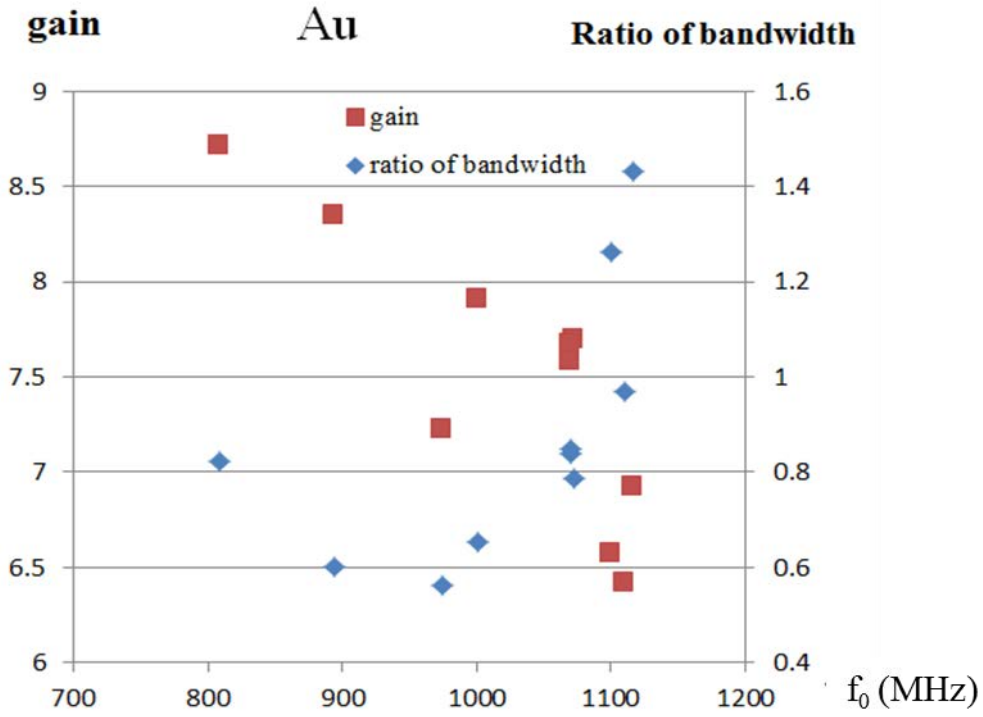

Figure 3.2.7 Data graph of *gain and bandwidth ratio comparison with 800 nm gold layer on mirrors. f_0 is the experimental central frequency of transducer. The frequency ranges from 800MHz to 1200MHz.*

For the acoustic matching layer comparison, SiO_2 layer shows high value of gain (9.2 at 1GHz), but the film heterogeneity due to the high internal stress hindered the stability of the process fabrication and potentiality for low frequency devices. Copper layer shows the highest value of gain (11.2 at 906 MHz) but a low bandwidth ratio (0.68). Au layer shows an available value of gain (8.7 at 800 MHz) and a higher bandwidth ratio than copper. For high frequency acoustic detection above 800 MHz, gold and copper are good choices for acoustic matching layer and can be obtained by directly sputtering technology. However, for the acoustic actuator in lower frequency, the thickness of coating layer is required to increase linearly when the frequency is decreasing.

As an example at 300 MHz working frequency, 1.8µm gold coating layer is needed. It can be obtained by two or three times sputtering. For the alternative copper layer, 3.8

μm in thickness is required which must be fabricated by electroplate deposition. Nevertheless, this method will introduce an excessive roughness of the mirror surface and heterogeneous thickness of film. Otherwise, at 300 MHz frequency, 10 μm SiO_2 film would be fabricated which is impossible to be reached using our present technology.

To sum up, the system with the single gold film on 45° mirrors offer a good compromise between acoustic gain and bandwidth performances and can preserve the stability of our process. Besides, gold layer can be easily removed in room temperature without damaging silicon wafer. These advantages of fabrication make us adopt gold material as our acoustic matching layer on 45° mirrors and vertical mirrors in subsequent process.

3.3 Acoustic characterization in microfluidic channel

3.3.1 Waveguiding with vertical mirrors

Prior to our acoustic characterization of lower frequency in the integrated microchannel, vertical mirrors have been firstly validated according in the previous PhD work in the gigahertz frequency range [6]. The acoustic wave emitted by the ZnO transducer is not a plane acoustic wave, so the acoustic diffraction can scatter the acoustic energy and lead to acoustic noise.

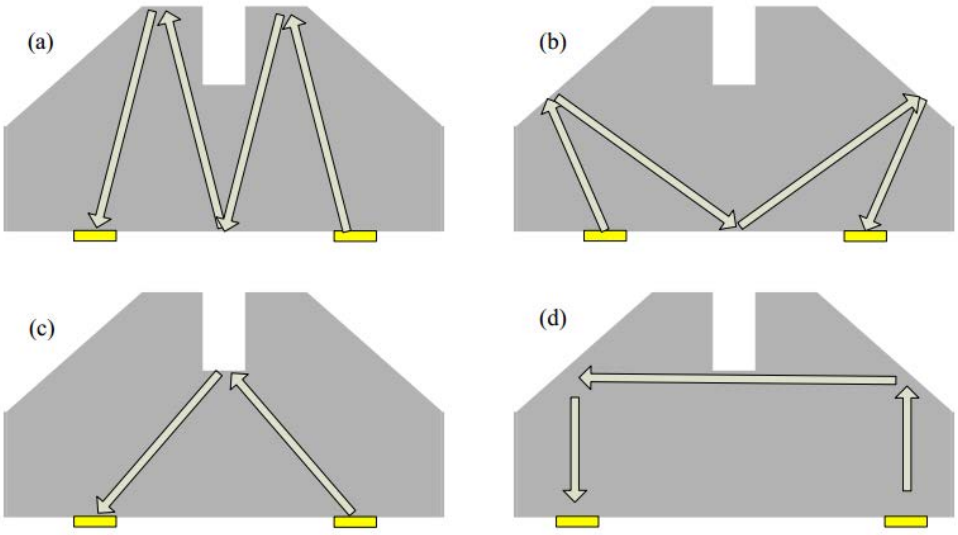

Figure 3.3.1 Different paths of parasitic acoustic wave propagation. (a) three time reflections by top surface and bottom of the wafer, (b) three time reflections by 45° mirrors and bottom of the wafer, (c)reflection by bottom of the channel, (d)no propagation in the channel.

In our microsystem including 45° mirrors and microchannel, the acoustic waves can be reflected by the 45° mirrors, the top surface of silicon wafer and the bottom of the

microchannel as shown in figure 3.3.1. Previous results showed that the parasitic signals have been labeled in the transmission impulse response with sizeable amplitude peak which hindered the useful signals to be identified. To solve this problem, two vertical mirrors were integrated in the acoustic transmission path to filter the parasitic wave which propagates under the channel.
The acoustic wave generated by the emitting transducer will be reflected two times by 45° mirrors in plane perpendicular to the surface of the wafer and two times in a plane parallel to the surface before to be converted into electrical signal by the receiver.
To avoid mode conversion, 4 μm SiO_2 film was deposited on all the mirrors in our integrated acoustic system. This method decreased simultaneously not only the acoustic noise and but also the useful transmitted signals due to the increase of the reflection number.
Due to the technology limitation of PECVD, there is a large variation for the thickness of SiO_2 film on the surface of 45° mirrors and the surface of vertical mirrors. In fact, the average thickness of SiO_2 layer is around 1μm on the trench wall of vertical mirrors, thus mode conversion is not avoided at the silicon-air interface of vertical mirrors when the longitudinal acoustic wave is reflected.
Anyway, the phenomenon of longitudinal wave converted to shear wave is partially limited by the SiO_2 coating layer, parallel with an increase of the signal to noise ratio (SNR). It has been established that the pairs of two vertical mirrors added has improved the sensitivity for acoustic detection at 1 GHz central frequency.

3.3.2 Liquid characterization with water and KI solution

The detailed geometry of the structure is shown in figure 3.3.2. The distance from the center of the transducer to the middle of the 45° mirror e is 305 μm. W_t is the center to center distance of the pair of transducers. W_c is the width of the microchannel. W_{2v} is the acoustic propagation length between 2 vertical mirrors and W_{1v} is the acoustic propagation length from emitter to 1 vertical mirror. Hence, the time of flight from emitter to receiver can be deduced:

For 2 vertical mirrors structure $t = \frac{2e+W2v+Wt-Wc}{V_L} + \frac{Wc}{V_{liquid}}$

and for 1 vertical mirror structure $t = \frac{2e+W1v+Wt-Wc}{V_L} + \frac{Wc}{V_{liquid}}$

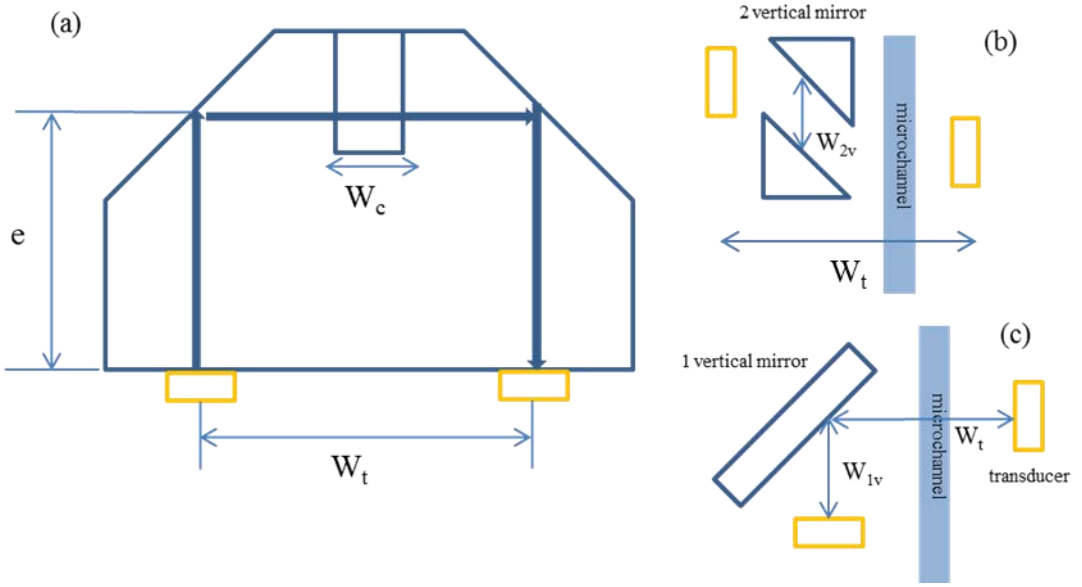

Figure 3.3.2 Geometry of the devices (a) dimension on cross-section view, (b) scheme and notation of the top view of the 2 vertical mirrors structure, (c) scheme and notation of the top view in the case of the 1 vertical mirror structure.

Where V_L = 8432 m/s is the acoustic longitudinal speed in silicon wafer and V_{liquid} = 1482m/s is speed in water at measured temperature of 25 ˚C. Here the shear wave is not taken into account due to the high attenuation of shear waves in low viscosity liquids. Therefore, the limitation of mode conversion is needed in order to get high-sensitivity acoustic characterization of liquid in microfluidic channels.

sample	W_c (µm)	Predicted (ns)	Measured (ns)	Difference (%)
C_0	150	413.6	412	0.4
C_1	250	436.4	454	3.8
C_2	200	408.6	405	0.9
C_3	150	380.8	377	1

Table 3.3.1 The predicted and measured time delay of transmitted longitudinal acoustic waves for sample C_0, C_1, C_2, C_3.

Geometry of the different devices: sample C_0 is a 2 vertical mirrors structure with W_{2v}=500 µm, W_t=1670 µm and W_c=150 µm.
For sample C_1, C_2, and C_3, W_{1v}=705 µm, W_t=1193 µm, but the values of W_c are different. These values are given in table 3.3.1. The differences in the time of flight are less than 4% for both of the measured samples and the $S_{ij}(t)$ parameters can be determined.

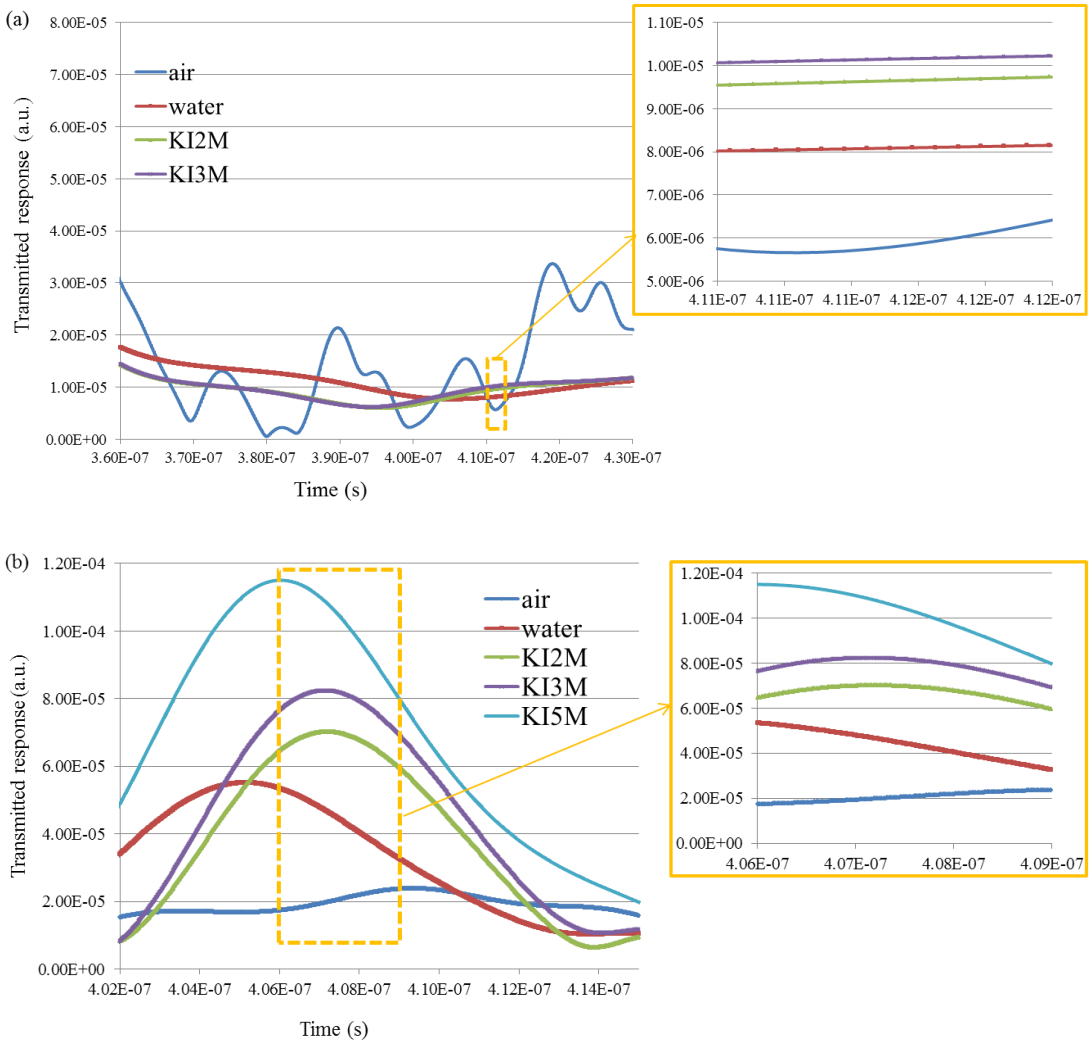

Figure 3.3.3 Transmitted time domain response S_{12} (t) for sample with two vertical mirrors (a) and sample with one vertical mirror (b) the channel width is 250 µm. Useful amplitude comparisons are in yellow dash box. Signal characterization in empty channel, deionized water, 2mol/L, 3mol/L and 5mol/L KI solutions respectively.

KI solution has already been used in order to characterize high frequency acoustic scanning microscopes. One benefit in using KI solution is the nearly constant acoustic velocity independent of concentration, in a certain concentration range. Besides, the attenuation coefficients of KI depending on the concentration have already been characterized, which can be taken as a reference for our experiments.

The time domain transmitted responses of previous samples are presented in figure 3.3.3. For sample using 2 vertical mirrors (figure 3.3.3a), we measured large acoustic noise signals with amplitude higher than useful signals. At 458 ns a very strong signal variation can be seen when the empty channel was changed by introducing liquid. Without liquid injected into the channel, a large static echo appears in the response but disappears immediately as water and KI solution are injected in the system. Because the acoustic wave (both longitudinal wave and shear wave) cannot be transmitted through the empty channel, this strong noise can be explained by the

strong acoustic diffraction with multiple reflection at the 45° mirrors, top surface of the wafer, the sidewall of the channel. When the acoustic wave propagates over a long distance between 2 vertical mirrors, the beam width is increased due to the diffraction phenomenon and random reflections happen within the device. This phenomenon introduces a lot of noise and reduces the transmitted energy. In this case, the transmitted signals for KI concentration characterization show very low amplitudes (less than 1×10^{-5}v). The strong peak of noise is four times bigger than the useful echo and the measurement sensitivity of this system.

Another way to reduce the acoustic noise transmitted under the channel is to use only 1 vertical mirror and to tilt the 45° mirror above the receiver. Results presented (in figure 3.3.3b) validate the good sensitivity of this new geometry. Different concentrations of KI solutions (2 mol/L, 3 mol/L and 5 mol/L) have been used to measure the acoustic losses of these solutions. We can observe that the parasitic acoustic noises are strongly decreased which allows an improvement of measurement sensitivity (dash box). The time delay of useful $S_{12}(t)$ echo is 454 ns read from the curve with a 3.8% difference of the predicted time (table 3.3.1). The amplitude of the useful echo in the case of KI 5 mol/L is 1.16×10^{-4} V which is ten times larger than the value in the "2 vertical mirrors" system. The structure using 1 vertical mirror reduces the propagation distance before the channel and the acoustic beam spreading, thus a high sensitivity acoustic detection can be achieved.

In order to explain the measurement method of the acoustic attenuation of an unknown fluid, we have to analyze in detail the contributions in the microsystem losses. For each system sample, the losses in the transmission mode can be divided into several parts:

- conversion loss of the transducer including the probe contact losses and referred to as A_{Cn} for the microsystem C_n. This part of the losses is largely modified when the measurement probes are removed and placed again on the same transducer.
- diffraction and propagation absorption in silicon labeled for the microsystem C_n : D_{Cn}.
- reflector and conversion mode losses labeled for the microsystem C_n : R_{Cn}.
- transmission losses at the silicon/liquid interfaces which will be considered as independent of the liquid under characterization in a very first approximation. We labeled this part for the microsystem C_n : T_{Cn}. Nevertheless, we have to introduce the accurate value of this coefficient if the variation of the losses between the reference liquid (water) and the liquid to be characterized across the channel is not significant.
- absorption losses in the liquid to be characterized, herein after referred to as $A_{liquidCn}$

In consideration of the system C_n in dB scale, the losses $A_{sysCn} = D_{Cn} + R_{Cn} + T_{Cn}$.

Then, the total losses of the acoustic system can be written as:

$S_{12}(f, liquid, C_n) = A_{Cn} + A_{sys\,Cn} + A_{liquid\,Cn}$.

In order to determine the terms $(A_{Cn} + A_{sys\,Cn})$, we will use two measuring condition: measurement of the losses of the system using a known and the unknown liquid without removing the measurement probes on system C_n (attenuation in water at the

temperature will be used as an input data).
For measurements of the same device without removing the probes, the total system losses $A_{Cn} + A_{sys\ Cn}$ are the same. Thus $A_{Cn} + A_{sys\ Cn} = S_{12}(f, KI) - A(f, KI) = S_{12}(f, water) - A(f, water)$, for water and KI solution,
Where:

- transmission in KI solution $A(f, KI) = \alpha_{KI}(f) \cdot W_{cn}$,
- transmission in water $A(f, water) = \alpha_{water}(f) \cdot W_{cn}$,
- $S_{12}(f, water)$ and $S_{12}(f, KI)$ are the measured S_{12} parameters by VNA for water and KI solution,
- α is the attenuation coefficient which is a frequency function, f is the frequency in the bandwidth of the ZnO transducer, W_{cn} is the width of the channel in the system C_n.

Finally we obtain $\alpha_{KI}(f) = \alpha_{water}(f) + [S_{12}(f, KI) - S_{12}(f, water)] / W_{cn}$
For water α/f^2 is a constant over a wide range of frequency and typically is 22×10^{-17} $cm^{-1}sec^2$ at 25 ˚C [7]. Besides, acoustic velocity in KI solution is slightly concentration dependent. That's why we compared water and KI liquid as references to evaluate the performance of our device.
The typical value for attenuation of ultrasound in water is about 220 dB/mm at 1GHz at room temperature, thus $\alpha_{water}(f_0) = 5.5$dB/cm at 500 MHz, f_0 is the central frequency of the transducer.
Thanks to the Inversed Fourier transform, we can achieve the data analysis in time domain. The attenuation coefficient can be deduced from the measurement of the ratio of the pick amplitude of the transmitted echo through the channel.
In order to improve the accuracy of the attenuation measurement for the unknown liquid, we characterized the 1 vertical mirror reflection system of three channel widths for three concentrations of KI solution to calculate the attenuation coefficient $\alpha(f_0)$. As shown in table 3.3.2, for each concentration of KI solution, the echo amplitude $S_{12}(t, liquid)$ are measured for different channel widths.

sample	W_{cn} (μm)	Transmitted echo amplitude (10^{-5} V)				$\alpha(f_0)$ ($10^{-17}s^2/cm$)		
		KI2M	KI3M	KI5M	water	KI2M	KI3M	KI5M
C1	250	2.53	3.15	6.86	1.87	4.45	3.72	0.98
C2	200	6.9	8.18	11.4	5.5	4.51	3.78	2.33
C3	150	7.26	8.45	9.06	5.2	3.56	2.69	2.28

Table 3.3.2 Measurements of echoes amplitudes in samples C1, C2 and C3 with different microchannels widths. Attenuation coefficient of KI at f_0 (around a central frequency of 500 MHz) is also deduced. All the transducers are kept with the same dimension of 120 × 160 μm.

We compared calculated values of attenuation coefficient for KI solution in time domain, as well as referenced values is at 514 MHz central frequency, as presented in figure 3.3.4. In the cases of KI in lower concentrations (2 mol/L and 3 mol/L), the deviations (between the calculated values and referenced values) increase when

channel width decreases from 250 µm to 150 µm. The underestimate of the value may be due to smaller propagation distance of acoustic wave in the liquid. As the total attenuation in liquid decreases, the differentiation of the assessment for attenuation coefficient becomes smaller.

In another case at 5 mol/L KI solution, the amplitude coefficient has a strong deviation from reference to sample C2 (30.8%) and C3 (32.3%). Meanwhile, there is an abnormal value in sample C1 with amplitude of 0.98. In the case of high KI concentration KI crystals may appear in the aqueous solution and the crystals can be stuck on the sidewalls of the channel. It can also be observed that channel is blocked by growing KI crystals in repeated experiments. As a consequence, the insertion losses for acoustic transmission are then increased. In fact, the attenuation measured corresponds to a modified concentration of KI solution. The attenuation coefficient value is in good agreement with reference for KI at 2 and 3 mol/L in system C1 and C2 (250 and 200 µm), with a deviation of 3.3%.

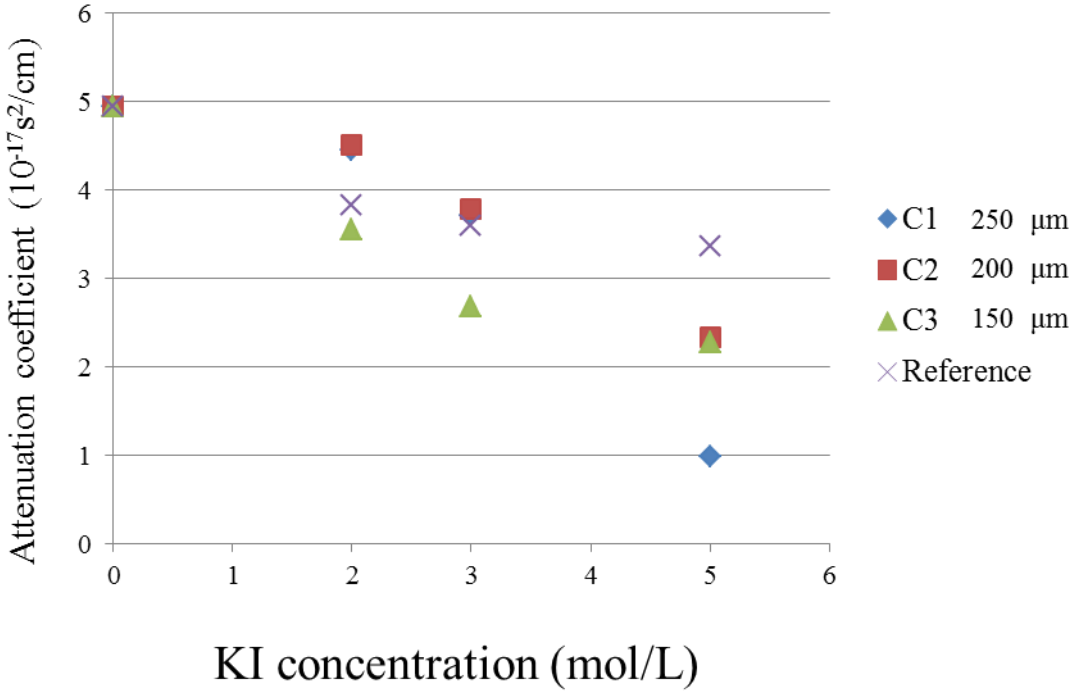

Figure 3.3.4 Calculated attenuation coefficient by time domain echo response for KI solution at 2 mol/L, 3mol/L , 5 mol/L at 25 ˚C. C1, C2, C3 are channels with different widths of 250 µm, 200 µm and 150 µm respectively. Reference value for the coefficient was deduced from J. Attal's work [7].

Measurements of S parameters in time domain are deduced from the Inversed Fourier Transform which is a value of signal attenuation integrated in the whole bandwidth of the frequency. However, the acoustic attenuation coefficient of an unknown liquid is frequency dependent, thus we try to characterize the frequency responses for the evaluation of the attenuation of unknown liquid. The results of time domain analysis are incapable of determining the frequency dependent of the liquid attenuation. For this purpose, we have to compare the measurements for different channel widths as a

function of frequency.

A time domain window is used in order to pick up the useful signals and the frequency response of S_{12} curves in a limited frequency range for KI solution is shown in figure 3.3.5.

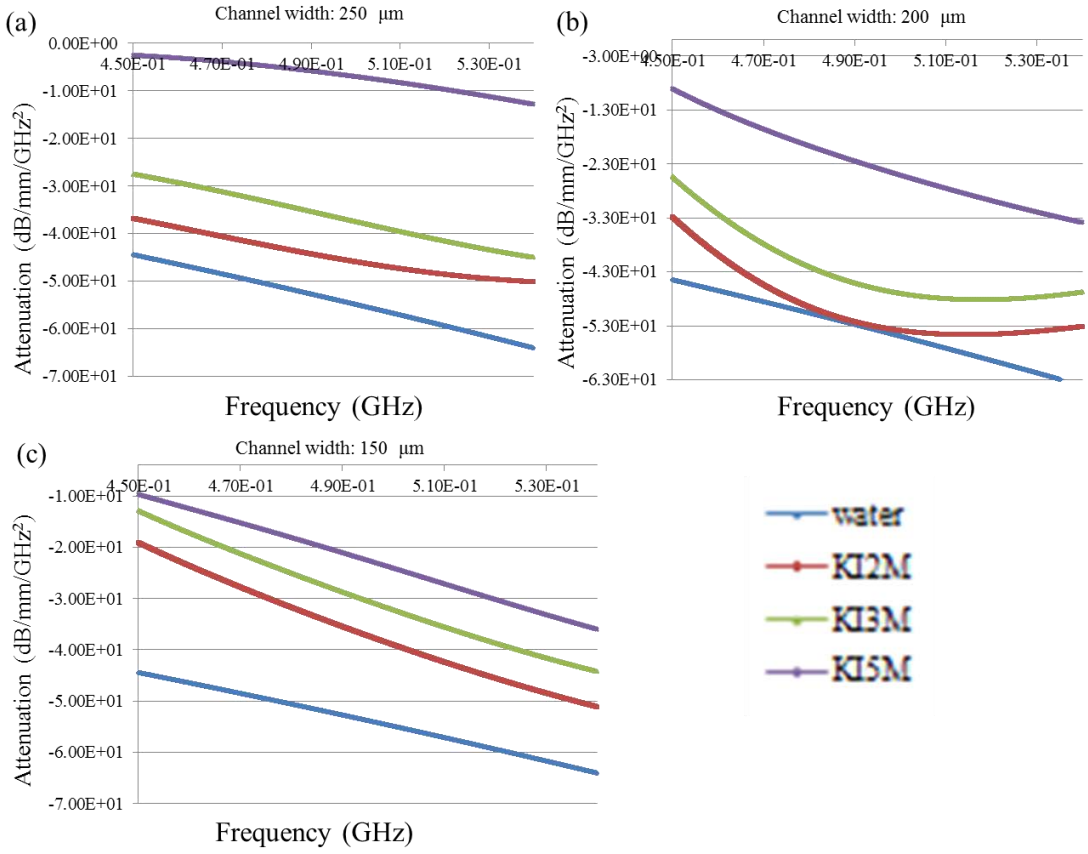

Figure 3.3.5 frequency response of S_{12} curves for KI solution at 5 mol/L, 3mol/L and 2 mol/L. (a) channel width 250 µm, (b) channel width 200 µm, (c) channel width 150 µm. The frequency ranges from 450 MHz to 540 MHz.

From the curves, we can find a good agreement between already published value of attenuation and our measurements, but only over a small frequency bandwidth.

The main problems appear with the acoustic noise in the useful time domain window and the consequence of the time windowing parasitic signals which are of the same amplitude than the useful signal.

Besides, compared to the previous J. Gao et al"s work [6], the initial choice to investigate low frequency application (decrease from 1GHz to 500MHz) introduces more diffraction and spreading of the acoustic wave, but less effect of the propagation attenuation. A way to decrease the noise is to increase the transducer dimension, but limitation is related to the ICP process for channel grinding (not more than 150 µm).

To increase the accuracy of attenuation measurements of KI solution, we optimize the calculation for the attenuation of KI in a small propagation distance in the liquid. It is well known that the α_{water}/f^2 is a constant value of 217.2 dB/mm at 20 ˚C. Thus α_{water} can be deduced as a function of frequency, and then introduced in the

following formula. In order to increase the accuracy we will use the difference of attenuation between the two systemsC1 and C3:
$\Delta A_{Cn} = S_{water\ C1} - S_{water\ C3} + \alpha_{water} W_c$. This difference is mainly induced by the probes contacts of the transducers.
Then, the attenuation of KI 3mol/L in 100 µm liquid can be deduced as $A_{KI3} = S_{KI3\ C1} - S_{KI3\ C3} - \Delta A_{Cn}$. Meanwhile, $A_{KI3} = \alpha_{KI3} Wc$, thus we can acquire the attenuation coefficient of KI 3mol/L α_{KI3}, which is a function of frequency.

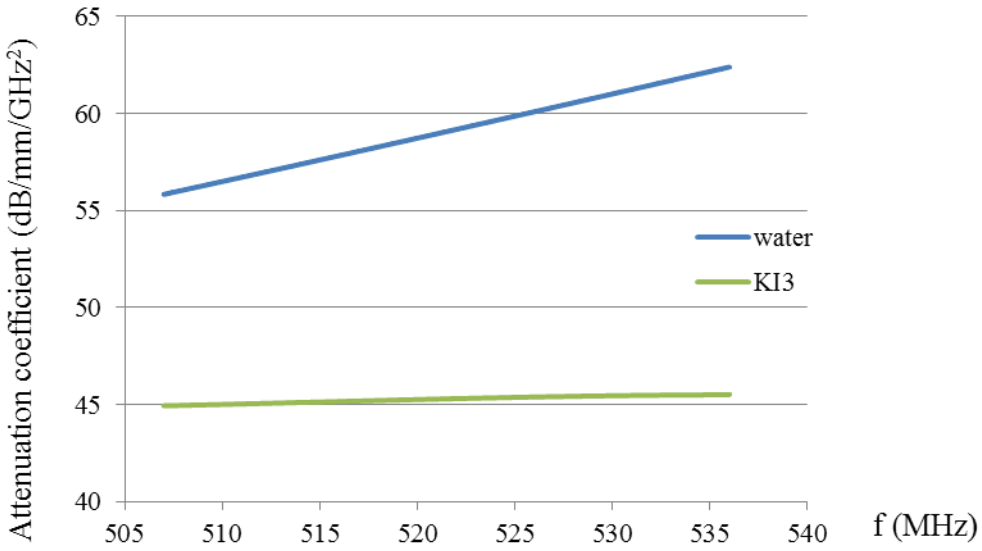

Figure 3.3.6 Deduced attenuation coefficient of 3mol/L KI solution at 20 ˚C, as a function of the frequency in a range of 505 MHz to 540 MHz.

Then the attenuation coefficient of KI 3 mol/L is calculated and shown in figure 3.3.6 for a frequency bandwidth from 505 MHz to 540 MHz. At 514 MHz, the attenuation coefficient of KI 3 mol/L is 45.1 dB/mm, which is close to the comparison of the theoretical attenuations in present publication (43.6 dB/mm of KI 3mol/L) [7].
Our device shows good accuracy in this frequency range. For wider frequency range and higher precision, the effective way is to optimize the fabrication technology of device and channel geometry in order to lower the acoustic noise. The increase of transducer dimension and the decrease of the propagation distance in each modulus of the system can intensely reduce the acoustic noise in the propagation. As long as the amplitude of the useful signal is high enough, the parasitic signals of the time windowing and noise can be distinguished and separated easily.

3.3.3 Particles detection in the microchannel

Particles detection have been an active area of research in the microfluidics community for over a decade for the potential applications in particles counters, FACS, cell sorting and so on [8]. The polystyrene (PS) latex particles (granuloshop, 10% monodisperse suspension) of 30 µm diameter were used for acoustic detection

within the channels. The monodisperse suspension of PS latex particles has been diluted to 0.1% concentration and injected into the microchannel through driving air pressure controlled by the MFCS controller. The characterization system was chosen with 1 vertical mirror with the channel width of 150 µm and the expected time of echo is 380.8 ns.

Thanks to the low concentration of PS solution and wide channel width, we can control particles staying in the detection area by flow controller. After the particles were injected the microchannel, their trajectory can be observed by the microscope while the driven pressure in the channel is controlled in real time, so that particles can be moved to the detection region in front of the mirrors and settled in the acoustic wave transmission path.

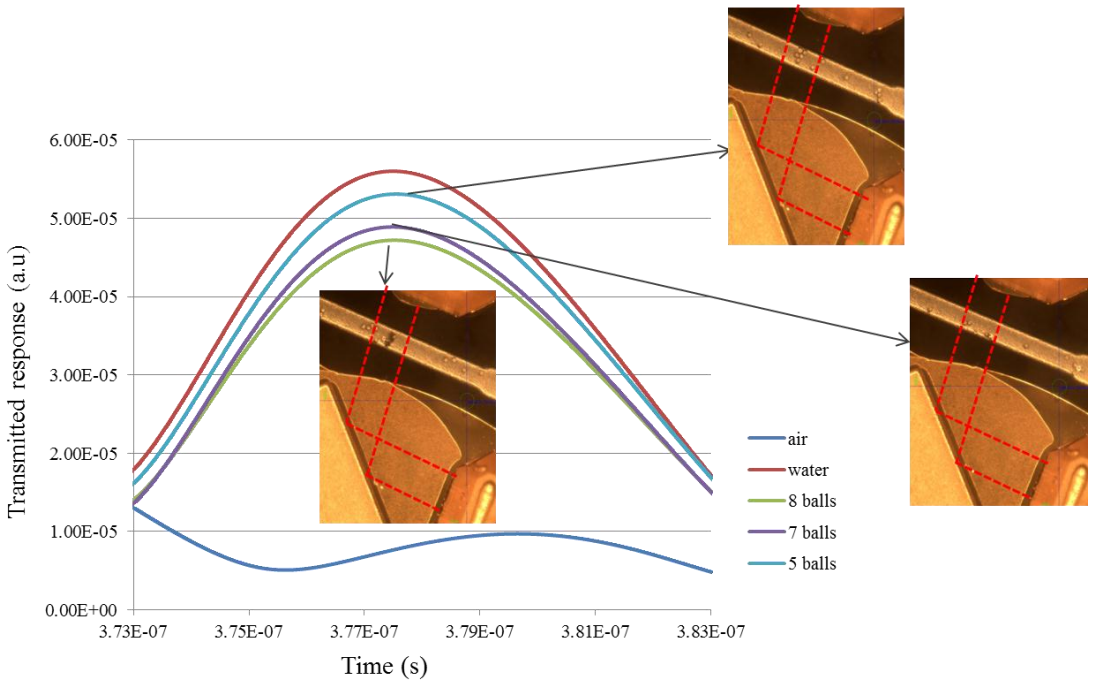

Figure 3.3.7 Acoustic characterization of particles in 1 vertical mirror system. Different numbers of particles stay in the detection region (red dash lines indicate the acoustic beam propagation) and presented increasing values of attenuation with the number of balls.

When PS latex particles are driven near the detection region, we decrease slowly the driven pressure to limit the particle velocity. Finally particles stop and stay in front of the 45˚ mirrors thus the numbers of particles in the detection region. Then the numbers of particles affected in acoustic field are counted. The detection region is evaluated in consideration of the geometry of transducers and matched 45˚ mirrors, so the lateral displacement of the 45˚ mirrors along the length and width cannot be ignored. As shown in figure 3.3.7, 5 balls, 7 balls and 8 balls are characterized respectively in the region. The transmitted S_{21} response reflected the total attenuation for acoustic beam transmitted through the channel. For elastic particles, the attenuation is prominently smaller than water. Thus the S_{21} amplitude for water is

always the highest. In another point of view, more balls introduce more diffraction and scattering of the propagated acoustic waves and the attenuation grows strongly. In our curves, the amplitude goes lower with the numbers of balls increasing. It can be deduced that the amplitude difference between 7 balls and 5 balls is 4.1×10^{-6}v, while the difference between 7 balls and 8 balls is 0.4×10^{-6}v.

3.4 Acoustic lens integration

3.4.1 Lens design and characterization

For higher resolution of acoustic detection and manipulation, a confocal system must be integrated in the system to focus the parallel acoustic beam into a small area for the purpose of higher spatial resolution and sensitivity. Compared to the transmission through parallel channel wall, the confocal lens system can gather more acoustic energy diffracted by the encountered obstacles, besides, the cylindrical wall can focus the acoustic energy to a focal plane to create very strong acoustic streaming around which can be used for particle mixing and manipulation. A confocal system with two cylindrical walls was used for particle characterization. Meanwhile, an acoustic lens using only one cylindrical lens and a vertical reflected wall has also been studied as shown in figure 3.4.1.

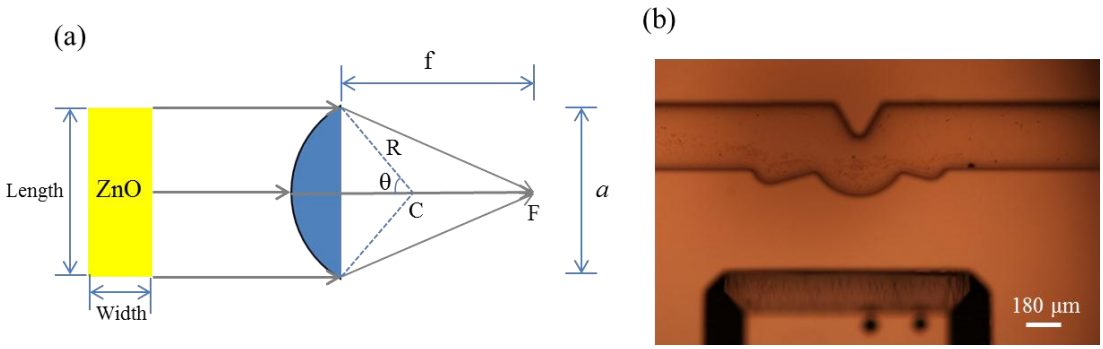

Figure 3.4.1 Scheme of the acoustic wave transmission through an acoustic lens. (a) structure chart of the cylindrical lens, (b) photo of the 45° mirror-lens system. The width of reflection wall is 30μm. R is the radius of lens, θ is the angle of aperture, a is the aperture, C is the center of the curvature and F is the focus. The length of transducer is the same with the aperture. .

The paraxial acoustic focal length of the lens, as in the case of optical lens, the paraxial acoustic focal distance is given by

$f = \frac{n}{n-1}R$, where $n = \frac{v_{si}}{v_w}$ =5.7

where f is the focus length measured from the top of the lens, n is the relative acoustic index, v_{si} is the acoustic velocity in silicon and v_w is in water.

Making use of the geometry relationship, the aperture width can be deduced from a=2Rsinθ. The length of the transducer is equal to the aperture so that the whole generated acoustic beam can be focused by the lens, as well as to limit the

transmission losses. The length of the transducer is linked to the aperture of the lens while the width of the transducer is linked to the depth of the microchannel.
In our design, the width of transducer is fixed to be 120 μm and the area S=55080 μm^2 has been chosen in order that the a real part of electrical impedance of the transducer is close to 50 Ohms for a ZnO film at the resonance frequency f_r=650 MHz. Using the formula $(f_r) = \frac{A}{Sf_r^2} - j\frac{1}{c_0}\frac{1}{2\pi f_r}$, where C_0 is the static capacitance of the transducer, we can calculate the real part impedance of transducer R(Ω) for different lens, as shown in table 3.4.1.

Lens radius R (μm)	80	100	120	150
angle of curvature θ (˚)	60	60	60	60
focal length F (μm)	97	121	146	182
aperture A (μm)	139	173	208	260
Transducer area (μm^2)	16560	20760	24960	31200
real part impedance (Ω)	165.5	132.5	110.3	88

Table 3.4.1 Geometrical parameters of the cylindrical lenses and corresponding real part of the impedance of the ZnO film transducer.

In the case of the focalization of acoustic beam, the amplitude distribution in the focal plane can be modified with respect to the paraxial focal length. It can be explained by different phenomena:
1. after reflection and refraction, the shape of the initial wavefront can be modified;
2. the transmission coefficient between solid and liquid is a function of the incidence angle;
3. the absorption of the propagating medium induce an weighting function of the wavefront
To determine the experimental focal distance of the acoustic lens, we design a channel with the same lens geometry on one side of the channel and three different distances of a small reflector on the other side, around the expected paraxial focal length.
The maximal channel width is designed from the top of the lens to the reflection wall. The radius of lens is 150 μm with an angle of aperture of 60˚. Thus the predicted focal length is 182 μm. KI 3 mol/L solution was injected in the channel in order to characterize the S_{11} reflection coefficient.
As shown in figure 3.4.2, for the *d* (distance between the reflector and the bottom of lens) is 182 μm, it corresponds to maximal amplitude of 2.92×10^{-4}v, which is in agreement with the predicted value. For the minimum d=182 μm, the amplitude is lower at 2.80×10^{-4}v.
When the reflector distance is decreased of 2μm from the paraxial predicted focal length, the amplitude value is at the smallest 2.68×10^{-4}v. The estimated value of the depth of focus is around ±5 μm which is in agreement with the experiment result.

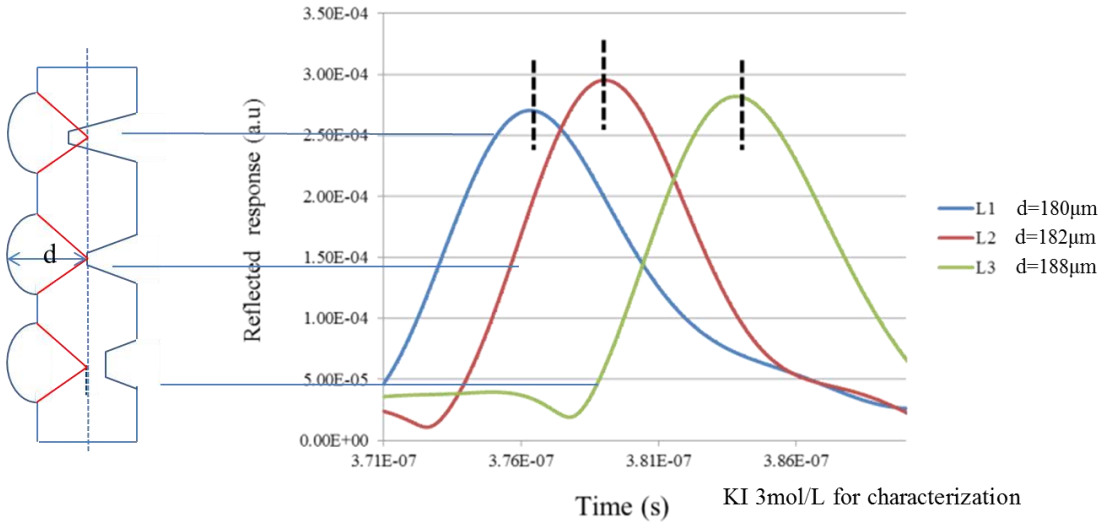

Figure 3.4.2 S_{11} reflection coefficient parameters for KI solution in lens of different focal lengths. L1: d=180μm, time echo is376 ns; L2: d=182 μm, time echo is 379 ns; L3: d=188 μm, time echo is 384 ns. d: distance between the reflector and the bottom of lens.

3.4.2 Particles detection using acoustic lens

We have characterized the detection sensitivity of the previous lens system (radius 150 μm, focal length 182 μm) using 30 μm PS particles which were injected into the microchannel and driven to the focal area of the lens by microfluidic pump.

In our case, when particle moves in the channel and stops in the lens area, they are forced to the focal plane. In the lens structure, the acoustic force overcomes the viscous force in the fluid and pushes particle toward the sidewall. This situation will be analyzed in the subsequent section. As shown in figure 3.4.3, the numbers of balls which are pushed to the sidewall of the lens are counted and S_{11} reflection coefficient is measured. Water led to maximum amplitude of 1.18×10^{-4}v in the lens which shows larger attenuation with particle balls. The S_{11} reflection coefficient for 1 ball of PS particles is 9.88×10^{-5}v with a 16.3% deviation from water. The S_{11} reflection coefficient for 2 balls of PS particles is 8.69×10^{-5}v with a 26.3% deviation from water. For 3 balls the signal can also be recognized with amplitude of 7.80×10^{-5}v, with a deviation of 33.8%. The deviation accuracy (around 10%) showed the ability for our lens system to discriminate single particle in fluid.

Compared to the previous 1 GHz detection in a 50 μm channel width (J. Gao's work), our system avoid particles block even for limited concentration. In the figure 3.4.3 it is found that for numerous balls (several balls around 10 balls) detection, the amplitude is too low to be discriminated from level of acoustic noise. Here the local detection region is blocked by elastic balls and mainly a diffusion process occurs which the acoustic waves are spread when absorbed by particles.

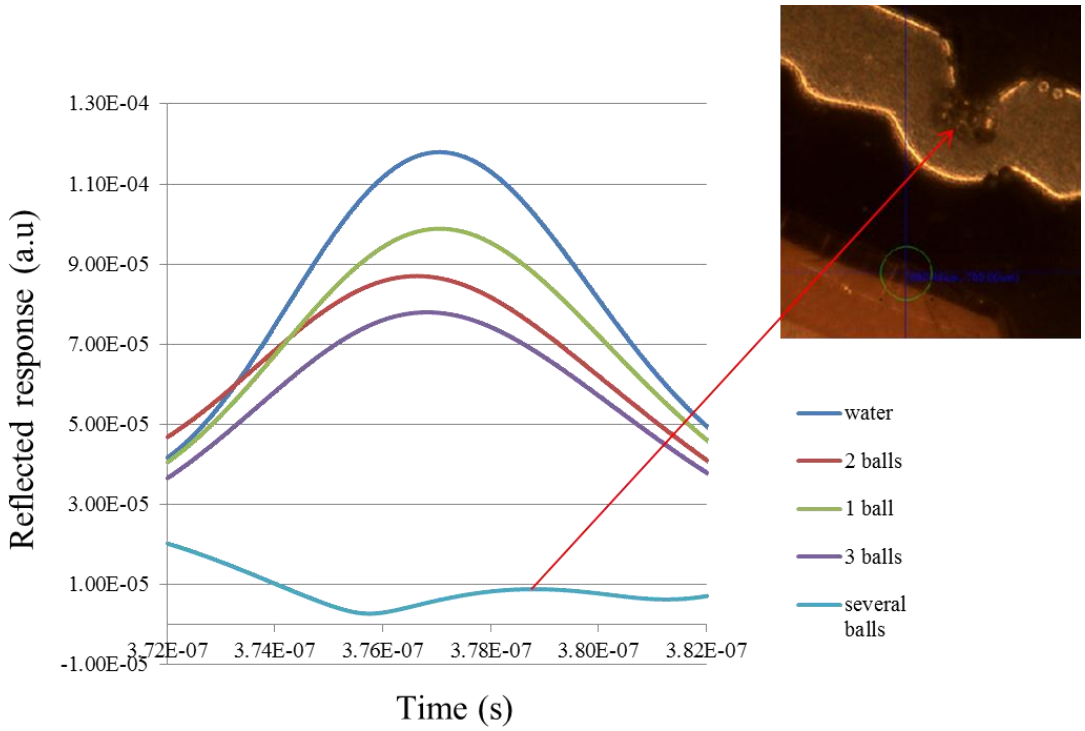

Figure 3.4.3 S_{11} parameters for 30 µm PS particles characterization in lens.

In this lens structure detection, the amplitude difference between water and 1 ball is 89.2 µv. For one vertical mirror system, the amplitude difference between water and 5 balls is 2.9 µv, as indicated in figure 3.3.7. In this comparison, we can conclude that the sensitivity using focused beams in reflection mode is higher than using one vertical mirror system which flat channel walls in the transmission mode.

3.5 On-chip temperature measurement using acoustic wave

The control of the physical experimental conditions is extremely important as well as from the point of view of biological needs than from that of ultrasound effects or measurements interpretation.

Temperature has a strong influence in the cell activity, such as cell proliferation, morphological change and activity recovery. As the liquid viscosity, diffusion and even buffer pH are related to temperature, cell sorting and isolation may also induce a change in temperature. Besides, the possibility to perform chemicals/biological experiments within microfluidic environments is critically dependent on rapid and precise thermal transfer [10]. For example, a single cell performs thousands of biochemical reactions per second which are all directly dependent on temperature. High efficiency polymerase chain reaction (PCR) requires temperature control in precision of 0.1 ˚C [10]. Furthermore, in the electrophoresis experiments, the generated Joule heating influences the temperature gradient around the zone of action, so the spatially resolved temperature analysis is necessary for a high separation performance [11].

For the biological and medical characterization in the microfluidics, the extrinsic

temperature of a device can differ dissimilarly from the internal temperature within the fluid. The on-chip temperature monitor is becoming a key area of interest in the emerging microfluidic platforms dedicated to cell biology research field. However, analysis of the temperature of cellular microenvironment in lab-on-a-chip field remains an issue to be addressed. In the microscale, the traditional thermocouple is hardly integrated into the microchannel, and laminar flow makes thermal exchange less easy, thus the local temperature detection in the zone of action for bio-samples is of great importance. Here we introduce some representative methods for on-chip temperature detection with high-precision.

3.5.1 Methods for on-chip temperature monitoring

- Temperature sensor

A thermocouple is a temperature-measuring device with principle based on the Seebeck Effect. As shown in figure 3.5.1, it is comprised of two conductors that contact each other at one or more spots. Once the different conductors experienced a temperature differential, then the contact points undergo temperature variation from the reference temperature, which results an electrical current generated in the circuit. The wide range of temperature measurements for thermocouple sensors makes it widely used in temperature control. Considering the dimensions of the thermocouple probe (> 100 μm), the main limitations of operational performance for thermocouples are accuracy and resolution ratio of space distribution. It is difficult to obtain system errors of less than one degree Celsius (°C).

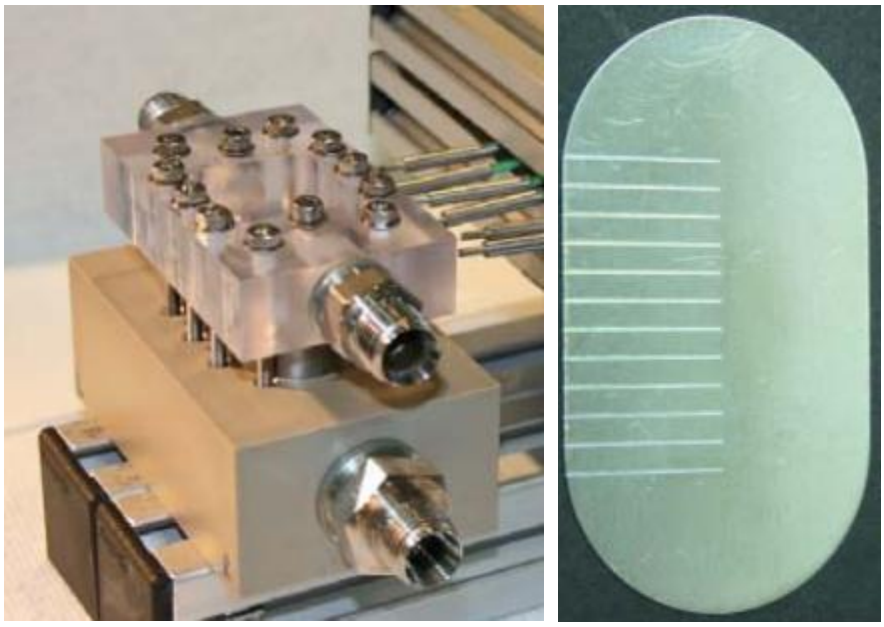

Figure 3.5.1 Assembled experimental micro heat exchanger for fouling investigation. The heat transfer foil with 12 micro slots for thermocouples [12].

- Temperature-dependent fluorescent dye – TFD

Rhodamine B is a kind of temperature sensitive fluorescent reagent whose fluorescent

intensity is strongly temperature dependent. After added Rhodamine B into the working fluid, the in situ temperature field can be determined by monitoring the fluorescent intensity using microscopy [13]. David et al. takes advantage of the temperature dependence of this diluted dye to measure temperatures in microfluidic channels. They compared the fluorescence intensity of images at uniform room temperature before the trial calibrations, later the corresponding temperatures of unknown can be deduced [14]. Thanks to the fluorescent agent which was added to the sample fluid at the beginning, the temperature distribution can be obtained through the record of the distribution of the fluorescence intensity. The fluorescence intensity is imaged using a standard fluorescence microscope and a CCD camera, thus the spatial resolution is determined by the microscope optics (~1μm) as well as the temporal resolution is determined by the rate of captured video frames (dozens of milliseconds).

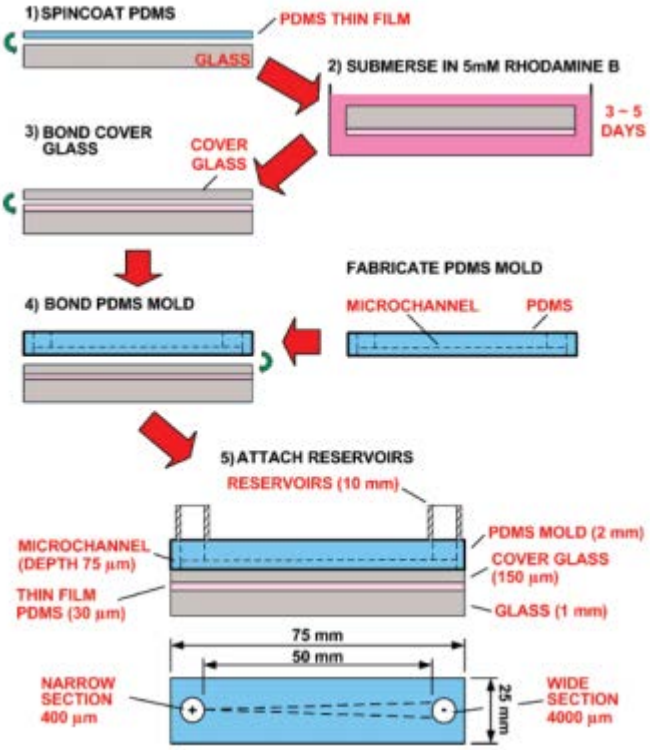

Figure 3.5.2 Schematic of the fabrication process for the Rhodamine B embedded into thin film PDMS and the microchannel.

For the neutral hydrophobic fluorescent dyes used in polymer based microfluidic chips, the compatibility issue should not be ignored. As an example, Rhodamine B will adsorb and diffuse into the PDMS layer which is commonly used in electrophoresis experiments. When dye particles gather at solid-liquid interface, it will introduce intensity peaks in the detectable fluorescent intensity graph and disturb the temperature detection. To solve this problem, Razim et al. embedded Rhodamine B dye particles within PDMS film in the measurements of temperature distributions in PDMS microchannels [15]. As shown in figure 3.5.2, a thin glass substrate was

inserted between the PDMS thin film mixed with dye particles and PDMS mold with microchannel, then Rhodamine B is successfully separated from the fluid and PDMS channels in the measurements. This method prevented dye diffusion and reduced the false intensity reading.

The sensitivity of fluorescence intensity-based techniques to conduct quantitative measurement of on-chip temperature is largely determined of the length of optical path, scattering of light source, variation of the dye concentration. In other words, the toxicity of fluorescent dye probe could hinder the applications in biocompatibility and target-labeling.

- Thermochromic liquid crystals (TLCs)

Thermochromic liquid crystals (TLCs) are temperature-sensitive liquid crystals that manifest properties of both liquids and solids, and the deciding factor of transition between the two phases is heat. This kind of material would reflect direct color at a specific temperature when the ambient temperature varies. As the temperature increases, the TLCs color could change from colourless (black against a black background) to red, yellow, green, blue and violet finally, according to the visible spectrum in sequence. It is a reversible process with a 10 ms time response when removed the heat source.

- Other methods

Both the thermochromic liquid crystal method and temperature-dependent fluorescent dye method will introduce additional material within the microfluidic channel, which may influence the viability of the biological specimen in the characterization. Therefore, a growing number of spectroscopic methods, including nuclear magnetic resonance (NMR) [16] and Raman spectroscopy [17], have been used for the non-contact and non-invasive measurement of temperature.

Nuclear magnetic resonance thermometry is an expedient method implemented to measure buffer temperatures in microfluidic chips, since the ^{1}H NMR signal frequency of water shows a strong linear dependence on temperature [18]. This measurement can be made fairly rapidly without requirement of the addition of probes to the buffer. A disadvantage of this technique is the limited spatial resolution. As the NMR thermometry uses a section of capillary surrounded by a radio frequency probe coil, the typically dimension of 1 mm coil restricts the spatial precision in the measurements.

Similar to NMR thermometry, the Raman spectroscopy based technique, which monitors the temperature dependence based on the O-H stretch equilibrium in water, is also applied to any aqueous buffer. It offers high spatial resolution (1-5 μm), but only for one point at a time with a slow acquisition rate of 2 s/point [19].

For the purpose of accurately validating the cell behavior in the response of temperature variation, a localized and non-invasive method of high sensitivity is compulsory for medical and biological application, such as *in situ* cell culture and reaction control. The acoustic means show promise as a non-contact mode for temperature characterization in local area. In high frequency domain, the short

wavelength helps to confine the detection area in the cell size.

3.5.2 Temperature characterization in the channel

Numerous experiments were studied for the temperature dependence of the velocity of acoustic propagation in water. Willard proposed a simple model of the sound speed in water:

$c = 1557 – 0.0245(T-74)^2$

where c is the sound speed in meters per second and T is in degrees Celsius over the range of 25 to 85 ˚C [20]. It is worthwhile to note that only water shows a parabolic temperature dependence, and the other single component liquids or salts-water mixers present a linear temperature dependence in this range.

Pinkerton et al. measured the absorption of ultrasonic waves at 15 MHz in water as a function of temperature [21]. The absorption decreased with increasing temperature by a factor of 8 between freezing and boiling points. Besides, the absorption coefficient varied as the square of the frequency over a wide range of temperatures.

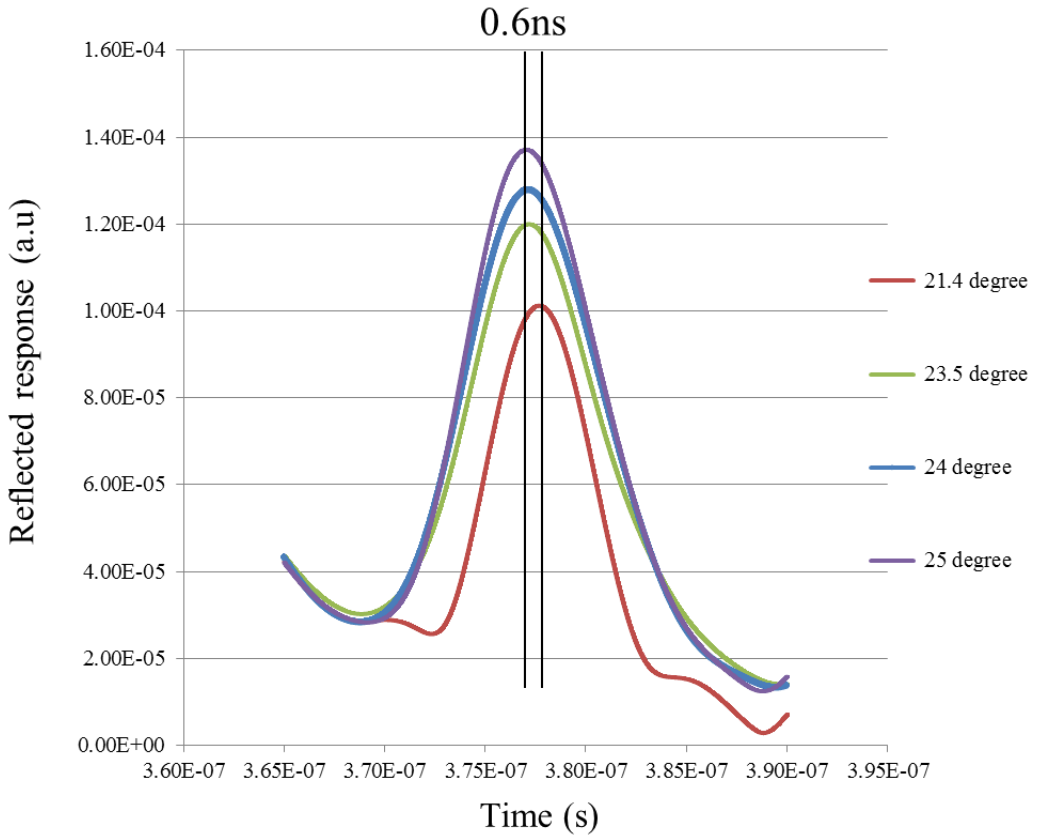

Figure 3.5.3 Measurements of temperature characterization in lens in time domain with a bandwidth from 300 MHz to 700 MHz. The maximum time delay of flight is 0.6 ns. Time value is read from the thermocouple contacted of the PDMS surface.

Using the lens structure (L2: channel width 182 µm), we try to detect local temperature in water within microchannel around 500 MHz central frequency. Thanks to the light source of the microscope, the water in channel can be slowly heated and

the local temperature is elevated for an interval of several minutes.
As a reference comparison to acoustic monitoring, a classical thermal sensor is used in contact with the PDMS right above the lens to measure the temperature inside the microfluidic chip. When the temperature increases, S_{11} reflection coefficients are measured by VNA in order to record the amplitude of the reflected acoustic wave crossing the channel. Results are shown in figure 3.5.3 where four temperatures are discriminated from 21.4˚C to 25 ˚C, as results displayed in the thermal sensor.
It was observed that the higher the temperature, the shorter the time display of the echo and the higher of the amplitude. The temperature affects the viscosity of the liquid and velocity of acoustic velocity, which determines the attenuation of sound in liquid. Meanwhile, the rise of temperature will reduce the liquid viscosity, thus the sound attenuation will be lower.
In this system integrating a lens and working at a central frequency of 500 MHz, we have observed a variation of the time delay of the echo of interest due to temperature variation. However, this is not the most interesting structure to study temperature variation. When the speed changes at different temperatures, the focal length of the lens will also be modified. Nevertheless, the high resolution of lens structure shows the sensitivity to temperature variation. As we work in a high frequency domain, the attenuation variation (law proportional to $1/f^2$) will be strong even if the dimensions of the channel are small.
Besides, the actual temperature within the channel may be very different from outside, due to different heat exchange within the microchips. Thermal conductivity of PDMS, silicon and liquids are very different. Thus the temperature measured by the thermocouple contacted with the PDMS will be less than the temperature of water within the lens. A more accurate calculated way is required to determine the on-chip temperature for the reference of our acoustic method.
For further investigation, it will be more interesting to work in a system having parallel walls (no lens) to study attenuation and speed variation due to the temperature. If we consider speed and attenuation variation of the ultrasonic waves depending on the temperature, the strongest effects appear in a range from 10 to 50 °C which is interesting for biological applications so as to obtain a good sensitivity.

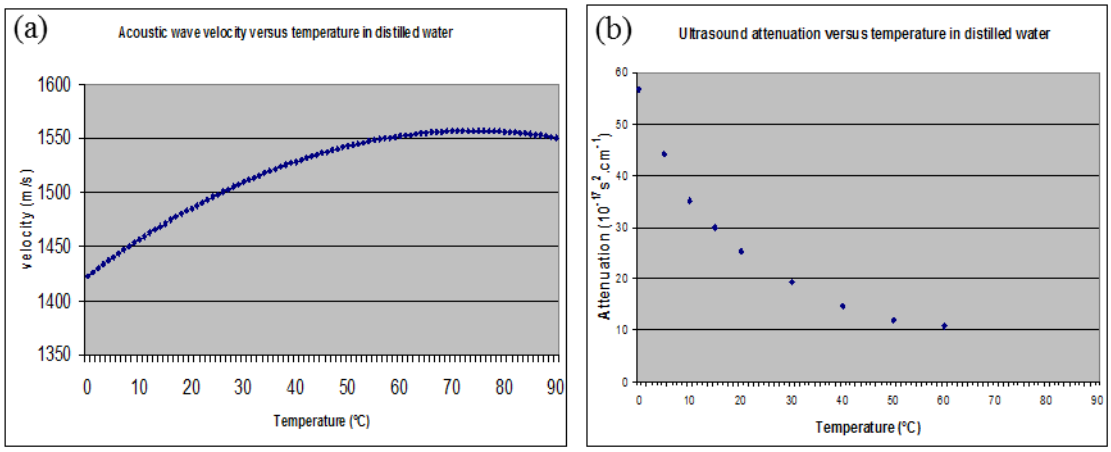

Figure 3.5.4 (a) Velocity-temperature curve for water from 0 ˚C to 90 ˚C [20]. (b) The acoustic absorption α/v^2 for water as a function of frequency and temperature [21].

To obtain the actual acoustic velocity in the microchannel, we take full advantage of the model of acoustic velocity in water *via* temperature proposed by Willard and the absorption versus temperature, as shown in figure 3.5.4. The acoustic velocity can be deduced from S parameters measurements, and the absorption in water can be deduced from the S_{21} amplitude. As the acoustic velocity in silicon has very small variation in different temperature, we consider that the variations of time delay of the echo in S parameters measurements are only induced by the change of acoustic velocity in water.

As shown in figure 3.5.5, the acoustic propagation through the microchannel can be divided into three parts:

1. from transducers, reflected by the 45° mirror, and then propagates toward the vertical sidewall of the channel. The propagation time is named as t_{11};
2. acoustic propagation in the channel full of water, the used time is named as t_c;
3. acoustic wave propagates from the other sidewall of the channel to the 45° mirror, then to the received transducer, the propagation time is named as t_{22}.

When the temperature changes, the delay of acoustic wave in silicon wafer does not change, but after crossing the channel full of water the time delay varies due to the high sensitivity of speed *versus* temperature. Through measuring the reflected responses S_{11} and S_{22}, t_{11} and t_{22} can be acquired from the time delay of the echo (divided by two). After measuring the time delay of the S_{21} transmitted response in each temperature measurement, the delay for acoustic transmission in water can be extracted by $t_c = t_{21} - (t_{11} + t_{22})/2$. Then the acoustic velocity $v = W_c/t_c$

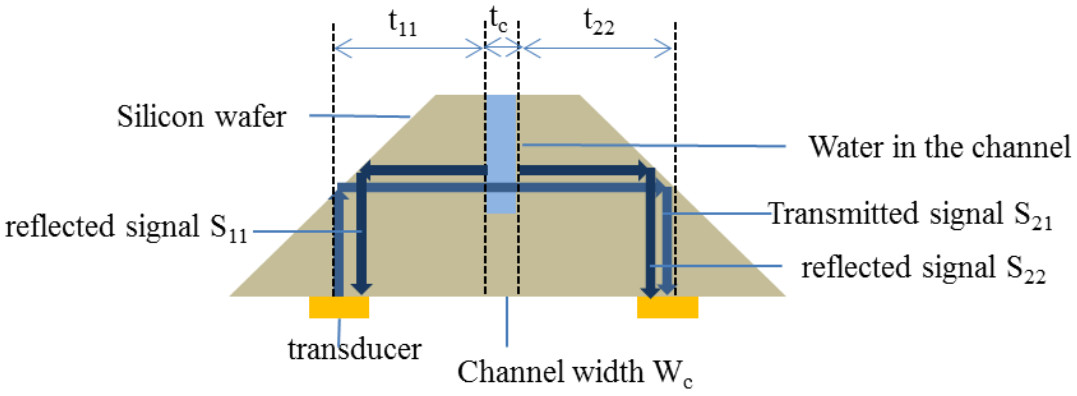

Figure 3.5.5 time interval in the acoustic propagation. t_{11}: time for acoustic wave from the generator to the microchannel, t_c: time for acoustic transmission in the water with the channel, t_{22}: time for acoustic wave from the channel wall to the receiver. W_c is the channel width.

In this method, the evaluation of the microchannel width is particularly important. Even an error of the channel width of 1 μm variation can lead an error of several degrees Celsius in the estimation. All the MEMs technology steps such as lithography, etching and so on, lead to a variation of the actual geometry of the channel. Herein, we use acoustic method to calculate the precise channel width W_c after the fabrication.

At the beginning, we measure the acoustic propagation time t_{11} and t_{22} with the empty microchannel, these delays are constant even after water introduction. Then we inject water into the microchannel and measure the transmitted signal response S_{21} immediately. The water stabilized temperature is the same than the room temperature which can be read from the thermocouple. Then the time delay of the echo through the S_{21} measurements corresponds to the acoustic velocity v_0 in the room temperature t_0, and channel width can be deduced as $W_c = v_0 t_c$.
As shown in table 3.5.1, we characterize two channels and calculate the effective channel width. The percentage error of the width expectation is less than 5%. This error can be accepted in the fabrication but will bring about large error in our temperature characterization.

channel	t_{11} (ns)	t_{22} (ns)	channel width expectation (μm)	channel width calculation (μm)	percentage error
1	72.74	75.98	200	208.4	4.20%
2	69.58	72.85	250	259.8	3.92%

Table 3.5.1 channel width calculation in the case of two channels. The injected water temperature is 20.6 ˚C read from the thermocouple.

We characterize the water temperature in the channel with parallels walls and a channel width of 208.4 μm. After the water is injected into the channel, light source is used to heat the liquid in the chip. As shown in figure 3.5.6, the time delay of echo is extracted from the peak of the S_{21} response. In the process of the water heating, we measure successively the S_{21} response 7 times in agreement to the curve 1, 2 … 7.
From curve 1 to curve 5, the time delay decreases and the S_{21} amplitude increases. As the temperature in water increase (less than 74 ˚C), the acoustic velocity also increases but the attenuation decreases.

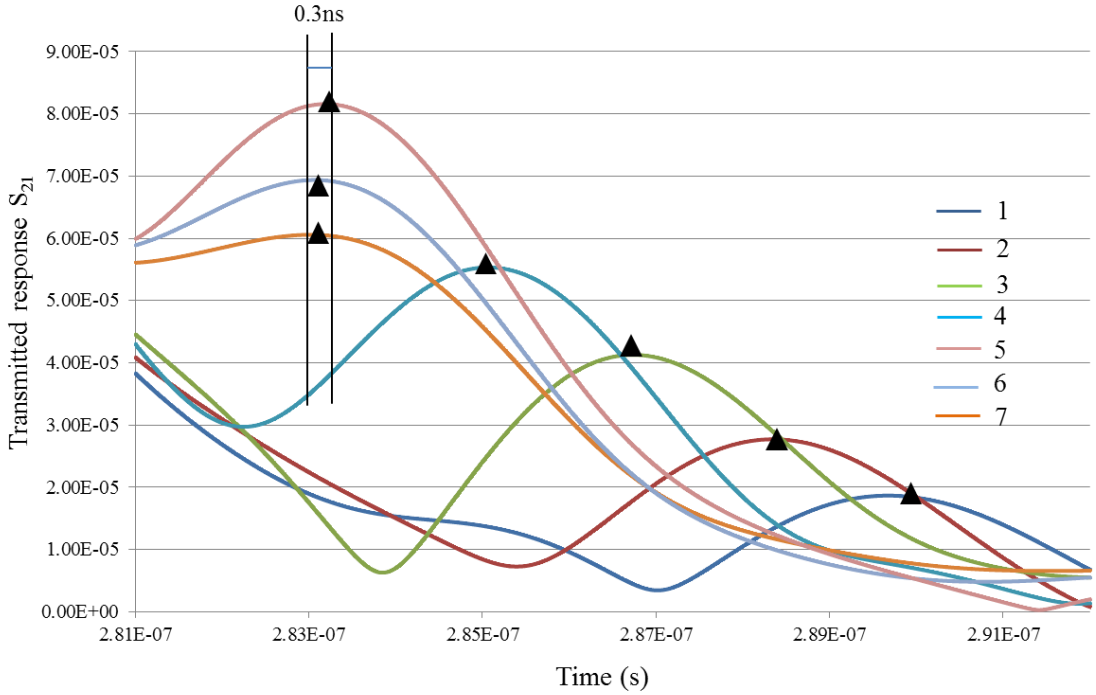

Figure 3.5.6 Transmitted response measurements in water in 7 curves. The working frequency ranges from 300 MHz to 1300 MHz.

In the case of curves 5, 6 and 7, the time delay decreases while the amplitude increases. The main error comes from the resolution in the measurement. As shown in table 3.5.2, the time delay between curve 5 and curve 7 is 0.3 ns. However, the measurement bandwidth is 1 GHz, which gives around 1 ns resolution in time domain according to the Inversed Fourier Transform. Besides, the amplitudes of the acoustic noise increases, which lead to an error on the amplitude of the transmitted signal. The acoustic noises come from the diffraction of the generated acoustic beam and multiple reflections in the propagation. Especially, when the amplitude of noise is comparable to the useful signals, the S_{21} amplitude is largely modified in the calculation

The sensitivity in the temperature estimation is linked to the variation of the velocity of acoustic wave versus the temperature. A consequence is that the resolution of temperature measurements is determined by the time domain resolution.

The results show a time delay variation of less than 0.3 ns. On the other side, even if the measured value of the temperature is not the actual value inside the channel, the different acoustic measurements indicate the precise temperature variation. This leads to the conclusion that the sensitivity of the acoustic measurement of the temperature variation is 0.1 ˚C. For the improvement of the characterization resolution, we have to optimize the chip geometry and fabrication to reduce acoustic noise.

Curve	Time t_{21} (ns)	$S_{21}(10^{-5}v)$	calculated velocity (m/s)	temperature (˚C)
1	289.6	1.8	1478.5	17.4
2	288.3	2.7	1492.6	22.7
3	286.7	4.1	1510.0	30.2
4	285.0	5.5	1528.5	39.9
5	283.2	8.1	1549.7	56.8
6	283.1	6.9	1551.3	58.7
7	283.02	6.1	1551.74	59.3

Table 3.5.2 Table of the measured velocity variation as a function of temperature deduced from curves of figure3.5.6.

3.6 Acoustic manipulation in microfluidic channels

3.6.1 Force analysis of particles in acoustic field

When particles are provided in an ultrasonic field in fluids, the interactions can be linked to several linear interaction forces including added mass, drag, lift, and Basset forces while nonlinear ones include radiation pressure forces and drag forces due to acoustic streaming. We consider ultrasound in a liquid induces several consequences:
-oscillation of particles suspended at the ultrasound frequency which generates acceleration
-acoustic streaming of the fluid
-radiation pressure force at the interfaces
In the following part, our goal is to calculate some order of magnitude of the different forces.

The added mass force F_{ma} in fluid mechanics is the inertia added of particles to the surround [22]. For a spherical particle, this force F_{am} is parallel to the direction of the acceleration, and the magnitude of added mass force is linear with the frequency, as described by $F_{ma} \% \rho R^3 v$,

Where F is the acoustic wave frequency
ρ is the density of the fluid
R is the radius of the particle
v is the instantaneous fluid particle velocity

v can be deduced from the acoustic wave intensity I by $v = [I / Z_{ac}]^{1/2}$
where Z_{ac} is the mechanical impedance of the fluid and can be written as $Z_{ac} = \rho C$
where C is the phase velocity of the acoustic wave in the fluid.

The lift force F_p: for a particle in an inviscid flow of a non-conducting fluid, the pressure difference between the bottom and top will generate a lift force to move the particle. The lift force can be estimate from the Bernoulli‟s equation $F_p \% \rho (R v)^2$

The drag force F_{ts}: F_{ts} depends on the regime of the flow Reynolds number $R_e = \rho R$

v/η, where η (Pa.s) is the dynamic viscosity of the fluid.
When Re<< 1, Stokes drag force can be expressed by: F_{ts} %Rνη; when Re>> 1, the drag force is of the order F_t % ρ(R v)^2 . The viscosity of the liquid, the diameter of the particle and the velocity will determine the different Reynolds numbers.
Basset force: F_B modifies the mass added force and has only to be considered if the particle radius is comparable to the boundary layer thickness δ, if the particle is close to the walls of the channel. We have not to consider this force if the particle is considered in the middle of the channel.
Radiation Pressure: The plane wave induced radiation pressure force on an isolated solid particle in an ideal fluid was deduced by King [23]. The radiation pressure force F_{PR} induced by a plane acoustic wave can be written as:

- F_{PR} % 64ρ. (2πf /C)^4 R^6 v^2 [1+2(1-k^2)/9]/(2+k)^2 if R<< λ

where k=(ρ/ρ$_p$), ρ$_p$ is the density of the particle and λ is the acoustic wavelength.
or

- F_{PR} %ρ. (v C/2πf)^2 (95-48k+36k^2)/89/(5+6k+2k^2) if R~λ

Acoustic streaming: The acoustic streaming motion causes a drag force for particles near a solid surface. Eckart streaming is mainly fluid absorption dependent. Let us consider a plane acoustic wave (characterized by ω the angular frequency, C the phase velocity in the liquid and the intensity I) which propagates in a fluid characterized by

- a volume viscosity ζ (2.3 mPa.s at 23°C) ζ =η‟‟+(2/3). η

where η‟‟ is the second viscosity (3.09mPa.s for water at 15°C)

- a dynamic viscosity η
- a density ρ

The absorption α (m^{-1}) is mainly linked to the viscous dissipation (100 times higher than the thermal dissipation in water):

=α^2 (4η/3 +ζ)/ (2ρC^3)

When the acoustic wave propagates, the acoustic wave release momentum to the fluid, which induce a volume force distributed in the fluid.
This volume force f_{st} can be expressed as:

- f_{st} = 2αI/C

For a focused acoustic wave (w focal spot radius, focal depth p) , W.L.Nyborg calculates the streaming fluid velocity V_{st} (component on lens axis) as:

- .V_{st} = (ω^2 /ρC^4).(1/3 +ζ/4η).I.w^2 .Ln {[(4w^2+p^2)$^{1/2}$ +p]/ [(4w^2+p^2)$^{1/2}$ -p]}

(For fluids characterized by a shear viscosity η higher than 3mPa.s, the volume viscosity ζ is around ζ =10η)
In the case of water as the propagating medium, for an acoustic frequency 1GHz and a focusing lens characterized by a 150 µm radius of curvature and an angular aperture of ±60° and we can estimate w at 1.5 µm and p at 3 µm.
V_{st} =7.22 10^{-9} .I m/s
In our case we will assume that the electrical power applied to the transducer is 1W and the losses from the transducer to the focal plane are 40 dB.

We can deduce that the acoustic power in the focal plane will be at the level of -10dBm. (0.1mW), which led to an acoustic intensity 0.14×10^{8} W/m^2 and a value of the acoustic pressure in the focal plane of the order of 5MPa in water.
Then $V_{st} = 7.22\ 10^{-9} \times 0.14 \times10^{8}$ m/s
And $V_{st} = 0.1$ m/s
We can deduce the Reynolds number due the Eckart streaming: $Re = (\rho V_{st}\ w)/\eta=0.15$
We can then consider that the flow can be described by the Stokes drag force formula:

$F_{St}=\eta R\ V_{st}$

We can deduce the drag force due to the streaming on a particle 10µm in diameter:
$F_{St}= 10^{-9}$ N

	frequency: 1 GHz			
	Added mass (N)	Lift (N)	Drag(N)	Radiation Pressure (N)
Particle Radius	F_{ma}	F_p	F_d	F_{pr}
10µm	6×10^{-4}	10^{-9}	10^{-9}	5×10^{-15}
1µm	6×10^{-7}	10^{-11}	10^{-10}	$\sim5\times10^{-15}$
0.1µm	6×10^{-10}	10^{-13}	10^{-11}	2.3×10^{-14}

Table 3.6.1 Comparison of the different forces on a particle at 1 GHz

As shown in table 3.6.1, around 1 GHz frequency, the added mass force plays a dominant role in the particles manipulation than other forces. As the added mass force is linear to the volume of particles, larger particles experience forces greater than smaller particles. In another aspect, the acoustic streaming phenomenon in the liquid due to the absorption of acoustic energy has very strong affection on particle movements, but these forces are independent of particle size. Under the combined actions of added mass force and acoustic streaming, we can mix, deflect, capture and separation particles. The geometry of the channel and the lens position will be used to modify the manipulation function.

3.6.2 Manipulate particles in microchannels

A travelling wave generated by one ZnO transducer was used to deflect particles in channel in a continuous flow. As shown in figure 3.6.1, several 9 µm PS particles moved along the injected flow in the upper side of the channel at the beginning. When it reached the acoustic field, the radiation force started to force the particle to the downside of the channel. Then a curved trajectory of the particle can be seen and it is reaching the downside of the channel in 1 second.
At the next moment, the particle kept moving to the outlet under the fluid force, but along the downside wall of the channel due to the vertical acoustic radiation force. As a result, particles switching can be achieved if a bifurcation outlet is integrated in the

channel. Targeted particles can be collected in one outlet *via* acoustic excitation, and unwanted particles can be driven to the other outlet by hydrodynamic force.

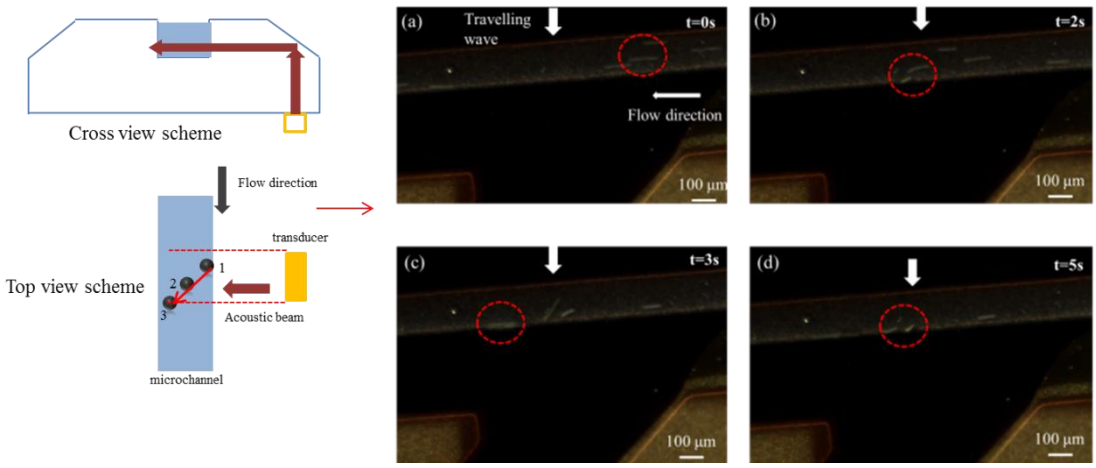

Figure 3.6.1 particle switch using one travelling wave. (a) t=0s, particle move along the flow in the middle of the channel, (b) t=2s, particle started to move perpendicularly to the channel in acoustic field, (c) t=3s, particle was driven to the down side of the channel by acoustic force, (d) t=5s, particle move along the flow in the down side of the channel. Input power is 5 dBm, flow rate is 0.5 μL/min. Particle was inside the dash circle.

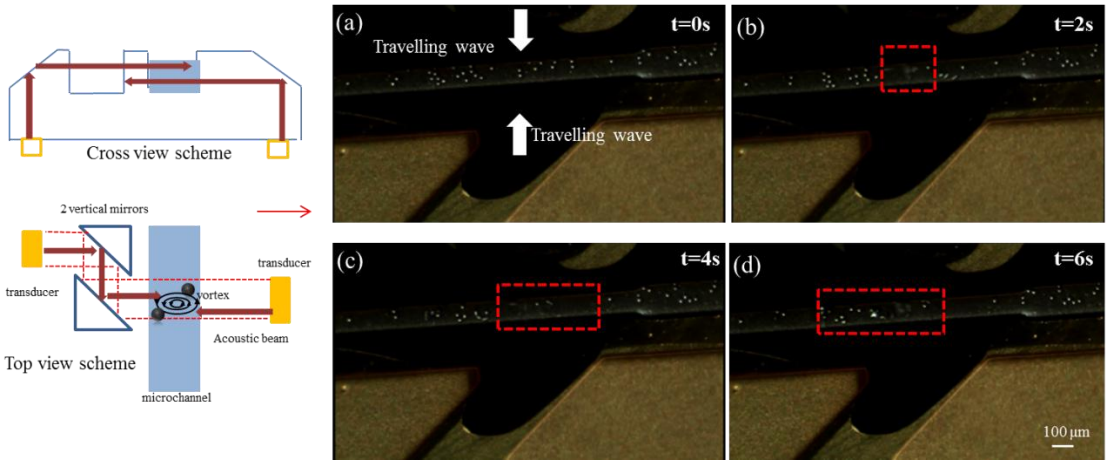

Figure 3.6.2 Vortex induced by two travelling wave of 5dBm input power. Particles are 9 μm in diameter. Strong acoustic streaming happened in dash box.

Two opposite travelling wave were applied in the channel for 9 μm particles manipulation. One wave was directly sent into the channel and the other wave was applied on the other wall after being reflected by two vertical mirrors. Hence the center of each acoustic beam was not in the same position. As shown in figure 3.6.2, particles were suspended in the channel statically at the beginning of experiment.

After the acoustic excitation is applied in opposite direction, a forceful vortex is formed within the channel due to the strong streaming, and particles follow the streamlines to rotate rapidly. A streaming flow perpendicular to the plane surface was also generated because of compressibility of the medium. The asymmetric travelling waves induced strong acoustic streaming which dominated the added mass force and drag forces in liquid. Particles in the center of the acoustic streaming field rotated in a high speed, while those particles away from the center area moved slowly, but still followed the streamline. As time went by, all the particles in the acoustic pressure field were driven along the streamline. This phenomenon can be used for fast mixing of laminar flow in microfluidic channel.

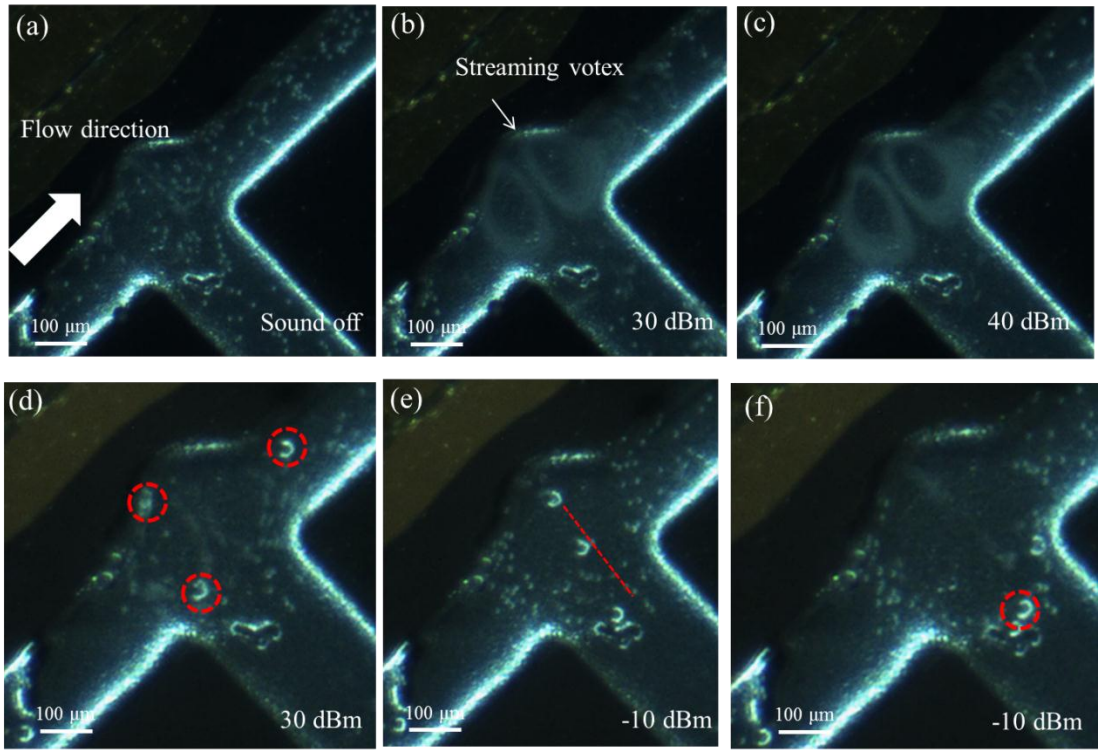

Figure 3.6.3 Acoustic focusing in lens (Radius 150 μm and focus length 364 μm) for strong mixing of 9 μm particles (a-c) and separation of 30 μm particles into another branch (d-f) in dynamic flow. Red dash lines indicate 30 μm particles movement. The central frequency of transducer is 600 MHz.

When increasing the input frequency excitation, the added-mass forces attained high value but there is also a quadratic increase of the attenuation with the driving frequency. A large part of the energy in the plane wave would be attenuated thus compromising the effective ultrasound energy for particles manipulation. Thanks to the lens design, energy can be directed to the focal region and generate highly localized velocity and acceleration fields.

Here we demonstrated the lens structure in a fork structure channel for strong mixing of 9 μm PS particles and separation of bigger particles (30 μm balls) from small

particles (9 μm balls). As shown in figure 3.6.3 a-c, 9 μm PS particles in water are injected into the microchannel slowly by flow controller. When the acoustic field is excited with a 30 dBm input power, a very strong streaming flow is generated and two vortexes are formed around the focus point. Particles in the fluid in lens area appeared to rotate and align themselves along the streamlined shape. In this effect, streaming motions are presented in the particles trajectory which in a spherical focusing. When the input power is increased to 40 dBm, the streaming motions are noticeably more vigorous beyond the beam, and 9 μm PS particles are highly stirred.

To further study the acoustic streaming effect in particles, we mixed 9 μm PS particles and 30 μm PS particles into the same lens structure. As shown in figure 3.6.3 d-f, in 30 dBm input power which generated very strong streaming, both large particles and small particles are yielded to the acoustic field and move in a votex. However, when the input power is decreased to -10dBm, the big particles start to move in a straight line to the focus point, while the small particles are still following the vortex streamlines. After several seconds big particles which successfully reach the focus point would stay still. Then big particles are distinguished and separated from small particles in a non-contact mode.

As the acoustic radiation force is proportional to the volume of particles, particles with larger diameters suffered stronger acoustic force than smaller particles (proportional to its cubic radius). When the input power is not high enough, streaming force is unable to drive big particles along the vortex and keep 30 μm particles stable in motionless. On the other side, 9 μm particles with smaller acoustic force are driven by the force generated by a strong streaming.

3.6.3 Loss evaluation of the chip and matching design

In our microchip integrated high frequency acoustic modulus, the energy loss from emitter to receiver is mainly due to the factors:

1. acoustic diffraction in the propagation;
2. acoustic transmission losses between silicon and liquid;
3. power loss of the transducer due to mismatching of impedance.

These losses will reduce the amplitude of useful signals and increase the noise, which make it difficult for our high sensitivity acoustic characterization and actuation.

Taking our 1 vertical mirror structure as an example, the ZnO transducer patterns are designed as a rectangle with dimension of 120 × 160 μm^2, and the acoustic propagation distance from generator to the microchannel is 2580 μm. Using the equation of the diffracted beam width $h_{-3dB} = 1{,}4\lambda\frac{d}{a}$, the generated acoustic beam can be estimated as a larger rectangle with dimension of 516 × 722 μm^2. The diffraction loss then is deduced as 13dB from the area ratio. Higher frequency used can avoid larger acoustic diffraction but introduces higher attenuation. Larger width of the transducer and lower propagation distance can also reduce acoustic diffraction, but the limitation is the global geometry of each modulus in the chip.

When the acoustic beam transmits the microchannel with water, transmission loss happens due to the mismatching of acoustic impedance. The reflection coefficient is given as $r = \frac{Z_{Si}-Z_{water}}{Z_{Si}+Z_{water}}$, where acoustic impedance of silicon Z_{Si} is 20 MRayl, acoustic impedance of water Z_{water} is 1.5 MRayl, and reflection coefficient r is calculated as 0.86, thus the transmission coefficient $t = \sqrt{1-r^2}$ can be deduced as 0.5, that means for each acoustic propagation between silicon and water 3 dB is lost.
To achieve the acoustic impedance, a simple way is to deposit a layer film on the sidewall of the microchannel, meanwhile, the acoustic impedance of this layer should meet the value $Z_p = \sqrt{Z_{Si}Z_{water}}$, where Z_p is the characteristic impedance. For the previous 1 GHz frequency acoustic detection, 4 μm SiO_2 layer was used on the channel wall for a better acoustic energy transmission. However, for 500 MHz acoustic sensor, 8 μm SiO_2 layer is required as a matching layer but it is very difficult in the fabrication. On the other hand, the acoustic matching layer is not obligatory for lower frequency actuator. This acoustic loss can be compensated by increasing the input power.
Let us consider a piezoelectric transducer the electrical impedance of which is:
$Z(\omega) = R_e(Z(\omega))+j\Gamma_m(Z(\omega))$ where $R_e(Z(\omega))$ is the real part of impedance and $j\Gamma_m(Z(\omega))$ is the imaginary part of impedance. ω is the working frequency of the transducer. When the transducer is excited by a signal source with 50 Ω internal resistance, its electrical power loss

$$L|_{dB} = 10lg\frac{200\mathrm{Re}(Z(\omega))}{[50+\mathrm{Re}(Z(\omega)]^2+\Gamma m^2(Z(\omega))}$$

In the case of our ZnO transducer with dimension of 120 × 160 μm^2 and of a working frequency of 500 MHz, the impedance can be calculated that $\mathrm{Re}(Z(\omega))$ = 242 Ω and $\Gamma_m(Z(\omega))$ = 1347.5 Ω. Then the power loss can be deduced to be 16 dB.

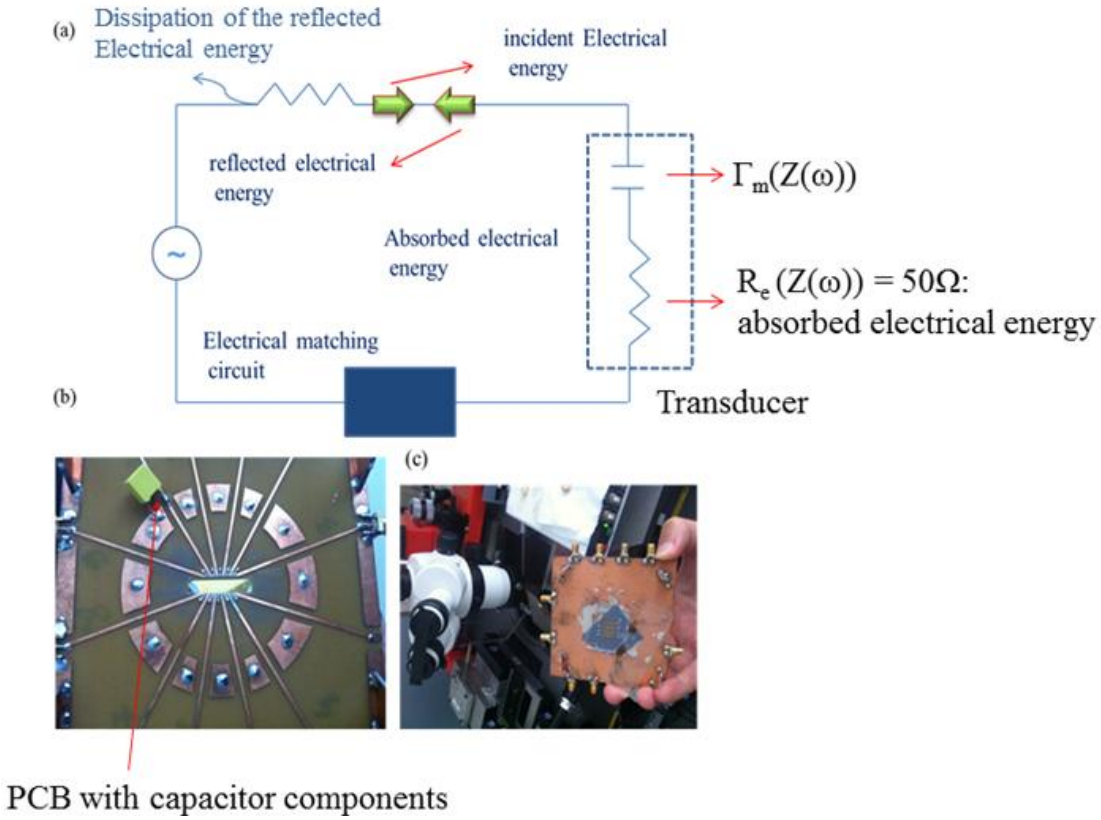

Figure 3.6.4 (a) Principle for electrical matching of transducer. The microfluidic chip is connected to a PCB with gold wire-bonding of transducer (b) and top surface of chip on PCB (c).

The power losses will hinder the working performance of the transducers and increase the needed input power for actuation. Besides, the reflected electrical energy will be dissipated in the internal resistance of the generator, which can damage it.
To avoid this phenomenon, a flexible way is to add an inductance in the matching circuit to tune the transducer at the resonant frequency. As shown in figure 3.6.4, we clamp the actuator chip to a printed circuit board (PCB) while the top electrodes of transducers are also connected with PCB. Gold wire bonding technique is used to achieve a stable circuit electrical connection. Then the circuit elements can be simply bonded to the PCB to keep the load circuit in a 50 Ω real part of impedance as well as the imaginary part of impedance is compensated at the resonant frequency. This simple matching circuit will lead to narrow bandwidth matching circuit. Another way is to use multiple stage microstrip line to keep the initial acoustic bandwidth of the transducer. It will be study in future works.

3.7 Summary and outlook

In this chapter, we experimentally optimized the coating layer thickness on 45° mirrors for avoiding mode conversion. By characterizing the transmission coefficient in cases of 800 nm gold, 1.26 μm copper and 3.8 μm SiO_2 layers on mirrors, the 800 nm gold layer presented a good performance for the longitudinal wave energy propagation. This material also showed the feasible for fabrication and fine homogeneity on mirror structures.

In the acoustic characterization around 500 MHz central frequency, systems of 1 vertical mirror, 2 vertical mirrors and channels with only parallel walls were compared. 1 vertical mirror system exhibit better performance in time domain response with solution introduced of water, KI 2 mol/L, KI 3 mol/L, KI 5 mol/L and 30 μm particles.

Considering the limitation of crystallization in high concentration of KI and the acoustic transmission losses of our system, 3 mol/L KI solution in 200 μm microchannel was noticeable characterized in time domain. Meanwhile, attenuation coefficient of 3 mol/L KI solution was deduced as a function of frequency.

Acoustic cylindrical micro-lens were firstly integrated in microfluidic chip and presented high-sensitivity for KI concentration characterization, as well as particles detection. In addition, the temperature variation of water can also be reflected by acoustic lens in the reflected responses. On the other side, channel with parallel sidewalls was used to characterize the on-chip water temperature in an estimated resolution of 0.1 °C.

In the frequency range of 500~650 MHz, a high-frequency acoustic actuator in lab-on-chip was demonstrated to mix, trap and separate particles with low input power from 0 dBm up to 30 dBm. 30 μm PS particles and 9μm particles were separated in the lens system. An electrical matching network is under study for maximal energy transmission. We are aiming at capture and release human cells clusters using low input power, and manipulate single cancer cell in microfluidic chip for cell culture and in situ analysis.

References

[1] Agilent (June 9, 2003), Electronic vs. Mechanical Calibration Kits: Calibration Methods and Accuracy, White Paper, Agilent Technologies.

[2] J. Choma & W.K. Chen (2007), "Feedback networks: theory and circuit applications", Singapore: World Scientific. Chapter 3, p.225 ff. ISBN 981-02-2770-1.

[3] P. Campistron, J. Carlier, N. Saad, J. Gao, M. Toubal, L. Dupont, G. Nassar, and B. Nongaillard, "High Frequency Ultrasound, a Tool for Elastic Properties Measurement of Thin Films Fabricated on Silicon", Advanced Materials Research, vol. 324, pp. 277–281, Aug. 2011.

[4] S. Wang, J. Gao, J. Carlier, P. Campistron, A. NDieguene, S. Guo, O. B. Matar, D. -C. Dorothee, and B. Nongaillard, "Controlling the transmission of ultrahigh frequency bulk acoustic waves in silicon by 45° mirrors," Ultrasonics, vol. 51, no. 5, pp. 532–538, Jul. 2011.

[5] S. Li, J. Carlier, F. Lefebvre, P. Campistron, D. Callens, G. Nassar, and B. Nongaillard, "Optimization of high Frequency 45° Acoustic Mirrors for Lab on Chip Applications", Physics Procedia, Volume 70, 2015, Pages 918–922, Proceedings of the 2015 ICU International Congress on Ultrasonics, Metz, France.

[6] J. Gao，J. Carlier，S. Wang，P. Campistron，D. Callens, S. Guo, X. Zhao and B. Nongaillard, "Lab-on-a-chip for high frequency acoustic characterization", Sensors and Actuators B: Chemical, Volume 177, Pages 753–760, Feb 2013.

[7] J. Attal and C. F. Quat, "Investigation of some low ultrasonic absorption liquid", Acoust. Soc. Am., Vol. 59, No. 1, January 1976.

[8] H. Zhang, C. H. Chon, X. Pan and D. Li, "Methods for counting particles in microfluidic applications", Microfluidics and Nanofluidics, December 2009, Volume 7, Issue 6, pp 739-749.

[9] A. NDIEGUENE, "Contribution au développement de microcomposants pour la caractérisation ultrasonore en canal microfluidique sur silicium : modélisation de la propagation", L'UNIVERSITE DE VALENCIENNES ET DU HAINAUT CAMBRESIS, 2011.

[10] V. Miralles, A. Huerre, F. Malloggi and M. C. Jullien, "A Review of Heating and Temperature Control in Microfluidic Systems: Techniques and Applications", Diagnostics 2013, 3, 33-67; doi:10.3390/diagnostics3010033

[11] G. Tang, D. Yan, C. Yang, H. Gong, J. C. Chai and Y. C. Lam, "Assessment of Joule heating and its effects on electroosmotic flow and electrophoretic transport of solutes in microfluidic channels", Electrophoresis. 2006 Feb; 27 (3):628-39

[12] F. J. Disalvo, "Thermoelectric Cooling and Power Generation", Science 285 (5428): 703–6.

[13] H. Watzig, "The measurement of temperature inside capillaries for electrophoresis using thermochromic solutions", Chromatographia1992, 33, 445-8.

[14] D. Ross, M. Gaitan, and L. E. Locascio, "Temperature Measurement in Microfluidic Systems Using a Temperature-Dependent Fluorescent Dye", Anal.

Chem. 2001, 73, 4117-4123
[15] R. Samy, T. Glawdel, and C. L. Ren, “Method for Microfluidic Whole-Chip Temperature Measurement Using Thin-Film Poly(dimethylsiloxane)/Rhodamine B”, Anal. Chem.2008,80,369-375.
[16] M. E. Lacey, A. G. Webb and J. V. Sweedler, “Monitoring temperature changes in capillary electrophoresis with nanoliter-volume NMR thermometry”, Anal. Chem., 2000, 72, 4991–4998.
[17] S. H. Kim, J. Noh, M. K. Jeon, K. W. Kim, L. P. Lee and S. I. Woo, “Micro-Raman thermometry for measuring the temperature distribution inside the microchannel of a polymerase chain reaction chip”, J. Micromech. Microeng, 2006, 16, 526–530.
[18] J. C. Hindman, “Proton resonance shift of water in the gas and liquid states”, J. Chem. Phys.1966, 44, 4582-92.
[19] K. L. K. Liu, K. L. Davis and M. D. Morris, “Raman spectroscopic measurement of spatial and temporal temperature gradients in operating electrophoresis capillaries”, Anal. Chem.1994, 66, 3744-50
[20] G. W. Willard, “Temperature coefficient of ultrasonic velocity in solutions”, J. Acoust. Soc. Am. 1947, 19, 235.
[21] J. M. M. Pinkerton, “The Absorption of Ultrasonic Waves in Liquids and its Relation to Molecular Constitution”, Proc. Phys. Soc. Section B, Volume 62, Issue 2, 1949, pp. 129-141.
[22] C. E. Brennen, “A Review of Added Mass and Fluid Inertial Forces”, Naval Civil Eng. Lab Port Hueneme, Calif., 1982, Report CR82.010.
[23] L. V. King, “On the Acoustic Radiation Pressure on Spheres”, Proceedings of the Royal Society A Mathematical Physical and Engineering Sciences, 01/1934; 147(861):212-240.
[24] Q. Qi and G. J. Brereton, “Mechanisms of Removal of Micron-Sized Particles by High-Frequency Ultrasonic Waves”, IEEE TRANSACTIONS ON ULTRASONICS, FERROELECTRICS, AND FREQUENCY CONTROL, VOL. 42, NO. 4, JULY 1995

Conclusions and perspectives

We successfully achieve a high frequency bulk acoustic device for the realization of both characterization and manipulation in lab on chip field. The objective of this thesis is to optimize the device for characterization in broadened frequency range and on-chip manipulation of particles/cells. To achieve this goal, we have to optimize the design and fabrication for transfer acoustic energy and reduce the losses. A primary purpose is to reduce working frequency from 1GHz to 500 MHz. We have improved the integrated acoustic system developed in a previous PhD work and developed new acoustic functions. Integrated bulk acoustic wave actuator was firstly implemented in this frequency range. The improvements conclude as follows:

- Technology improvements: The change of the central frequency induced various modification of parameters in each part of the final device. Depth of 45° mirrors was enlarged to 210 μm maximum with smooth surface, high flatness and controllable underetching. Depth of channel and vertical mirrors are also prolonged to 150 μm with vertical sidewalls.

Matching layers (gold, copper and silicon oxide) on mirrors has been studied from the point of view in theory, simulation and experiments verification. We have demonstrated that conversion mode can be avoided and that most of the longitudinal wave energy is kept after reflection. Finally we choose gold layer as our matching layer and validate the efficiency of such matching layer.

Thicker transducers of 6 μm fabrication were integrated in our device. To do this, we change the deposit method, ground electrode and separate the sputtering process along with annealing.

- System optimization: We validate new design: one vertical mirror system and single lens structure in reflection mode. In comparison with the previously used two vertical mirrors system, the new design shortens acoustic propagation path in order to limit diffraction. The lens structures have sensitivity compared to one vertical mirror system due to the reflection mode used which filter parts of acoustic noise. Moreover, lens structures are optimized and used to generate strong acoustic streaming for particles manipulation.
- Applications:
  1. We firstly achieve acoustic measurements for on-chip temperature detection of water.
  2. Firstly achieve on-chip attenuation coefficient characterized of liquid in frequency domain.
  3. Firstly achieve on-chip bulk acoustic manipulation of particles in high frequency range: particle deflection, fast mixing and separation *via* radius.

To extend this task, we aim at improving signal-to-noise ratio and the portable device preparation:

1. Optimization of the microsystem to reduce the acoustic losses: we have to limit the acoustic propagation distance from the emitter to the receiver.

2. Fabrication of a matching layer on the sidewalls of microchannel, in order to optimize the acoustic energy transmission (reduce the acoustic losses from silicon wafer to liquid).
3. Validate the device (wire bonding with a PCB) in Wuhan University. The biological experiments will be implemented on this portable device.

In the long term plan, we target the biological and medical applications:
1. Separate cancer cells (larger dimension) and white cells (smaller dimension) and red blood cells (smaller dimension and easy to be deformed): potential for circulating tumor cells (CTCs) separation from patient blood.
2. Acoustic modulus integrated in the immune-chips for cell array culture.
3. a miniaturization device for acoustic detection and sorting (similar to FACS): low cost and portable device.

Publications

1. Li S, Lamant S, Carlier J, Toubal M, Campistron P, Xu X, Vereecke G, Senez V, Thomy V, Nongaillard B. High-Frequency Acoustic for Nanostructure Wetting Characterization, Langmuir 05/2014; 30(25).
2. S. Li, J. Carlier, F. Lefebvre, P. Campistron, D. Callens, G. Nassar, B. Nongaillard, Optimization of high frequency 45˚acoustic mirrors for lab on chip applications, International Congress on Ultrasonics, ICU 2015, Metz, France, may 10-14, 2015, Phys. Procedia 70 (2015) 918-922
3. Carlier J., Toubal M., Li S., Campistron P., Callens D., Thomy V., Senez V., Nongaillard B. High frequency acoustic reflectometry for solid/liquid interface characterization : application to droplet evaporation, International Congress on Ultrasonics, ICU 2015, Metz, France, may 10-14, 2015, Phys. Procedia 70 (2015) 459-462
4. Li S, Lefebvre F. Carlier J, G. Nassar, Campistron P, Callens D, Nongaillard B, High frequency acoustic 45˚ mirrors coating for longitudinal wave transmission optimization : application to wave guiding in silicon, To be submitted.